THESE

PRESENTEE A

L'UNIVERSITE DE PAU ET DES PAYS DE L'ADOUR

ECOLE DOCTORALE DES SCIENCES EXACTES ET DE LEURS APPLICATIONS

EN COTUTELLE AVEC **L'UNIVERSITE D'UPPSALA (SUEDE)**

PAR

Bertrand PHILIPPE

POUR OBTENIR LE GRADE DE

DOCTEUR

Spécialité : **Chimie-Physique**

Etude d'interfaces électrode/électrolyte dans des batteries Li-ion par spectroscopie photoélectronique à différentes profondeurs

---

Soutenue le 24 mai 2013 devant le jury composé de :

Mme. M. ALFREDSSON	Senior Lecturer Université de Kent, UK	Rapporteur
Mme. R. PALACIN	Directeur de recherche ICMAB-CSIC, Espagne	Rapporteur
M. J.-P. RUEFF	Directeur de recherche Synchrotron Soleil	
M. P.-E. LIPPENS	Directeur de recherche Université Montpellier 2	
Mme. K. EDSTRÖM	Professeur Université d'Uppsala, Suède	Directeur de Thèse
M. H. RENSMO	Professeur Université d'Uppsala, Suède	
Mme. D. GONBEAU	Directeur de recherche au CNRS IPREM, Université de Pau	Directeur de Thèse
M. R. DEDRYVERE	Maître de Conférences HDR IPREM, Université de Pau	Co-directeur de Thèse

Acknowledgments

café ou pendant le déjeuner toujours très joviales. Un grand merci à ma collègue et ami Lulu, nous avons commencé notre thèse presque en même temps et tu as toujours été d'une grande écoute et d'un grand soutien au cours de ces trois ans et demi. Un grand merci à mes anciens et actuels colocs de bureau, Laurent, Nathalie, Tien Khoa puis Samantha et Arnaud. Lucile, Pierre et Wanjie, se fut un plaisir de vous rencontrer et je vous souhaite le meilleur pour votre fin de thèse. Je remercie également les personnes croisées au sein de l'équipe : Sébastien C., Benoit, Alexis, Marianne et Jennifer.

Je souhaite également remercier Jean-Bernard pour son aide précieuse avec les équipements au sein du laboratoire, mais aussi pour avoir partagé ta connaissance des appareils qui fut très importante pour réaliser les manips, et également lors de notre session à Bessy. Un grand merci à l'administration, Jany et Patricia pour votre disponibilité et gentillesse.

Pour finir, je voudrais remercier les autres thésards et post-doc croisés au sein de l'IPREM: Romain, Alain, Marc, Hind, Oihan, Filippo, Dorra, Vincent. Merci pour les bons moments passés au labo mais surtout en dehors lors d'after-work ou festivals. Merci également de votre aide lors de ma période d'infirmité☺.

In the Synchrotron facilities, I would like to thank Mihaela Gorgoi for her support at KMC-1 beamline and her unfailing quick feedbacks and answers to my questions.

Je voudrais remercier mes amis d'enfance, de lycée ou d'école : Dam, Sandrine, Hervé, Aurélien et Kiki, Anaïs, Margaux, Podo. Un grand merci à Alex pour ton soutien et tes encouragements.

Enfin, je voudrais remercier ma famille, mon frère et mes parents pour m'avoir soutenu et poussé très vite vers les études. Un Grand Merci !

Bertrand PHILIPPE

Contents

Abbreviations

AC	Activated carbon
ARXPS	Angle-resolved X-ray photoelectron spectroscopy
CB	Carbon black
CMC	Carboxyl methyl cellulose
CNT	Carbon nanotube
CTAB	Cethyl trimethylammonium bromide
CVD	Chemical vapor deposition
EC	Ethylene carbonate
EIS	Electrochemical impedance spectroscopy
ESCA	Electron spectroscopy for chemical analysis
EMC	Ethyl methyl carbonate
DEC	Diethyl carbonate
DMC	Dimethyl carbonate
FEC	Fluoroethylene carbonate
FTIR	Fourier transform-Infrared spectroscopy
FWHM	Full width at half maximum
HAXPES	Hard X-ray photoelectron spectroscopy
(HR)TEM	(High resolution) transmission electron microscopy
IMFP	Inelastic mean free path
LE	Liquid electrolyte
LiPON	Lithium phosphorus oxynitride
MCMB	Mesocarbon microbead
NF	Nanofiber
NMP	N-Methylpyrrolidone
NMR	Nuclear magnetic resonance
NP	Nanoparticle
NT	Nanotube
OCV	Open circuit voltage
PAA	Polyacrylic acid
PAN	Polyaniline
PC	Propylene carbonate
PCD	Polycarbodiimide
PEO	Polyethylene oxide
PES	Photoelectron spectroscopy
PVDF	Polyvinylidene fluoride
PVD	Physical vapor deposition
(RT)IL	(Room temperature) ionic liquid
SBR	Styrene-butadiene rubber
SEI	Solid electrolyte interphase
SEM	Scanning electron microscopy
SHE	Standard hydrogen electrode
SPE	Solid polymer electrolyte
SR	Synchrotron radiation
TEOS	Tetraethyl orthosilicate
TOF-SIMS	Time-of-Flight Secondary Ion Mass Spectrometry
TMO	Transition metal oxide
TVD	Thermal vapor deposition
VC	Vinylene carbonate
XPS	X-ray photoelectron spectroscopy
XRD	X-ray diffraction

Introduction

Reducing the consumption of fossil fuels and the replacement of these resources is currently a necessity in our energy demanding society. First, fossil fuels reserves are finite and these resources (coal, oil and gas) could be consumed in less than 100 years if no alternative energy sources are developed. In addition, it is now an environmental obligation to limit the greenhouse gas emissions resulting mainly from the exploitation and the use of fossil fuels that exacerbate global warming. The motivation to develop renewable energies has never been so important and a main goal is the slow transfer from fossil fuels towards new sources of energy. Energy storage technologies, such as rechargeable batteries, play an important role since the last 20 years. In particular, the Li-ion battery technology occupies a major position because it exhibits higher gravimetric and volumetric energy density and longer lifespan than traditional rechargeable battery technologies such as lead-acid, Ni-Cd, etc. The Li-ion technology quickly dominated the market of power sources for portable electronics. However, more recently other markets are emerging, such as stationary storage or batteries for transportation. Many scientists are dedicated to the development of low cost, safe, rechargeable battery of high voltage, capacity and rate capability for a potential mass market of electric vehicles.

A Li-ion battery is composed of several electrochemical cells connected in series and/or in parallel. An electrochemical cell is composed of a positive and a negative electrode separated by an electrolyte (lithium salt in an organic solvent) and a separator that prohibits contact between the two electrodes. Most commercial lithium-ion batteries use carbonaceous materials as negative electrode. More recently, metals and semimetals that can electrochemically form alloys with lithium have been investigated as interesting alternatives, because they lead to very high rechargeable capacity values. Among these materials, silicon and tin can alloy with 3.75 and 4.4 Li atoms per atom (i.e. $Li_{15}Si_4$ and $Li_{22}Sn_5$) which corresponds to a maximum capacity of 3578 mAh.g^{-1} and 994 mAh.g^{-1}, respectively. This is much higher than the conventional materials commercialized, namely the graphite with a theoretical capacity of 372 mAh.g^{-1}.

A crucial problem is the large volume changes undergone upon alloying and de-alloying with lithium, which result in strong mechanical strains and subsequent loss of electrical contacts between the active particles (Si or Sn), the conductive matrix and the current collector. Several strategies have been considered to reduce this volume change and improve the stability of the electrodes, either by using nanosized particles, polymeric binders, or specific cycling conditions (current rates, cut-off voltages, pre-cycling). Besides, silicon has the advantage, compared to tin, to be a light and abundant element, so it appears as an ideal candidate for the next generation of negative electrodes.

However, despite these improvements, cycling performances of silicon/tin electrodes still remain unsatisfactory for use in practical Li-ion batteries. Particularly, some limitations are due to electrode/electrolyte interfaces. Therefore it is necessary to better understand this interface reactivity. Compared to interface phenomena on carbonaceous electrodes that have been extensively studied for many years, much less research attention has been devoted to interfacial mechanisms on silicon or tin negative electrodes. However, the formation of the Solid Electrolyte Interphase (SEI) layer is recognized as one of the key points for Li-ion battery performance and safety, which are strongly dependent on the stabilization of electrode/electrolyte interfacial reactions.

This PhD work has started in 2009 in this context. A co-shared position was created within Alistore ERI (European Research Institute) and was performed under the joint supervision of two laboratories:
- IPREM-ECP located at Université de Pau et Pays de l'Adour in France
- The Department of Chemistry-Ångström laboratory, located at Uppsala University in Sweden.

In this thesis, these two laboratories, forming the "PES/XPS Alistore platform", have combined their expertise in the field of Li-ion batteries materials and surface analysis using photoelectron spectroscopy (PES). X-ray Photoelectron Spectroscopy is recognized as a powerful technique to obtain chemical information on materials surfaces and the electronic structure of solids and this technique has become one of the most efficient to chemically characterise electrode/electrolyte interfaces in Li-ion batteries.

The scope of this thesis was to investigate and have a better understanding of the mechanisms occurring at the electrode/electrolyte interfaces of new negative electrode materials by improving photoemission spectroscopy methodology.

In our approach, by varying the energy of the X-ray photons a non-destructive depth-resolved analysis has been developed, as an alternative to the destructive argon ion sputtering. With this aim, the electrodes were studied by using low energies (100-800 eV) corresponding to soft X-ray PES, middle energy (1486.6 eV) corresponding to in-house XPS and high energies (2000-7000 eV) corresponding to hard X-ray PES. Soft and hard X-ray PES were performed at two different synchrotron facilities: MaxIV Laboratory, Lund, Sweden; and Helmholtz Zentrum Bessy, Berlin, Germany. The increase of the photon energy results in an increase of the kinetic energy of the photoelectrons. Since the inelastic mean free path of the photoelectrons is highly dependent on their kinetic energy this leads to a significant change of the PES analysis depth. The variation of the photon energy allows thus to highlight the extreme surface of the particles or, at the opposite, to enhance the signal of the bulk. This experimental approach provides information about the repartition of species at the surface of the samples and avoids the argon-ion sputtering technique commonly used for depth-profiling, which is destructive for delicate surfaces such as those of Li-ion battery electrodes.

This thesis is divided into three chapters that describe the work carried out and the results obtained, and are then summarized in the final conclusions. A brief outline of the chapters is given below.

Chapter one provides a general overview on Li-ion batteries and describes the main components found in a battery. Positive and negative electrodes and electrolytes studied so far are described and their advantages and drawbacks are pointed out. General reactions occurring at the negative electrode/electrolyte interface are explained. At the end of this chapter, special attention has been devoted to silicon negative electrodes and a review of the current approaches used to limit the volume expansion of such a material observed upon insertion/extraction of lithium is addressed.

Chapter two develops the experimental work performed during this thesis and the approaches adopted are explained. Sample preparation and electrochemical tests are described and an important section is devoted to the theory of photoelectron spectroscopy. An approach by varying the energy of the X-ray photons for non-destructive depth-resolved analysis was developed and an important part of the results presented were obtained with this method. General aspects of in-house PES and synchrotron PES are described in this chapter.

Chapter three reports the main results obtained during this thesis and it is split in two parts. The first part is focused on the studies of Si/C/CMC composite electrodes. The interfacial phenomenon occurring during the first electrochemical cycle was studied as well as upon a long-term cycling. Two different salts have been used: a classical one ($LiPF_6$) and a new salt (LiFSI), the latter showing very promising performance. The second part of this chapter is devoted to a step by step analysis of the first electrochemical cycle of $MnSn_2$, a new tin-based intermetallic compound.

CHAPTER I

General aspects on Li-ion batteries
and state of the art

1. The emergence of Li-ion batteries

1.1. Historical development of battery systems

A battery is an electrochemical device that converts chemical energy into electrical energy through reduction-oxidation reactions occurring at the electrodes. The term battery often refers to a single electrochemical cell but it can equally well refer to a stack of electrochemical cells, in series and/or in parallel. This thesis will mainly discuss single cell batteries. An electrochemical cell is composed of three main components: a positive electrode, an electrolyte and a negative electrode

We can distinguish two types of batteries: the primary (or galvanic) and secondary (or electrolytic) batteries. In a primary battery, the redox reactions taking place at the electrodes are not reversible, so the battery cannot be recharged once used. In secondary batteries, reactions are reversible when an external voltage is applied to the electrode (rechargeable batteries).

The first primary battery was made in 1800 by Alessandro Volta (voltaic cell) by assembling piles of zinc plates alternating silver with copper plates and by using a cloth of acid in between as the electrolyte. Later came the well-known Daniell cell (1836) consisting of a copper pot filled with a copper sulphate solution in which an unglazed earthenware container filled with sulphuric acid and a zinc electrode was immersed. Manganese was first used in a primary battery as suggested by the French engineer, Georges Leclanché ($Zinc/MnO_2$) in 1866. Even today manganese dioxide is found as an electrode material in many different battery systems.

The first rechargeable battery, which is still widely used in automobiles, was the lead-acid battery (Pb/PbO_2 in H_2SO_4) invented by Gaston Planté (1859).

The replacement of the acid as electrolyte appeared in 1899 with the first rechargeable alkaline battery Ni-Cd (Nickel-Cadmium in KOH) created by the Swedish engineer Waldemar Jungner. Similar to this system, the Ni-MH battery (Nickel/metal hydride in KOH) battery was invented in 1967 at the Battelle Geneva Research Center in Switzerland. The negative electrode was a hydrogen-adsorbing alloy instead of the toxic cadmium leading to a significant increase of the cell capacity and cycle life.
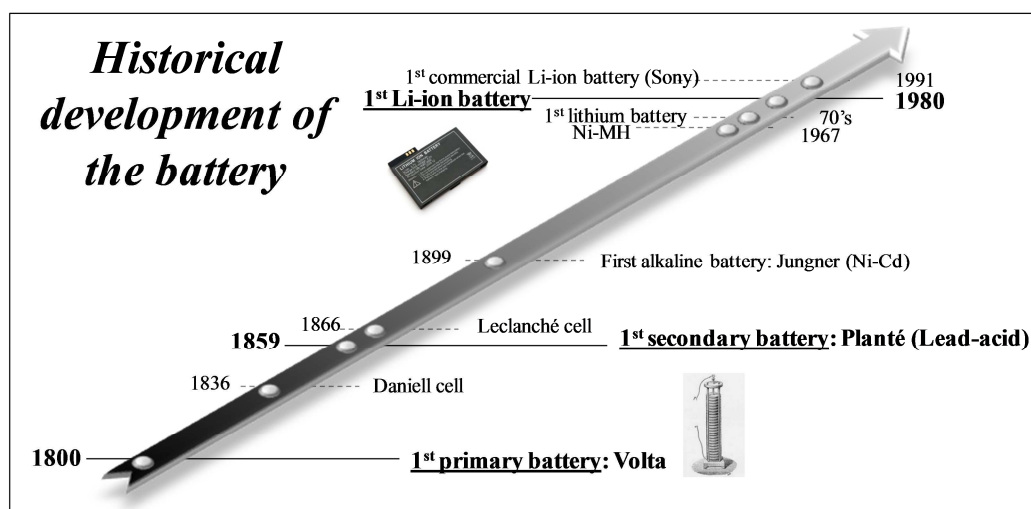
Figure I.1 : Historical development of the battery from the first primary battery to the first commercialized Li-ion battery.

Since the 1970's, a lot of attention has been devoted to the use of lithium in batteries. First, it was used in primary lithium batteries (mainly as MnO_2), and then it has become common in secondary lithium-metal and Li-ion batteries in the 1980's and early 1990's. Figure I.1 represents a time scale with these main events.

Lithium is an interesting element because it is the lightest solid element ($M_w=6.941$ g.mol^{-1}) thereby, it presents the lowest density ($\rho=0.54$ g.cm^{-3}) and the redox couple Li$^+$/Li has the lowest electrochemical potential value among all the metals (-3.04 V *vs.* SHE). As a consequence, batteries using lithium metal offer the possibility of high voltage and high energy density.

1.2. The rechargeable battery: from Li(m) to Li-ion batteries

The first concept of a rechargeable lithium battery was successfully achieved and commercialized by Exxon using a transition metal sulfide as cathode: the titanium sulfide TiS_2.[1] Other chalcogenides (mainly sulfides and selenides)[2] but also oxides were then investigated as positive electrode materials. The latter are more oxidizing than sulfides, which means that they have a higher insertion potential. Some examples of the first materials are: MoS_2, $NbSe_3$,[3] MoO_3, MnO_2 [4] or the vanadium oxides V_2O_5 [5] and V_6O_{13}.[6]

However, the main drawback of these systems was associated to the use of the highly reactive metallic lithium as the negative electrode and the formation of dendrites upon cycling, thus leading to safety problem because of internal short circuits. The risk of thermal runaway coupled with the release of toxic fumes was too high for these batteries to be commercialized. Even though the use of a solid electrolyte was suggested to prevent dendrite formation, this safety issue was the starting point for studying other systems leading to the Li-ion technology in the 1980's.

A crucial improvement has been to replace the metallic Li with a lithium intercalation compound which has a chemical potential close to that of lithium metal.[7] Such a battery does not contain metallic lithium and the process is based on Li-ions "rocking back and forth" between the two electrodes during charge and discharge. The Li-ion battery technology was born.

In the 1980's, Goodenough *et al.* focused their work on studying lithium-containing transition metal oxides (TMO): $LiCoO_2$ [8] or $LiMn_2O_4$,[9] and at the same time Yazami *et al.* [10] showed that graphite was able to electrochemically accept and release lithium-ions at a relative low voltage (0.2V *vs.* Li$^+$/Li). These works led to the commercialisation of the Li-ion battery by SONY in 1991[11] with $LiCoO_2$ as cathode and graphite as anode. It is important to note that this commercialisation depended on the finding of a lithium-containing positive electrode material and $LiCoO_2$ was the choice which was an invention by Goodenough. Earlier positive electrode materials did not contain lithium and the source of lithium was provided by the negative electrode. These early materials usually inserted lithium electrochemically at potentials below 3 V *vs.* Li$^+$/Li, and their lithiated states were usually not stable to air and moisture. On the contrary, lithium-containing transition metals (TMO) (discharged state) act as the lithium source allowing for the replacement of the Li metal as the negative electrode. They present a higher potential (~4V) and are stable to air and moisture.
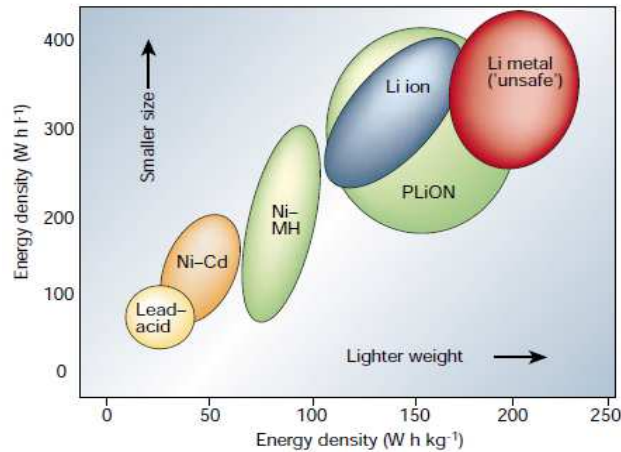
Figure I. 2 : Comparison of the different battery technologies in terms of volumetric and gravimetric energy density. Reprinted with permission from ref [12].

The Li-ion technology quickly dominated the market of power sources for portable electronics and this can easily be explained by Figure I. 2 which compares the gravimetric and volumetric energy density of the main rechargeable technologies. We can see that more compact and lighter devices can be achieved which constitute a key point for practical applications. Today, the main domains for Li-ion batteries are portable devices, transportation and stationary storage.[13]

1.3. Future rechargeable systems - beyond lithium?

The Li-ion technology is not the final point and battery performances can still be considerably improved as well as the cost can be lowered by using various alternative technologies.[14] Recently, the Li-air (Li-O$_2$) or Li-Sulfur (Li-S) systems have been investigated with the goal to increase the gravimetric and volumetric energy density compared to the classical Li-ion batteries.[15]

The replacement of lithium by its following element in the alkaline family; sodium (Na), is another interesting alternative because sodium intercalation chemistry is very similar to that of Li and Na has the advantages of being much more abundant (so cheaper) than Li and easier to recover.[16]

In the next part, we will describe the specifications of Li-ion technology and explain its operating principle based on the classic battery system developed by Sony. The electrochemical characteristics used to evaluate battery performance will be defined, and finally we will focus on the driving force behind the current research in Li-ion battery, the objectives and the main issues to be addressed.

2. Li-ion battery

2.1. Principle of a Li-ion battery

The principle of a Li-ion battery is based on the conversion of chemical energy into electrical energy through two half-cell redox reactions: a reduction half-cell reaction at one electrode and an oxidation at the other. For the Li-ion technology (also referred to as *rocking-chair battery*), this conversion is the result of the reversible exchange of Li^+ ions and electrons between the positive and the negative electrode.

Most of the commercial Li-ion batteries are based on intercalation compounds that can reversibly host Li^+ ions in their structure at both the positive and negative electrodes. The electrode with the highest potential is referred to as the positive electrode and generally it consists of a lithium containing transition metal oxide (e.g., $LiCoO_2$, $LiMn_2O_4$, $LiFePO_4$) whereas carbonaceous materials are used as negative electrodes (electrode with the lowest potential).

The electrodes are separated by an ion conducting, electronically insulating medium: the electrolyte which generally is liquid and composed of a lithium salt dissolved in a mixture of organic solvents.

The active materials are deposited on current collectors (copper for the negative, and aluminium for the positive electrode). A separator, generally made of a microporous polyethylene or polypropylene film is used as a physical barrier between the electrodes in the presence of a liquid electrolyte. This barrier can also be a solid polymer electrolyte, a lithium-conducting glass (LiPON) or an ionic liquid.

In the first commercialized Li-ion battery, layered structure electrodes, $LiCoO_2$ and hard carbone, were used as positive and negative electrodes, respectively. $LiPF_6$ was used as the electrolyte salt in the organic solvent. Figure I. 3 illustrates the operating principle of this Li-ion battery upon charge and discharge.

In classical Li-ion batteries, the first step will always be to charge the battery by extracting the lithium-ions from the positive electrode (oxidation) and to intercalate them into graphite at the negative electrode (reduction). The ions migrate through the electrolyte while the released electrons migrate from one electrode to the other via an external circuit to maintain the neutrality of the electrodes. During the charge, these reactions are forced so an external power source is necessary. The opposite redox reactions occur spontaneously during the discharge.
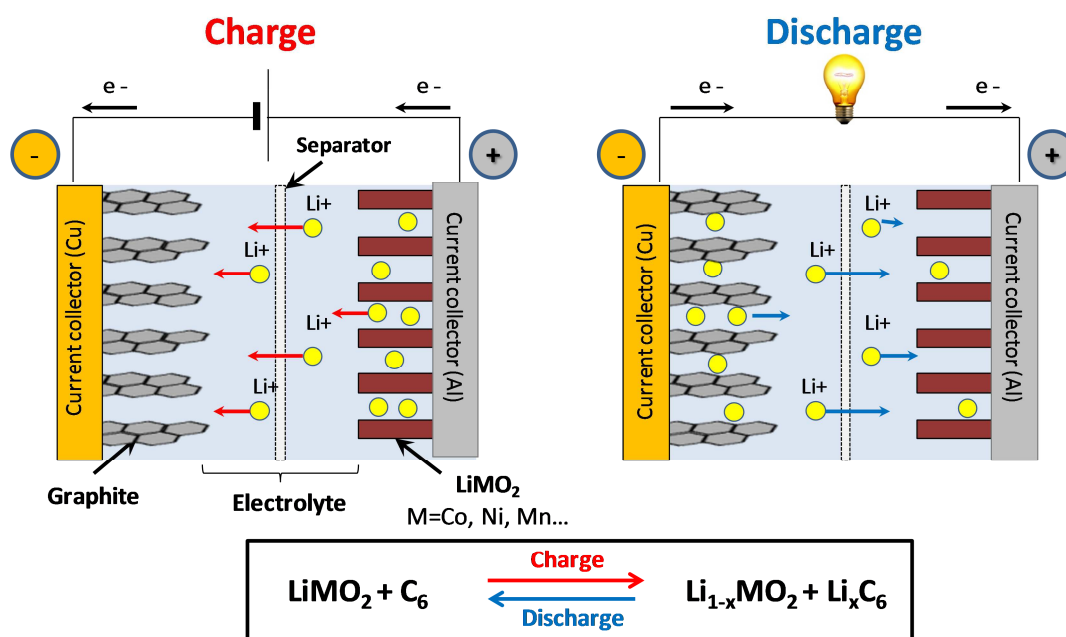
Figure I. 3 : A schematic representation of the operating principle of a Li-ion battery.

By definition, the electrode where a reduction takes place is the cathode while the electrode where oxidation occurs is the anode. However, oxidation and reduction are carried out at each electrode in a rechargeable battery and hence the electrodes are commonly named in accordance with their spontaneously process occurring upon discharge. As a consequence, it is common to find the term cathode for the positive electrode and anode for the negative electrode in the literature, although it is in contradiction to the electrochemical process occurring upon charge.

Other important components in a Li-ion battery:
The scheme in Figure I. 3 shows the main components of a Li-ion battery: the active materials, the electrolyte (salt + solvents) and the current collectors. However, there are many more components composing a real system. The electrodes are made as a composite where additives are used to enhance the performance of the complete system.

The electronic conductivity is improved with the incorporation of **conductive additives**, typically carbonaceous species: graphite, carbon black (CB), activated carbon (AC). More recently carbon nanotubes/nanofibers or graphene[17] have attracted a lot of interest.

Another component usually found in the electrode formulation is a **binder**. The main purposes of the binder is to maintain a mechanical integrity and to ensure a good contact between the active material, the conductive additives and the current collector and thus to maintain a good electronic conductivity. The binder is also crucial for the accommodation of the possible volume expansion usually observed upon lithiation of the active materials. Several polymeric species have been investigated but the poly(vinylidene fluoride) (PVdF) is still the main binder used.

We will see later that there are also additives in the electrolyte.

2.2. Electrochemical aspects and evaluation of battery performance

Battery performance can be expressed by different characteristics:

- ***Cell voltage (U)***

The first important value of an electrochemical cell is the cell voltage U (in Volts) and it is defined as the potential difference between the two electrodes:

$$U = \Delta\mu$$

This voltage is also referred to as open circuit voltage (OCV or V_{oc}) when no net current is applied to the battery.

- ***Capacity (Q)***

The capacity is a measure of the total amount of charge that can be stored in the battery and it is given by the relation:

$$Q = \int_0^t I.dt$$

where I: the current applied through the battery (in Ampere)

t: the time while the current is delivered (in seconds)

Q: the capacity in Coulomb (C) or more usually in Ampere-hours   (Ah),   (1Ah=3600 C).

It is also possible to estimate the theoretical capacity from the number of electrons exchanged per formula unit of the host material (usually assimilated to the number of Li^+ inserted per mole of active material) using the following relation:

$$Q\,(C) = \frac{m.F.\Delta x}{M} \quad or \quad Q(mAh) = \frac{m.F.\Delta x}{3.6M}$$

where m: weight of the active material (g)

M: molecular weight of the active material (g.mol^{-1})

F: Faraday's constant (96485 C.mol^{-1})

Δx: number of electrons exchanged per formula unit of the host material (= number of Li^+ inserted in the host material)

In practice, the specific capacity is used and it is defined as the capacity per unit of weight of active material (gravimetric specific capacity in mAh.g^{-1}) or per unit of volume (volumetric capacity in mAh.dm^{-3}).

Upon galvanostatic testing, current is often expressed as a **C-rate** in order to normalize against battery capacity, so the notation C/n can be used and the definitions are linked to the capacity of the battery. In a first definition, the C-rate is a measure of the time taken to deliver the full capacity of the battery, i.e. C/n means that the maximal theoretical capacity C is obtained upon a discharge (or charge) of n hours.

A second definition is used which corresponds to the time required to exchange one lithium-ion, i.e. C/n means that one Li^+ is inserted (or extracted) in n hours.

- ***Energy (W)***

The energy of a battery is the measure of the amount of energy that the battery can deliver, given in Wh (Watts hour). It is defined by the relation:

$$W = \int_0^t U.I.dt = QU^2$$

where U: the cell voltage (in Volt)

I: the current applied through the battery (in Ampere)

Q: the capacity (in Coulomb or Ah)

t: the time while the current is delivered (in seconds)

The energy is generally expressed per unit of weight (specific energy $Wh.g^{-1}$) or per unit of volume (energy density $Wh.dm^{-3}$).

- ***Power (P)***

The power (in Watts) represents the ability of the battery to quickly deliver electrons and Li-ions, thus it depends on the kinetics of the redox reaction. It is defined as the energy per time unit and depends on the electronic conductivity and Li^+ ion mobility.

$$P = U.I$$

As for the energy, the specific power ($W.kg^{-1}$) and the power density ($W.dm^{-3}$) are generally used.

- ***Cyclability or cycle life***

The cyclability corresponds to the number of discharge-charge cycles that can be carried out before a lower limit of the capacity is reached (usually set as 80% of the initial capacity).

- ***Coulombic efficiency (Eff)***

The coulombic efficiency (%) is the ratio of the charge capacity over the discharge capacity and has to be as close as possible to 100% for a Li-ion battery used in commercial applications.

$$Eff = \left(\frac{Q_{ch}}{Q_{disch}} \right) * 100$$

2.3. Main drawbacks and challenges of the Li-ion technology

Li-ion batteries present several drawbacks: the main one is that any Li consumed by secondary reactions cannot be retrieved leading to capacity loss, poor cyclability or self-discharge. Since the beginning of the 1990's and the first commercial product, researches have been focused on improving the performances of the system, to increase the safety and to decrease the cost. Work is done at different scales of the battery going from the active material to the whole system.

A first challenge is to improve the active materials used as positive and negative electrodes. Future materials need to be able to accommodate as much lithium as possible, and thus, present a larger capacity. On the other hand, the two materials chosen must present a large electrochemical potential difference to reach higher cell potentials (~5V). This increase of cell potential is mainly the focus of the positive side of the battery and the choice of a good redox couple. An overview of the investigated materials is presented in Figure I. 4. In addition to the electrochemical performance, the nature of the materials is an important parameter (shape/size of the particles, etc...). They must also be safe, eventually recyclable and cheap: for example, the replacement of cobalt appears as a necessity mainly because of its cost.

The formulation of the electrode is another important issue. As we said earlier, an electrode is a mixture of active materials, binder and conductive additives, and the assembly process, the choice of the components as well as their proportion have a strong impact on the global performances.
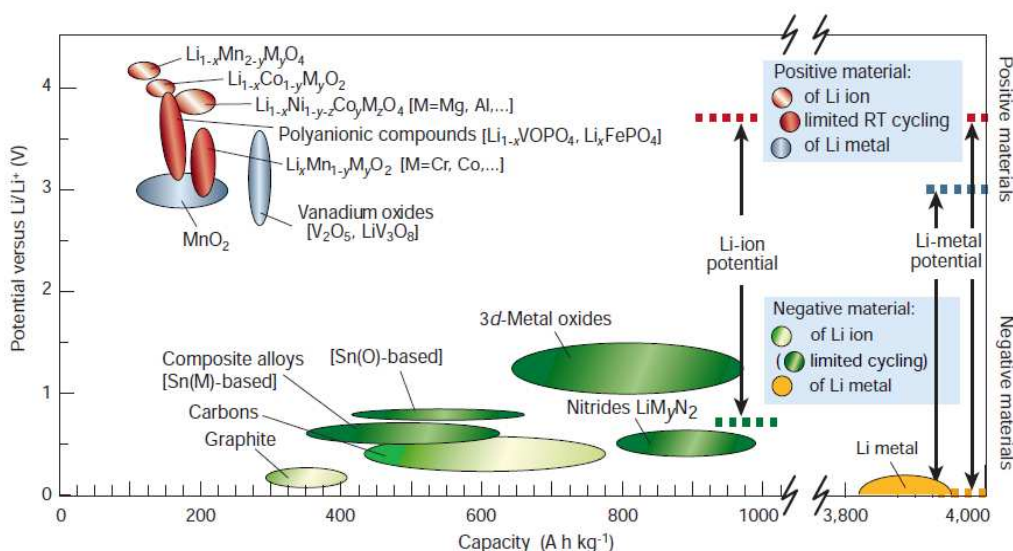
Figure I. 4 : Voltage vs. capacity for current positive- and negative-electrode materials used and investigated for the next generation of rechargeable Li-ions batteries. Reprinted with permission from ref [12].

A lot of attention has also been devoted to the electrolyte and its compatibility with the electrodes. The electrolyte has to be chemically inert in a large electrochemical window. However, in non-aqueous liquid electrolytes, reduction of classical solvents occurs just below 1V (*vs.* Li^+/Li) at the surface of the negative electrode leading to the formation of a passivation layer. This electrolyte/electrode interface is constituted of different decomposition products from the electrolyte. Even if lithium is consumed to form this layer, named SEI (Solid Electrolyte Interphase),[18] once it covers the surface of the electrode, it prevents further decomposition of the electrolyte by an increase of its electrochemical window (function of extended electrolyte that leads to the kinetic stabilisation of the system) (cf. Figure I. 14 later in the thesis). The stability of this layer presents a strong impact on the safety and cyclability of the battery, and its nature will depend on the electrolyte but also on the electrodes.

In the next part of this thesis, we will briefly describe the main materials used and investigated as positive, negative electrodes, and the main components of the electrolyte. An overview of the major degradation reactions and products usually found in the SEI will be given; a special attention will be devoted to the materials selected for study in this PhD thesis.

3. Materials for positive electrodes in Li-ion batteries

3.1. General aspects and requirements

The choice of the positive electrode is crucial in terms of cost, safety, energy and power of the battery. In a Li-ion battery, positive electrodes are commonly referred to as cathodes and they are typically intercalation compounds made of Li-metal oxides, which provide a source of lithium. They are stable in air with a relatively high potential.

The general formula of such intercalation materials can be simplified as $Li_xM_yX_z$, where M is a metal (usually a transition metal) and X the anion (oxides, or polyanions $(XO_4)^{n-}$). To successfully be used as positive electrodes in a Li-ion battery, the material has to fulfil several requirements reviewed by Manthiram [19] or Whittingham [20] and listed below:

- The material should contain a readily reducible/oxidizable ion, for example a transition metal.
- The material should react reversibly with lithium with minimal or no structures changes upon insertion/extraction of the lithium leading to a good cycle life.
- The material may host several Li-ions per formula unit in order to deliver high capacity, and the insertion/extraction process should operate at high voltage (around 4 V) to provide high-energy storage.
- The insertion/extraction process has to be fast to achieve high power density.
- The material should have a good electronic and Li-ion conductivity.
- The material must be thermally and chemically stable, have low cost and be environmentally benign.

In the next part, dedicated to the materials for positive electrodes, an overview of the main materials used in Li-ion batteries will be given. Since the first commercialized Li-ion battery, reversible lithium insertion/extraction has been performed on a variety of compounds containing different transition-metal cations and different structural architectures; they have been described in several reviews.[20,21,22,23,24,25]

The main studied systems are: transition-metal oxides (TMO's), transition metal- chalcogenides (sulfides, selenides, or tellurides) or transition-metal salts with oxoanions (*e.g.*, phosphate, sulphate or arsenate) also referred to as polyanionic structures. It was established that polyanionic compounds and TMO were more attractive candidates than chalcogenides due to their higher cell voltages *vs.* Li^+/Li giving high specific energies. They present a better reversibility than sulfides and they fulfil most of the requirements announced above.

The intercalation materials used in a Li-ion battery can be classified into three main categories relative to the structure of the Li-ion pathways:

- two-dimensional Li-ion pathways also referred as layered structure ($LiCoO_2$, for example),
- three-dimensional Li-ion pathways in which Li-ions are inserted in channels forming a 3D framework,
- one-dimensional Li-ion pathways in which Li-ions are inserted into unidirectional channels.

3.2. Classification of the positive electrode materials

3.2.1. Layered-type compounds

3.2.1.1. An historical material: TiS₂

Before introducing the materials used in the Li-ion battery technology, it is wise to briefly describe an early system used in the rechargeable (secondary) lithium metal batteries: the titanium sulphides (TiS_2). Indeed, the Li-ion battery was the natural evolution of the Li-metal battery and thus it has benefited from the development of intercalation chemistry in the 1970's in parallel with the Li-metal battery technology.

TiS_2 adopts a CdI_2-type layered structure, that consists in a hexagonal close-packed sulfur lattice with the titanium ions in octahedral sites between alternating sulfur sheets, as shown in Figure I. 5. During discharge, the lithium ions from the anode (Li metal) are inserted into the empty octahedral sites of TiS_2 and the transition metal is formally reduced from Ti^{+4} to Ti^{+3}. The reverse reaction is obtained during charging. No phase transition occurs upon the insertion or extraction of the lithium (*i.e.* no structural changes between TiS_2 and Li_xTiS_2 (x≤1)) allowing a very good reversibility of the system.
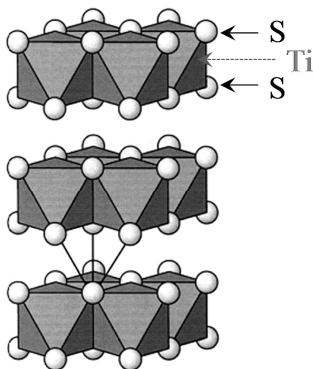
Figure I. 5 : Schematic representations of the layered structure of TiS₂ (from ref [21])

3.2.1.2. Layered-type oxides: LiMO₂

Transition metal oxides with the general formula $LiMO_2$ (M=V, Cr, Fe, Co and Ni) adopt a similar layered structure as the TiS_2 system presented above, and they constitute good candidates for positive electrodes for Li-ion batteries.

These lithium-containing compounds crystallise in a α-$NaFeO_2$-type structure where the Li^+ and M^{3+} ions are distributed in the octahedral interstitial sites of a cubic close-packed oxygen array, in such a way that MO_2 layers are formed consisting of edge-sharing MO_6 octahedra, as shown in Figure I. 6. Lithium is located between these MO_2 layers forming LiO_6 octahedra. A complete extraction of the lithium leads to the layered CdI_2 structure-type (similar to TiS_2) as shown for CoO_2 by Amatucci *et al.* [26]

- ***LiCoO₂***

$LiCoO_2$ was the positive electrode incorporated in the first commercialized Li-ion battery. It was suggested by Goodenough's group [8] and it is still the most commonly used TMO in commercial Li-ion batteries due to its high potential (3.9V *vs.* Li^+/Li) and its good life time.

$LiCoO_2$ has a theoretical capacity of 274 mAh.g^{-1} but only half of this capacity (~ 140 mAh.g^{-1}) can be used in practical cells because just 0.5 Li can be reversibly cycled without capacity loss (Eqn 1). Indeed Li_xCoO_2 exhibits structural and chemical instabilities when x<0.5.[26,27]

$$LiCoO_2 \leftrightarrow Li_{1-x}CoO_2 + xLi^+ + xe^- \quad (x<0.5) \qquad \text{Eqn. 1}$$
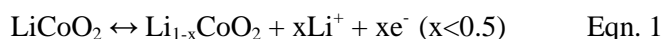
The dissolution of Co in the electrolyte upon delithiation, the formation of cracks in the particles due to changes in the lattice parameters [28] and the shearing of the CoO_2 layer in the fully delithiated materials are the main sources for its reported instability.[24] Note that no structural changes were observed with Li_xTiS_2.[20]

During cycling, there is a risk for structure destabilization close to the cut-off potentials which leads to a safety risk. This, together with the low abundance of Co, the high cost of $LiCoO_2$ and its high toxicity, makes it urgent to find alternative materials, especially for large-scale applications.

- ***LiNiO$_2$***

There are other transition metal oxides isostructural with $LiCoO_2$ that have been investigated; one example is $LiNiO_2$.[29,30] Following cobalt in the classification table, Ni is less toxic and cheaper. However, because of the structural instability of the compound, it has not been able to be commercialized as a Li-ion electrode material. Indeed, a stoichiometric compound has been difficult to obtain due to the unstable Ni^{3+} ion: an excess of nickel ($Li_{1-x}Ni_{1+x}O_2$) was reported, leading to the presence of Ni^{2+} ions in the lithium conduction layers. The poor structural stability upon cycling with low lithium content makes this system unsafe.[31]
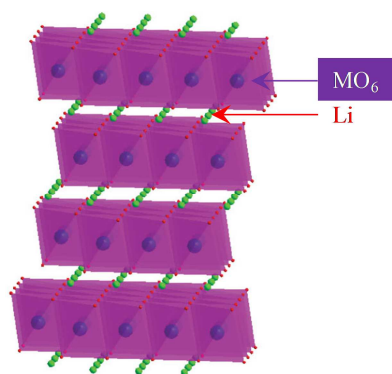
Figure I. 6 : Structure of the layered-type oxides LiMO$_2$ (M=Co, Ni) (from ref [19])

$LiNiO_2$ cannot be used directly as it is, but a partial substitution of Ni by other transition metals or by redox inactive metals can stabilize this system.

- ***Other layered structures: mixed transition metal oxides***

A large variety of other transition metal oxides (mixed or not) adopting the layered α-NaFeO$_2$-type structure has been investigated and the results can be found in several reviews.[21,23]

Some of the most interesting compounds were obtained by replacing a part of nickel by cobalt ($LiNi_xCo_{1-y}O_2$) and thus combining the merits of both $LiCoO_2$ and $LiNiO_2$. Cobalt allows the stabilisation of the structure by suppressing the migration of nickel to the lithium sites. With a cyclability comparable to $LiNiO_2$ or $LiCoO_2$, but cheaper than $LiCoO_2$ and an initial capacity loss lower than $LiNiO_2$, a compound containing mostly nickel ($Li[Ni_{0.8}Co_{0.2}]O_2$) was reported to give the best results.[32]

The additional incorporation of aluminium has stabilized the structure by limiting the removal of all the lithium and thus also preventing the phase transformation at low lithium content. The resulting compound $Li[Ni_{0.8}Co_{0.15}Al_{0.05}]O_2$ [33] (or NCA) has been commercialized and it also adopts also the α-NaFeO$_2$ structure.

Finally, the material $Li[Ni_{1-x-y}Mn_xCo_y]O_2$ (or NMC) is also an interesting alternative to $LiCoO_2$, especially the commonly used NMC containing equal amounts of the three transition metals, i.e. $Li(Ni_{1/3}Mn_{1/3}Co_{1/3})O_2$.[34] NMC has currently a greater commercial success than NCA.

The cycling of layered oxides, mainly used in the first generation of lithium batteries, unfortunately led to structural instabilities and loss of capacity when the compounds were almost fully delithiated.

To solve this problem, more stable three-dimensional frameworks have been investigated.

3.2.2. Three-dimensional and one-dimensional compounds

The 1D and 3D structures (from the point of view of Li-ion pathways) have three-dimensional frameworks structures (from the point of view of the host materials) containing channels allowing the insertion/extraction of the Li-ions. Such structures present the advantage of possibly avoiding the co-insertion of bulky species such as solvent molecules from the electrolyte. Also the degree of expansion/contraction of the framework structure upon lithium insertion/de-insertion is smaller than those observed for two-dimensional layered structures.[21]

3.2.2.1. 3D structures - Spinel oxides: $LiMn_2O_4$
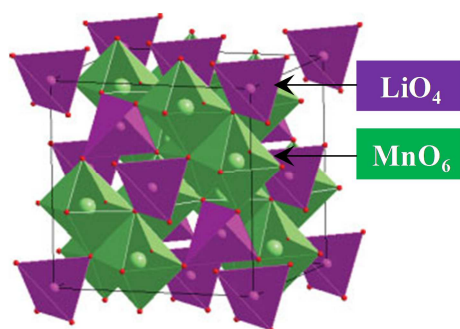
Figure I. 7: Structure of $LiMn_2O_4$ (from ref[19])

Interesting compounds are the oxides of general formula LiM_2O_4 which adopt the cubic spinel structure: the most commonly used being $LiMn_2O_4$.[9] Manganese occupies octahedral sites of a cubic close-packed oxygen array. The MnO_6 octahedral are connected to each other through edge-sharing and thus forming a three-dimensional framework (Mn_2O_4) containing channels. Lithium occupies the tetrahedral sites in these channels,[35] as shown in Figure I. 7.

In spite of a lower capacity than the layered oxides presented above, ($\sim$120 mAh.g^{-1} corresponding to the insertion/extraction of 0.8 Li$^+$), $LiMn_2O_4$ is considered as a non-toxic and low cost material with an operating voltage of 4.1 V *vs.* Li$^+$/Li.

However, also $LiMn_2O_4$ appears to be unstable especially at elevated temperature ($>$50°C) and capacity losses are observed upon long-term cycling [36] and on storage due to the dissolution of Mn into the electrolyte[37]. As previously described for the $LiMO_2$ compounds, the system can be stabilized with a partial substitution of Mn by other elements (Li, Co, Cr, Fe [38,39] or Ni [40,41,42]) or by a stable surface coating (e.g. Al_2O_3).[43]

3.2.2.2. Polyanion-based positive electrode
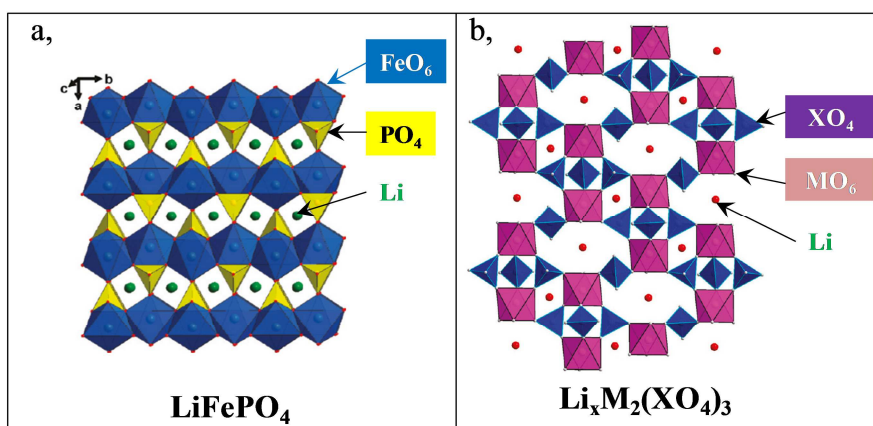
Figure I. 8: a) Olivine structure of LiFePO$_4$ (from ref [23]).b)NASICON framework of Li$_x$M$_2$(XO$_4$)$_3$ (from ref [25])

The family of the polyanionic –based compounds are another interesting three-dimensional framework made of transition metals and polyanions $(XO_4)^{n-}$ (X= P, S, Si, As, Mo or W).

Such compounds are attractive in spite of the presence of heavy polyanion groups leading to a low gravimetric capacity. Indeed, an inductive effect of the polyanion groups $(XO_4)^{n-}$), as introduced and described by the group of Goodenough,[44] increases the energies redox of the $M^{n+}/M^{(n-1)+}$ couple compared to those of oxides (in particular for PO$_4$ and SO$_4$ anions). This gives the structure a high stability improving the safety and the electrochemical behaviour over a long period of cycling.

The phospho-olivine LiFePO$_4$ is the most widely studied and potentially the most useful for the next generation of positives electrodes.

- *1D structure – Olivine: LiFePO$_4$*

The triphylite lithium iron phosphate (LiFePO$_4$) appears as an interesting alternative to the materials described so far and therefore, it has been the object of many studies since Padhi *et al.* in 1997 showed its ability to reversibly insert lithium.[45]

This compound adopts the olivine structure-type. Based on a distorted hexagonal close-packed oxygen array, Li$^+$ and Fe^{2+} occupy half of the octahedral sites and P occupies 1/8th of the tetrahedral sites. In other words, the framework is made of MnO$_6$ octahedra and PO$_4$ tetrahedra with Li-ions in edge-sharing chains of LiO$_6$ octahedra, as shown in Figure I. 8.

LiFePO$_4$ has a reversible capacity of ~160 mAh.g^{-1} and an operating voltage of ~3.45V *vs.* Li$^+$/Li. LiFePO$_4$ contains abundant and low cost elements and it is environmentally friendly. LiFePO$_4$ and its delithiated phase, FePO$_4$ are highly stable (chemically towards electrolyte instability, thermally and structurally) and thus it is safer than the TMO oxides presented so far. No main capacity fading is observed and the electrochemical performances can be enhanced at high temperature (up to 85°C) over a long cycle life.[46]

However, the main drawback of LiFePO$_4$ is its poor electrical conductivity which limits the reversible capacity. Several strategies have been used to improve the conductivity of this material, for example: by doping,[47] by carbon coating of the particles,[48] or by using nanosized particles.[49] Further details of this material are reviewed in a recent paper by Zhang.[50]

In parallel, the formation of complex compounds with partial substitution of Fe by other transition metals (Ni, Co, Mn) is used to increase the operating voltages.[24] Indeed, LiMnPO$_4$, LiCoPO$_4$ and LiNiPO$_4$ that also form the olivine structure have operating voltages of 4.1, 4.8 and 5.1V *vs.* Li$^+$/Li respectively (redox couple M^{2+}/M^{3+}).

- *Other polyanionic compounds*

A lot of other polyanionic compounds are currently investigated and lithium iron phosphates and sulphates appear to be good candidates for positive electrode materials. We can cite the compounds adopting the NASICON structure (Figure I. 8) (with the general formula Li$_x$M$_2$(XO$_4$)$_3$ or

$Li_xMM'(XO_4)_3$[51] but also the diphosphates ($Li_2FeP_2O_7$) or the silicates (Li_2MSiO_4) (M= Fe, Mn) [52,53,54,55] that theoretically can accommodate two lithium per transition metal.

A last promising family of materials are the fluoro-phosphates ($LiVPO_4F$,[56] $LiFePO_4F$ [57]) and sulphates fluorides. With a tavorite structure, they have multidimensional pathways for Li^+ migration, different from the one-dimensional chains observed for the olivines, $LiMPO_4$.[58] Recently $LiFeSO_4F$ has shown an interesting performance. Despite of a lower capacity than $LiFePO_4$ (151 mAh.g^{-1}), this compound presents good ionic and electronic conductivities.[59]

4. Materials for negative electrodes in Li-ion batteries

4.1. General aspects and requirements

The negative electrode is commonly referred to as the anode and it is the second important part of a Li-ion battery.

We have seen in the historical development of the battery that metallic lithium was first used as negative electrode. However, safety issues due to dendrite formation during cycling made it necessary to replace by other compounds that could store lithium at low potentials $vs.$ Li$^+$/Li. Nonetheless, several strategies currently exist in order to be able to use Li metal, because of the high capacity of Li^0 (3860 mAh.g^{-1}). The incorporation of a metal, for example aluminium, was a first approach to avoid/limit dendrite formation.[60] Other strategies have been to protect the lithium surface with the use of a polymer electrolyte or by the development of special ceramic membranes.[61,62] We will not give any more details about the Li metal anode and will instead focus on other materials that have been proposed as negative electrodes in Li-ion batteries.

Potential materials for negative electrode have to fulfil the following requirements:
- React reversibly with lithium
- Accommodate several Li-ions per metallic atom to provide high capacity
- Insertion/extraction processes should take place at a low potential close to Li$^+$/Li (-3.04V $vs.$ SHE) to obtain a wide cell voltage
- The insertion/extraction process has to be fast to achieve high power density.
- Good electronic and Li-ion conductivities.
- Low cost and environmentally benign.

In the previous section, we have seen that all the positive electrodes were based on intercalation materials. The types of reactions involved at the negative side of the batteries are much more diversified and we can distinguish three main families according to their reaction with lithium: (1) insertion/intercalation materials, (2) alloying materials and (3) conversion materials. These three families will be described in this part.

4.2. Classification of the negative electrode materials

4.2.1. Insertion/intercalation materials

4.2.1.1. Carbonaceous materials

Carbonaceous materials were the first materials used as negative electrodes in the Li-ion battery, and they are still the main compounds found in current commercial products. They belong to the first family based on the intercalation of lithium in vacant sites. Graphite has been paid a special attention due to its ability to accommodate lithium. This was shown in 1955 [63] but Yazami et $al.$ were the first to use graphite in an electrochemical cell.[10]

Graphite is made of graphene sheets stacked in ABAB (hexagonal) or ABCABC (rhomboedral) and lithium can be reversibly intercalated between these sheets [64] (Figure I. 9, Eqn.2). At room temperature, one lithium reacts with six atoms of carbon (Eqn. 3) giving a theoretical capacity of 372 mAh.g^{-1}, which is much higher than the capacities reported for all the earlier described positive electrode materials. During lithiation the graphene stacking shifts towards an AAA pattern as shown in Figure I. 9.

$$xLi^+ + xe^- + C_n \leftrightarrow Li_xC_n \qquad \text{Eqn. 2}$$
$$Li^+ + e^- + 6C \leftrightarrow LiC_6 \qquad \text{Eqn. 3}$$
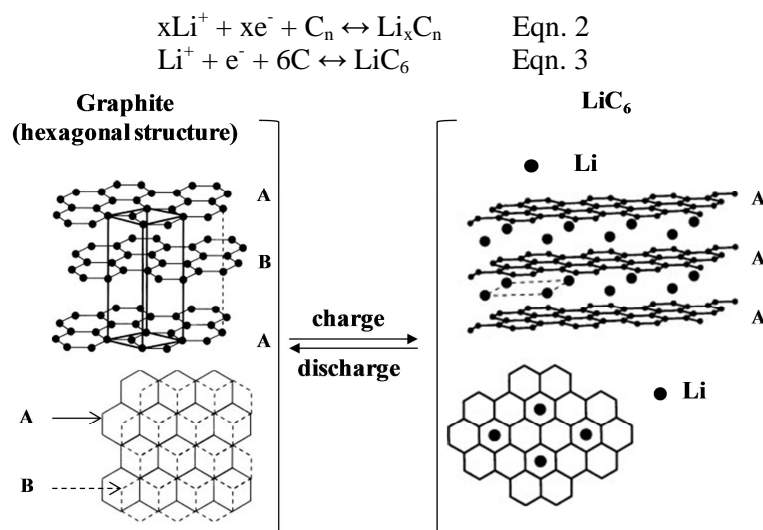
Figure I. 9: Principle of the insertion/extraction of Li$^+$ in graphite, side and top view (Inspired from ref [21])

Graphite has a low insertion voltage (~0.2-0.05 V *vs.* Li$^+$/Li), and good electrical and Li-ion conductivities. This material is abundant in nature, cheap and non toxic. The lithium insertion/extraction process does not involve any major structural changes. The volume expansion is ~10% which can explain the good reversibility of this material and why graphite is still mainly used in current devices.

However, some disadvantages using graphitic carbons can be noted: firstly the reaction with the electrolyte leads to an important irreversible capacity loss (SEI formation), secondly a stable SEI must be formed before the intercalation of Li$^+$ to avoid co-intercalation of solvent molecules.[65] Indeed, graphite exfoliation was reported upon cycling with an electrolyte containing propylene carbonate solvent (PC).[66] However, the use of non-graphitic carbons and later the replacement of PC by EC (ethylene carbonate) in the electrolyte solved this problem.

The structure presented in Figure I. 9 shows an ideal graphitic structure, but in practice there is a wide variety of different carbon compounds ranging from highly crystalline graphite to highly disordered amorphous carbon, and the differences in crystallinity, size and shape of the particle have an influence on the insertion process (theoretical capacity and insertion potential). It is more common to find polycrystalline structures made of aggregates of ordered graphite (crystallites) separated by disordered regions referred to as non-graphitic carbons in which graphene sheets are not stacked.[21] Non-graphitic carbons including soft or hard carbons (i.e. soft if they are graphitizing when heated (adopting the graphite structure) or hard if they are not graphitizing when overheated) have been widely studied. A hard carbon generally exhibits a porous structure and has a reversible capacity up to 500 mAh.g^{-1}.[21]

There are also other carbon structures, as reviewed by Endo *et al.*[67] and more recently by Li *et al.*[68] Some examples are mesocarbon microbeads (MCMB) or carbon fibres. Carbon nanotubes are a more recent example with a high reversible capacity over 600 mAh.g^{-1} but they exhibit a large irreversible capacity during the first cycle.[69,70]

There are few reported alternatives to the intercalation materials mainly because carbonaceous materials have been functioning satisfactorily in terms of cost and performances. Intercalation materials containing a 3d-transition metal, however, are attractive negative electrode compounds but their high intercalation voltages have reduced their usefulness for practical applications. The most successful compounds in this context are the titanium-containing negative electrode materials.

4.2.1.2. Transition metal oxides

Titanium oxide based materials represent the main alternative to carbonaceous compounds. The lithium insertion/extraction mechanisms are similar to those occurring in a cathode material where the

metal is reduced and the coordination to the oxygen atoms changes. In this case, the couple Ti^{4+}/Ti^{3+} is involved with the general reaction given in Eqn. 4:

$$Li_xTi_yO_z + wLi^+ + we^- \leftrightarrow Li_{(x+w)}Ti_yO_z \qquad \text{Eqn. 4}$$
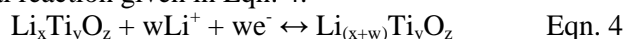
The most widely used titanium oxide is the spinel $Li_4Ti_5O_{12}$ ($Li[Li_{0.33}Ti_{1.67}]O_4$), called titanate, which forms the rock salt $Li_7Ti_5O_{12}$ phase when reduced. $Li_4Ti_5O_{12}$ has a low theoretical capacity (175 mAh.g^{-1}) but a coulombic efficiency close to 100% [71] and a limited volume change (~0.2%) during cycling. Its main advantages are its insertion voltage around ~1.55V $vs.$ Li^+/Li, above the SEI formation at 0.8 V $vs.$ Li^+/Li enhancing the general safety of the battery, and a fast transport of Li-ions. The titanate is excellent for power applications. However, this material is an insulator but several strategies have been developed to enhance its conductivity.[72]
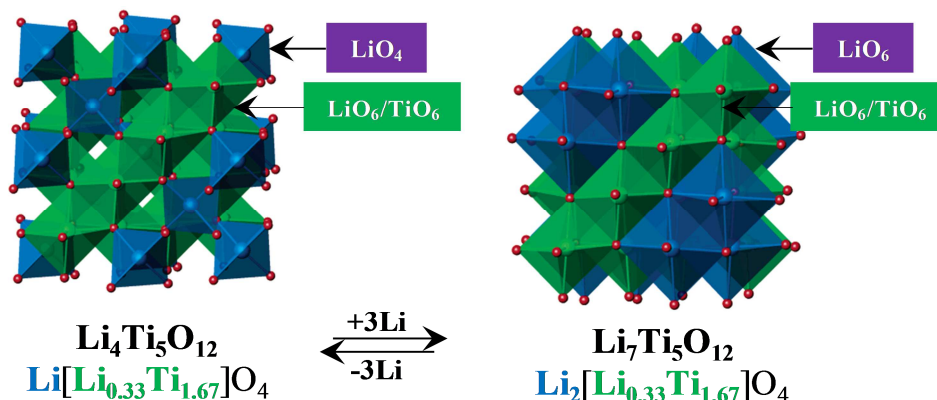
Figure I. 10 : Structure of $Li_4Ti_5O_{12}$ and illustration of the insertion/extraction of Li in its structure (Adapted from ref [73])

Other interesting materials are the ramsdellite $Li_2Ti_3O_7$ and the monoclinic $Li_2Ti_6O_{13}$ that both present better conductivities thanks to the presence of channels in their structures allowing the fast transport of Li^+. These materials have a specific capacity of 235 mAh.g^{-1} and 200 mAh.g^{-1}, respectively, but a important capacity loss is observed in both cases. TiO_2 polymorphs have also been widely investigated: anatase, rutile and TiO_2-B (Bronze). The general formula involved in the electrochemical cell is given in Eqn. 5:

$$TiO_2 + xLi^+ + xe^- \leftrightarrow Li_xTiO_2 \qquad \text{Eqn. 5}$$

The capacity of these materials (x value in Eqn. 5) is dependent of the type of structural polymorph or if the materials are nanostructured or not. This was recently detailed by Yang $et\ al.$[74]

The last but not the least interesting family of titanium compounds is $M_{0.5}TiOPO_4$ (M= Ni^{2+}, Fe^{2+}, Mn^{2+}, Co^{2+}, Mg^{2+})[75] inspired by the olivine $LiFePO_4$, but with operating cell voltages below 2V. $Ni_{0.5}TiOPO_4$ oxyphosphate can accommodate three Li-ions, but only two can reversibly be extracted giving a practical capacity around 275 mAh.g^{-1} (operating cell at 1.8 V $vs.$ Li^+/Li).[76]
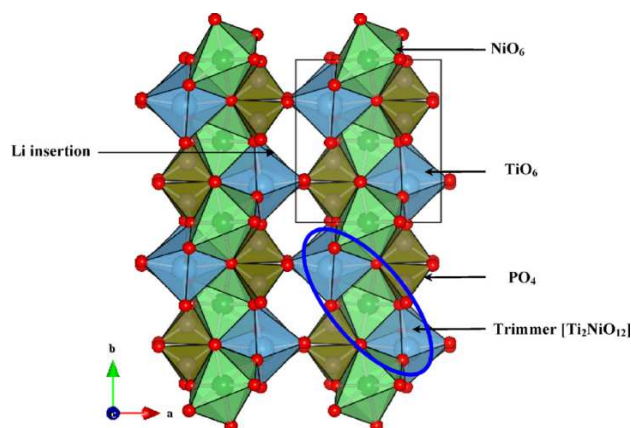
Figure I. 11: Structure of $Ni_{0.5}TiOPO_4$ (Reprinted with permission from ref [77])

Note that vanadium oxide based materials have also been suggested as insertion materials for negative electrodes. Examples are Li_xMVO_4 [78] or $MV_2O_{6+\delta}$ [79] and more recently, interesting results were obtained with the layered structure $Li_{1+x}V_{1-x}O_2$ (iso-structural to $LiCoO_2$)[80] showing a low insertion voltage close to the graphite electrode (~0.1V *vs.* Li^+/Li).

The main insertion materials used as negative electrodes have been described and all of them present the advantages of small structural changes; however the insertion/intercalation is limited in terms of capacity (a limited number of lithium can be inserted). In addition, due to the redox couples involved, the operating cell voltage of a full Li-ion battery will be narrow: this is particularly true for titanium based materials.

In the quest towards increasing the energy density of the battery, other concepts and materials have to be developed in order to store more lithium than with the insertion materials described above. Compounds able to form an alloy with lithium constitute an interesting alternative to the insertion materials and lead to very high specific capacities, close to or even higher than for the metallic lithium (3860 mAh.g^{-1}).

4.2.2. Alloying materials

4.2.2.1. General

In the 1970's, Dey[81] showed that the electrochemical formation of alloys between lithium and a metal was possible in non-aqueous electrolytes and at room temperature. The alloying takes place according to the general equation (Eqn.6):

$$M+ xLi^+ + xe^- \leftrightarrow Li_xM \qquad \text{Eqn. 6}$$

Many metals and semi metals are reactive towards lithium and they are mainly found in group 13 (Al, Ga, In), 14(Si, Ge, Sn, Pb) or 15 (As, Sb, Bi) of the periodic table. Firstly, they present much higher volumetric and gravimetric capacities than the insertion materials described before (graphite, $Li_4Ti_5O_{12}$, etc). Secondly, the alloying occurs at low working potential ~ 0.3V to ~ 0.9V *vs.* Li^+/Li.[82,83] Important characteristics of the main investigated Li(m) alloys found in the literature are given in Table I. 1 as well as their abundance in the Earth's crust. Carbon and $Li_4Ti_5O_{12}$ are included in the table for comparison.

Table I. 1 : Comparison of various anode materials: theoretical specific capacity and volumetric capacity, mass density, potential (vs. Li$^+$/ Li) and abundance. (Adapted from ref [83])

Material	Li	Si	Ge	Al	Sn	Sb	Bi	C	Li$_4$Ti$_5$O$_{12}$
Mass density of the element (g.cm^{-3})	0.53	2.33	5.32	2.7	7.29	6.7	9.78	2.25	3.5
x in the lithiated phase Li$_x$M	-	3.75	4.4	1	4.4	3	3	1/6	3
Specific capacity (mAh.g^{-1})	3862	3578	1624	993	994	660	385	372	175
Volumetric capacity (mAh.cm^{-3})	2047	8336	8639	2681	7246	4422	3765	837	613
Potential (V $vs.$ Li$^+$/Li)	0	0.4	0.3	0.3	0.6	0.9	0.8	0.05	1.6
Abundance on Earth's crust (ranking)	34th	2th	51th	3th	47th	62th	68th	10th	-

The combination of the electrochemical properties (potential, capacities) as well as the intrinsic characteristics of the elements (abundance, cost, toxicity, etc) easily explains why much attention has been devoted to silicon and tin-based electrodes.

Upon cycling, however, the capacity is generally constantly decreasing so poor cycling performance is observed. In contrast to the attractive properties shown in Table I. 1, a large volume expansion occurs upon lithiation of the material. The successive lithiations/delithiations cause high mechanical strain in the particles that lead to pulverization of the active material (Figure I. 12 (a)). The volume change can also destroy the electrode structure, due to a loss of contact between the active material, the current collector and the conducting additives (Figure I. 12 (b)).[84] Particles of active material may become electrically isolated in the electrode and therefore are not able to take part in the electrochemical process in the following cycles.

The alteration of electrode structure is not the only reason for the capacity loss and other parameters that impact capacity fading have to be taken into account.[83] The formation of the SEI (electrolyte reduction) contributes mainly to the initial irreversible loss of capacity just as for carbon materials. In further cycles the capacity fade continues because of repeated volume expansion and the formation of cracks in the particles leads to a continuous reformation of the SEI (Figure I. 12 (c)). Lithium might also be trapped in the alloys. Indeed, all the inserted Li cannot be extracted due to kinetic and thermodynamic factors (slow Li release, formation of very stable Li-species, presence of defects).

Another important point is the reduction of the native oxide layer present at the surface of most of the metal particles with the formation of Li$_2$O and the metal. This reaction mainly occurs upon the first cycles. Finally, aggregation of active particles can lead to increased Li diffusion paths, and the SEI (and Li) is kept trapped contributing to the capacity loss.
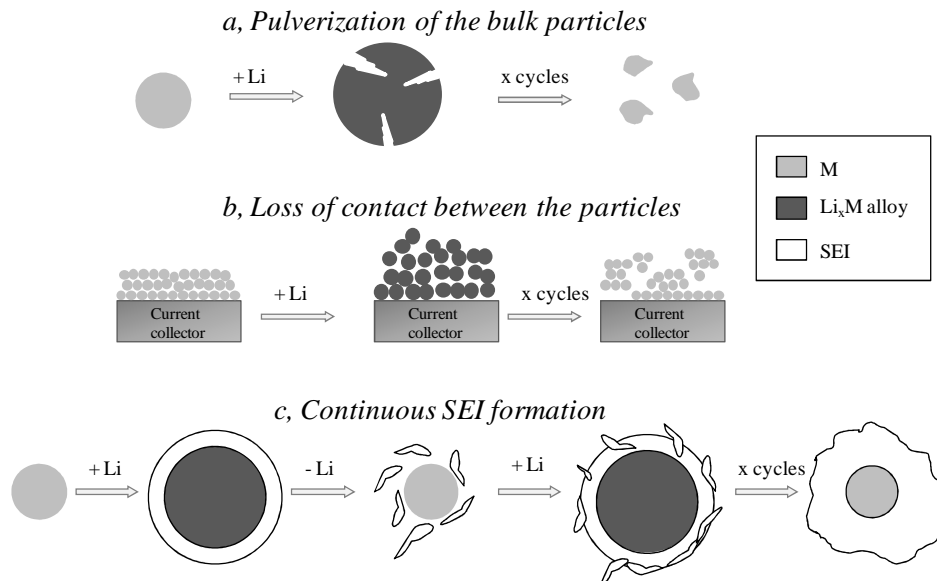
Figure I. 12 : Suggested electrode failure mechanisms for alloying materials (Adapted from ref [85])

Most of these issues are linked to the volume expansion and it seems difficult to find an efficient negative electrode material made of one single active phase. The main research activity on alloying materials is nowadays turned to developing strategies to avoid or at least limit the volume expansion; some of the general strategies are listed below.

4.2.2.2. Limitation of the volume expansion: several strategies

- ***Limitation of the capacity***

The first idea that comes in mind is to limit the amount of lithium inserted in the host material (limitation of the capacity) as suggested by the linear relationship between insertion and expansion.[86] The capacity can be limited experimentally by controlling the voltage (lower cut-off voltage especially). The importance of this last point will be discussed later in the case of silicon-based electrodes.

- ***Modification of the morphologies/structures of the active material***

  ✓ *Nano-sized particles, nanostructure and thin films:*

The decrease from large particles to micro-particles has shown to improve the cycling performance of alloy-materials since it was suggested in 1996.[87] Lately, the use of nanoparticles has shown to enhance the capacity. Indeed, when a large expansion occurs, the absolute volume changes stay low and no cracking of the particles are observed. Moreover, the electronic and ionic transport distance decreases thus facilitating Li-ion and electron transfer leading to better electrochemical performances.[21]

  ✓ *Porous and 3D structures:*

In order to limit the effect of volume expansion, one efficient way is to give enough space for the particle to expand, therefore a three-dimensional porous electrode structure can be used which has a sufficient porosity for accommodating the volume expansion of the active material.

- ***Addition of a second phase to buffer the volume expansion***

  ✓ *Dispersion in a composite matrix*

Another approach is to disperse the active material in a phase that can act as a buffer to accommodate the large volume expansion and prevent the agglomeration of the active particles. This matrix needs to present good electronic and ionic conductivities to not slow down Li-ion and/or electron transfer. The matrix must also be inert towards the electrolyte and it needs to have an appropriate mechanical strength.

Carbon materials totally fulfil this requirement and carbon-based composites show better results than carbon free systems in several systems, such as Sn-C, Si-C [88] or Sb-C.

The use of a binder is also highly recommended because in addition to be an efficient buffering medium, it will maintain the electrode mechanical integrity and the contact between the current collector, the conductive additive and the active material.

  ✓ *Use of intermetallic materials*

The addition of a second metal is another alternative.[89] By using intermetallic materials the volume expansion can be buffered. The additional metal can be either electrochemically inactive or active towards lithium which leads to several reactions. Intermetallics have mainly been used for Sn and Sb-based electrodes and several examples can be found in the review of Park *et al*.[90]

In the first case, we can have ***inactive-matrix composites*** where the intermetallic compounds have the general formula AB with A being the active material and B the inactive one. Possible reactions upon lithiation are given in Table I. 2.[91]

In the addition-displacement process, the displacement of the inactive elements can be reversible or not while the active material is alloying with lithium.

In a second case, we can have ***active-matrix composites*** where the two phases of the intermetallic compounds AC_y are both electrochemically active towards lithium and form two alloys after the displacement, as shown in Table I. 2. Such materials are interesting when the potential of the two metals are different with the alloying of the metals taking place in two different steps. Antimony (Sb) is often used because of its high potential (SnSb, InSb).

Table I. 2 : Reactions involved in intermetallic alloying materials

Intermetallic materials	Type of reaction	Reaction(s)
Inactive matrix	*Alloying - internal displacement*	$AB + xLi^+ + xe^- \rightarrow Li_xAB$
	Alloying - substitution	$AB + xLi^+ + xe^- \rightarrow Li_xAB_{1-y} + yB$
	Alloying - displacement	$AB + xLi^+ + xe^- \leftrightarrow Li_xA + B$
		$AB + xLi^+ + xe^- \rightarrow Li_xA + B \leftrightarrow xLi^+ + xe^- + A + B$
Active matrix	*Alloying with both active components - displacement*	$AC_z + (x+y)Li^+ + (x+y)e^-$ $\leftrightarrow$ $Li_xA + zC + yLi^+ + ye^-$ $\leftrightarrow$ $Li_xA + zLi_{y/z}C$

This concept has been widely used for Sb and Sn-based electrodes and in 2005, Sony Corporation commercialize a battery based on the nanostructured alloying material, Sn–Co–C as negative electrode (NEXELION®).

The main intermetallic Sb-based electrodes that have been studied are: Cu_2Sb, $CrSb_2$, InSb, GaSb, AlSb, [92,93,94] and also NiSb, CoSb, FeSb, MnSb.[95,96]

Tin-based electrodes, however, have been much more investigated and various Sn-based intermetallic compounds have been studied: $NbSn_2$,[97] Al-Sn,[98] $FeSn_2$,[99] Ni_3Sn_4,[100,101] $CoSn_2$,[102,103] Cu_6Sn_5[104,105] or $CrSn_2$.[102] Paper IV and V in this thesis will be devoted to another Sn-based intermetallic using manganese as the inactive metal, $MnSn_2$. So far, only few papers have reported the use of this compound.[106,107]

The compound SnSb is the most studied intermetallic compound having two active elements.[108,109] Recently, Monconduit et al. have used TiSnSb. [110,111]

✓ *A special case: metal oxides*

The metal oxides, such as SnO, SnO_2, Sb_2O_3 etc., are the last family of compounds also based on the alloying-displacement reactions.[112] We have seen in the presentation of the alloys that the initial capacity loss is partially due to the reduction of native oxide layers resulting in Li_2O and the metal. This unwanted reaction can, however, be attractive and the irreversible formed Li_2O matrix can in this case buffer the volume expansion. This process is divided into two steps (Eqn. 7 and 8):

$$MO_x + 2xLi^+ + 2xe^- \rightarrow xLi_2O + M \qquad \text{Eqn. 7}$$
$$M + yLi^+ + ye^- \leftrightarrow Li_yM \qquad \text{Eqn. 8}$$
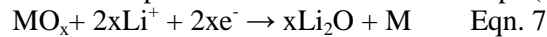
Tin-based composite oxides (TCO's) were commercialized by Fujifilm in the late 90's (STALION®).[113] SnO is used in this anode material and the reactions occurring are given in the following equation (Eqn. 9 and 10):[114]

$$SnO + 2Li^+ + 2e^- \rightarrow Li_2O + Sn \qquad \text{Eqn. 9}$$
$$Sn + 4.4Li^+ + 4.4e^- \leftrightarrow Li_{4.4}Sn \qquad \text{Eqn. 10}$$
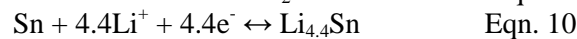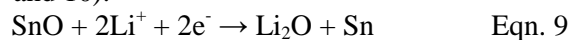
In this section, we have seen how the main strategies described are used to avoid/limit the volume expansion of alloying materials and a combination of these approaches might be necessary to obtain efficient negative electrodes which can be commercialized. More specific examples of systems developed for Si-based electrodes will be described in the next part. But before this, the last family of potential materials for negative electrodes needs to be briefly introduced: the conversion materials.

4.2.3. Conversion materials

The last family of materials investigated as a candidate for the negative electrode is referred to as *conversion materials* and it contains a transition metal coupled with an anion. During lithiation of this material, the general reaction involved is given in Eqn. 11:

$$M_yX + n\ Li^+ + n\ e^- \leftrightarrow yM + Li_nX \qquad\qquad Eqn.11$$
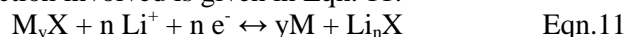
where M = transition metal, X = anion, and n = formal oxidation state of X.
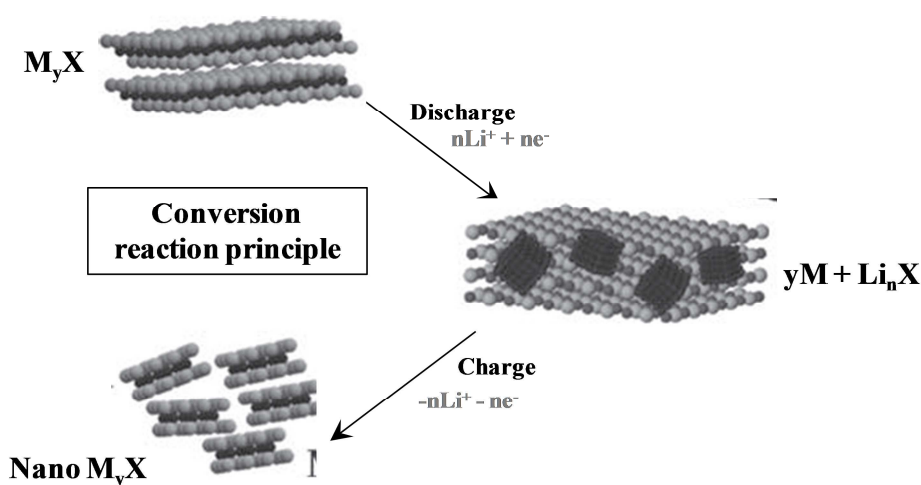
Figure I. 13 : Schematic illustration of the conversion reaction principle (inspired by ref [115])

The originality of conversion reactions is the complete reduction of the transition metal to the metallic state leading to high capacity (up to three times that of carbon). Intermediate phases, Li-M-X, can be formed but full reduction leads to the formation of metallic nanoparticles (M) homogenously embedded in a Li_nX matrix as shown in Figure I. 13. When Li is removed from the structure, the MX phase reforms but in a nanosized scaled phase that is maintained upon further cycles. By the decrease of particle size, the high surface area will increase with many more active particles leading to higher electrochemical reactivity of these particles.

Conversion reactions allow the use of binary transition metals compounds (MX) dismissed from the insertion materials family because they do not present vacant sites/channels in their structure, as described in the positive electrodes part of this first chapter. Most of the 3d transition metals as well as Mo, W and Ru in the following d-periods of the periodic table belong to this family. In the anionic side, phosphides, sulfides, nitrides or fluorides have been reported (X=P, S, N, F).

The potential of the conversion reaction strongly depends on the nature of the anion and of the transition metal, thus it can easily be tuned. It usually varies between 0.2V and 1.5V (*vs.* Li$^+$/Li) for oxides, sulfides and nitrides but can even reach values up to 3V for fluorides. Applications of conversion materials could be found as both negative and positive electrode materials.

In general, conversion materials show higher capacity upon the first discharge than their theoretical capacities. This has been explained by two phenomena: the reduction of the electrolyte solvent but also by an interfacial deposition of lithium between M and the matrix LiX that can be described as a capacitor with Li$^+$ in the LiX phase and e$^-$ in the M nanoparticles. [116]

However, as for all the systems investigated so far, conversion materials present some weaknesses. Just as for alloying materials, large volume changes occur due to structural reorganization that leads to

degradation of the electrode and bad cycling performance. Secondly, a large voltage difference between charge and discharge (voltage hysteresis) is commonly observed which gives poor energy efficiency and finally, after the first cycle a large capacity loss can be seen.

Several strategies have also been employed to limit these drawbacks and they are similar to those used for alloys: the use of polymeric binder, the formation of a composite with carbon, the use of mixed transition-metals compounds or the development of nanostructures. All these strategies are leading to improvements.

Since 2000, most of the attention has been devoted to transition metal oxides (TMO) [88,115,117] and they usually present a very high capacity retention and high theoretical capacities (up to 1233 mAh.g^{-1} for MnO_2). The general reaction is described in Eqn. 12 and we can note that this reaction is very similar to Eqn. 8 observed for metal oxides. However, in the case of TMO, the metal does not form an alloy with the lithium and the conversion reaction is reversible.

$$M_xO_y + 2yLi^+ + 2ye^- \leftrightarrow yLi_2O + xM \qquad \text{Eqn. 12}$$

Among the materials reviewed by Cabana *et al.*, cobalt oxides are among the most explored TMO such as CoO. We would like to specially emphasise on iron oxides that appear as good candidates. The hematite Fe_2O_3 or the magnetite Fe_3O_4 have both the advantages of being highly abundant (Fe is the 3rd most abundant element in Earth's crust), non-toxic and they present an interesting theoretical capacity (1007 and 926 mAh.g^{-1}, respectively).

5. Electrolytes

5.1. Requirements and types of electrolytes

The electrolyte is the third main part of a Li-ion battery. It ensures the conduction of the lithium-ions between the negative and the positive electrodes and acts as a physical barrier between the two electrodes (when coupled with a separator for liquid electrolytes). The chemical nature of the electrolyte has a strong impact on battery performance, especially at the electrode/electrolyte interfaces. The constituents of the electrolyte can indeed be the object of redox reactions close to the electrodes leading to possible decomposition of the electrolyte and deposition of some products at the interfaces. A section in this first chapter will be devoted to these interfacial reactions.

An ideal electrolyte has some general requirements to fulfil: [25,118]

- Large electrochemically potential window: the redox potential of both electrode materials must fall within this window to avoid oxidative or reductive degradation of the electrolyte, i.e., $V_{oc} = E_+ - E_- \leq E_g$ in Figure I. 14. Thus, with a limited E_g (~ 1.3V), aqueous electrolytes are excluded in favor of non-aqueous electrolytes.
- High ionic conductivity ($\sigma_{Li} > 10^{-4}$ S.cm^{-1}) and low electronic conductivity ($\sigma_e < 10^{-10}$ S.cm^{-1}) over a wide range of temperature range (-40°C to +60°C)
- Chemically stable towards all the cell components (separator, current collectors, cell packaging materials)
- Should form a stable passivation layer at the surface of the electrodes if outside the electrochemically potential window.
- Be able to tolerate extreme conditions (electric, mechanical and thermal abuse)
- Low toxicity and low cost
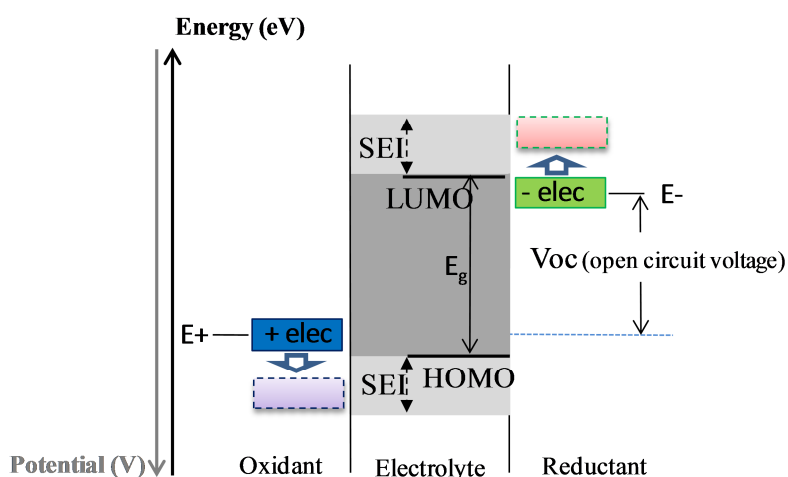
Figure I. 14 : Schematic open-circuit energy diagram of an electrolyte. Redraw from ref [25]

Electrolytes mainly used in Li-ion battery are *liquid electrolytes* (LEs) and are composed of a lithium salt dissolved in mixtures of several organic solvents. However, other types of electrolytes exist and are used in particular battery applications.

Another type of electrolyte is the *gel polymer electrolyte* which consists of a liquid electrolyte incorporated into a polymer matrix.[119]

Solid polymer electrolytes (SPEs) are also developed and have been used in micro battery devices or in batteries using metallic lithium (SPE is used in some electric cars, for example Autolib in Paris). In this case, lithium salts are directly incorporated in a polymer matrix. The first and most commonly used polymer electrolyte was based on polyethylene oxide (PEO).[120] SPEs can act as a separator in the battery to prevent short-circuiting the electrodes, and they do not contain organic solvents (flammable molecules) enhancing the safety of the system. Other solid electrolytes have been developed, glass or ceramic electrolytes, for example.[121]

The last family considered as an alternative electrolyte for Li-ion batteries is also solvent free: the *ionic liquids (ILs)* based electrolytes.[122] ILs are molten salts (constituted of discrete anions and cations) which are in the liquid state at the operating temperature. The classical definition of an IL is a salt with a melting temperature below 100°C. The family of the room temperature IL (RTIL) contains the IL with a melting point below 25°C. However, ILs are viscous, very expensive and are hard to synthesize without impurities, so for Li-ion battery applications, IL-based electrolytes are mostly used as additives.

5.2. Non aqueous liquid electrolytes

5.2.1. Solvents

A huge variety of solvents can be used in a liquid electrolyte and some additional necessary requirements for a liquid electrolyte are the following: [118]
- Be able to dissolve a lithium salt to a sufficient concentration (high dielectric constant ε)
- Have a low viscosity η to facilitate ion transport.
- Be in the liquid state in a wide temperature range (low melting point (T_m) and high boiling point (T_b))
- Be aprotic because of the strongly reducing negative electrodes and the strongly oxidizing positive electrode
- It should also be safe (high flash point T_f), nontoxic, and cheap.
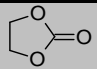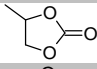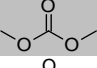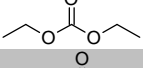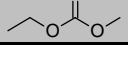
In practice, it is difficult to find a single compound with all these properties and therefore mixtures of solvents are generally used.

The common solvents used in Li-ion batteries belong to two main families: the ethers (R-O-R') and esters (R-COO-R'). Usually incorporated in the electrolyte in the 1980's, ethers have slowly being replaced and in the 1990's, only esters are used in electrolytes. A special attention is being devoted to carbonate esters commonly named alkyl carbonates (R-O-COO-R').[118]

The main used esters and alkyl carbonates can be cyclic as ethylene carbonate (EC) or propylene carbonate (PC), linear symmetric as dimethyl or diethyl carbonates (DMC and DEC) or linear asymmetric as ethyl methyl carbonate (EMC). These solvents and their physical and chemical characteristics are reported in Table I. 3 :

Table I. 3 : Main solvents used in non-aqueous liquid electrolytes: Melting point, boiling point, dielectric constant, viscosity, flash point and mass density (From ref [118] and Sigma Aldrich)

Solvent	Structure	T_m(°C)	T_b(°C)	η (cP) (25°C)	ε (25°C)	T_f(°C)	ρ (g.cm⁻³)
EC		37	248	1.9 (40°C)	89.78	160	1.321
PC		-55	240	2.53	64.92	132	1.200
DMC		2-4	90	0.59	3.107	18	1.063
DEC		-43	126	0.75	2.805	31	0.969
EMC		-14.5	107	0.65	2.958	23	1.006

Carbonates present a wide electrochemical window between 1.0V (LUMO) and 4.7V (HOMO) *vs.* Li^+/Li. EC is almost always used because it provides a better SEI on the surface of the negative electrode and prevents solvent co-intercalation. However, EC is solid at room temperature and presents a high viscosity at 40°C, so it is always coupled with linear carbonates such as the much less viscous (DMC and/or DEC). It must be pointed out that carbonates have a main weakness; they are highly flammable (low flash points (T_f)).

We can note that inorganic "solvents" have been used but they present a narrow electrochemical window unsuitable for Li battery applications.[123]

5.2.2. Lithium salt

The lithium salt is essential to ensure high ionic conductivity of the electrolyte. As for the solvents, specifications for the salt are the following:

- Complete dissolution and dissociation in non-aqueous solvents
- High mobility of the solvated ions in the solvents selected (Li^+ especially)
- Inert anion towards the solvents and stable against oxidative decomposition at the positive electrode

5.2.2.1. Classical lithium salts

The main lithium salts classically used in Li-ion batteries are reported in
Table I. 4.

Table I. 4 : Main lithium salts used in non-aqueous liquid electrolytes and their characteristic parameters: molar mass (M), melting point (T_m), decomposition point (T_{dec}) and conductivity (σ). (Adapted from ref[118])

Salt	M (g.mol^{-1})	T_m(°C)	$T_{decomposition}$(°C) in solution	Al corrosion	σ (mS.cm^{-1}) 1.0M, 25°C in PC	in EC/DMC
Li tetrafluoroborate **LiBF₄**	93.9	293	>100	No	3.4	4.9
Li hexafluorophosphate **LiPF₆**	151.9	200	~ 80 (EC/DMC)	No	5.8	10.7
Li hexafluoroarsenate **LiAsF₆**	195.9	340	>100	No	5.7	11.1
Li perchlorate **LiClO₄**	106.4	236	>100	No	5.6	8.4
Li Trifluoromethanesulfonate **LiTf** $Li^+CF_3 SO_3^-$	155.9	>300	>100	Yes	1.7	--
Li bis(trifluoromethanesulfonyl)imide **LiTFSI** $Li^+[N(SO_2CF_3)_2]^-$	286.9	234	>100	Yes	5.1	9.0

LiPF₆ is the most commonly used salt in commercialized Li-ion batteries, and viewing the properties in Table I. 4, it can be a bit surprising that it outperforms all the other salts. Indeed, LiAsF₆ has a better ionic conductivity in EC/DMC, LiBF₄ has a higher ionic mobility and LiTFSI has a higher dissociation constant.[124] LiPF₆ is also known to be thermally instable and extremely sensitive to traces of water and alcohol.[125,126]

However, all the other classical salts suffer many weaknesses: LiAsF₆ is toxic, LiBF₄ presents a too low ionic conductivity, the risk of violent reactions is too high with LiClO₄ due to peroxide formation from perchlorate (ClO_4^-) decomposition and finally, LiTf and LiTFSI are corrosive towards the aluminium current collector.
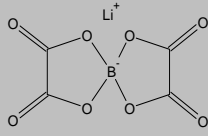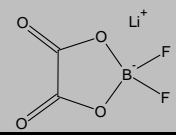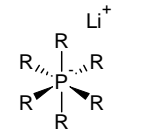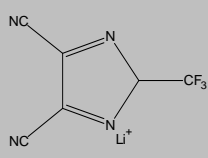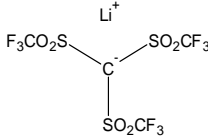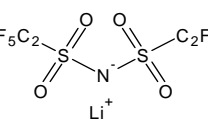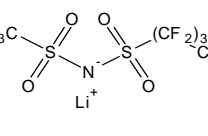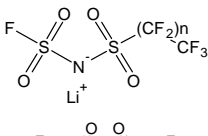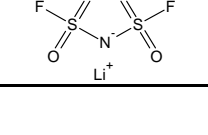
LiPF₆ has the advantage to not present any eliminatory weakness and the combination of its properties currently makes it the most widely employed lithium salt.

5.2.2.2. Alternative lithium salts

New lithium salts have been studied as an alternative for LiPF$_6$. The sensitivity of LiPF$_6$ to water or alcohol leads to the formation of hydrofluoric acid, HF,[127, 128] and its thermal instability can result in a safety problem that needs to be solved. The replacement of the classical LiPF$_6$ salt has therefore to be considered.

A lot of alternative salts have been reviewed by Xu [118] and they can be classified in different families. For example we can cite lithium phosphates (for example LiFAP), lithium borates with aromatic or nonaromatic ligands such as LiBOB and LiDFOB, lithium methide (LiMe) or heterocyclic cyano-based lithium salts (for example LiTDI). The salts that have attracted most attention are presented in Table I. 5.

Table I. 5 : Alternative proposed lithium salts.

	Salt	Usual name	Structure	Ref.
Borates	Li - bis(oxalate)borate	**LiBOB**		129
	Li - difluoro(oxalato)borate	**LiDFOB**		130
Phosphates	Li - fluoroalkylphosphate $Li^+[(C_nF_{2n+1})_xPF_{6-x}]^-$ *for example*: $Li^+[(C_2F_5)_3PF_3]^{-\,131}$	**LiFAP**	R = F or perfluorinated alkyl	131
Heterocyclic cyano	Li - 4,5-dicyano-(2-trifluoromethyl(imidazolide))	**LiTDI**		132
Methide and imides	Li – tris(trifluoromathanesulfonyl) methide $Li^+[C(SO_2CF_3)_3]^-$	**LiMe**		133
	Li – bis(perfluoroethylsulfonyl) imide $Li^+[N(SO_2C_2F_5)_2]^-$	**LiBETI**		134
	Li – (trifluoromethanesulfonyl) (nonafluorobutanesulfonyl) imide $Li^+[N(SO_2CF_3)(SO_2C_4F_9)]^-$	**LiTNSI**		135
	Li - (fluorosulfonyl) (nonafluorobutanesulfonyle) imide $Li^+[N(SO_2F)(n\text{-}C_4F_9SO_2)]^-$	**LiFNSFI**		136
	Li - bis(fluorosulfonyl)imide $Li^+[N(SO_2CF_3)_2]^-$	**LiFSI**		137

The imides constitute another interesting family. Inspired by the structure of LiTFSI and LiBETI, other new imides salts have emerged recently, such as LiTNSI or LiFNSFI (in Table I. 5), but the large sizes of these anions have shown negative impact on the conductivity of the electrolyte.

Instead, successful tests with imide salts that are smaller and lighter than LiTFSI, have been carried out and one of the most effective salt is lithium bis(fluorosulfonyl)imide: ($Li[N(SO_2F)_2]$) (LiFSI).

The FSI^- anion is commonly used in ionic liquids (ILs).[138,139,140] but also in gel polymer electrolytes[141] and carbonate-based electrolytes.[142,143] The LiFSI salt presents a better ionic conductivity than $LiPF_6$ and exhibits good anticorrosive properties towards aluminium when it is very pure.[137,143] Electrochemical performances achieved with LiFSI outperform the ones with $LiPF_6$ when used as salt in non-aqueous carbonates solvents in half-cells, such as $Li/LiFePO_4$[140,142], $Li/LiCoO_2$[143], Li/Graphite[140,142] and in a full cell graphite/$LiCoO_2$.[143] LiFSI also presents the advantage to have a good stability towards hydrolysis[143] and does not form HF. LiFSI appears as a good alternative to $LiPF_6$ and will be investigated in this thesis as a lithium salt in non-aqueous electrolytes (Paper III).

5.2.3. Electrolyte additives

The lithium salt and the solvent are the two crucial components of the electrolyte. However, in commercial batteries, additives are always used as they improve performance and cycle life, and have been reviewed by Zhang *et al.*[144] Additives can aim at improving the formation and stability of the SEI, protecting Al towards corrosion, stabilizing the lithium salt, improving the safety of the battery etc.

Among these additives, vinylene carbonates (VC) has been used in several studies and improvements of the performance of graphite system are reported. Studies have shown that the degradation of VC can give polymeric chains by a radical polymerization process involving the double bond. The resulting SEI presents a better mechanical properties and enhances the protection and cohesion of the electrode. [145,146,147]

It must be stated that no additives were used in this work.

6. The negative electrode/electrolyte interface

We have seen in the part related to the electrolyte that it can react at electrode surfaces due to redox reactions. This leads to electrolyte decomposition and deposition of reaction products at the interfaces between the electrode and electrolyte. The discussion about these battery interfaces were first introduced by Peled *et al.*[18] : the reaction products were described as forming a layer named SEI (Solid Electrolyte Interphase). It is now admitted that this layer constitutes a crucial part of a Li-ion battery influencing many aspects of the battery performance.

The SEI formation has been widely studied for negative electrodes made of metallic lithium or of carbonaceous materials.

In this part we will discuss the general aspects about SEI formation on carbonaceous electrodes in non-aqueous liquid electrolytes (with $LiPF_6$ as lithium salt, cyclic and linear alkyl carbonates as solvents). Its main components will be described as the proposed formation mechanisms at the surface of the negative electrode. The discussion will then be focused on the nature of this layer on Si-based electrodes.

The electrolyte/positive electrode interface will not be discussed in this thesis.

6.1. General aspects of interfacial phenomena

6.1.1. The SEI formation

During the first lithium insertion into the negative electrode host, lithium also reacts with and decomposes the electrolyte, thereby forming a passivation layer on the surface of the electrode, the SEI. The electrolyte (mainly the solvent molecules) is electrochemically unstable during reduction because the potential of the negative electrode is out of the range of the electrochemical window of the electrolyte. As a consequence the SEI formation is generally reported to start below 0.8V *vs.* Li^+/Li.

However, when the SEI totally covers the electrode material and reaches a critical thickness preventing the migration of electrons, the electrolyte no longer decomposes and further reduction is stopped. During cycling, a continuous dissolution/deposition is often observed.[148]

The typical SEI thicknesses have been reported to be from a few Å to tens or hundreds of Å. [149] The SEI has to be electronically insulating but ionically permeable to ensure good cyclability of the battery. The SEI on graphite is important because it acts as a physical barrier preventing intercalation of solvent molecules between the graphene sheets, leading to electrode exfoliation. [150]

6.1.2. Another interfacial phenomenon: lithium plating

Lithium plating is another phenomenon that might occur at the interface of a carbonaceous electrode. The formation of dendrites when cycling with metallic lithium is well known, but it has also been observed on carbon that has an insertion potential very close to that of Li^0.[149,151] This dendrite growth presents the same safety issues as for the Li metal: possible short-circuit of the cells, and a loss of lithium. Most of these interfacial phenomena are described in Figure I. 15.
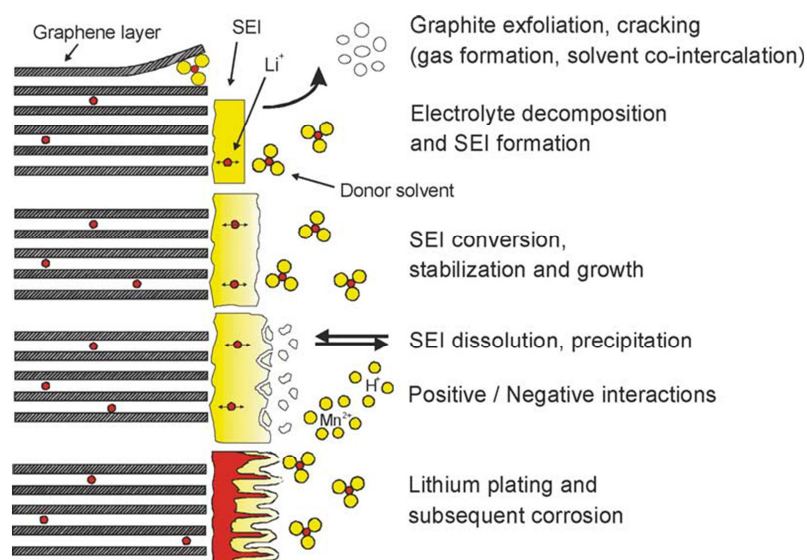
Figure I. 15 : Modifications occurring at the graphite/electrolyte interface upon cycling. Reprinted with permission from ref [151]

6.1.3. Description of the SEI

6.1.3.1. SEI models and parameters influencing its properties

The performance of a battery is tightly related to the properties of the SEI. The SEI formation contributes, firstly to a part of the initial irreversible capacity loss, and then, its properties (composition, thickness, morphology, density) are crucial for the battery behaviour upon long-term cycling. An ideal SEI has to meet several requirements:

- Very low electronic conductivity ($t_{e-} \sim 0$)
- High ionic conductivity ($t_{Li+} \sim 1$)
- Uniform and stable composition and morphology to prevent further electrolyte decomposition
- Good adhesion to the electrode materials
- Good flexibility and mechanical properties to accommodate the volume expansion
- Low solubility in the electrolyte to avoid further electrolyte degradation

Few other factors that affect the SEI appear more obvious than the chemical factors (the nature of the solvents, salt, whether additives are added or not, the nature of the electrode materials, the presence or not of a binder, etc.), the electrochemical cycling conditions (C-rate, depth of discharge, etc.) or the temperature. All these parameters have an important impact on the SEI.[65]

The SEI formation comes from the simultaneous decomposition of the lithium salt and reduction of the solvents. Therefore, its composition is complex and still controversially debated in the literature. Made of organic and inorganic compounds, several models have been suggested to describe the SEI formed on carbon. These models have some similarities but also differences. While Peled *et al*. proposed a mosaic-type structure,[152] Aurbach *et al*. suggest a multilayer structure for the SEI on graphite with an inner compact layer covered by an outer porous layer.[153,154] More recently, one model described the SEI consisting of a first dense layer mainly formed of inorganic compounds ensuring the protective role of the SEI towards reduction. This inorganic layer is covered by an organic or polymeric layer allowing good Li^+ transport. LiF crystallites can also be found in this organic layer.[155] Another detailed study has shown the potential depende character of the formation process of the SEI, the main species being carbonates, alkyl carbonates and LiF.[148]
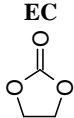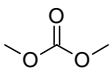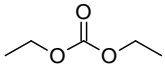
6.1.3.2. SEI composition at the carbon/electrolyte interface

We will now report on the principal species present in the SEI and on the reactions leading to the formation of these species. In literature, three kinds of reactions are distinguished: solvent reduction, lithium salt decomposition and reaction of side products with impurities or other SEI compounds. These reactions have been proposed using several experimental procedures, among them XPS and FTIR appear to be the most relevant spectroscopy techniques.[65]

- *Solvent reduction*

The reduction reaction of the cyclic (EC) and the linear (DEC and DMC) alkyl carbonates solvents are listed in the Table I. *6*. As transesterification and polymerisation reactions can take place, they are also considered here.

Table I. 6 : Main reactions and SEI products resulting from the degradation of the alkyl carbonates solvents EC/DEC/DMC (From ref [156,157,158,159,160,161,162])

	Reactions
EC (structure)	$2EC + 2e^- + 2Li^+ \rightarrow (CH_2OCO_2Li)_2 + CH_2=CH_2\uparrow$
	$EC + 2e^- + 2Li^+ \rightarrow Li_2CO_3 + CH_2=CH_2\uparrow$
	$nEC \rightarrow -(CH_2-CH_2-O)_n- + nCO_2\uparrow$ PEO
	$n(x+y)\ EC \rightarrow -[(CH_2-CH_2-O)_x-/-(CH_2-CH_2-OCO_2)_y]_n- + nxCO_2\uparrow$
ROCO₂R **DMC:R=CH₂** (structure) **DEC:R=C₂H₅** (structure)	$ROCO_2R + e- + Li^+ \rightarrow ROLi + RC\bullet O_2$ $RC\bullet O_2 + Li^+ + e^- \rightarrow ROLi + CO\uparrow$
	$2ROCO_2R + 2e- + 2Li^+ \rightarrow 2ROCO_2Li + R\text{-}R\uparrow$ $DMC + e- + Li^+ \rightarrow CH_3OCO_2Li + R\bullet$ $nR\bullet \rightarrow Rn\ (polymers)$ $nR\bullet + e^- + Li^+ \rightarrow RLi$
	$ROCO_2R + 2e^- + 2Li^+ \rightarrow Li_2CO_3 + R\text{-}R\uparrow$
Reaction between solvents	$EMC \leftrightarrow DMC + DEC$ $ROCO_2R + EC \rightarrow ROCO_2CH_2CH_2O_2CO_2R$
Main species found in the SEI resulting of solvents degradation	**Li₂CO₃, Lithium alkyl-carbonates** (ROCO₂Li), **alkoxides** (ROLi) **Poly(ethylene oxides)** (PEO), **poly(ethylene carbonates)**

To this list, we can add lithium oxalate $(Li_2C_2O_4)$[163] and lithium succinate $(LiO_2CCH_2CH_2CO_2Li)$ that have been reported in few papers.[164] Polymers (extended hydrocarbons chains) have also been reported using TOF-SIMS characterisation.[165]

- *Salt decomposition*

The decomposition of the salt has also been widely studied. Lithium hexafluorophosphate in carbonate solvents is known to form an equilibrium with lithium fluoride (LiF) and phosphorus pentafluoride (PF_5) [166, 167] giving rise to several secondary reactions. On top of that, $LiPF_6$ is very sensitive to water,

moisture and alcohol[168, 169] and formation of hydrofluoric acid (HF) is a result of this sensitivity. Reactions where $LiPF_6$ is involved are reported in Table I. 7:

Table I. 7 : Main reactions and SEI products resulting from the degradation of $LiPF_6$ (From ref [170,171,172,173])

	Reactions
$LiPF_6$ and secondary reactions	$LiPF_6 \rightarrow \textbf{LiF} + PF_5$ $LiPF_6 + ne^- + nLi^+ \rightarrow LiF + \textbf{Li}_{\textbf{x}}\textbf{PF}_{\textbf{y}}$ $PF_5 + 2xe^- + 2xLi^+ \rightarrow xLiF + Li_xPF_{5-x}$ $LiPF_6 + Li_2CO_3 \rightarrow 3LiF + POF_3 + CO_2$ $PF_5 + Li_2CO_3 \rightarrow 2LiF + POF_3 + CO_2$ $POF_3 + 2xe^- + 2xLi^+ \rightarrow Li_xPF_{3-x}O + xLiF$ $POF_3 + 3ROLi \rightarrow OP(OR)_3 + 3LiF$ $OP(OR)_3 + -(CH_2-CH_2-O)_n \rightarrow -(O-CH_2-CH_2)_n-O-OP(OR)_3$
Reactions with impurities (H_2O/HF)	$LiPF_6 + H_2O \rightarrow LiF + POF_3 + 2HF$ $PF_5 + H_2O \rightarrow POF_3 + 2HF$ $ROCO_2Li + H_2O \rightarrow Li_2CO_3 + CO_2 + ROH$ $H_2O + Li^+ + e^- \rightarrow Li_2O + H_2\uparrow$ $H_2O + Li^+ + e^- \rightarrow LiOH + 1/2H_2\uparrow$ $ROCO_2Li + HF \rightarrow LiF + ROCO_2H$ $Li_2CO_3 + HF \rightarrow 2LiF + H_2CO_3$ $Li_2CO_3 + HF \rightarrow 2LiF + H_2O + CO_3$ $Li_2O + 2HF \rightarrow 2 LiF + H_2O$ $LiOH + HF \rightarrow LiF + H_2O$
Main species found in the SEI resulting from salt degradation, reported in the literature	**LiF, Fluorophosphates** (Li_xPF_y , $Li_xPF_{3-x}O$)**,** **Phosphates** (as $OP(OR)_3$))

The reactions and products given in Table I. 6 and Table I. 7 do not constitute an exact list of the SEI compounds formed on carbon electrodes. There is no general recipe as a lot of factors can influence this layer and papers can sometimes be contradictory about some compounds, regarding for example, the presence of polymers. The techniques and methodology used to evaluate the SEI compositions have also to be carefully handled because some procedures can be destructive and modify the real compositions. Argon sputtering is commonly used to carry out depth profiling and it is known, for example, to create/enhance Li_2O formation.

The SEI layer is complex and that is why the number of research papers on this subject is continuously growing. The current emergence of new electrode materials in Li-ion batteries generates the need for a systematic SEI investigation to fully understand the mechanisms occurring upon cycling.

The next part will be focused on the Si-based negative electrodes. After a presentation of the reaction mechanisms involved upon lithiation of the system, we will see the main approaches considered to limit the problem of volume expansion and then discuss about the SEI in such a system.

7. Silicon anodes as negative electrodes in a battery: a good candidate?

Silicon belongs to the alloying materials and in addition to its interesting electrochemical properties, its high abundance on Earth, low cost and low toxicity make this material an interesting alternative material as negative electrode and a research subject widely studied. Figure I. 16 shows the number of publications related to the use of silicon as anode in Li-ion batteries and we can see an exponential increase these last twenty years.

In this part, we will describe the reactions occurring upon silicon lithiation and see several examples of the general strategies used to limit the volume expansion of Si-based electrodes (see anode part described earlier in this chapter). Some material from reviews focussing on alloy materials and more specifically on silicon has been used for this part and can be found in references. [68,82,83,85,86,90,174,175]
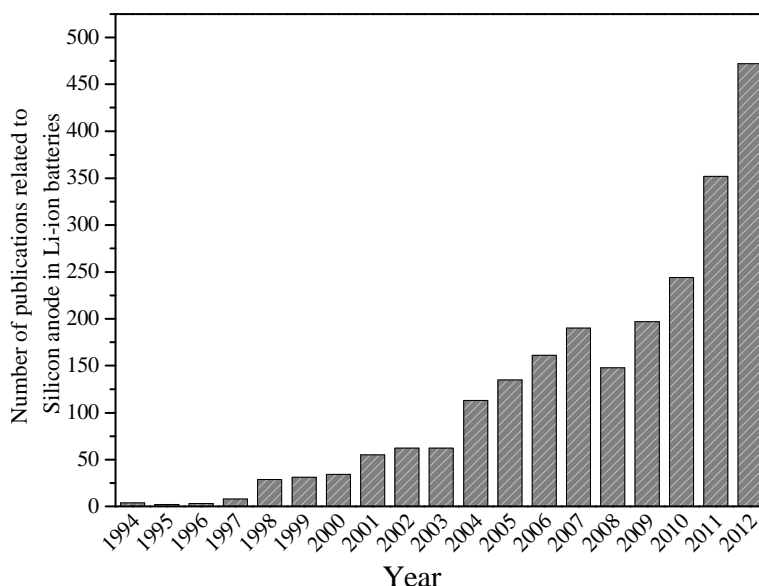
Figure I. 16 : Number of publications related to the use of silicon anode materials for lithium-ion battery electrodes as a function of the publication year (collected with SciFinder database, ''Silicon'', "anode" and ''lithium-ion battery'' as search items).

7.1. The Li-Si alloy

The ability of silicon to electrochemically form an alloy with lithium was firstly demonstrated at high temperature by Sharma *et al.* in 1976.[176] Other works by Huggins *et al.*[177,178], have shown that the lithiation of silicon was following the equilibrium Li-Si phase diagram with four distinct voltage plateaus corresponding to four distinct crystalline lithium silicides: $Li_{12}Si_7$, Li_7Si_3, $Li_{13}Si_4$ and $Li_{22}Si_5$.[177] The formation of the highly lithiated phase $Li_{22}Si_5$ ($Li_{4.4}Si$) corresponds to theoretical capacity of ~ 4200 mAh.g^{-1} which is much higher than the theoretical capacity of metallic lithium (3862 mAh.g^{-1}).

However, the formation of Li_xSi alloys appears to be different at room temperature. The first electrochemical discharge curve just exhibits only a single long voltage plateau due to a two-phase addition reaction around 0.1V *vs.* Li$^+$/Li and suggests that none of the phases previously mentioned are

formed. In fact, it was shown that micrometric-sized crystalline silicon particles are converted into a amorphous Li_xSi alloy and a continual lithiation of this alloy takes place during this first discharge.[179] Obrovac et al.[180] and Hatchard et al.[181] confirmed these results by ex-situ and in-situ XRD and showed that a crystalline phase, $Li_{15}Si_4$, was formed at low potential (< 50 mV vs. Li^+/Li), and this when either crystalline particles or amorphous film were used. Note that this crystallisation only concerns micrometric particles (325 mesh size) or films thicker than 2 μm [181] but not the nano-Si based system.[182] During charging, a plateau at ~0.4V is observed corresponding to the two-phase reaction from crystalline $Li_{15}Si_4$ to amorphous Li_zSi (z~2) then followed by the formation of amorphous Si evidenced by Li et al. by in-situ XRD.[183] The incomplete delithiation of the Li_xSi is often reported and explained as one part of the irreversible capacity loss.

To summarize, during the first cycle, phase changes are observed and the highest lithiated phase obtained at room temperature is $Li_{15}Si_4$ ($Li_{3.75}Si$) with a theoretical capacity of 3578 mAh.g^{-1} according to the reaction given in Table I. 8:

Table I. 8 : Reactions of Li insertion and extraction into silicon (from ref [90])

Reaction	Equation and phase changes
Partial discharge (lower cut-off > 50mV vs. Li^+/Li)	Si (crystalline or amorphous) + xLi^+ + xe^- → Li_xSi (amorphous)
Full discharge	$4Si + 15Li^+ + 15e^-$ → $Li_{15}Si_4$ (crystalline)
Charge	$Li_{15}Si_4$ → 4Si (amorphous) + yLi^+ + $y15e^-$ (+ remaining Li_xSi)

- ***Reaction with SiO_2***

Some remarks should be added about the behaviour of SiO_2 towards lithiation/delithiation. Silicon is often covered by a native oxide layer that Li-ions might have to cross to reach the much more active Si. A lot of work has been done on SiO_x as anode material which appear to be attractive due to its limited volume expansion compared to pure Si. However, the nature of this material is not very clear. Careful PES analyses of SiO_x layers forming at the SiO_2/Si interface have been carried out in previous works. [184,185] However, the Si 2p signature of these "SiO_x" species is always very weak with respect to SiO_2. Moreover the "SiO_x" signal most often consists of a gradual shift between several components assigned to Si^+, Si^{2+} and Si^{3+} oxidation states, with binding energies distributed between Si^0 and Si^{4+}. SiO_x can also be seen as a mixture of Si and SiO_2 [90] (Paper I).

The reaction of SiO with Li has been studied by various techniques (XPS, NMR, HRTEM) and the formation of Li_xSi, Li_2O and lithium silicates are often reported, the last two compounds buffering the silicon volume expansion. Among the several lithium silicate compounds reported ($Li_2Si_2O_5$, Li_2SiO_3, $Li_2Si_2O_3$) the formation of Li_4SiO_4 is often described as the main irreversibly formed lithium silicates.[186,187,188] We have clearly proved its irreversibility in paper I as well as in paper II and more recent papers have then confirmed this point.[189,190,191,192] It has also been shown that Li_4SiO_4 could be formed mechanochemically by simply milling metallic lithium with a silicon oxide.[193]

In addition, a NMR study by Kim et al. suggested that inactive SiO_2 can be made active when in the nanoscaled size and that the formation of Li_2O could be reversible: $2Li_2O + Si → SiO_2 + 4Li^+ + 4e^-$. [188]

Since then, scientists have been open to the studies of the low cost material SiO_2 which is widely present on Earth.[194] Guo et al. proposed by XPS and NMR the following irreversible reactions (Eqn. 13 and 14), both reactions giving Si that then reversibly reacts with Li forming the alloy Li-Si: [195]

$$2\ SiO_2 + 4Li^+ + 4e^- → Li_4SiO_4 + Si \qquad \text{Eqn. 13}$$
$$SiO_2 + 4Li^+ + 4e^- → 2Li_2O + Si \qquad \text{Eqn. 14}$$
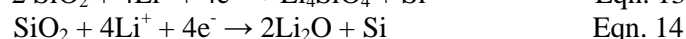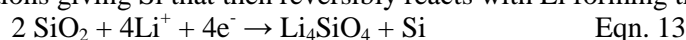
Additional reactions are found in the literature. The reversible reaction of $Li_2Si_2O_5$, for example has been proposed:[194,196] $(5SiO_2 + 4Li^+ + 4e^- → 2Li_2Si_2O_5 + Si)$

At this stage of the research on SiO_2, it appears difficult to clearly distinguish if there are lithium silicates that might be cycled reversibly or not. However, most of the current studies agree about the irreversible formation of the lithium orthosilicate Li_4SiO_4 upon the first lithiation process and it can now be considered as reliable information. The reaction between SiO_2 and Li will be discussed in paper II.

Finally, the lithiation of Si into $Li_{15}Si_4$ leads to an important volume change (~280%) that has tremendous impact on the battery performance as described earlier. The main impacts are schematised in Figure I. 12. In the following part of the thesis, the strategies developed to avoid/limit the volume expansion will be described with several examples. They will be divided into three categories: (1) a modification of the cycling conditions, (2) a modification of the nature of the silicon (size, morphology, crystallinity) and (3) the incorporation of other phases to buffer the expansion.

7.2. Improvement of the Si-based electrode materials

7.2.1. Operating voltage control

Limitation of the capacity is the easiest way to reduce the volume expansion and enhance the cyclability of an alloying electrode. Already in 1999, Li *et al*. showed that cycling performance could be improved by reducing the upper cut-off voltage from 2.0V to 0.8V *vs*. Li^+/Li of a Si/C/PVdF composite electrode cycled versus Li^0.[182]

The modification of the lower cut-off has been more carefully studied for silicon because the depth of the discharge is directly linked to the amount of lithium introduced into silicon. Jung *et al*. showed in 2003 that the change of the lower limit voltage window from 0V to 0.2V was beneficial to the cycling performance of an amorphous Si thin film, however, the capacity was limited to ~400 mAh.g^{-1}.[197]

It was later found that the limitation of the lower cut-off was even more important in the case of silicon with micro-meter sized particles. Indeed, the highly lithiated crystalline phase $Li_{15}Si_4$ formed at full discharge undergoes a volume expansion of 280% and it appears not to release the lithium as easily as the amorphous Li_xSi phase. During long-term cycling, the $Li_{15}Si_4$ phase contributes to the irreversible capacity and it was suggested to avoid the formation of this phase. With this aim and on the basis of in-situ XRD study, Li *et al*. proposed to limit the voltage to 70 mV.[183] Obrovac *et al*. proposed in 2007 a procedure to reversibly cycle crystalline Si particles. Through this procedure, the core of pristine crystalline silicon is kept unlithiated with a shell of amorphous silicon that reversibly will be lithiated/delithiated.[198] This method is made up of two steps: the particles are first partially lithiated and converted into a desired amount of amorphous silicon during some activation (or conditioning) cycles, the electrode is then cycled with a lower cut-off voltage of 170 mV to avoid over-lithiation and to maintain the crystalline core. A capacity of 960 mAh.g^{-1} was obtained with a very good coulombic efficiency. Li *et al*. used this procedure but simplified the conditioning cycles by four initial pre-cycles.[199]

Improved cycling performance can be obtained by limiting the insertion of lithium into the Si particles and thus limiting the structural changes which means less cracking occurring upon lithium extraction. This method lowers the capacity of the cell but it is important to keep in mind that the insertion of 3.75 Li per Si atom gives a theoretical capacity of 3579 mAh.g^{-1} and the insertion of just 1 Li per Si atom gives a capacity around 960 mAh.g^{-1} which is still much higher that current insertion materials.

7.2.2. Modification of the Si morphologies

Great improvements have been achieved by scaling down Si particles to nanosize, or by using Si thin film, nanostructures or amorphous materials.

7.2.2.1. Nanosized particles and thin film silicon.

The benefit of using nanosized silicon particles (<100nm) compared to bulk silicon (250 meshes, corresponding to a distribution of particles with sizes <50μm) was shown by Li *et al*. in the late 1990's.[182] It is now known that nanoscale particles are much better than bulk materials and mitigate

problems due to volume expansion because they can sustain higher strain and generally they do not crack after full lithiation.[83] In addition, electron and ion diffusion paths are shorter so better kinetic is obtained. Liu *et al*. have estimated the critical particle diameter (at ~150 nm), below which the particles did not crack upon cycling. [200]

Even greater enhancements were obtained later by Graetz *et al*. and the use of an amorphous Si thin film instead of crystalline nanoparticles gave a reversible capacity of 2000 mAh.g^{-1} over 50 cycles.[201] Amorphous materials are reported with better results because the phase transition (crystalline/amorphous) is avoided and an isotropic expansion is observed opposite to the anisotropic expansion of crystalline particles.[82]

A lot of work has been done to study thin film Si electrodes,[202,203,204,205] and the advantage of not using additional inactive materials. Thin films are usually prepared by rf magnetron sputtering (PVD) and also in this case full discharge leads to micro cracks of the electrode.[202] As previously discussed, the limitation of the lower cut-off voltage improves the cycling performance and reduces these cracks for thin films.[203] The roughness of the substrate (current collector) has also an importance and rough Cu-foil appears to give better results than flat foils due to a better adhesion between active particles and the substrate.[205]

7.2.2.2. Three-dimensional current collectors and porous silicon particles

Various studies these last 10 years have been focused on finding new systems or architecture of the negative electrode to mitigate the bad effects of the volume expansion. The use of 3D-current collectors, such as Ni foam,[206] Cu foam [207] or Cu cellular architecture[208] casted with Si composite materials have been some of the first approaches. These systems have shown improvements over the classical 2D-system by restricting the huge volume changes of silicon particles. The improvements, however, seem to mainly be due to the good conductivity given by the 3D metallic structure and unfortunately loss of particle contact remains a problem.

The use of porous Si particles (Figure I. 17 (a)) seems to be a good solution. Most of the 3D porous silicon particles are made with an etching process that involves the use of HF acid, chemical etching[209,210] and electrochemical etching.[211]

7.2.2.3. Nanoparticles, 1D and 2D architectures

The combination of the two latter concepts (nanosized particles and a porous system) has lead to a wide variety of objects. Si interconnected hollow spheres, for example, have shown great improvement and high capacity over 700 cycles.[212] Hollow porous Si nanoparticles were prepared later by Chen *et al*. using another synthesis approach than the chemical SiO_2 etching by HF for hollow spheres. Polystyrene nanoparticles (120 nm) are used as the template, tetraethyl orthosilicate (TEOS) as the Si source and cetyltrimethylammonium bromide (CTAB) as a pore forming surfactant; TEOS and CTAB are then chemical etched. This procedure confers high porosity to the Si particles (Figure I. 17(b)). [213]

The use of homogeneous films often leads to cracks when cycling them as electrodes and an area with a critical size is formed.[214] This observation has lead to the investigation of 2D structured electrodes as arrays of nanopillars[215] or well defined patterned surfaces (Figure I. 17(c)).[216] Fracture of the composite could be avoided leading to improvement of the cycling performance. More fundamental studies on single-crystalline silicon as model system have allowed the understanding of the structural evolution that occurs during electrochemical lithiation of Si nanostructures[217] and it has been shown that the evolution of the strain is highly anisotropic in the crystalline sample.[218]

The main attention these last years has been devoted to Si nanowire[219,220,221,222,223,224] and Si nanotube[225] -1D-structures to get a large surface area, to allow for a lateral relaxation and an efficient 1D electron transport. These 1D systems show currently very promising performances and constitute good model systems for research. Taking advantages of the transparency of these nanostructures, important information about anisotropic expansion,[226] critical diameter of the nanowires before fracture (~300 nm) [227] or about the lithiation processes that occurs[228,229] have been obtained using in-situ TEM.

The design of nanostructured architectures has permitted great improvements, for example, the pulverization of the active particles limiting the effect of volume changes can be avoided. Nevertheless, there is still expansion occurring which affects the global battery performance due to the loss of contact between the particles. The use of nanoparticles has also disadvantages as cost, and a large surface area that will require further SEI formation, so the benefits gained on one side (no pulverization) can be lost on another (SEI side-reactions).

a, 3D porous Si

b, Hollow nanosphere
with or without porosity

c, 2D patterned surface

d, Si nanotubes

e, Si nanowires
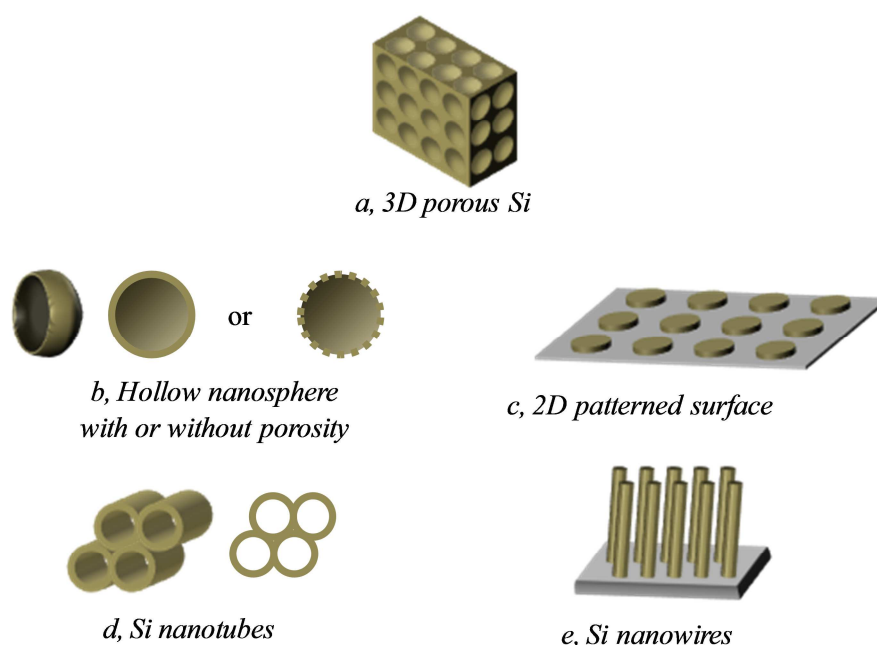
Figure I. 17 : Novel Silicon anodes architectures

6.2.3. Use of an additional phase
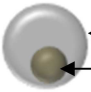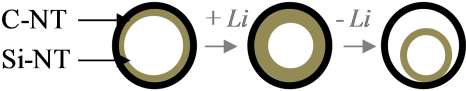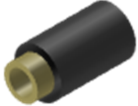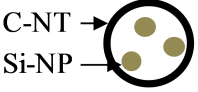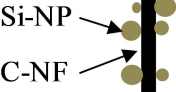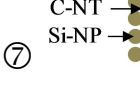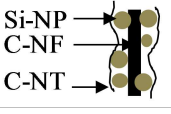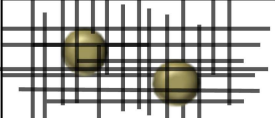
Several kinds of additional phases have been investigated for Si electrodes (carbon matrices, active or inactive intermetallic compounds or by the use of different polymeric binders) with the main purpose to buffer the volume expansion during lithium alloying of Si and to avoid the aggregation of the particles upon long-term cycling.[230]

6.2.3.1. Si-carbon composite electrode

Graphite and more generally carbonaceous materials appear as good phases that can buffer the volume expansion and improve the electronic conductivity of the electrode. More or less active towards lithium, carbon has a low volume expansion and a significant proportion is beneficial for the cycle-life of the electrode.[231] Carbon coating on Si has a good impact and can restrict the Si volume expansion.[232] On the top of that, a stable SEI can be formed on the carbon coating and the continuous reformation of SEI is avoided.[85] Binder is often involved in such a composite and the main drawback of adding additional phases is a lower specific capacity of the electrode.

In the literature, the term Si/C materials can refer to either silicon coated by carbon, carbon coated by silicon [233,234,235] but also to a mechanically mixed carbon and silicon to get a composite with dispersed particles. All these concepts have led to a large variety of materials and techniques. Si-carbon composites can be obtained by CVD, TVD (thermal vapour decomposition) using carbon precursors (such as benzene, for example) or silicon precursors (such as SiH_4) or spray-drying techniques. [236] A last technique mainly used is a simple ball milling.[237,238,239] These techniques are widely reviewed by Kasavajjula *et al*.[86]

Table I. 9 : Novel Si-C composite systems found in the literature: nanoparticles-1D and 3D systems

2D and/or 3D representation

①

C-hollow sphere
Si NP

②

Si NP
C

③

C-NT
Si-NT

+ Li   - Li

④

C-NT
Si-NP

⑤

Si-NP
C-NF

⑥

C-NT
Si

⑦

C-NT
Si-NP

⑧

C
Si
C-NT

⑨

Si-NP
C-NF
C-NT

⑩

Carbon coatings have recently been used to improve the battery performance using Si nanoparticles and 1D nanostructures (described above). In 2006, Ng *et al.* coated silicon nanocomposites by a spray-pyrolysis method. [240] A Yolk-shell structure was suggested lately by Liu *et al.* [241] consisting of Si nanoparticles completely sealed inside conformal, thin, self-supporting carbon shells (① in Table I. 9). A similar approach has been used in the work of Iwamura *et al.*, [242] where they formed Si nanoparticle/carbon composites in which each Si nanoparticle was embedded in a spherical nanospace (② in Table I. 9

Table I. 9). Hertzberg *et al.* proposed rigid carbon nanotubes used as outer shells with Si coated on the inside supporting the volume expansion due to the empty core (③in Table I. 9). [243] Similarly, Wu *et al.* suggested sealing Si nanoparticles in a carbon tube (④in Table I. 9). [244] All these concepts are made of silicon surrounded by carbon but the other way around can also be seen where silicon can coat or be loaded on carbon.

Carbon additives can be used with different morphologies. Some of the simplest structures are the commonly used carbon black, acetylene black or graphite. Recently, more complex structures have been investigated as additives such as fullerene,[245] graphene,[246,247] nanotubes [248,249,250] or nanofibers that usually are loaded with Si nanoparticles (⑤in Table I. 9).[251,252,253,254,255] Carbon–nanotubes can be coated with a thin Si film (⑥in Table I. 9) or by droplet structures (⑦ in Table I. 9)[256] and an additional carbon coating being added by Evanoff *et al.* (⑧in Table I. 9).[257]

3D porous carbon scaffold structures (⑩in Table I. 9) [258] have also been reported as well as mixed nanopaper aerogels which can incorporate carbon nanotube (CNT) structures[259] or Si/carbon nanotube/carbon fiber composites ⑨.[260]

Composites using 1D structures (nanotubes or nonfibers) and 2D structures (graphene) have the advantages of excellent electronic conductivity and good mechanical flexibility. They are chemically and thermally stable with large surface area. They can be used together with the active materials and do not require binders and additional conductive compounds which explain their current interest.

Most of the recent concepts based on Si/C composites presented in this part are illustrated in Table I. 9.

6.2.3.2. Intermetallic compounds

Addition of a metal is another direction used to buffer the volume expansion and enhance the performance of the Si electrode. Note that this strategy has been much more used with Sn or Sb-based electrodes than Si-based electrodes. Some intermetallic compounds have been investigated with Si (active and inactive).

Among Si-inactive materials added to or coated on Si, we can note the presence of some metals, such as Fe, [261,262] Co, Ni, [263,264] Cu,[265,266] Cr,[267] Ti.[268,269] Oxides and ceramics have also been used as well as Al_2O_3,[270] Co-Co_3O_4 ,[271] TiN, SiC, TiB_2 or TiC.[272]

From the side of adding lithium-active materials with Si, fewer compounds have been studied and the four main active elements that have been used are: Mg,[273] Ag,[274] Sn, [275,276,277] and Al.[278,279]

These approaches have only shown a slight improvement of the cycling performance and they are less investigated than Si-C composites previously described.

6.2.3.3. Binders used with Si-based electrodes

The intermetallic materials or the 1D or 2D structures present some drawbacks such as cost, high weight for some metals or multistep synthesis that can be difficult to scale up for massive production. As a consequence, silicon particles combined with simple and cheap conductive additives (carbon black or acetylene black) are still the main compounds used and a simple polymeric binder is usually added to maintain a good contact between the particles.

PVdF (polyvinylidene fluoride), the binder commonly used in carbonaceous negative electrodes was naturally the first one to be tested with Si-based electrodes (Figure I. 18(a)). However, the properties of this poor elastomeric binder appear incompatible with the huge volume expansion of the silicon. In addition, the solvent NMP (N-methyl-2-pyrrolidone) used to dissolve PVdF is toxic with CMR properties (Carcinogenic, mutagenic or toxic for reproduction), and there is hence a necessity to avoid its use.

It was first believed that more elastomeric binders or copolymers were required to accommodate this expansion, for example, elastomeric tether binders were used (poly(vinylidene fluoride–tetrafluoroethylene–propylene).[84] Later a water soluble binder containing styrene-butadiene-rubber (SBR) with a carboxylmethylcellulose sodium salt (Na-CMC) was explored. [280,281]

A surprising and considerable improvement was reached by using the single stiff and brittle binder, carboxymethyl cellulose (Figure I. 18(b)).[199,282,283] The superiority of CMC over PVdF is believed to be due to the chemical interaction of CMC with the active particles: an esterification bond forming between hydroxyl groups on the Si surface and the carboxyl group in CMC creating a covalent bond.[284,285,286,287] PVdF chains contrary to CMC form polymeric networks into which the powder is mechanically entrapped. Key *et al.* showed that the strong binding in CMC-Si was important to prevent capacity loss.[288] Recently, Bridel *et al.* have shown that CMC chains can bind to Si via covalent but also by hydrogen bonding depending on the pH of the solution.[289] CMC is still very attractive and improvements are still obtained by playing with, for example, a CMC porous scaffold which seems to improve the performance compared to conventional slurries with CMC.[290]

The interaction due to the carboxyl group of the CMC has led to the investigation of another binder containing this group: the polyacrilic acid (PAA). Indeed, CMC has several weaknesses: it is not soluble in organic solvents and requires the use of water that can later oxidize Si. Its mechanical properties are fixed (cross-linking is not possible) and so it cannot be optimized for Si anodes. PAA is easily tunable (formation of block and graft copolymer architectures, for example) and is soluble not only in water but also in organic solvents such as, e.g. ethanol. Magasinski *et al.*[291] proposed to use poly(acrylic acid) (PAA, Figure I. 18(c)) as binder and showed better performances than CMC on Si-based electrodes. The improvement was suggested to be due to high concentration of carboxylic groups.

Its polyacrylate derivative poly(sodium acrylate) (PAANa)[292,293], has also shown interesting results. It has been concluded that PAANa forms a uniform thin layer covering the active material and acting as an artificial SEI further reducing electrolyte decomposition usually observed upon long-term cycling. A combination of PAA (also referred as PAH) and PAANa was found recently by partial neutralization of the polyacrylic acid leading to the binder $PAH_{0.2}Na_{0.8}$ which was shown to outperform the performance of PAA or PAANa.[294]

Finally, the same team also reported good behaviour of a cross-linked polymer between PAA and polycarbodiimide (PCD) giving a stronger adhesion of the active material and improving the capacity retention of the system compared to PAA without PCD.[295]

Polysaccharides are a family of binders that has recently been investigated. Kovalenko *et al.* extracted the alginic acid (alginate) from brown algae, which also contains carboxylic groups (Figure I. 18(d)).[296] Surprisingly in view of the similarities in chemical structures (Figure I. 18), electrochemical results appear to be better than those obtained with CMC based electrodes. One explanation is that one carboxylic group is naturally present in each monomeric units of alginate whereas the synthetic CMC has a random distribution and either none or more than one group per monomeric unit leading to a worse coverage than with alginate.

Other polysaccharides have also been studied, such as amylose, amylopectin, and glycogen[297], which are common natural products (major components of starch in corn, potato or rice) and they all give better results than PVdF.

a, Polyvinylidene Fluoride (PVDF)   *c, Polyacrylic acid (PAA)*

b, Carboxylmethyl cellulose sodium salt (Na-CMC)   *d, Alginic acid (Alginate)*
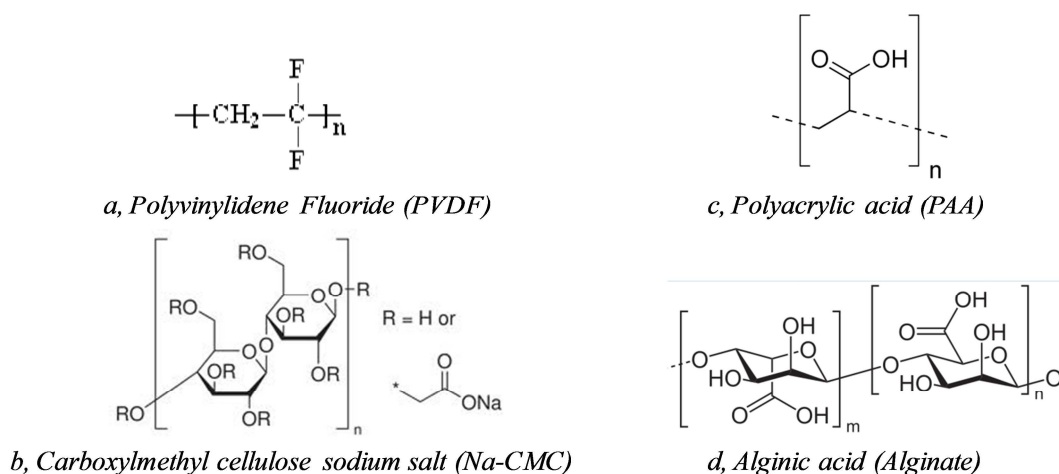
Figure I. 18 : Main polymeric binders used and investigated for Si-anode materials.

All the binders described above are considered as polymeric, or as non-conductive binders. We can, however, note some few conductive binders which have been used with Si-based electrodes and which present the dual advantages of acting as a binder and a conductive additive. Polypyrrole[298,299] or polyaniline (PAN)[300] are two examples but the main improvement in this field was obtained with a PFFOMB,[301] a polymer based on polyfluorene (PF)-type polymers.

The research field on binders is currently very active and recent results are very promising. A wide panel of ecofriendly and abundant binders are now found and investigated as alternatives to PVdF.

6.3. SEI formed on silicon negative electrodes

6.3.1. Composition

When the negative silicon materials alloy with the lithium, the huge volume change will have an effect on the SEI preliminary formed during the first discharge. As we have seen in Figure I. 12, a continuous reduction of the electrolyte occurs during subsequent cycles due to the formation of cracks. In addition to a consumption of the electrolyte (Li source), a growth of the SEI limits Li-ion diffusion through it and reduce the kinetics and performance of the system. Consequently, a SEI with good mechanical properties is required.[302]

In spite of the attractive performance of silicon electrodes, few reports are focused on the interfacial reactions of the silicon electrode with electrolytes. The earlier works, performed on SEI of carbon and metallic lithium electrodes have been a considerable help. Indeed, the low potential of Li insertion into Si and the use of a similar electrolyte ($LiPF_6$ in alkyl carbonates) make the reactions previously shown in this chapter usable and the products reported can potentially be found also in the SEI on Si electrodes.

As for carbon, it appears difficult to give a general reliable and conclusive chemical composition of the SEI on Si materials because of the use of different material architectures, binders, electrolyte components and different experimental techniques (XPS, [303,304,305,306,307,308,309,310,311,312,313] FTIR, [306,323,310,312,313,314,315,316] TOF-SIMS, [305,308] NMR, [320,317,318] SEM, EIS[303,304,312,319,320]). SEI studies of binder free and conductive additives free systems have often been analysed, such as Si films/thin films [303,305,306,307,308,309,323,310,314,315] or Si nanowires,[304,308,312] but few studies of composite electrodes have been reported.[320,317,321]

Table I. 10 gives the main SEI species reported in the literature for $LiPF_6$ -based electrolytes in non-aqueous solvents (EC, DEC, DMC, PC).

Table I. 10 : The main SEI species of Si-based anodes reported in literature

Compounds	Ref.
Li_2CO_3	303,304,306,307, 308,310,312,315,317
Lithium alkyl-carbonates ($ROCO_2Li$)	303,304,306,307, 308,309,310,312,314,315
Alkoxides (ROLi)	304,305,307,312
Poly(ethylene oxides) (PEO)	304,307
Li_2O	304,312,317
Poly(ethylene carbonates)	310
Oxalates	307,312
LiF	303,304,305,306, 307,308,309,312, 314,315,317
Fluorophosphates (Li_xPF_y)	303,304,305,306,309, 312,314,315,317
$Li_xPF_{3-x}O$ Phosphates	304,306,314,315

As depicted in this Table I. 10, similar SEI compounds have been identified on carbon- and silicon-based electrodes, respectively. A SEI structured with an inner inorganic layer and an outer organic layer has been suggested. [304,308] The SEI on Si is also voltage dependent with a thick layer formed on the Si particle surfaces at low potential[304] and the use of PC gives a thicker organic layer richer in alkyl-carbonates than EC based electrolytes [308] leading to lower electrochemical cyclability and more rapid capacity fade.[313]

However, some detected and suggested species are still controversial. The presence of Si-F_x in the SEI is sometimes reported [304] and proposed to be due to a reaction of SiO_2 with HF. This kind of reaction does not occur when a carbon coating is applied on the Si particles and no SiO_2 is present. In this case, the formation of siloxanes (R-Si-OR) has instead been reported.

The SEI formed on a Si/C/CMC composite electrode has been examined in papers I, II and III. The first two papers study the common salt $LiPF_6$ and the monitoring of the first electrochemical cycle (paper I) as well as a long term-cycling (paper II) have been performed. Paper III analyses the SEI formed with another salt, LiFSI.

6.3.2. Additives

The use of additives has also been investigated for Si-electrodes and VC has been successfully used in several studies. [307,310,313,316,317,321] Martin *et al*. have concluded to the formation of poly VC as previously observed on graphite. Dalavi *et al*. also reported the formation of this polymer as a beneficial point and noted the decrease of the amount of LiF. Chen *et al*. pointed out the uniformity and smoothness of the SEI with VC giving an impermeable layer while the VC-free SEI was getting thicker and thicker upon cycling.[310]

Similar to VC, FEC (Figure I. 19) is another good candidate as an additive and has been investigated on Si-based electrodes in several papers.[305,309,312,313,316]

The SEI layer formed in a FEC-based electrolyte is thinner, smoother and more stable than with a FEC-free electrolyte. It consists of a layer rich in fluorine: the stable LiF and fluorinated Si compounds maintaining a stable interface. [309] Nakai *et al*. have confirmed that a thinner SEI rich in LiF was obtained and proposed the formation of polyene (-(-CH$_2$=CH$_2$-)$_n$.[305] Etacheri *et al*. have also proposed the formation of a polycarbonate as the major surface film component via HF elimination and polymerization of the resulting VC. These results are nonetheless contradictory to the work of Dalavi *et al*. that reports no polymerization phenomenon when FEC is used and a decrease of the amount of LiF compared to a classical electrolyte with EC/DEC/EMC.

Both VC and FEC have shown to form stable SEI films at elevated temperatures.[312,316]

a, Vinylene carbonate
(VC)

b, Fluoroethylene Carbonate
(FEC)
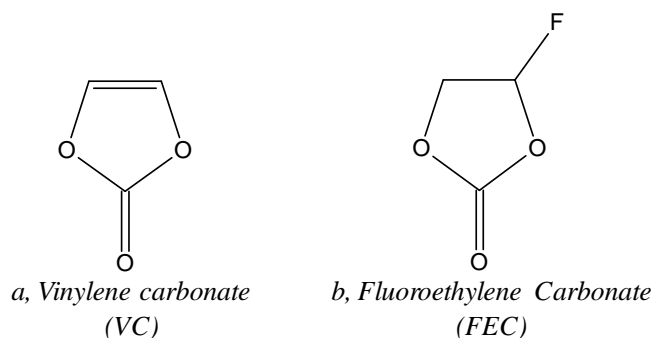
Figure I. 19 : Structures of (a) VC and (b) FEC

Another approach is to directly modify the surface of the Si particles by addition of an alkoxy silane ((CH$_3$O)$_x$Si(CH$_3$)$_{4-x}$) that can react with hydroxyl groups (SiOH) and create siloxane Si-O-Si linkages (Eqn. 15) passivating the Si surface and thus stabilizing the SEI: [315,322]

$$-Si-O-R+ HO-Si \rightarrow -Si-O-Si- + ROH \qquad \text{Eqn. 15}$$

Finally, a last way to improve the SEI stability is to use another electrolyte or a mixture of lithium salts.

Choi *et al*. [323] suggested the replacement of LiPF$_6$ by LiBOB and improvement of the discharge capacity retention of a Si//Li half-cell was evidenced. The SEI formed had a less-porous structure and the formation of electrochemically inactive Si phases was observed to be limited.

Li *et al*. [321] have investigated several classical salts, LiBF$_4$, LiClO$_4$, LiBOB and LiPF$_6$. But the best performance was achieved using a mixed electrolyte of 0.5MLiBOB + 0.38MLiPF$_6$ containing VC leading to a compact and stable SEI. An improvement by addition of LiBOB or LiFOB in LiPF$_6$ based electrolytes was also reported by Dalavi *et al*.[313]

7. Conclusion

To conclude this first part, we have seen that the world of Li-ion battery technology is wide, in continuous development and the attention is still turned to the three main components of the battery cell (electrolyte, negative electrode and positive electrode) in order to obtain a system that is very competitive, safe and as eco-friendly as possible.

The good properties exhibited by the alloying materials based on Si or Sn make these materials attractive alternatives to the carbon negative electrode used in commercial systems. But the volume expansion remains the main problem and needs to be solved for a potential commercialisation of these systems.

The interfacial phenomena occurring at the surface of these new materials have also been poorly investigated and it is the purpose of this PhD study. In addition to the analysis of the SEI formed on Si/C/CMC composite electrodes (Paper I, II and III) or on the intermetallic $MnSn_2$ (Paper IV and V), alloying and dealloying mechanisms have been studied in this work.

XPS has shown its ability to give crucial answers regarding the SEI layer composition and interfacial phenomena in a wide variety of battery related compounds. In this study, investigations have been performed using an innovative methodology consisting of a non-destructive depth profiling of the electrode/electrolyte interface.

This methodology and the experimental details surrounding the work carried out during this PhD are described in chapter 2.

CHAPTER II

Methods

1. Sample preparation

1.1. Si electrode preparation
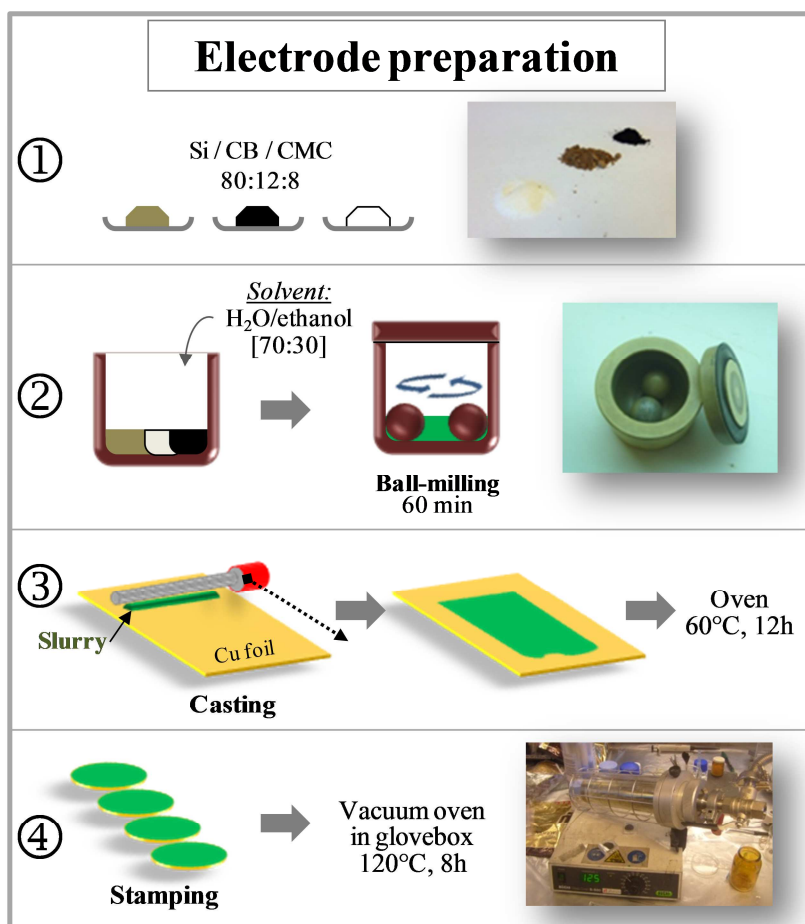
Figure II. 1 : Si/C/CMC composite electrode preparation

Si electrodes used in papers I-III were prepared by mixing 80% of crystalline silicon powder (<50nm, Alfa Aesar), 12% of carbon black (SuperP, Erachem Comilog) and 8% sodium-CMC (CMC-Na, M_w= 700.000, DS=0.9, Sigma Aldrich). The solvent mixture for the slurry preparation was a water-ethanol solution EtOH/H_2O, 70:30. This ratio was chosen because its higher viscosity improves the homogeneity of the slurry. All components were blended in a Retsch planetary mill for 60 min. Resulting slurry was casted on a 20 μm thick copper foil and dried 12h at 60°C in an oven and the coating thickness was checked with a Mitutoyo absolute digimatic micrometer (≈0.012-0.013 mm). Circular electrodes (diameter: 2 cm) were punched out and dried inside an Argon filled glovebox (< 5 ppm O_2, < 2 ppm H_2O) for 8h at 120°C and at a reduced pressure in a vacuum oven. This procedure is summarized in Figure II. 1.

Each electrode was weighed inside the glovebox to evaluate the amount of silicon ($m_{silicon}$):

$$m_{silicon} = 80\% \ (m_{electrode} - m_{foil})$$

m_{foil} was determined by punching out several copper foil circles and the weight average was calculated. The average mass loading of the electrodes was around 0.5 mg of Si per cm^2.

1.2. Battery assembly

Electrochemical half-cells were assembled by stacking the Si-based composite electrode (working electrode), a lithium foil (counter and reference electrode), and a polymer separator (Solupor) soaked with the electrolyte.

1 M $LiPF_6$ (papers I-II-III) or 1 M LiFSI (paper III) ($Li[N(SO_2F)_2]$, Suzhou Fluolyte Co., purity > 99.9%, H_2O < 50 ppm, Cl^- <1 ppm, SO_4^{2-} < 1 ppm) was dissolved in EC/DEC (2:1 (v/v), Novolyte Purolyte®). Karl Fischer titration showed the water content to be below 10 ppm (the detection limit of the instrument).

This assembly was hermetically vacuum-sealed in a polyethylene-coated aluminum bag with attached nickel tabs as current collectors (see Figure II. 2).
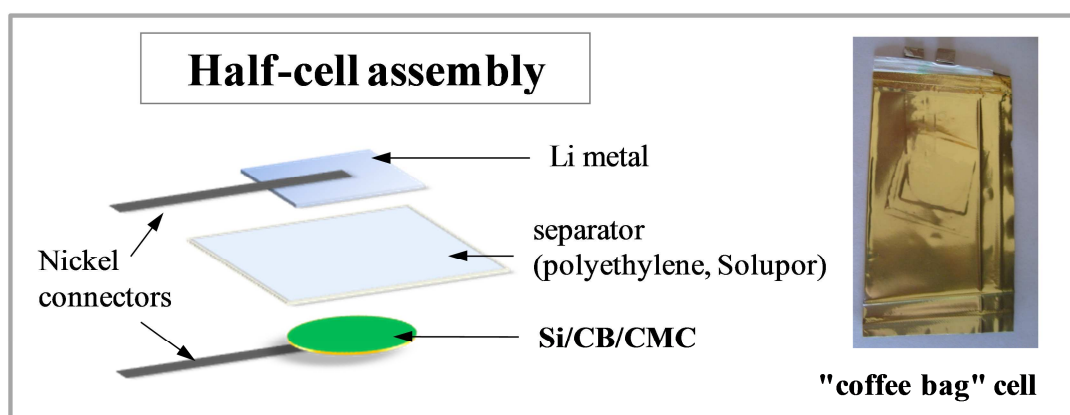
Figure II. 2 : Schematic representation of a half-cell used in papers I-III (on the left). "Coffee-bag" half-cell (on the right)

1.3. Electrode washing prior to surface characterization

Before each surface characterization (PES, SEM), Si half-cells were carefully disassembled in an argon filled glovebox and electrodes were washed with DMC solvent in three successive baths to remove the electrolyte. Then the electrode was quickly dried and mounted on the sample holder in an argon-filled glovebox for PES or SEM analysis.

1.4. Other sample preparations

The work in this thesis also involves the use of other sample preparations briefly described here.

1.4.1. Sol-gel synthesis (Paper I)

The sol-gel process is a wet-chemical synthesis technique inherited from soft-chemistry[324] that involves in the preparation of inorganic and hybrid materials at low temperature (generally below 100 °C). The inorganic sources are metal or silicon alkoxides (typically tetraethylorthosilicate TEOS) that undergo hydrolysis and condensation steps providing a transition from a colloidal sol and a gel-like network resulting from the polycondensation of the inorganic species in solution.[325,326] Both reactions are generally catalyzed either by acidic or basic conditions that determine the morphology, structure

and organization of the network. Hydrolysis and condensation reactions of TEOS involved in sol-gel process are presented in Eqn.16 and 17.

Hydrolysis:
$Si(OR)_4 + H_2O \rightarrow HO\text{-}Si(OR)_3 + R\text{-}OH$ Eqn. 16

Condensation:
$(OR)_3\text{–}Si\text{-}OH + HO\text{–}Si\text{-}(OR)_3 \rightarrow [(OR)_3Si\text{–}O\text{–}Si(OR)_3] + H\text{-}O\text{-}H$ Eqn. 17
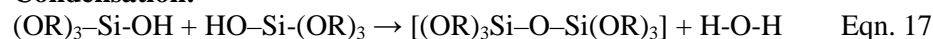
On the basis of such easy to handle reactions, a wide variety of materials can be elaborated at nanoscale with high degree of definition. In the past two decades, the use of organo-alkoxides with a non hydrolysable leaving group has led to a wide field of investigations focused on the development of fine-tuned functional inorganic and organic-inorganic nanomaterials specifically designed for a multitude of applications including nanomedicine, electronic, energy, optics and so forth.[327,328]

Within the framework of the present work, sol-gel process as well as conventional precipitation process was performed to design lithium metasilicate materials (Li_2SiO_3 and Li_4SiO_4) serving as reference materials for X-ray photoelectron spectroscopy characterization of nanosilicon electrode for lithium-ion battery. The precursor used were tetraorthosilicate (TEOS) and lithium ethoxide mixed in appropriate amounts to tune the molar ratio Li/Si that influence the formation of the targeted Li-substitued silicon oxide materials.

1.4.2. Sn electrode preparation (Paper IV-V)

The $MnSn_2$ samples were provided by Charles Gerhardt Institute (AIME, Université Montpellier II). They were prepared by mixing a stoichiometric amount of high purity manganese and tin powders (Sigma-Aldrich). The powder was mechanically milled during 3 days at 400 rpm using a planetary ball mill. The obtained powder was then heated at 500°C for 15 days and cooled down rapidly by water quenching to result in the final active material.

The electrodes used for the PES analysis were prepared by mixing active material and carbon black (90:10). The composite powder was assembled in a Swagelok[TM] type cell using a glass microfiber paper separator (Whatman), 1M $LiPF_6$ in EC:DMC (1:1), as electrolyte, and Li foil as a counter and reference electrode.

After cycling, Swagelok cells were disassembled and the powder collected, washed, hermetically sealed and sent for the PES analysis. (Details are given in Paper IV-V)

2. Electrochemical tests

- ### *Standard galvanostatic cycling (paper I-V)*

Si electrodes:
Galvanostatic cycling has mainly been used during this PhD work. A constant current (i) was applied to the half-cell while the potential was recorded as a function of time (t). The current chosen is preliminary calculated and depends on the C-rate (C/n) selected (c.f. Chapter 1): $i = (C/n)* m_{silicon}$ with $m_{silicon}$ the mass of active material.

The specific capacity proper to the cycled system is then directly calculated using the experimental values i (in Ampere) and t (in second): $C = i.t / m_{silicon}$.

Galvanostatic tests used for the studies related to the 1st electrochemical cycle (papers I and III) were carried out with a current of 150 mA.g^{-1} of silicon between 0.01 and 0.9 V (*vs.* Li$^+$/Li) and stopped at various potential values, with a break of 5 min between discharge and charge.

For studies related to long-term cycling (papers II and III), cells were cycled between 0.12 V and 0.9 V with a current of 700 mA.g^{-1} of silicon (and 150 mA.g^{-1} in paper III). Four pre-cycles were performed prior to this standard procedure in which the electrodes were discharged to 500, 1000, 1500, and 2000 mAh.g^{-1} and charged up to 0.9 V.

Sn electrodes:
A standard galvanostatic test was performed between 0.01 and 1.2V *vs.* Li$^+$/Li, at C/10 (1 C corresponds to the current of 1 Li/Sn in 1h).

- ### *Rate capability tests (paper III)*
A rate capability test consists in varying the C-rate of the cells upon the measurement. The cells used for these tests were successively cycled at constant current rates of 150, 300, 750, 1500, 3000, 7500, 15000 mA.g^{-1} and a last step back to 150 mA.g^{-1} with 5 cycles at each rate. The cells were cycled between 0.12 and 0.9V and the four pre-cycles were also performed prior to rate capability tests.

- ### *Fixed capacity test (paper III)*
A last cycling test was performed with a current rate of 700 mA.g^{-1} of silicon (paper III). The discharge capacity was limited to 1200 mAh.g^{-1} or a cut-off voltage of 0.005V, whichever occurs first. The cut-off voltage in the charge state was limited to 1.0 V. No pre-cycling was performed for this study.

Two testing apparatus have been used in this thesis work, a Digatron BTS-600 (papers I and II) and an Arbin Instruments BT-2043 multi-channel (paper III).

3. Surface analysis

One aspect of this work was to develop/improve non-destructive analysis techniques for a better understanding of electrode/electrolyte interfaces. PES (Photoelectron Spectroscopy) is one of the most powerful techniques to investigate the chemical nature of material surfaces and the electronic structure of solids.[329,330,331] In the field of Li-ion batteries, due to its surface sensitivity, it has become one of the most efficient ways to chemically characterise electrode/electrolyte interfaces. Our objective was to further develop the photoemission spectroscopy methodology and to take advantage of these developments for a better understanding of the reaction mechanisms occurring at the interfacial layers of new negative electrodes battery materials.

3.1.   Photoelectron spectroscopy (PES)

3.1.1. Principle of the photoemission

Photoelectron spectroscopy (PES), also known as Electron Spectroscopy for Chemical Analysis (ESCA) was developed in the mid-1960's by Kai Siegbahn and his group at Uppsala University (Sweden).[332] This technique is based on the photoelectric effect[333,334] in which a core or valence electron is ejected when photons of a suitable energy (hν) ranging from a few eV to thousands are shed onto a sample. Photoelectrons emitted with a specific kinetic energy (E_k) are then collected and analysed. This principle is illustrated in Figure II. 3.

According to the principle of energy conservation, if the excitation energy is hν, the total energy of initial system (neutral, N electrons) $E_i(N)$ and the resulting one (cationic, N-1 electrons) $E_f(N-1)$, the following equation can be written:

$$h\nu + E_i\,(N) = E_f(N-1) + E_k$$
$$\text{i.e. } \mathbf{h\nu = E_B + E_k} \qquad \text{with } E_B = E_f(N-1) - E_i\,(N)$$

which allows to derive the binding energy of the photoelectron (E_B) from the experimental determination of E_k.
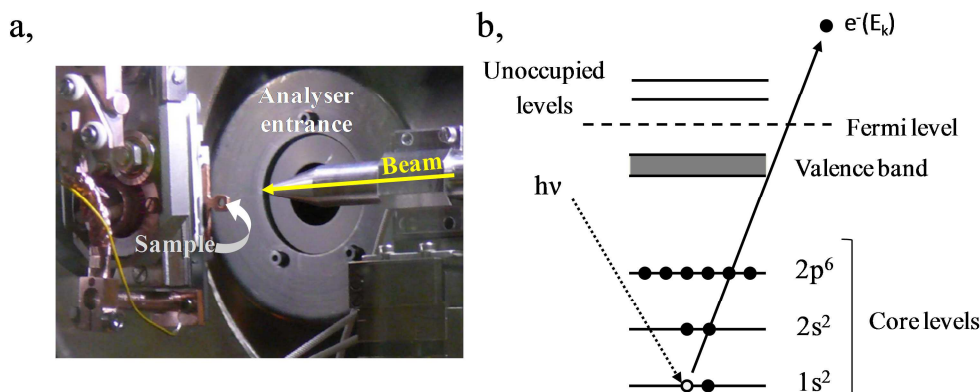
Figure II. 3: (a) Picture of an analysis chamber (inside view), the photon beam is directed towards the sample placed in front of the analyser entrance. (b) Illustration of the PES process.

The electrons can only be emitted if incident photons have energies larger than the electron binding energies (E_B). The electronic structure is unique for the different elements and the technique can therefore be used to obtain information at the atomic level.

Once a photoelectron is ejected, the final ionized state relaxes to its ground state by processes including Auger electron emission and X-ray fluorescence emission. These two processes are presented in Figure II. 4.

Note that Auger spectroscopy [1] has been used in paper IV, this spectroscopy is based on this Auger electron emission (Figure II. 4).

a, *Auger electron emission*   b, *X-ray fluorescence emission*
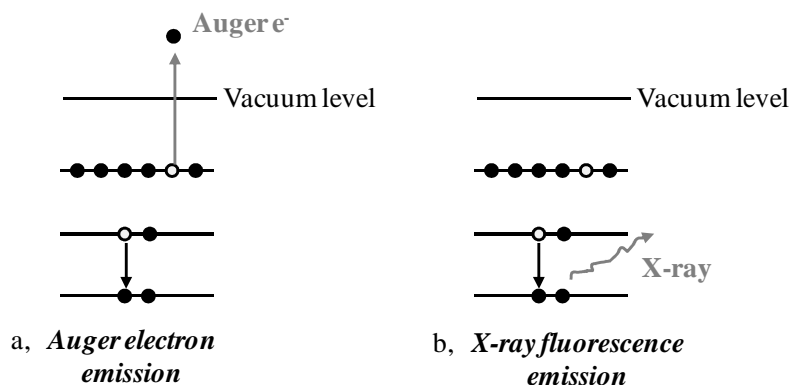
Figure II. 4 : Illustration of (a) the Auger electron emission and (b) of the X-ray fluorescence emission

3.1.2. Experimental measurement of the binding energy

In practice, the binding energy is calculated from the measured kinetic energy emitted from the sample after correction for a work function (Φ_{sp}) that represents the minimum energy required to remove a photoelectron from the surface.

The work function for a solid is defined to be the energy separation between the vacuum level and the Fermi level of the sample. When the sample is conductor, thermodynamic equilibrium between sample and spectrometer requires that their Fermi levels or electron chemical potentials should be equal (Figure II. 5(a)), leading to the following equation:

$$E_B = h\nu - E_k - \Phi_{sp}$$

It is important to note that the common convention for the electron binding energy scale is to place its zero at the Fermi level energy.

The situation is slightly more complex with insulating samples.[335,336,337] Residual charges can appear at the surface of the sample after emission of the photoelectrons. This charging effect results in a broadening of the peaks and the measured binding energy is shifted towards a higher value. This charging effect can be compensated by the use of a flood gun (low energy electron gun) but it is generally difficult to perfectly compensate for charging. As a consequence, Fermi levels of the sample and of the spectrometer are different leading to a shift in the binding energy as illustrated in Figure II. 5 (b).

$$E_{correct} - E_{measured} = \Phi*$$

In these cases, correct referencing remains an open question, often solved by taking an elementary peak of the sample, usually, the hydrocarbon surface contamination peak C 1s located at 285.0 eV.

---

[1] This spectroscopy corresponds to a three electrons process ending with the Auger electron emission. It is characterized by a small kinetic energy (~10-3000 eV) which is independent of the energy of the excitation radiation (electrons or photons).
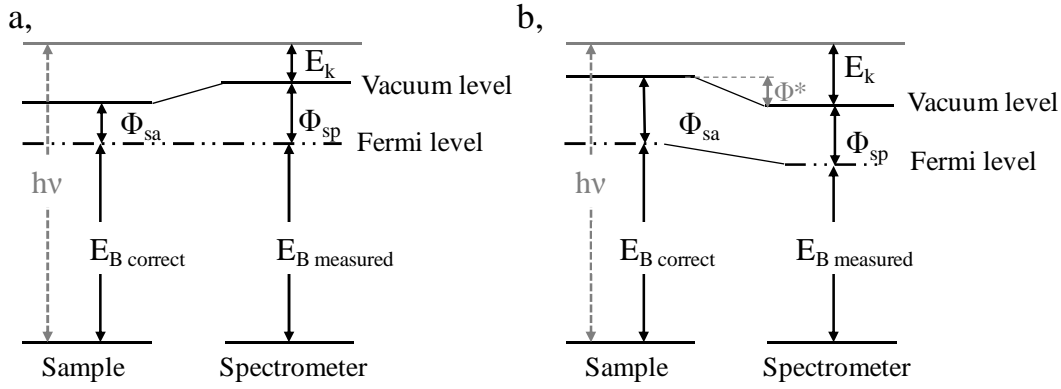
Figure II. 5 : Schematic energy level diagram of PES experiment for (a) a conducting sample and (b) an insulating sample.

3.1.3. The PES spectra – core peaks

In a photoemission experiment emitted electrons are counted within selected energy ranges and an energy distribution curve is obtained by plotting photoelectron counts as a function of their E_K or E_B as shown in Figure II. 6. Two distinct energy regions can be distinguished: the core level peaks ($E_B > 30$ eV) and the valence levels (0-30 eV).
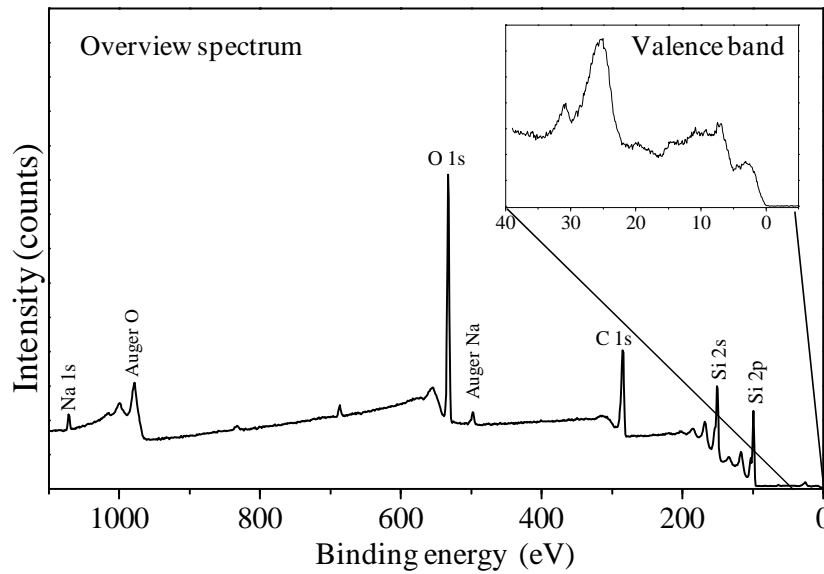
Figure II. 6: PES spectrum of the pristine Si/C/CMC composite electrode used in this thesis. The valence band spectrum is plotted in the inset.

From the binding energy of the core levels, we can first identify all the elements (except hydrogen and helium). Indeed, each element has a characteristic sequence of electronic states that can be easily recognized in an overview spectrum (acquired over a wide energy range, Figure II. 6). For a given element, peak positions can vary depending on its chemical environment and this variation is termed chemical shift. This notion will be developed in the next part.

It is also important to note that during the escape process, electrons may lose part of their kinetic energy due to different inelastic scattering processes (secondary electron tail). Other spectral features can accompany primary lines because of complexities in the final state of the photoemission process: satellite peaks (shake-up and shake-off) or multiplet splitting.

Another aspect is the core peak width expressed by the FWHM (Full Width at Half Maximum) which corresponds to the combination of three contributions:

- The inherent line width of a core level in relation with the life time of the ionized state (Heisenberg's uncertainty principle) remaining after photoemission
- The FWHM of the incident photons (X-ray line)
- The resolution of the analyser

These two last points will be discussed later.

3.1.3.1. Chemical shift

The discovery, during the early days of XPS that core level peak positions can vary by more than 10 eV for a single element depending on its chemical environment had certainly contributed to the important development of this spectroscopy. This variation is termed chemical shift and can be used for obtaining information on-short distance chemical environments of atoms, oxidation numbers, electronic charge transfers.

In a first basic qualitative model, we can consider a bond between two atoms with different electronegativities: valence electron density will be shifted towards the most electronegative atom, as a consequence, photoemission from the atom with decreased valence electron density will require more energy. The kinetic energy of the resulting photoelectron decreases, corresponding to a higher binding energy.

As an example, the high resolution Si 2p spectrum of a pristine Si/C/CMC composite electrode can be examined (Figure II. 7). We know that silicon is usually covered by a native surface oxide (SiO_2). The oxygen atom is more electronegative than silicon, thereby the binding energy of the Si 2p core peak for SiO_2 is higher than the one of bulk Si as shown in Figure II. 7.
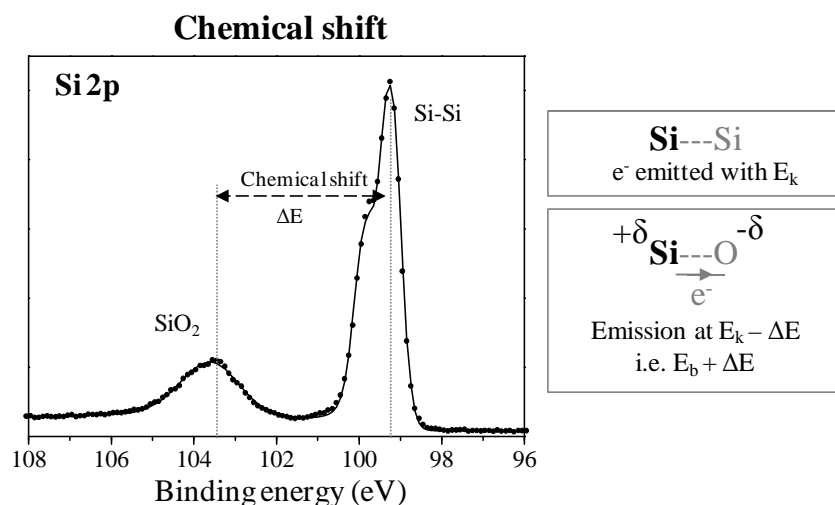
Figure II. 7: Si 2p core peak spectrum of the pristine Si/C/CMC composite electrode, and illustration and explanation of the chemical shift observed between bulk Si-Si and SiO_2.

Usually chemical shifts are interpreted in terms of a simple electrostatic theory, called "charge potential model". This model is based on the consideration of the electrical potential surrounding the atom.[330,338] If we consider a charge q uniformly distributed on a sphere (radius r), the potential inside the sphere will be $q/(4\pi\varepsilon_0 r)$. A transfer of a partial charge Δq to a surrounding species will modify the effective energy from $\Delta q/r$, and the binding energy of the electrons inside the sphere should be affected by the same amount.

Refinement of this model takes into account the charge on the neighbouring atoms. Besides these "initial state effects" a more realistic theory takes into account the relaxation effects (redistribution of the electronic charge during ionization) referred to as "final state effect". Modern theoretical tools allow the interpretation and prediction of chemical shifts (using for example, the so-called (Z+1) approximation).[339,340]

3.1.3.2. Spin orbit splitting

Core levels in XPS are first indicated using the main atomic quantum number *(n = 1, 2, 3…etc)* and angular momentum quantum number (*l* = 0, 1, 2, 3 i.e. s, p, d, f respectively) of the level from which the photo-electron is ejected.

Spin-orbital splitting arises from a coupling of the spin and orbital angular momentum. Such splitting is observed for *l≠0* (i.e. for all levels except s-states) resulting in a doublet associated to two possible states characterized by the quantum number *j* (*j = l ± s*, with s = ±½, the spin angular momentum number). Thus, core peaks are precisely identified by the nomenclature *nl_j*. The relative intensity of the components is given by the ratio (2*j*+1) based on the number of different spin combinations that can give *j* (degeneracy of each spin state).

Illustration of the spin-orbit splitting of high resolution Si 2p core level peak is shown in Figure II. 8.

Spin-orbit splitting
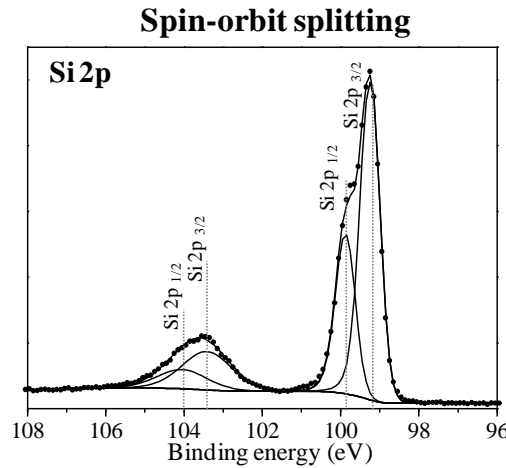
Figure II. 8: Si 2p core peak spectrum of the pristine Si/C/CMC composite electrode and illustration of the 2p spin-orbital slitting

3.1.3.3. Quantitative measurements and surface sensitivity

The photoelectron core level peak intensity can be used to give quantitative information on the surface composition after correction by a factor S that depends on the probability for a particular photoemission event to occur and on the probability to detect the photoelectron (i.e., an instrumental parameter).

The relative atomic ratio between two elements is given by the generalised formula:

$$\frac{N_A}{N_B} = \frac{I_A/S_A}{I_B/S_B}$$

Where N_x is the number of atoms of the element X per volume area of the surface

I_x is the peak intensity of the element X

S_x is the atomic sensitivity factor

The formula above presents the ratio between two elements but it is also common to calculate the atomic fraction of a specific element by replacing the denominator by the sum of the contribution of all elements:

$$C_A \, (\%) = \frac{N_A}{\sum_i N_i}$$

The atomic sensitivity factor is given by the following equation and its parameters are listed and explained below:

$$S_A = \sigma_A \lambda_A H_A \left[1 + \frac{\beta_A}{2} \left(\frac{3}{2} sin^2\theta - 1 \right) \right]$$

- H is a constant that depends on the spectrometer (transmission function)
- The factor β takes into account the anisotropic characteristic of the emission
- θ is the angle between the incoming unpolarized photon direction and the emitted photoelectron direction

- **The cross section σ**

A cross section value reflects the probability that incident photons cause ionization from a core level of a specific element (unit in barn , 1barn = 10^{-28} m^2). Values depend on photon energy and are known from theoretical calculations. They are reported in several databases.[341,342] Scofield has reported the cross sections of all the elements with a photon energy of 1487 eV (Al Kα) and 1254 eV (Mg Kα). Values are normalized by the cross section of C 1s (13600 barns at 1487 eV and 2200 barns at 1254 eV). The Yeh and Lindau database gives the cross section of all the elements with a photon energy varying from 0 to 1500 eV. In this work, quantification for in-house XPS data was performed on the basis of Scofield's values.

- **Depth profile analysis - Inelastic mean free path (IMFP) λ**

Peak intensity depends on the depth from where electrons can escape and is linked to the notion of mean free path which is defined as the average distance that an electron can travel through a solid without energy loss. The intensity of emitted electron decay is a function of the distance d that it has to travel; this decay follows the Beer Lambert law:

$$I(d) = I_0 \exp(-d / \lambda sin(\theta))$$

With I_0 the intensity of the emitted electron at depth d
        λ the inelastic mean free path of the elements
        θ the angle between the surface of the sample and the   emitted electron trajectory

The ratio $I(d)/I_0$ can be seen as the probability that a photoelectron, emitted at the depth d, can escape without suffering from inelastic energy losses. Figure II. 9 (b) shows the relation between depth of analysis and IMFP, for normal emission (a configuration adopted in many of the measurements presented in this thesis). We can see that 95% of the electrons contributing to a peak in a homogeneous material are emitted from a depth d<3λ. In this work, the probe depth of analysis was taken as three times the IMPF.

a,

b, $I(d)/I_0 = \exp(-d/\lambda)$ with $\theta = 90°$
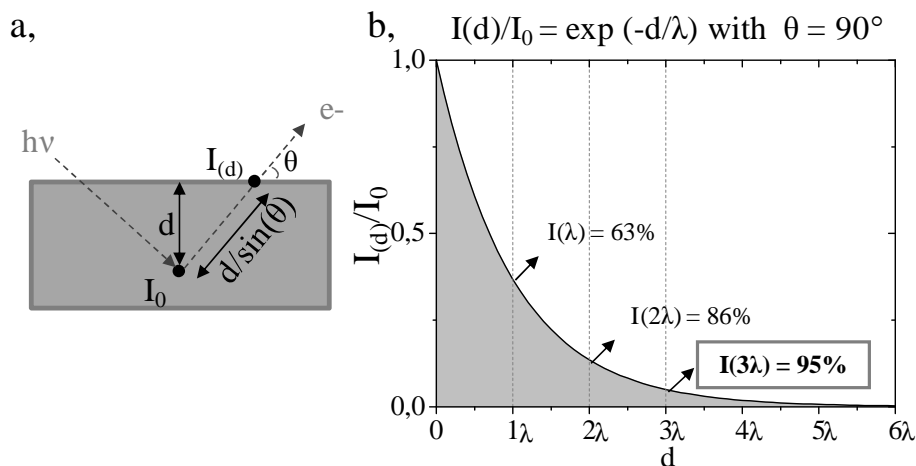
Figure II. 9: (a) Schematic illustration of the link between the electron intensity and the depth of analysis. (b)Intensity of the emitted electron as a function of depth of analysis, the grey area represents the probability that an electron has to come from a depth ranging between 0 and d (i.e. 63% between 0 and λ, 95% between 0 and 3λ) – $\theta = 90°$

The IMPF is directly dependent on the kinetic energy of the photoelectrons emitted, so it will be different for all elements and all core peaks of a given element. This dependence is approximately given by the universal curve presented in Figure II. 10 (a). However, there are models proposed in the literature[343,344] and it is now widely accepted that a common curve cannot be used and that a difference exists between a single element and a molecule as well as between inorganic and organic materials.

However, no matter the model used, the tendency of this curve is always the same, and in the X-ray range above about 100 eV, the mean free path increases when the kinetic energy increases.

If photons of energies up to 1000-1500 eV can penetrate to a few micrometers, electrons are significantly less penetrating, the inelastic mean free path being the decisive parameter which determines the escape depth. For Al Kα the maximal escape depth reached when $E_k \sim$1500 eV is below 10 nm ($\lambda\sim$2-3nm). This makes PES a surface analysis technique.
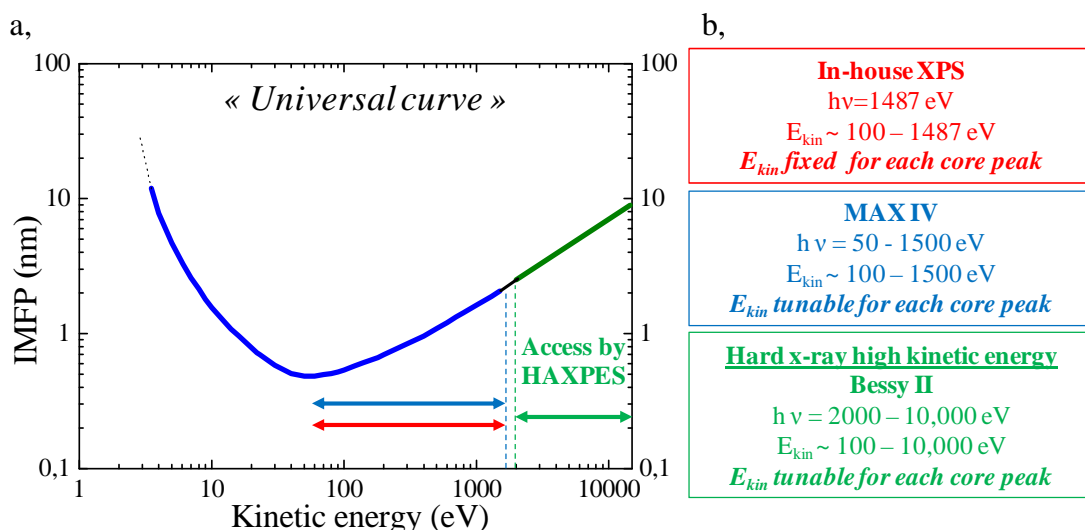
Figure II. 10: (a) Universal curve representing the IMFP as a function of the kinetic energy of the photoelectrons. (b) Facilities used in this thesis and their energy range (hv and E_k).

3.1.4. The PES spectra – Valence bands

Besides the classical core peak analysis, the study of valence band spectra that correspond to an experimental visualisation of the electronic DOS (density of states) of the occupied energy levels brings interesting information. Indeed, they are scrutinizing the less bound electrons - those that are directly involved in the chemical bonds and these spectra can be used as a fingerprint to identify a compound.

However, for a detailed interpretation, the help of calculations is necessary to take into account the modulation of DOS curves by photoionization cross sections. Calculations can also be used as a predictive tool for non-isolated compounds.

In the field of Li-ion batteries, the study of valence band spectra can efficiently address the electrode/electrolyte interface issues in combination with the analysis of core peaks.[345,346]

In this work, DFT calculations were performed (Gaussian 09 program package) to simulate XPS valence spectra using Koopman's theorem approximation (determination of monoelectronic energy levels). In addition, the Gelius intensity model was used [347] (paper III).

3.1.5. Depth profiling in PES – several approaches

In depth analysis, taking into account the third dimension perpendicular to the surface, it is of interest to investigate subsurface chemical and electronic structure.

Three main approaches can be used for depth profiling of a solid: Argon-ion sputtering, angle-resolved PES (variation of θ) and variation of the photon energy (hν).

The first approach is destructive and the principle is to slowly remove the first atomic layers of the sample by etching material from the surface by an argon-ion beam with successive recordings of spectra. However, this approach can cause changes in the surface composition due to sputter induced reactions leading to a risk for misinterpretation of surface chemistry. The surface of cycled Li-ion battery electrodes is composed of chemically sensitive compounds and it has been shown for example that Li_2O can be formed upon etching by the reactions: $Li_2CO_3 \rightarrow Li_2O + CO_2$ [348] or $2LiOH \rightarrow Li_2O + H_2O$.[349] New approaches have recently been developed to carry out depth profiling in a less destructive manner by macromolecules such as fullerene ($C_{60}H_{60}$), coronene ($C_{24}H_{12}$) or argon clusters (Ar^+_n, n=100, 10000).

Two other common approaches for depth profiling can be considered as non-destructive. One methodology is angle resolved X-ray photon spectroscopy (ARXPS) which is based on the variation of the analysis depth by collecting XPS spectra at different emission angles (from near normal to near grazing emission). This is achieved by tilting the samples and this approach is best adapted for thin film studies on flat surfaces.

The last approach for depth profiling relies on the variation of the photon energy using synchrotron radiation since this modifies the kinetic energy of the photoelectrons ejected and thus the surface sensitivity (larger depth sensitivity can be reached using "hard" X-ray (Figure II. 10) compared to ARXPS).

This approach, based on variation of the photon energy has been adopted in this thesis work and different excitation sources have been used: synchrotron radiation (SR) with hν = 50 to 1500 eV at MAXIV laboratory, SR with hν = 2000 to 10000 eV) at Bessy and Al Kα radiation (in-house XPS with hν= 1486.6 eV).

Figure II. 11 illustrates the dependence link between photon energy and probe depth of analysis for the Si 2p spectrum of the pristine silicon used in this thesis work. The spectrum displays a first Si 2p peak assigned to bulk silicon at ~99.5 eV (in grey) and another one assigned to the surface oxide (SiO_2) at ~103.5 eV (in red). The relative intensity of the two features changes dramatically when the photon energy changes and the signature of SiO_2 predominates at low photon energy (i.e. when the

extreme surface of the Si nanoparticle is probed) whereas the signal of the bulk Si is highlighted for the high photon energy.
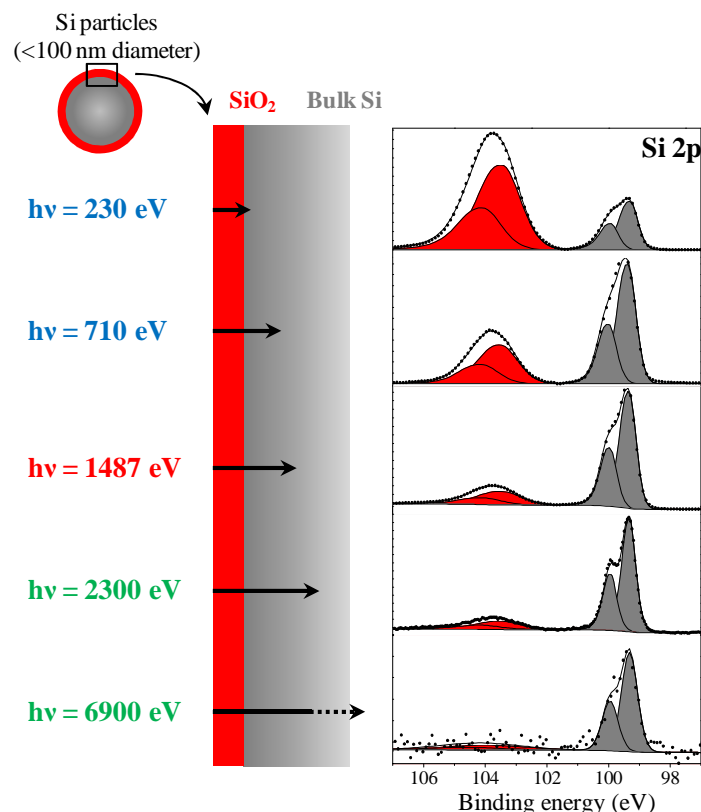
Figure II. 11: Influence of the photon energy on the Si 2p spectrum of the pristine Si/C/CMC composite electrode. Schematic view of the evolution of the analysis depth (arrow) as a function of the photon energy hν.

3.1.6. From the source to the detector – some technical details

3.1.6.1. The ultra-high vacuum

PES analysis requires an ultra-high vacuum (UHV) (~ 10^{-9} Torr / 10^{-7} Pa). First, the IMFP of the electrons is very short, so it is necessary to avoid any interaction between ejected electrons and gas molecules on their way to the analyser. In addition, UHV conditions prevent/reduce adsorption of contaminants on the analysed samples.

3.1.6.2. Type of sources

Photon sources used in this thesis were of two different types: one classical monochromatic X-ray source attached to an in-house XPS and a synchrotron source covering a wide range of photon energies.

- *X-ray tube (in-house XPS):*

Commercial and basic research High Resolution XPS equipments use a monochromatic X-ray source (Al). The principle of X-rays generation is the following: a tungsten filament (cathode) is heated up via a low intensity current (2-4 A) and produces electrons by thermionic emission. These electrons are then accelerated by an electrical field (typically 10-15 kV) and are focalised onto the anode (Al or other materials). The X-rays emission occurs by the electronic deceleration in the matter and the X-ray fluorescence effect is involved by this electronic anode irradiation (Figure II. 12). An X-ray spectrum is made of a continuous spectrum ("Bremsstrahlung" radiation i.e. radiation due to the deceleration of the charged particle) and a spectrum made of sharp peaks characteristics of the anode material (K-shell

emission radiation) (Figure II. 12). The X-ray used in our experiments is Al K$\alpha_{1,2}$ (hν = 1486.6 eV) and it is generated by the electron transition between the 2p orbital (L shell) and the most inner shell K (1s).

X-ray spectra are then monochromatized and focused on the sample using a quartz crystal monochromator positioned in a specific geometry (Rowland circle) to get a high intensity. X-rays are diffracted by a single array of quartz crystals mounted on a precision formed toroidal backplane. The large surface area of the crystals defines a large solid angle and hence a high X-ray flux: the crystals are also specially prepared to give maximum reflectivity and the arrangement is optimized for high energy resolution (FWHM of Al K$\alpha_{1,2}$ is reduced from 1.0 eV to 0.2 eV for the Kratos Axis spectrometer used in this PhD work). The fixed X-ray flux density and the absence of Bremsstrahlung minimize damage due to X-ray degradation.
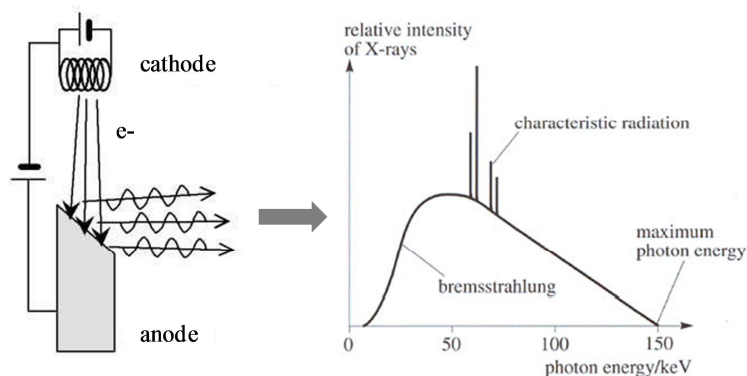
Figure II. 12 : Principle of an X-ray source

The monochromator used with an XPS spectrometer defines the "so called" High Resolution XPS (HR-XPS).

- *Synchrotron radiation:*
Contrary to the in-house XPS, synchrotron facilities are found in few places (about 15 in Europe).

A synchrotron is composed of several elements. The first part is constituted of an electron gun and a preinjector referred to as a Linac (Linear accelerator). In the electron gun, a cathode (for example, barium oxide metal at MAXlab) is heated (or irradiated with a short but strong laser pulse) leading to a cloud of electrons. The electrons are then transported by an electric field to the Linac where electrons are accelerated to higher energies, from few MeV (2MeV at MAXlab) to 100-200MeV depending on the facility. To increase the energy further, electrons are sent into the booster, a circular accelerator where they reach several hundred MeV or even few GeV. At this point, the electrons have nearly reached the speed of light. They are then injected in the storage ring.

The MAXIV laboratory has an alternative approach using a recirculator that consists of two magnet blocks that bend the electrons to 180 degrees, in order to bring them back to the beginning of the Linac and the electrons pass through it once again to reach 400MeV. Then, electrons are injected in the storage ring in a first step acting as a booster to bring electrons up to 1.5GeV. Some specifications of the synchrotrons used in this thesis together with the two French facilities are given in Table II. 1.

Table II. 1 : Energy and circumference of some synchrotrons

Synchrotron facilities	Energy (GeV)	Circumference booster/ storage ring (m)
MAX II (MAX IV lab, Sweden)	1.5	90/90
BESSY II (Germany)	1.7	96/240
Soleil (France)	2.75	156.6/354
ESRF (France)	6	300/844.4

The so-called Synchrotron Radiation or Synchrotron light is generated once the electrons are in the storage ring where they stay for many hours. Moving along a curved part, high velocity electrons lose energy by emission of electromagnetic radiation which is the synchrotron light. Photons are delivered tangentially to the trajectory of the electrons and pass through the beamline to the end-station where the radiation is used for experiments.

① The linac

② The booster

③ The storage ring

④ The beamline/end station
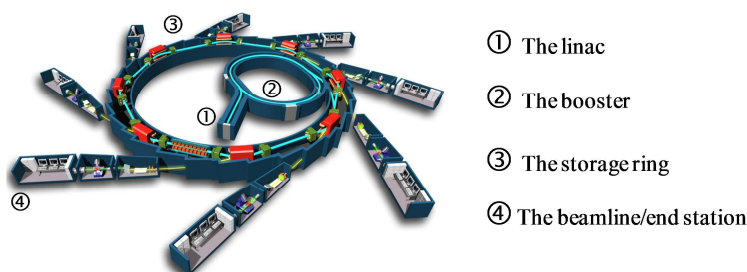
Figure II. 13: Illustration of the main parts of a synchrotron (image from Soleil website)

A storage ring is not a perfect circle but can be seen as a polygon where three main elements can be found: quadrupole magnets, bending magnets, and insertion devices. These elements are schematized in Figure II. 14.

Quadrupole magnets are made of four magnetic poles. They are used to focus the electron beam and act as a magnetic lens. Sextupoles or octupoles can also be found.

Bending magnets (dipole magnets) aim to guide the beam in the ring and they generate synchrotron light. Note that they constitute the only SR emission points in the first generation of synchrotrons.

The insertion devices are then introduced in the ring: they are found in the straight sections and are used to generate synchrotron light as well. Depending on the type of experiments and the nature of the desired light (high energy, particular polarization), two kinds of insertion devices are used: wigglers or undulators.[350] Both are made of several permanent magnets which force the electrons onto a sinusoidal trajectory generating synchrotron radiation each time the beam is bent.

a, Bending magnet

b, Quadrupoles and sextupoles magnets
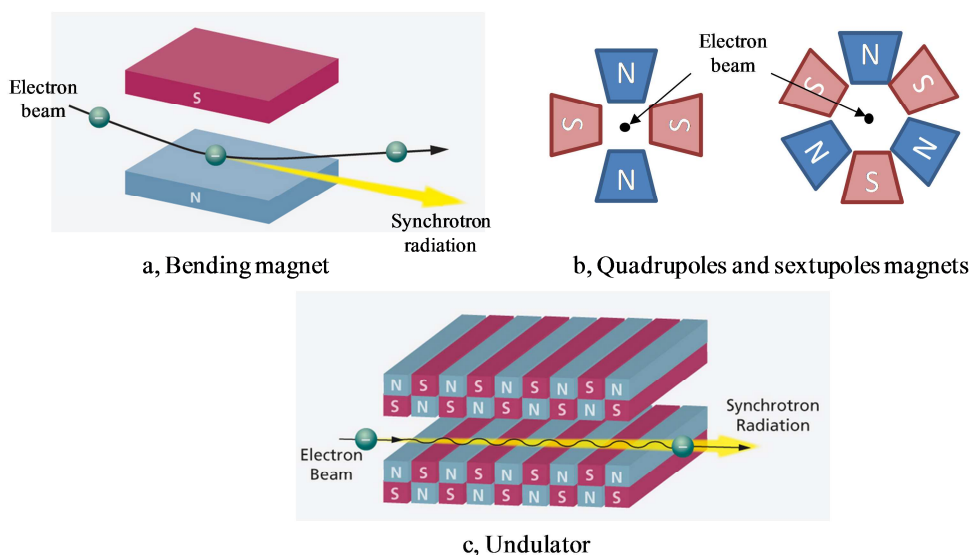
c, Undulator

Figure II. 14: Illustration of the main elements found in a storage ring (a) bending magnets, (b) quadrupole and sextupole magnets and an insertion device: an undulator (c). (a) and (c) are taken from the PSI website.

The synchrotron light gives access to a wide energy range from IR to "hard" X-rays.

The quality of the photon beam (well focalized and small size) used for the experiment depends on the electron beam in the storage ring. An important value is the emittance (nmrad) that takes into account the size and the angular proliferation of the beam; this value has to be as small as possible.

Monochromators, filters, mirrors, etc. are then found along the beamline to tune the photon beam for the experiments performed at the end-station.

At this point, we have seen how the incident beam is created. The resulting outgoing electrons with a certain value of the kinetic energy need to be analysed and the energy determined. This step is carried out in the last part of the spectrometer, the analyser and the detector. It is important to understand how some parameters can be adjusted, in particular, the pass energy (E_p) that affects the resolution of the spectra.

3.1.6.3. Electron analyser system

The analyser system can be divided into three parts (Figure II. 15(a)) permitting the collection and transfer, the energy selection and the detection of the electrons:

1- *Transfer lenses*

The electron lenses constitute the first part of the analyser. The electrons are collected, transmitted and accelerated or retarded to a pass energy (E_p) and focused to the entrance slit of the hemispherical system.

2- *Analyser*

The hemispherical system is composed of two hemispheres, a constant voltage difference is applied between them in order to circularly bend the electron trajectory: this defines "the pass energy" which is the kinetic energy of electrons circulating on the medium radius and which reach the detector through the exit slit centred on this geometry.

3- *Detector*

The detector collects and counts the electrons. This last part can be made of several aligned channeltron electron multipliers or by using a multichannel plate (MCP made of, e.g., 128 channels) (Figure II. 15 (b) and (c)). The principle is the same, an incoming electron is multiplied into multiple secondary electron cascades and accelerated by a high potential to obtain a detectable pulse.
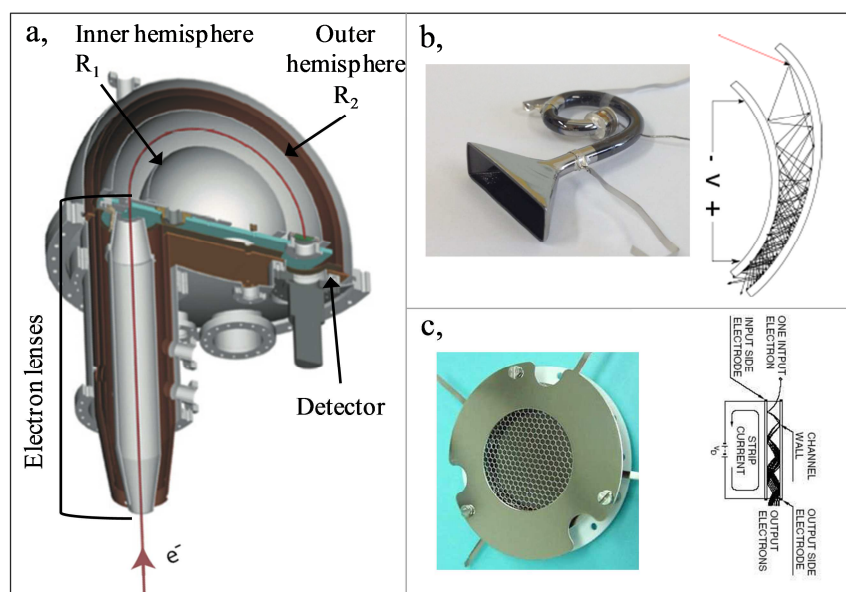
Figure II. 15: (a) Illustration of an HSA analyser. (b)Principle of a channeltron and (c) of a multichannel plate.

The energy resolution, ΔE of the analyser depends on the geometry (R_1, R_2 and mean radius of the R1 and R2 hemispheres: R_0), on the pass energy (E_p= f(V_1, R_1, V_2, R_2) with V_1 and V_2 voltages applied to the two hemispheres) and on the entrance slit width (w):

$$\Delta E \approx E_p * \frac{w}{2R_0}$$

This formula explains why different pass energies have been used for in-house XPS and synchrotron facilities (500 eV at Bessy and 20 eV in our in-house XPS) without having large differences in resolution. This is due to the different nature of the analyser (R_0 is higher and w smaller at Bessy).

3.1.7. Experimental setup – thesis work

3.1.7.1. In-house XPS

Two different in-house XPS have been used in this study.

Measurements in papers I, II and IV have been carried out with a Kratos Axis Ultra spectrometer. The spectrometer is fitted with:

- a focused monochromatized Al Kα radiation (500 mm Rowland circle, 225 W),
- a magnetic immersion lens for high photoelectron collection efficiency,
- a multi-element electrostatic transfer lens for high transmission and optimum performance for spectroscopic or imaging analysis,
- an hemispherical and spherical mirror energy analyser (165 mean radius double focusing 180°, FWHM of the Ag $3d_{5/2}$ line ≈ 0.58 eV under the recording conditions), the analysers run in fixed analyser transmission (FAT) for XPS measurements,
- a detector system based on eight channeltrons (spectroscopy) and a MCD for imaging,
- a coaxial charge neutraliser for charge compensation.

The aperture defined selected area of the samples was 300 × 700 μm^2 and the pressure in the analysis chamber was around 5.10^{-9} mbar.

Measurements in paper III were carried out with a Thermo K-alpha spectrometer using the same type of monochromatized source (250 mm Rowland circle) operating under 72W. The hemispherical analyser has a mean radius of 125 mm and the analysed area of the samples was defined by a focused X-ray spot size of 400μm. The pressure in the analysis chamber was also around 5.10^{-9} mbar.

Core level peaks were measured with pass energy (E_p) of 20eV with both equipments. Spectra were recorded before and after each long-time experiment and were compared to each other to check that the samples did not suffer from degradation during the measurements.
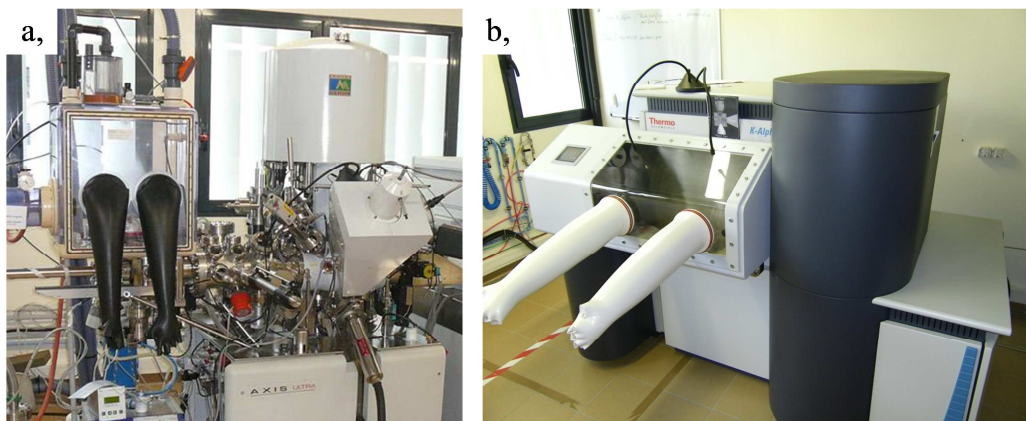
Figure II. 16 : (a) The Kratos Axis Ultra spectrometer and (b) the Thermo K-Alpha spectrometer

3.1.7.2. Synchrotron facilities

- *Beamline I-411 at MAX IV laboratory:*

Soft X-ray PES measurements (paper I, II, III) were carried out at the MaxIV Laboratory synchrotron facility in Lund (Sweden) at the beamline I-411providing a usable photon energy range from 50 to 1500 eV. The photon energy is selected using a modified Zeiss SX-700 monochromator with 1220 l/mm grating plan and a plan-elliptical focusing mirror.[351] The end-station is equipped with a Scienta R4000 WAL analyser (radius of 200 mm). The pressure in the analysis chamber was about 10^{-8} mbar and no charge neutralizer was used during the measurements.

Measurements were carried out in such a way that the same analysis depth was obtained for all spectra measured; thereby the same photoelectron kinetic energy was used for all probe elements. In this thesis work, two depths were investigated at BL I411 corresponding to a kinetic energies of 130 eV and 590 eV. This approach is possible by tuning the photon energy for each element probed (hv = $E_b + E_k$). An illustration of this methodology is given in Figure II. 17 (b) and the photon energies used to probe the different elements with a kinetic energy of 130 and 590 eV are reported in Table II. 2. Core peaks were measured with pass energy (E_p) of 200 eV.
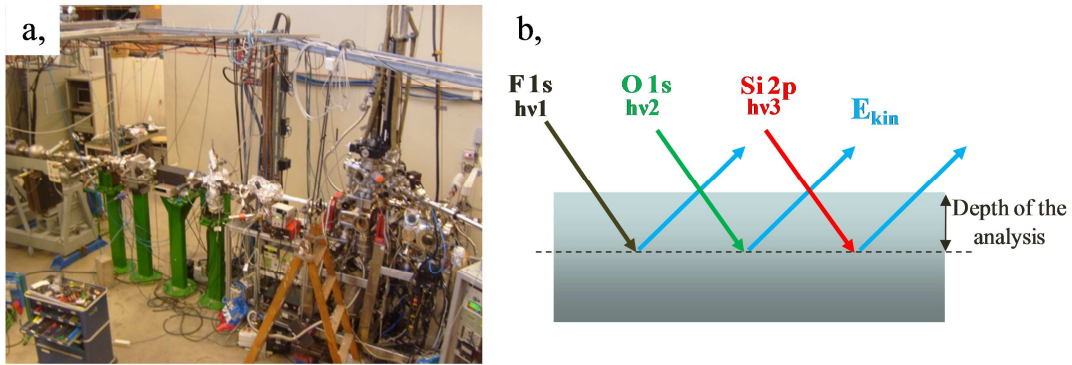
Figure II. 17: (a) I-411 Beamline at MAX IV laboratory and illustration of the measurement methodology adopted at MAX IV laboratory.

Table II. 2: Photon energy (hv) used at MAX IV laboratory

Elements	hv (eV) → E_k = 130 eV	hv (eV) → E_k = 590 eV
F 1s	810	1270
O 1s	660	1120
N 1s	530	990
C 1s	415	875
S 2p	300	760
P 2p	270	730
Si 2p	230	690
Li 1s	180	640

Beamline KMC-1, end-station HIKE at Bessy:

Hard X-ray PES (HAXPES) measurements were carried out at BESSY II synchrotron facility in Germany (Helmholtz Zentrum Berlin) using the KMC-1 beamline[352] equipped with the HIKE end-station[353] (paper I - IV) (Figure II. *19*(a)). This beamline has a usable photon energies ranging from 2000 to 10000 eV and the photon energy was chosen using a double-crystal monochromator (Oxford-Danfysik, see Figure II. 18). Three sets of crystals are available and listed in Table II. 3, the modification of the angle between the beam and the first crystal (Bragg's angle) allows the modification of photon energy leaving the monochromator according to Bragg's law:

$$n\lambda = 2\text{d}\sin(\theta)$$
$$h\nu = \frac{hc}{\lambda}$$

with   n: order of reflexion

λ: wavelength of the incident beam (m)

hν: photon energy (eV)

θ: angle between the incident beam and the crystal

d: spacing between the planes in the atomic lattice of the crystal (constant for each crystal)(m)

h: Planck's constant = 6.6×10^{-34} J. s

c: the speed of light in vacuum = 3.0×10^8 m.s^{-1}

The minimum photon energy is obtained with a Bragg angle of 82°. It is important to note that high photon energy can be selected by using higher order reflections (i.e. n = 3, 4…etc).
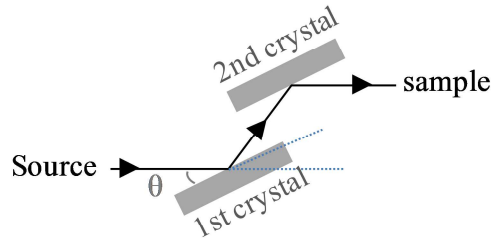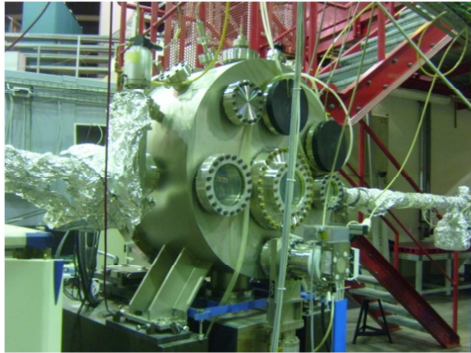
Figure II. 18: A double-crystal monochromator

Table II. 3: Energy range of the three sets of crystals available at Bessy.

Crystal	Energy range
Si(111)	1.997 – 12 keV
Si(422)	3.828 – 12 keV
Si(311)	5.639 – 12 keV

The measurement procedure was different for HAXPES measurements compared to the one used for soft X-rays at BL I411. In the procedure used for the HAXPES measurements, we assumed that for such high photon energies, the difference in probing depth for the different elements (core levels) is minor and can been neglected (justified by the logarithmic character of the universal curve). Two fixed excitation energies have been used: 2300 eV and 6900 eV.

    2300 eV was obtained by using the first order lights from the Si(111) crystal (paper I-IV), and 6900 eV was obtained in two possible ways:

- third order light from the Si(111) crystal tuned to 2300 eV (paper I)
- first order light from the Si(422) crystal tuned to 6900 eV (paper II-III)

The second configuration gives a somewhat poorer resolution than the first configuration but it is still sufficient for the measurement in this thesis work (Figure II. *19*) and delivers high flux allowing for fast measurements.
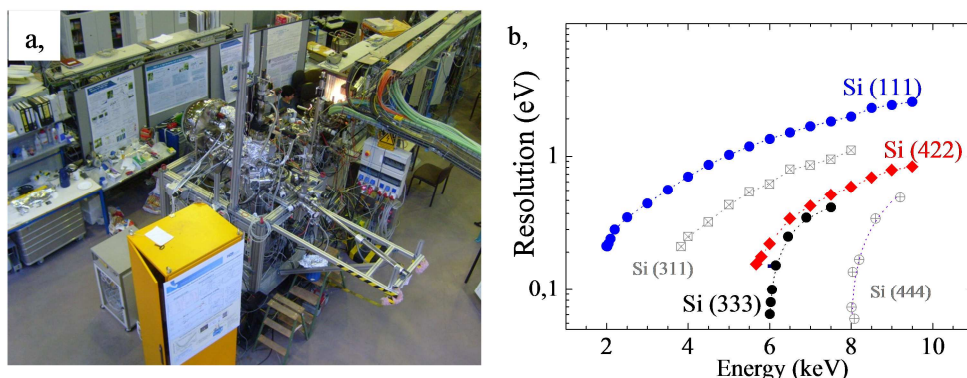
Figure II. 19: (a) HIKE end-station. (b) Experimentally determined resolution of the KMC-1 double crystal monochromator with Si-crystals with (111), (311) and (422) orientations. Si(333) and Si (444) correspond to higher-order reflection of the Si (111) orientation. (Replotted from ref[353])

The analyser was a Scienta R4000 (200 mm mean radius) optimized for high kinetic energies up to 10 keV. No charge neutralizer was used and the pressure was around 10^{-8} mbar in the analysis chamber and core peaks were measured with pass energy of 500eV. The beam passes through a capillary giving a spot size on the sample around 100µm-diameter (crescent moon shape).

3.1.7.3. Transfer of the samples – a crucial step

The cycled electrodes of Li-ion batteries are very air/moisture sensitive, thereby, a safe transfer between the glovebox and the spectrometer is crucial to minimize surface degradation.

Argon-filled gloveboxes are directly connected to the in-house XPS spectrometers. Classical Ar-filled gloveboxes are available both at MAXIV laboratory and Bessy. Samples were prepared (battery disassembling, washing of the electrodes) in the glovebox, mounted onto a sample holder (Cu or stainless steel plate). They were then introduced into a transfer chamber, to be transferred safely from the glovebox to the spectrometer. This system is presented in Figure II. 20 and is made of a stainless steel transfer rod with a manual valve. An adaptor (Figure II. 20 (c)) was plugged into the load lock of the glovebox in one side and the transfer chamber was connected to the other. Sample holders were attached at the end of the magnetic rod either as an Omicron fork (used at MAXIV, in Figure II. 20(e)) or as a specific magazine where up to six sample holders can be mounted (used at Bessy, in Figure II. 20(d)).
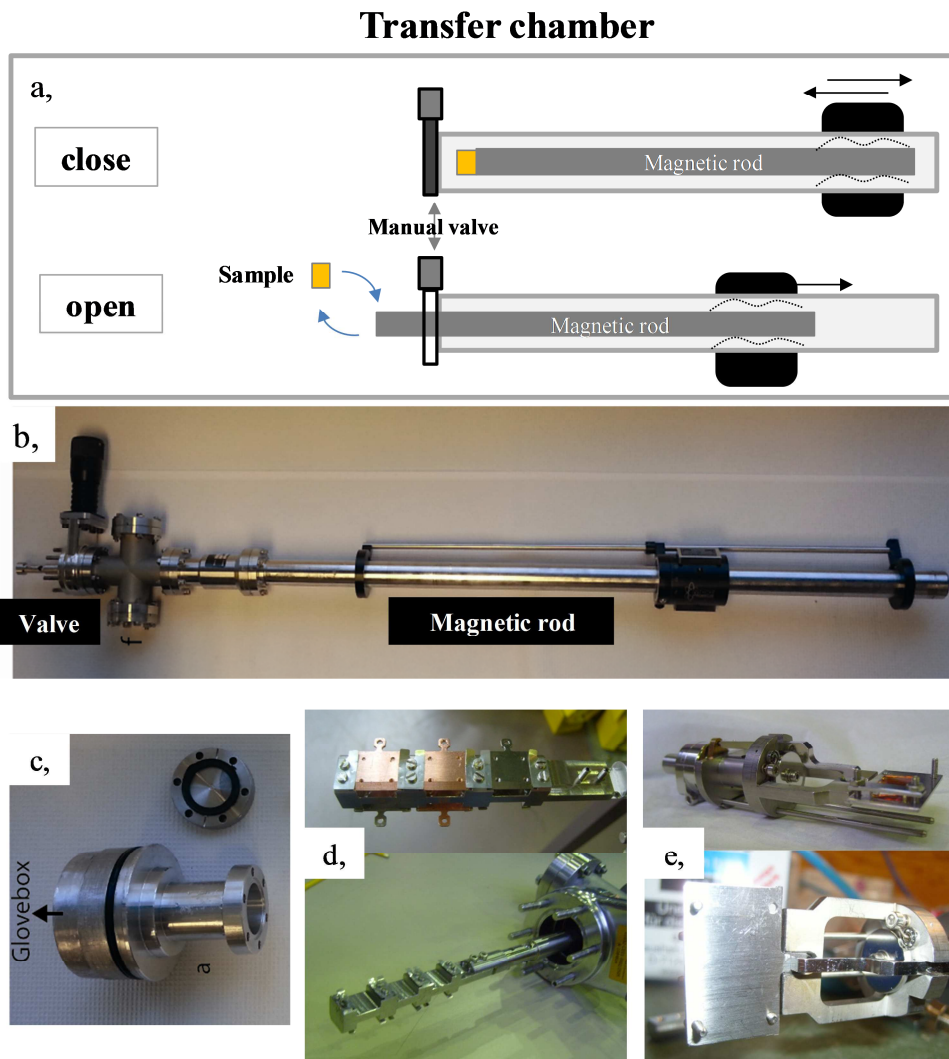
Transfer chamber

Figure II. 20 : (a) Schematic view of the transfer chamber. **(b)** Global picture of the transfer chamber. **(c)** Adaptor used to connect the transfer chamber to the glovebox. **(d)** Magazine used at Bessy. **(e)** Omicron fork used at MAX IV laboratory.

3.2. Scanning electron microscopy

The morphology of the Si-based electrodes has been analysed before and after cycling by scanning electron microscopy. SEM was carried out with a JAMP 9500F Field Emission Auger Microprobe fitted with a "non in-lens" secondary electrons detector. The image contrasts obtained are relative to the topography (SE emission) and the density of the material (SE included by electrons backscattering). In this work, no prior metallization step was required, the samples being conductive enough for the characterisation. Electrodes were directly deposited and clipped on the sample holder while powder samples (paper IV) were deposited on an indium foil. A transfer chamber was also used in this case to transport the sample from a glovebox to the apparatus.

The JAMP 9500F sample stage allows the user to tilt the sample from 0 to 90°. This rotation is eucentric and permits to scan the sample on the slice showing its roughness.

Figure II. 21 shows SEM pictures of the pristine Si/C/CMC composite electrodes used in this thesis (paper I, II, III). We can see that the composite is uniformly deposited onto the copper foil and presents an important porosity.
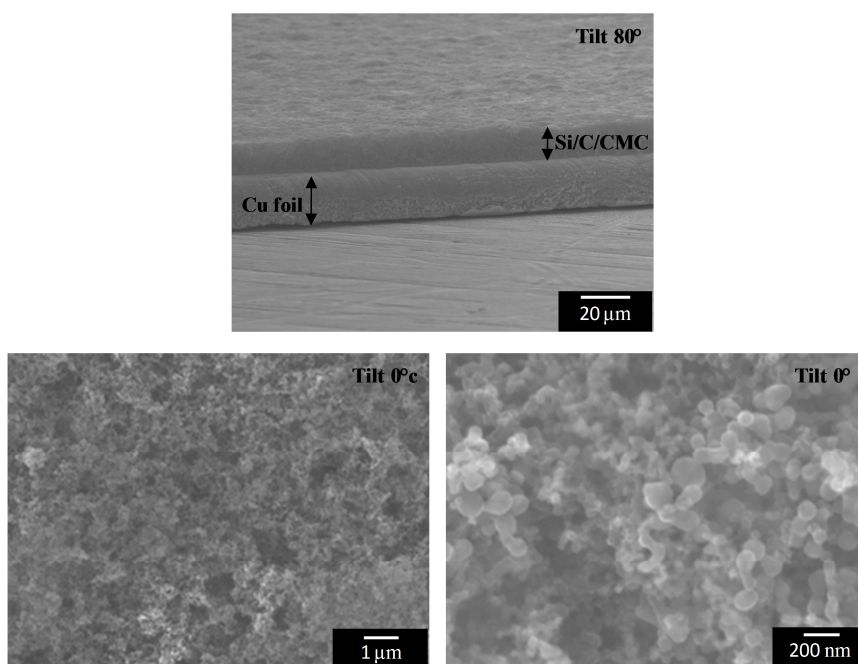
Figure II. 21: SEM pictures of the pristine Si/C/CMC composite electrode

CHAPTER III

Results and discussion

Electrochemical side reactions which affect the performance and cycle life of Li-ion batteries are linked to the complex reactions occurring at the electrode/electrolyte interfaces. To advance the use of new negative electrode materials, identification of the chemical composition of electrode/electrolyte interfaces as well as the mechanisms by which these layers form are key points to address.

Studies focused on silicon and tin-based intermetallics were, therefore initiated to answer these questions. Our results are mainly based on careful surface depth profiling characterization combining both soft and hard X-ray photoelectron spectroscopy.

1. Si-based electrodes

Interfacial reactions occurring upon the first lithiation/delithiation cycle of a Si/C/CMC composite electrode cycled *vs.* metallic lithium were investigated. The reaction of the surface oxide, the Li-Si alloying process and the formation of the passivation layer were studied through step by step analysis as a function of electrochemical potential (paper I).

An important issue is the control of interfacial layers upon cycling. In this section, we will follow the evolution of these processes upon long-term cycling with the classical salt LiPF$_6$ (paper II).

To improve the electrochemical performances, an alternative salt LiFSI was successfully used. Interfacial reactivity and reduction mechanism upon discharge with this new salt were studied and compared with previous work on LiPF$_6$ (paper III).

1.1. Interfacial reactions during the first electrochemical cycle using the LiPF$_6$ salt

The first electrochemical cycle of a cell with a Si-electrode was studied and is presented in Figure III. 1; the black points correspond to the samples analyzed by PES.
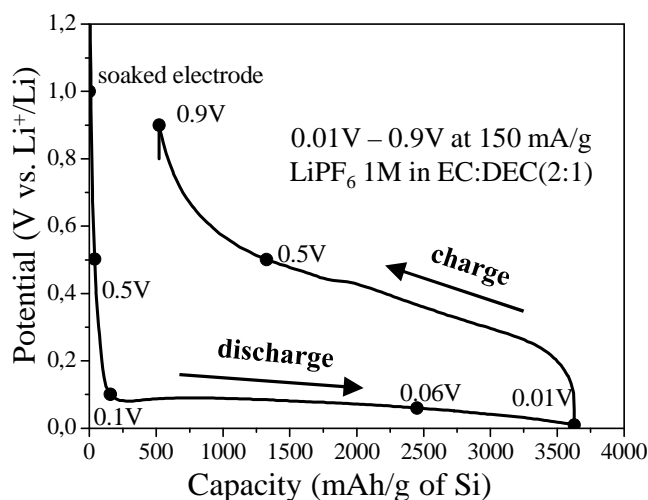
Figure III. 1 : First discharge/charge cycle of the Si/C/CMC composite electrode vs. Li^0 cell cycled between 0.01 and 0.9 V at 150 mA.g^{-1} (C/6 rate). The samples analyzed by PES are highlighted by black points.

1.1.1. Evolution and formation of silicon-containing surface phases
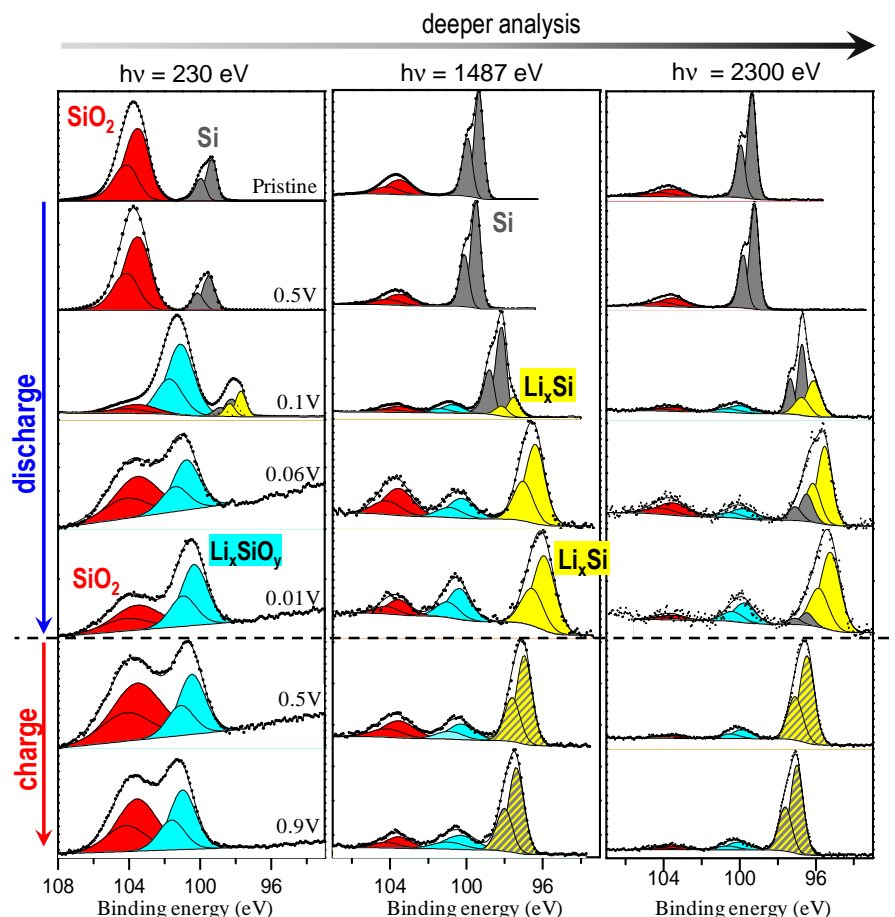
Figure III. 2 : Si 2p spectra of the Si/C/CMC composite electrodes upon the first discharge/charge cycle. Evolution as a function of the photon energy.

The evolution of the Si 2p spectra during the first electrochemical cycle and their dependence on the analysis depth (hv= 230 eV (MAX IV), 1487 eV (in-house PES), 2300 eV (BESSY II)) is shown in Figure III. *2*. As seen in the chapter II, the spectrum of the pristine electrode consists of two peaks: bulk Si (~99.5 eV in grey) and surface oxide (~103.5 eV in red). At 0.5V *vs.* Li^+/Li, no modification is observed and the first changes appear at the beginning of the plateau at 0.1V *vs.* Li^+/Li with the appearance of two additional components. The component at 97.5 eV, (in yellow) is attributed to the Li_xSi alloy while the second component appearing at 100-101 eV (in blue) corresponds to another silicon-containing phase.

This second component has a maximum intensity for the smallest analysis depth suggesting its localisation at the extreme surface of the Si particles.

In order to determine the nature of this silicon-containing phase, PES analysis has been performed with reference materials corresponding to probable species which may be formed: a commercial "SiO" powder and two lithium silicates (Li_2SiO_3 and Li_4SiO_4) prepared by sol-gel and precipitation synthesis has been performed. The results obtained strongly suggest the formation of a lithium silicate in agreement with the appearance of this phase as a consequence of the electrochemical lithium insertion (at the beginning of the plateau). In view of the data obtained (Si $2p_{3/2}$ peak at 102.3 eV for Li_2SiO_3 and 100.9 eV for Li_4SiO_4 (Figure III. 3(b))), we can conclude that Li_4SiO_4 is the most probable phase observed at the surface of the silicon electrodes according to the following mechanism:

$$2\ SiO_2 + 4\ Li \rightarrow Si + Li_4SiO_4$$
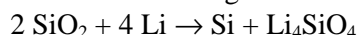
This mechanism occurs in parallel to the well-known reaction involving the reduction of SiO_2:

$$SiO_2 + 4\,Li \rightarrow Si + 2\,Li_2O$$
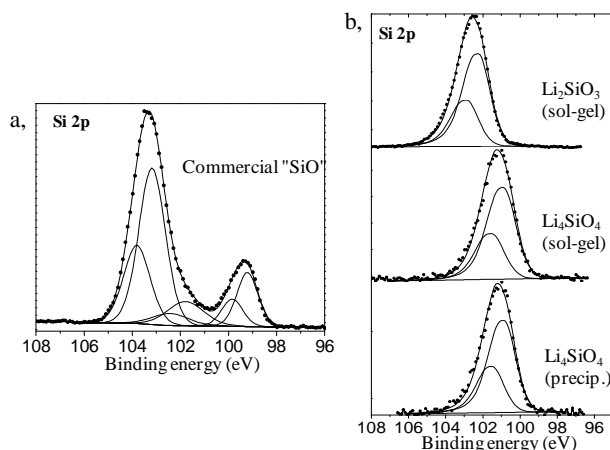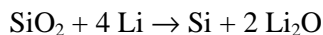
Figure III. 3 : Si 2p spectra (in-house PES, 1487 eV) (a) of a commercial "SiO" powder and of (b) Li_xSiO_y compounds obtained from various synthesis methods (sol–gel and precipitation).

From 0.06V to 0.01 V *vs.* Li^+/Li, the component assigned to silicon disappears corresponding to the almost complete alloying of Si into Li-Si (the component of Si remains however visible at the greatest analysis depth ($h\nu = 2300$ eV)). A gradual shift of the Li_xSi component towards lower binding energy is also observed and can be related to an increase of the lithium content in the alloy. The lowest analysis depth ($h\nu = 230$ eV) clearly shows that the core Li_xSi phase is covered by the surface oxide and the lithium silicate phases: SiO_2 and Li_4SiO_4.

During charging, a shift of the Li_xSi component towards higher binding energy is observed (decrease of the Li amount in Li_xSi) and the components of the surface phases SiO_2 and Li_4SiO_4 remain unchanged which shows the irreversible formation of the lithium silicate.
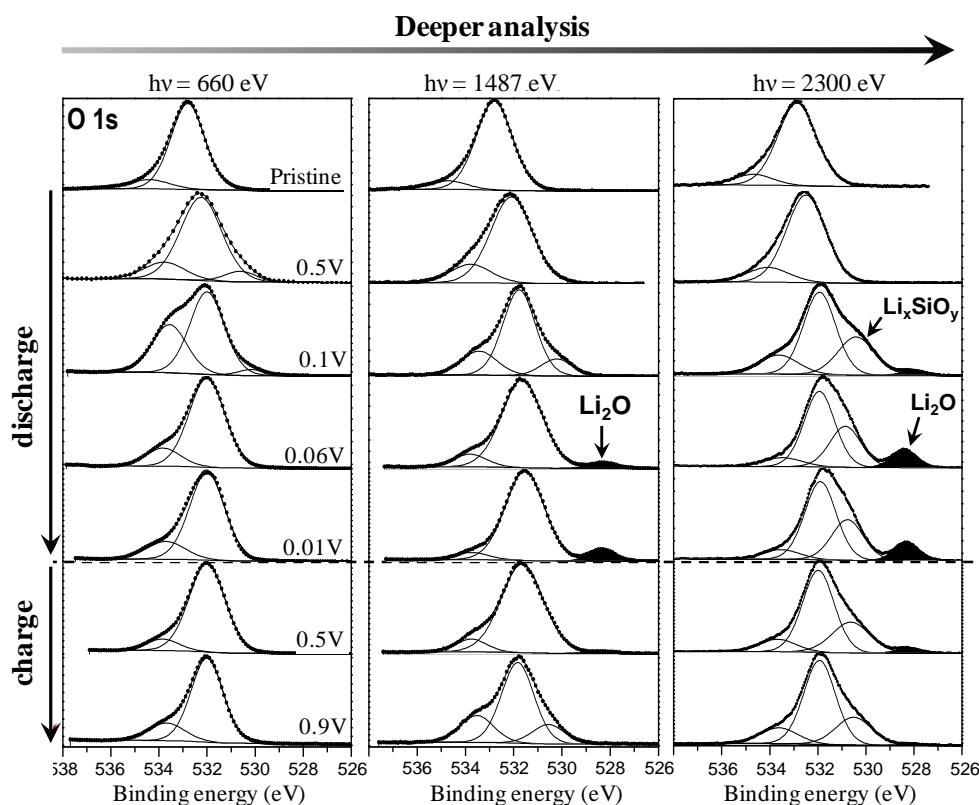
Figure III. 4: O 1s spectra of the Si/C/CMC composite electrodes upon the first discharge/charge cycle. Evolution as a function of the photon energy.

Figure III. 4 shows O 1s spectra of the Si/C/CMC composite electrode upon the first discharge/charge cycle, and their evolution as a function of the analysis depth. The main component observed in the pristine electrode spectra (532.9 eV) is assigned to the CMC binder and to the surface oxide SiO_2 (same binding energy). After the beginning of the electrochemical reaction, the maximum of the spectra shifts to lower binding energies (531.9-532 eV) and a component at higher binding energy (~533.5eV) is clearly visible. These two signatures are in good agreement with carbonates, alkyl carbonates and other organic species commonly found in the SEI.

Li$_2$O is also easily detected due to its specific O 1s signature at low binding energy (528.4 eV) and it is detected only with the highest photon energies which means that it is not located at the outermost surface of the samples, *i.e.* not in the SEI layer. Another component at ~530-530.5 eV is observed with the highest photon energies; this component is assigned to Li_4SiO_4. The photon energy dependency of these components suggests that Li_2O and Li_4SiO_4 are the most buried oxygenated phases; thereby they can be positioned at the interface between the SEI and the core Li$_x$Si phase of the particle.

In addition, while Li_4SiO_4 remains unchanged during the full electrochemical cycle (in agreement with its Si 2p signature), the formation of Li_2O takes place continuously until the end of discharge at 0.01V *vs.* Li$^+$/Li. Contrary to the irreversibly formation of lithium silicate, Li_2O formation is reversible during the first cycle as illustrated by the absence of the characteristic O 1s signature at the end of the charge.

1.1.2. Formation and features of the SEI
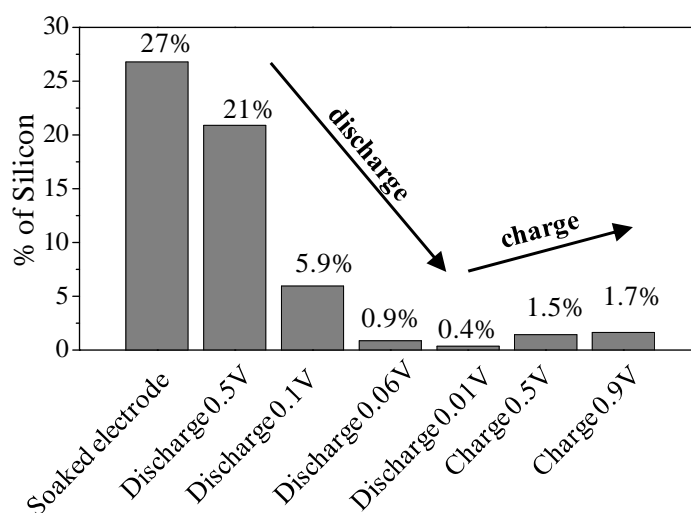
Figure III. 5 : Evolution of silicon content at the surface of the electrodes determined from XPS spectra of the Si/C/CMC composite electrodes upon the first discharge/charge cycle (in-house XPS, 1487 eV).

The increase (or decrease) of the thickness (or more generally the covering effect) of the SEI can be evaluated by following the evolution of the total amount of silicon measured at the surface of the electrodes (atomic % of Si 2p). Figure III. 5 shows this evolution upon the first electrochemical cycle of a Si/C/CMC//Li half-cell. A dramatic drop of the Si 2p signal is observed upon discharge due to the formation of the SEI. The percentage of silicon slightly re-increases upon charge up to 1.7% showing that the formation of the SEI is mainly irreversible during the first electrochemical cycle.
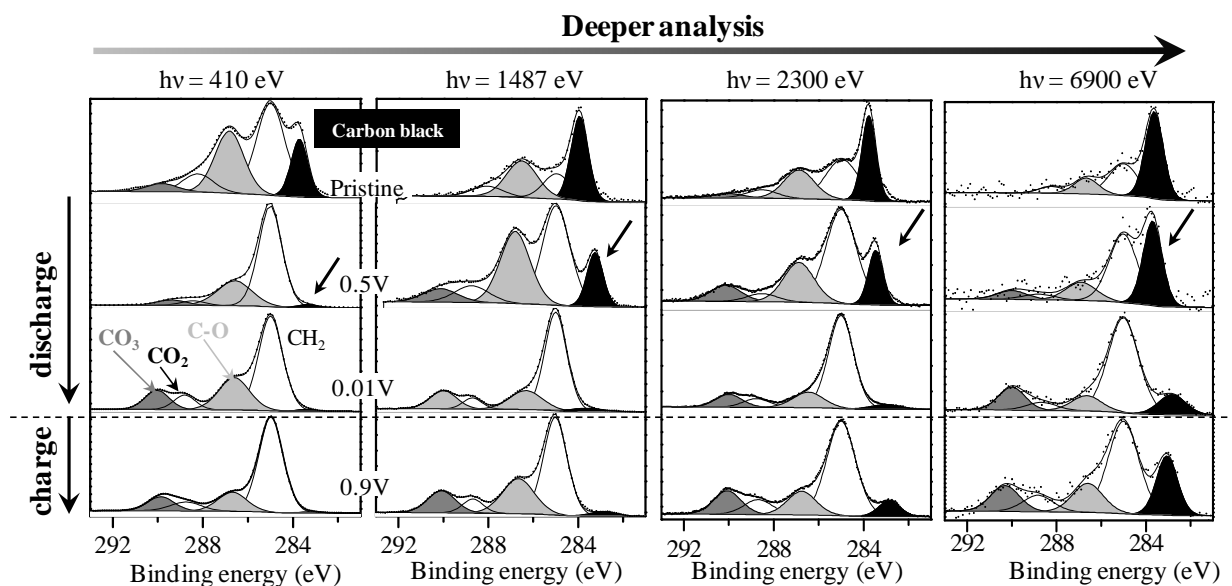
Figure III. 6 : C 1s spectra of Si/C/CMC composite electrodes upon the first discharge/charge cycle. Evolution of spectra as a function of the photon energy.

Figure III. 6 shows the evolution of the C 1s spectra during the first electrochemical cycle, as a function of the analysis depth. The spectra of the pristine electrode show the component of the carbon black additive: (narrow peak at ~284 eV in black). This peak is much easier to observe at greater analysis depth. Other components are assigned to the CMC binder and the two peaks at ~286.5 and ~288.5 eV can be attributed to C-O and O=C-O environments of carbon atoms, (grey and white, respectively). Finally the component at 285.0 eV (in white) is assigned to hydrocarbon surface contamination.

At the beginning of discharge (0.5 V *vs.* Li$^+$/Li), the formation of the SEI has started. We can see that the intensity of the peak attributed to carbon black (indicated by an arrow) has significantly decreased and it is barely detected at the lowest analysis depth while it is still observed for higher photon energies. At the end of discharge (0.01V *vs.* Li$^+$/Li), carbon black is only detected at 2300 and 6900 eV, this potential step corresponds to the stage where the SEI is the thickest as seen in Figure III. 5. C 1s spectra depict new carbonaceous species present in the SEI, deposited at the surface and replacing the peaks of the pristine electrode. The peaks corresponding to C-O (286.5 eV), O=C-O (288.5 eV) and CO$_3$ (290 eV) carbon environments are now assigned to carbonates like Li$_2$CO$_3$ and/or lithium alkyl carbonates (peaks at 290eV and 286.5eV). Oxalates (Li$_2$C$_2$O$_4$, peak at 288.5 eV) and PEO (-(-CH$_2$-CH$_2$-O-)$_n$, peak at 286.5 eV) may also be found in small amounts in the SEI.

The carbonaceous species found in the SEI are similar to those formed at the surface of graphite electrodes, or tin- and antimony-based intermetallic negative electrodes; their formation mechanisms can be found in the literature (see Chapter 1). Upon charge, the same overall shape of the C 1s spectra is observed; a slight increase of the carbon black peak can be noticed due to the decrease of the SEI thickness. We can also notice that at a given potential there is no major changes in the C 1s spectra as a function of photon energy, and thus of the SEI composition as a function of depth. In addition, at a given photon energy the C 1s spectra are rather similar from the beginning of discharge (0.5 V) to the end of the first cycle (0.9 V) suggesting that the composition of the SEI formed at the surface of the Si/C/CMC composite electrodes is rather stable during the whole first electrochemical cycle, and that its composition is homogeneous over its thickness.

89
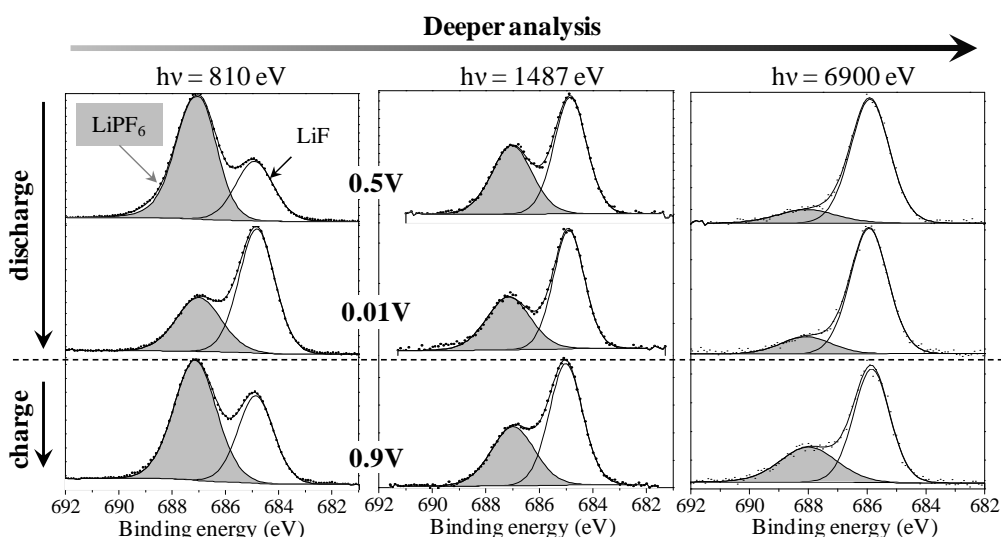
Figure III. 7 : F 1s spectra of Si/C/CMC composite electrodes upon the first discharge/charge cycle. Evolution of the spectra as a function of the photon energy.

Figure III. 7 shows the evolution of the F 1s spectra of the Si/C/CMC electrodes during the first electrochemical cycle for different photon energies. These spectra will provide information about the inorganic species formed in the SEI. Two components are observed, a first one at ~687 eV (grey) is attributed to the salt $LiPF_6$ remaining at the surface of the electrodes even after washing with DMC. The second one (~685 eV) is attributed to LiF, a degradation product of $LiPF_6$ (with phosphates). The remaining traces of the salt $LiPF_6$ are mainly located at the extreme surface of the SEI, while LiF is formed within the SEI layer as suggested by the decrease of the relative intensity of $LiPF_6$ as a function of the analysis depth at a given potential upon discharge or charge.

Results from quantitative analysis results show a deposit of carbonate species at the end of discharge and some increase of the amount of LiF at the end of charge: 4.2% (end of discharge) to 8.2% (end of charge). The SEI appears, however, mainly controlled by the solvent decomposition of the electrolyte, in agreement with previous results obtained at IPREM for graphite negative electrodes cycled in half-cells *vs.* Li^0 (Table III. 1).

Table III. 1: Main SEI species determined by PES (hv = 1487 eV) at the surface of different half-cells. $LiPF_6$ electrolyte salt. Potential given vs. Li^+/Li upon the first discharge.

Graphite // Li^{0*}	1V	0.2V	0.15V	0.01V
% LiF	5.6	3.0	3.6	4.8
% carbonates	23.4	34.8	34.8	30

* electrolyte: EC:DEC:DMC (2:1:2) – $LiPF_6$ 1M

Si/C/CMC//Li$_{0*}$	0.5V	0.1V	0.06V	0.01V
% LiF	4.8	5.4	5.6	4.2
% carbonates	11.9	30	27	25.7

* electrolyte: EC:DEC (2:1) – $LiPF_6$ 1M

1.1.3. Summary

The observed results are summarized in Figure III. 8 and provide a schematic view of the reaction mechanisms occurring at the surface of the Si nanoparticles (~50 nm mean diameter) during the first electrochemical cycle; the main conclusions are listed below:
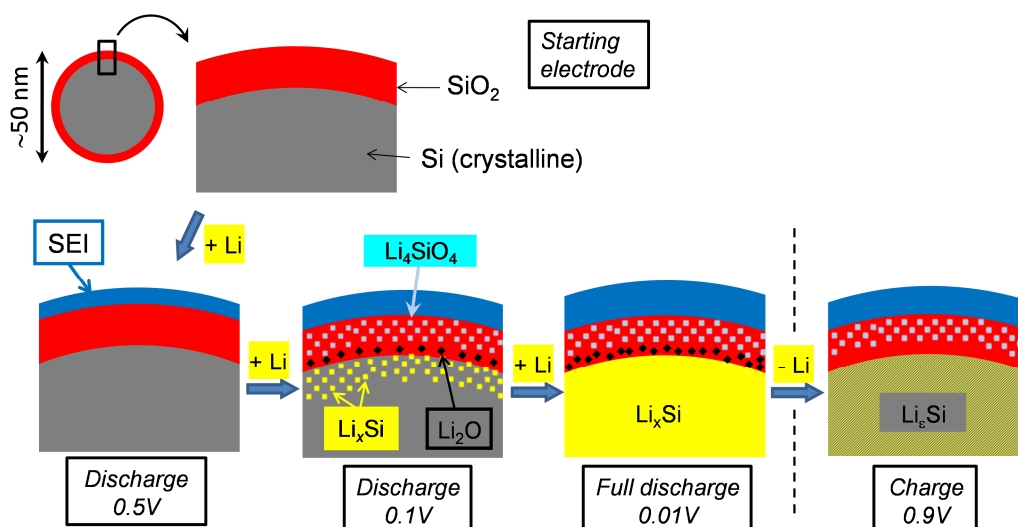
Figure III. 8 : Schematic view of the mechanisms occurring at the surface of the silicon nanoparticles.

- At the very beginning of discharge, the SEI is formed. Its composition is similar to the SEI formed on carbonaceous electrodes.
- After further discharge, there is formation of Li_2O ($SiO_2 + 4\,Li \rightarrow Si + 2\,Li_2O$) which is reversible upon charge.
  Formation of Li_4SiO_4 ($2\,SiO_2 + 4\,Li \rightarrow Si + Li_4SiO_4$) which is irreversible upon charge.
- Formation of the Li–Si alloy during the first electrochemical discharge occurs between 0.1V and 0.01V $vs.$ Li^+/Li ($Si + xLi \rightarrow Li_xSi$). Partial reversibility is observed upon charge ($Li_\varepsilon Si$ with ε tending to zero).

1.2. Evolution of the interfacial chemistry upon long-term cycling – LiPF$_6$ salt

The design of a successful silicon-containing battery requires a better understanding of the processes occurring at interfaces during long term cycling. In this next part, we will investigate the reaction of the surface oxide, the Li-Si alloying process and the SEI evolution upon long term cycling.

1.2.1. Electrochemical results

Half-cells were submitted to a four step pre-cycling and the capacity was then limited during the standard galvanostatic cycling between 0.12 and 0.9V. A limitation of the capacity was applied to enhance the cyclability of the system and to reduce the volume expansion of the Si particles (see chapter I).
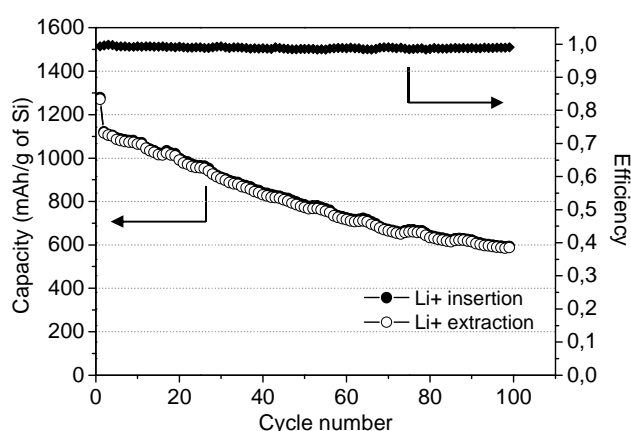
Figure III. 9: Capacity data and coulombic efficiency *vs.* cycle number of the Si/C/CMC composite electrode *vs.* Li^0, a cell cycled between 0.12 and 0.9 V at 700 mA.g^{-1} of Si. Pre-cycling is excluded.

Figure III. *9* shows the discharge/charge capacity and the coulombic efficiency (ratio of charge capacity of the nth cycle / discharge capacity of the nth cycle) as a function of cycle number. The four pre-cycles are not plotted. We can see that after the four steps of pre-cycling, the capacity is mainly lost between the 1st and the 2nd cycle (~150 mAh.g^{-1}). Afterwards, the capacity decreases from ~1100 mAh.g^{-1} to ~ 600 mAh.g^{-1} after 100 cycles and a stable coulombic efficiency above 98% is obtained.

1.2.2. Surface morphology

The morphology of the silicon electrode after a full discharge at 0.01V and a charge at 0.9V is shown in the SEM images of Figure III. 10 (a) and (b), respectively. Upon discharge, the electrode morphology appears quite uniform, whereas when lithium is extracted from the particles (upon charge) important cracks become visible within the electrode.

This phenomenon is significantly reduced by limiting the capacity. Changes in the silicon electrode morphology at different steps of cycling are presented in the SEM images of Figure III. 11 and we can see that after one cycle, only few and small cracks are formed (Figure III. 11 (b)). After 10 cycles, lithiated and delithiated samples (Figure III. 11 (c) and (d)) show very small cracks and no crack is observed after 100 cycles. The advantage of a limited voltage window (0.12V – 0.9V) is clearly shown: the cracking is reduced, so the loss of particle contact is prevented.

First cycle between <u>0.01V</u> and 0.9V
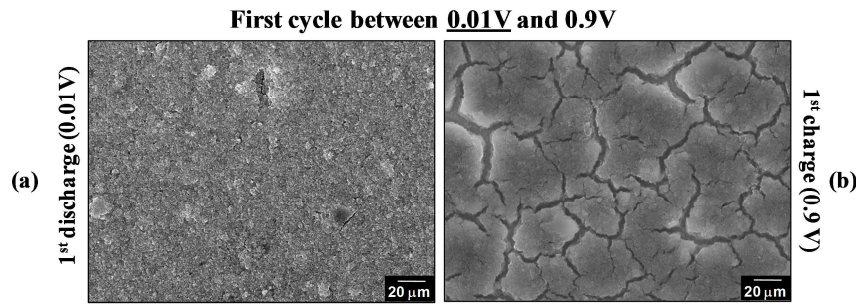
Figure III. 10 : SEM images of the Si/C/CMC composite electrode (20 µm scale horizontal): Cycling between 0.01 V and 0.9 V (a) after 1st discharge and (b) after the 1st charge.

Pre-cycling + cycling between 0.12V and 0.9V
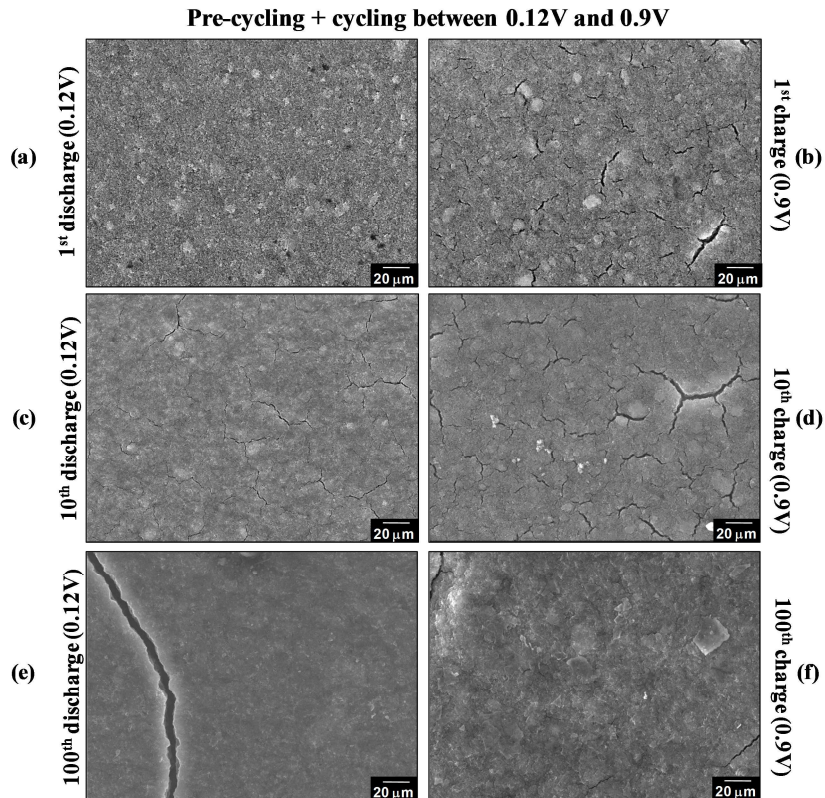
Figure III. 11 : SEM images of the Si/C/CMC composite electrode (20 µm scale horizontal): Cycling between 0.12 V and 0.9 V after the four steps of pre-cycling (a) after 1st discharge and (b) 1st charge, (c) after the 10th discharge and (d) 10th charge, and after (e) 100th discharge and (f) 100th charge.

1.2.3. PES Study

1.2.3.1. Effect of a long-term cycling on the electrode surface

1.2.3.1.1. Changes at the electrode/electrolyte interface - SEI analysis
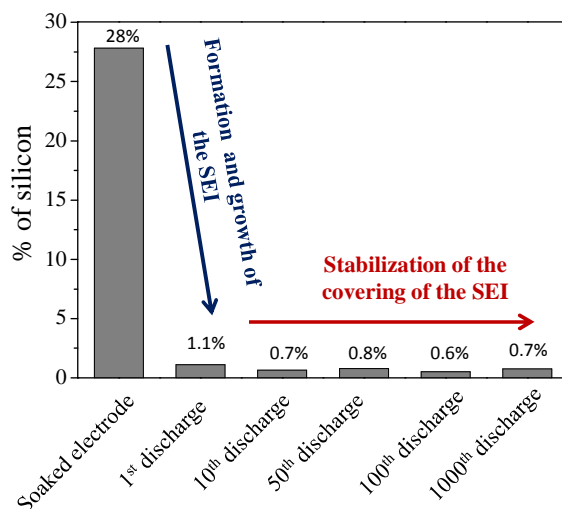
Figure III. 12 : The silicon content at the surface of the electrodes as a function of cycle number (after precycling). The data are based on in-house PES (hv = 1486.6 eV) Si 2p spectra of Si/C/CMC composite electrodes, and the values are given as traditional atomic percentages.

Figure III. 12 presents the evolution of the total amount of silicon measured (Si 2p spectra) at the surface of the sample after the 1st, 10th, 50th, 100th and the 1000th discharge down to 0.12V after the pre-cycling step. The trend observed clearly shows that the SEI covering of the Si particles is stable during a continuous long-term cycling.
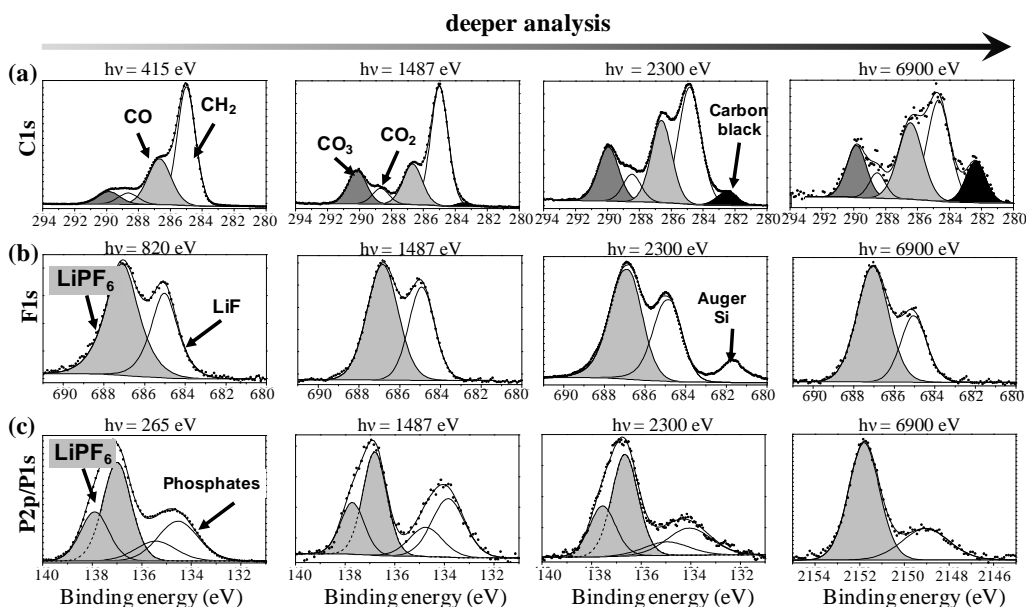
Figure III. 13 : (a) C 1s, (b) F 1s, and (c) P 2p/P 1s spectra of the Si/C/CMC composite electrodes after the 100th discharge shown as a function of the analysis depth.

Figure III. 13 (a) shows C 1s spectra of the Si/C/CMC composite electrode after the 100th discharge as a function of the photon energy. The four main components visible in these four spectra (in white and grey) represent the carbonaceous species deposited at the surface and composing the SEI. Compared to the first cycle, the same characteristic peaks are identified (see Figure III. 6), i.e. the carbon environments C-O at 286.5 eV, O=C-O at 288.5 eV and CO_3 at 290 eV. A slight increase of the ratios

94

CO_3/CO_2 and CO_3/CO is observed as a function of the analysis depth (mainly between hν = 410 and 1486.6 eV) and it suggests that Li_2CO_3 is found preferably close to the active particle as it has also been proposed in literature for the carbon negative electrode. Nevertheless, as previously seen after the study of the 1st cycle, by further increasing the depth of analysis, the overall shape of the spectra is rather stable, showing the homogeneity of the carbonaceous compounds within the SEI layer (with only small fluctuations occurring at its extreme surface). The component assigned to carbon black gradually increases with increasing photon energy; its detection after 100 cycles confirms the thickness/covering stability of the SEI upon cycling.

Information about the inorganic species in the SEI is given in Figure III. 13(b) and (c) with F1s and P2p/P1s spectra of the Si-based electrodes after 100th discharge as a function of the analysis depth. LiF (peak at 685 eV) and $LiPF_6$ salt (peak at 687 eV) are detected in the F1s spectra. While $LiPF_6$ was mainly present at the extreme surface of the SEI after a 1st discharge and charge, the ratio between LiF and $LiPF_6$ peaks barely changes from one analysis depth to another after the 100th discharge. After a long-term cycling, there is still $LiPF_6$ present in the surface which cannot be explained only as salt traces remaining after electrode washing. Instead, these results show that $LiPF_6$ forms an integral part of the SEI by diffusion of PF_6^- ions (as Li^+ ions) into the surface layer.

Concerning the evolution of the P 2p/P 1s peak as a function of the analysis depth (Figure III. 13(c)), it is first important to precise that P 1s provides information similar to P 2p. P 1s can only be recorded using high photon energies, with hν = 6900 eV. The cross section of P 1s exceeds that of P 2p, giving a better signal/noise ratio and a more efficient measurement. The spectra consist of two peaks: a first one at 137 eV (P 2p)/ 2152 eV (P 1s) (in grey) attributed to the salt $LiPF_6$, and a second one at 134 eV (P 2p)/ 2149 eV (P 1s) (in white) assigned to phosphates, which is another species commonly found in SEI layers obtained with similar electrolytes as shown in Chapter I. The signatures of both fluorine and phosphorus are very stable as a function of the analysis depth and this result confirms the presence of the PF_6^- ions as a part of the SEI after 100 cycles, and the homogeneous distribution of LiF and phosphates within the SEI layer.

1.2.3.1.2. Evolution of the surface oxide
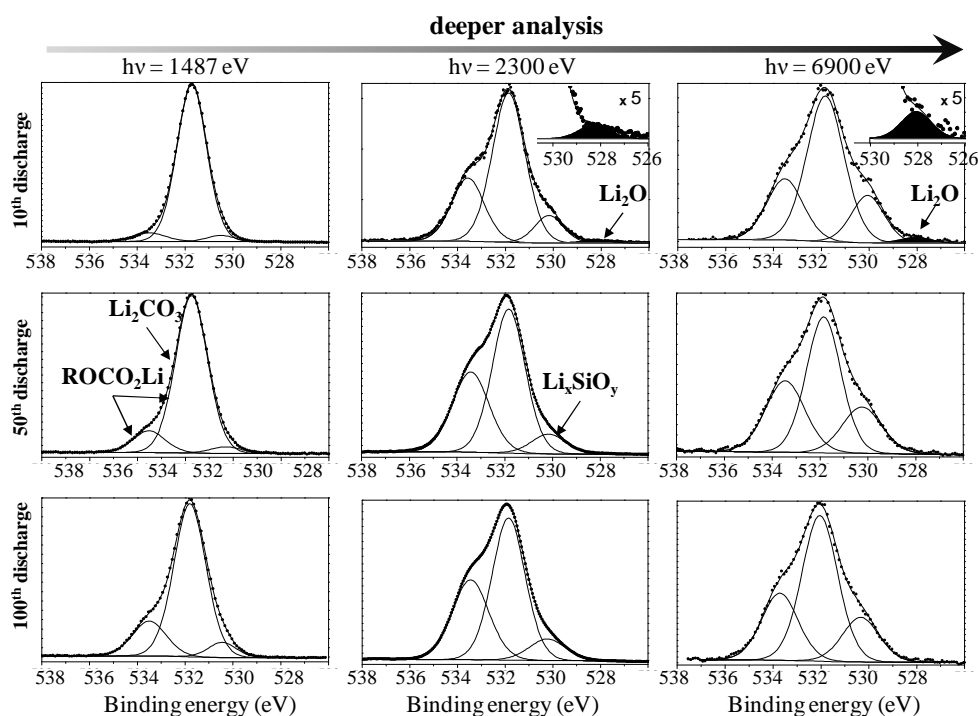
Figure III. 14 : O 1s spectra of the Si/C/CMC composite electrodes after the 10th, 50th, and 100th discharge. Evolution as a function of the analysis depth.

The O 1s spectra of the Si/C/CMC composite electrode after the 10th, 50th and 100th discharge are shown in Figure III. 14, as a function of analysis depth.

The evolution of spectra during cycling with three different photon energies (from the top to the bottom) shows the stability of the SEI composition with a good conservation of the overall shape of the two components at high binding energy, due to oxygenated species of the SEI (carbonates, alkyl carbonates and other organic species). At the same time the ratio between the signatures of Li_4SiO_4 (which is below the SEI layer) and the oxygenated peaks within the SEI remains constant demonstrating the stability in SEI thickness.

At a given state of discharge, if we compare data at 2300 and 6900 eV, we can see that the SEI oxygenated species are homogeneously distributed over the thickness of the SEI. The proportion of Li_4SiO_4 increases when using higher photon energy since this compound is buried underneath the SEI layer.

An interesting result is given by the evolution of the peak assigned to Li_2O (at 528 – 528.5 eV) upon long-term cycling. The detection of this component after the 10th discharge shows that the formation of Li_2O is reversible at least during the 10 first cycles. However, its peak intensity is clearly lower that after the first cycle demonstrating that the amount of Li_2O is decreasing upon cycling (see Figure III. 4). After the 50th and the 100th discharges, the peak attributed to Li_2O is not detected anymore in any of the O 1s spectra suggesting a consumption of this species. This point will be discussed later.

1.2.3.1.3. Evolution of Si compounds

- ***Lithium insertion/extraction upon cycling***
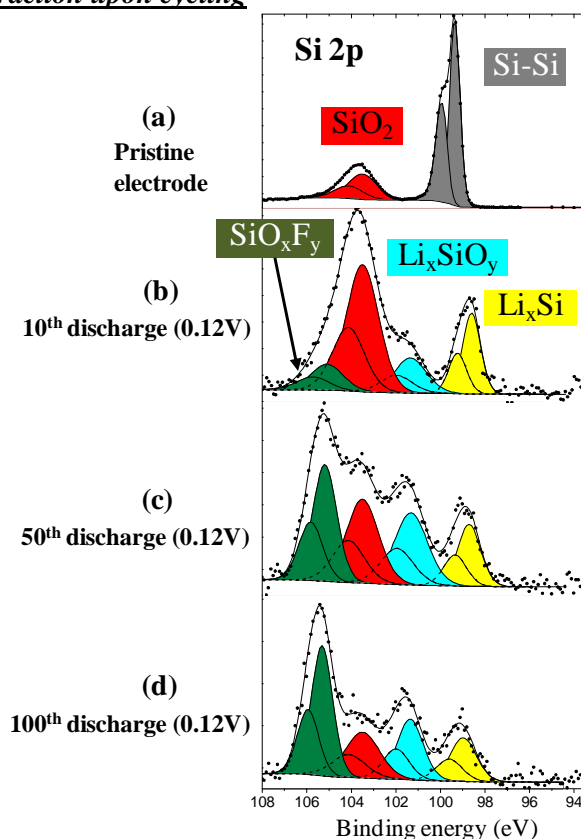
Figure III. 15 : Si 2p spectra (in-house PES, 1486.6 eV) of the Si/C/CMC composite electrode: (a) of the pristine electrode and after (b) the 10th discharge at 0.12 V, (c) the 50th discharge at 0.12 V, and (d) the 100th discharge at 0.12 V. Four pre-cycling steps and high C-rate were applied for (b), (c), and (d) samples.

Figure III. *15* shows the in-house PES Si 2p spectra of the Si/C/CMC composite of the pristine electrode (Figure III. *15* (a)) and after the 10th, 50th and 100th discharges at 0.12V (in Figure III. *15* (b)(c)(d) & (e), respectively).

After the 10th discharge, four silicon-containing phases are observed: SiO_2 (in red), lithium silicate (in blue), Li_xSi alloy (in yellow) and a fourth component at high binding energy (Si $2p_{3/2}$ at 105-106 eV, in green). This high binding energy is indicative of a fluorinated, or more probably a partially fluorinated species SiO_xF_y. The nature and origin of this phase will be discussed later.

After the 50th and 100th discharges, the same four components are detected and a significant increase of the amount of the fluorinated Si species is observed upon long-term cycling.

- ***Evolution of the Si 2p spectrum after 100 discharges as a function of the analysis depth***
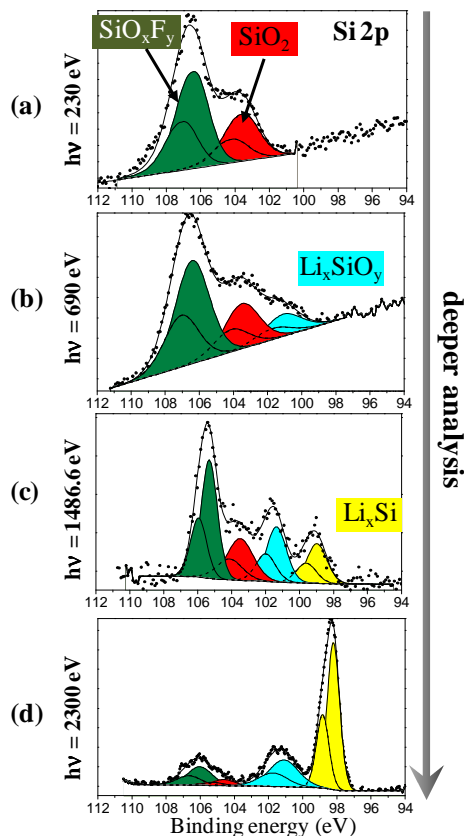
Figure III. 16 : Si 2p spectra of the Si/C/CMC composite electrode after the 100th discharge as a function of the analysis depth. (a) hν = 230 eV (MAX IV), (b) hν = 690 eV (MAX IV), (c) hν = 1486.6 eV (in-house PES), (d) hν = 2300 eV (BESSY II).

Table III. 2 : Photon energies (hν) and corresponding kinetic energies (K.E.) of the Si 2p core levels used in this work (B.E. Si 2p = 100 eV). The analysis depths were estimated according to the model of Tanuma et al. [53]

Photon energy hν	230 eV	690 eV	1486.6 eV	2300 eV
K.E. (eV)	130	590	1386	2200
Analysis depth (nm)	2	5	9	14

The discussion will now be focused on the SiO_xF_y component appearing and growing upon cycling.

Figure III. *16* shows the Si 2p spectrum of the Si/C/CMC composite electrode after the 100th discharge and its dependence on the photon energy. Table III. 2 shows the variation of the analysis depth as a function of the photon energy. When a lower photon energy is used (hν = 230 eV, *i.e.* analysis of the outermost surface), two components at ~ 106 eV (fluorinated environment of the silicon) and at ~ 103.5 eV (silicon dioxide) are observed (in green and red, respectively). The lithium silicate component appears when a higher photon energy is used (hν = 690 eV, Figure III. *16*(b)) and

finally, Li_xSi alloy is detected when $h\nu = 1486.6$ eV is used (Figure III. *16*(c)). At the greatest analysis depth ($h\nu = 2300$ eV, Figure III. *16* (d)), Li_xSi becomes the major component.

The depth-evolution of the Si 2p spectra observed in Figure III. *16* allows us to conclude that the SiO_xF_y phase is formed at the extreme surface of the silicon nanoparticles and that it is much more a surface phase than lithium silicate. So it is probably formed on top of or by reaction with the top layers of the SiO_2 covering the active particles.

- ***Nature of the new fluorinated phase - etching by HF***
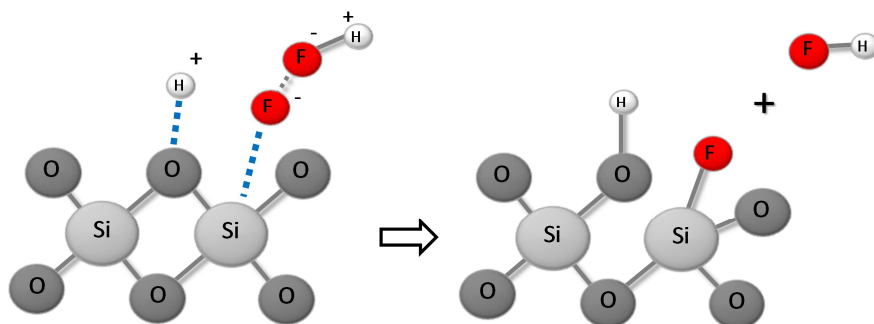
Figure III. 17 : Schematic illustration of the breaking of the Si–O bond as proposed by Mitra et al.[354]

The previous results suggest that the SiO_xF_y phase is formed at the extreme surface of the silicon nanoparticles due to a process occurring between the particles and the only source of fluorine: the electrolyte salt $LiPF_6$.

We have seen in chapter I that $LiPF_6$ is very sensitive to traces of impurities (water, moisture and alcohol) and forms hydrofluoric acid HF (Eqn. 18-19):

$$LiPF_6 \rightarrow LiF + PF_5 \qquad \text{Eqn. 18}$$
$$PF_5 + H_2O \rightarrow POF_3 + 2HF \qquad \text{Eqn. 19}$$
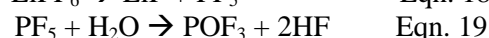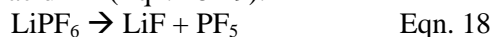
The generated HF can react with the native oxide at the surface of the silicon electrode. SiO_2 etching by HF is used in many technological fields and reaction mechanisms are proposed in several papers. Based on experimental results, it appears that the dissolution is a surface reaction-controlled process with adsorption of HF and HF_2^-: this last species being nearly four to five times more reactive than HF. The catalytic action of H^+ ions has also been pointed out especially for HF solutions of extremely low concentrations.

Ab initio quantum chemical calculations have shown that the etching reaction of SiO_2 by the HF molecule involves four steps, with each step consisting of an attack on the Si-O bonds by a HF molecule with generation of a Si-F bond. Mitra *et al.* proposed a reaction mechanism consisting of a simple elementary reaction that involves a coordinated attack of the Si-O bond by H^+ (electrophilic attack on the bridging oxygen atom) and HF_2^- (nucleophilic attack on the adjacent Si atom) as shown in Figure III. *17*. A multiple simultaneous bond break is not probable so it is expected that the process consists of a series of such elementary reaction steps.

The identification of SiO_xF_y species (with $y \leq 3$) at the extreme surface of the particles is consistent with this proposition. These results suggest that the reaction of HF with SiO_2 in a battery is more complex than the catalytic reaction pathway previously proposed with direct formation of volatile SiF_4 by etching of the SiO_2 layer.

The generation of HF can also explain the gradual disappearance of Li_2O during cycling with formation of LiF:

$$Li_2O + 2HF \rightarrow 2LiF + H_2O \qquad \text{Eqn. 20}$$
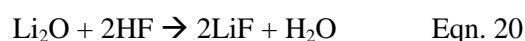
The H_2O formed in reaction (Eqn. 20) can regenerate HF (Eqn. 19) and both the consumption of Li_2O and the formation of the fluorinated silicon species are thus enhanced upon cycling.

It is worth noting that the formation of the fluorinated silicon species modifies the favourable interactions between the binder and the active material surface pointing out the important role of HF resulting from $LiPF_6$ degradation.

1.2.3.2. Reactivity of the pristine electrode with the electrolyte
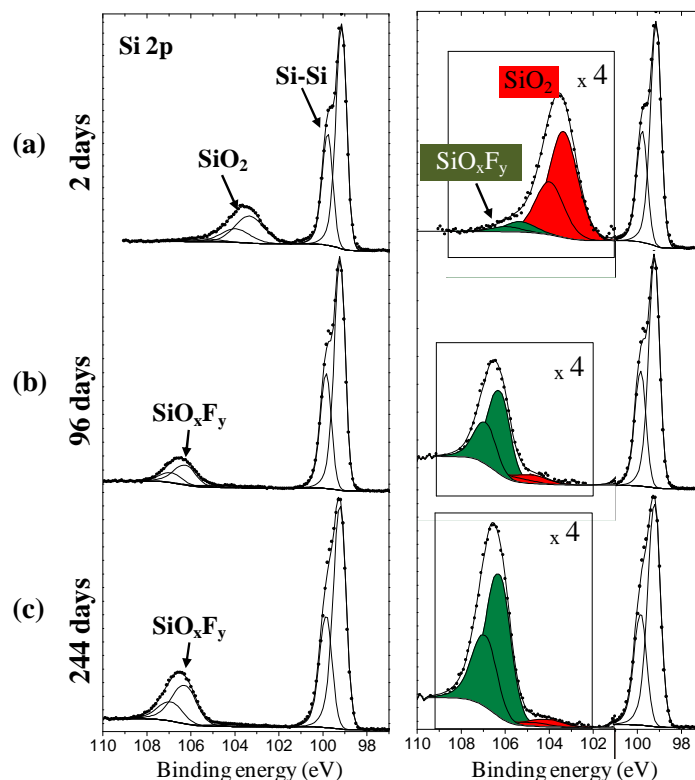
Figure III. 18 : Evolution of Si 2p spectra (in-house PES, 1486.6 eV) of the pristine Si/C/CMC electrode after contact with the electrolyte during (a) 2 days, (b) 96 days, and (c) 244 days. A zoom of the higher binding energy region is shown on the right-hand side.

An additional experiment has been performed to probe the reactivity of the pristine electrode with the electrolyte. The evolution of the chemical composition of the pristine electrode surface was followed as a function of storage time (electrode mounted in half-cells without any electrochemical cycling). Figure III. 18 shows the Si 2p core peak of the pristine electrode after contact with the electrolyte during 2, 96 and 244 days. After two days (Figure III. 18 (a)), two main components are observed are assigned to bulk silicon (Si $2p_{3/2}$ at ~99.5 eV) and silicon dioxide (Si $2p_{3/2}$ at ~103.5 eV). We can also notice the appearance of an additional peak at higher binding energy (~105-106 eV), corresponding to the fluorinated compound. After 96 and 244 days, a strong decrease of the silicon dioxide component is observed, and the intensity of the fluorinated compound increases. These trends are in agreement with the etching process described earlier, and are clear evidence that SiO_2 is reacting with the electrolyte as a function of storage time.

1.2.3.3. Formation of the fluorinated compound: the important role of the SEI layer
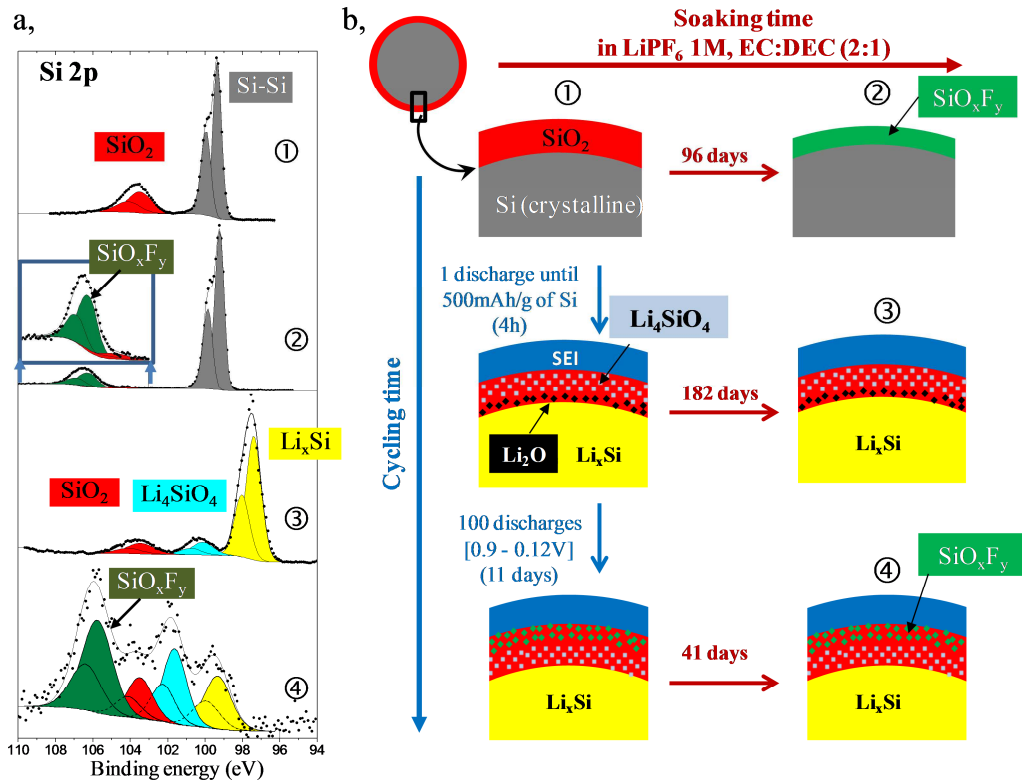
Figure III. 19 : a, Si 2p spectra (in-house PES, 1486.6 eV) (1) of the Si/C/CMC pristine electrode, (2) of a pristine electrode in contact 96 days with the electrolyte, (3) after a first discharge until 500 mAh.g^{-1} of Si, (4) after the 100th discharge at 0.12 V (with precycling) (to the left). b, Schematic view of the compounds formed on the silicon particle surfaces during cycling and/or during storage (to the right).

We have evidenced that the SiO_xF_y phase not only appears upon cycling but also after a simple contact with the electrolyte. In both cases, HF is involved but the kinetics of the reaction are quite different and can be related to the surface chemistry of the particles and particularly to the presence or absence of the SEI.

Figure III. 19 (a) shows the evolution of the Si 2p spectra of the Si/C/CMC electrode upon cycling and/or upon soaking in the electrolyte, compared to the Si 2p core peak of the pristine electrode (①). After 96 days of storage (②) the native SiO_2 layer (in red) has almost disappeared and a fluorinated compound is identified (in green).

The spectrum ③ shows the Si 2p core peak after a 1st partial discharge (up to 500 mAh.g^{-1} of Si). We know that the SEI is mainly formed at this state, Li_4SiO_4 has appeared in the SiO_2 layer and the Li_xSi alloy is formed. The interesting point is that after a first discharge, even after a contact of 182 days with the electrolyte, no fluorinated compounds appear. This feature points out the protective role of the SEI and once it is formed, the SEI behaves like a barrier prohibiting the HF acid to etch the oxide layer. However, this barrier allows the migration/diffusion of the acid during cycling (when a potential is applied), so the etching of the SiO_2 can occur and SiO_xF_y is formed at the interface between the SEI and the remaining oxide layer as seen in④ in Figure III. 19. When the potential is stopped, no further reactions are expected, since the SEI regains its protective role.

1.2.3.4. Effect of the depth of the discharge (capacity limitation) on the cycling performance and on the surface chemistry

Additional experiments have been performed to show the effect of the depth of discharge on the cycling performance and on the surface chemistry of the Si electrode.

We have shown earlier that fewer cracks were observed by limitation of the capacity (low cut-off potential at 0.12V instead of 0.01V) but other differences can be seen as briefly commented in this section.
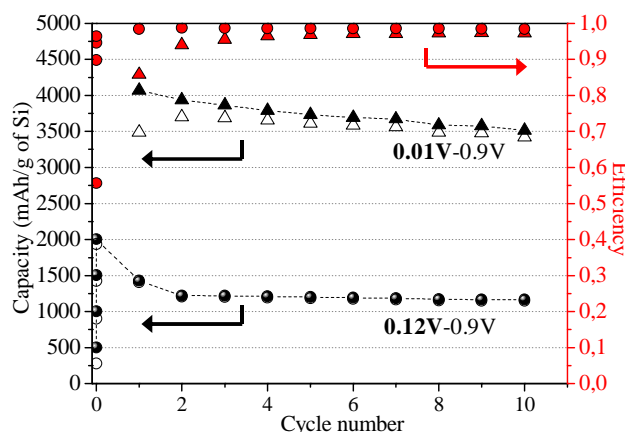
Figure III. 20 : Capacity data (in black) and coulombic efficiency (in red) vs. cycle number of the Si/C/CMC composite electrode vs. Li⁰ cell between 0.01 and 0.9 V at 700 mA.g⁻¹ of Si (triangle symbol) and between 0.12 and 0.9V (circle symbol). In this latter case, capacities of the four pre-cycles can be seen at cycle number = 0.

Figure III. 20 shows the discharge/charge capacities and the coulombic efficiency of the ten first electrochemical cycles of half-cells cycled between 0.01 and 0.9 V (triangle symbol) and between 0.12V and 0.9V (circle symbol) as a function of cycle number. When a cut-off voltage of 0.01V is used, we can see that the capacity is continuously decreasing and the coulombic efficiency after 10 cycles is around 97%. If the cut-off voltage is limited at 0.12V, a lower capacity is obtained but the capacity fading is significantly reduced and a stable coulombic efficiency around 98.5% is obtained after 10 cycles.
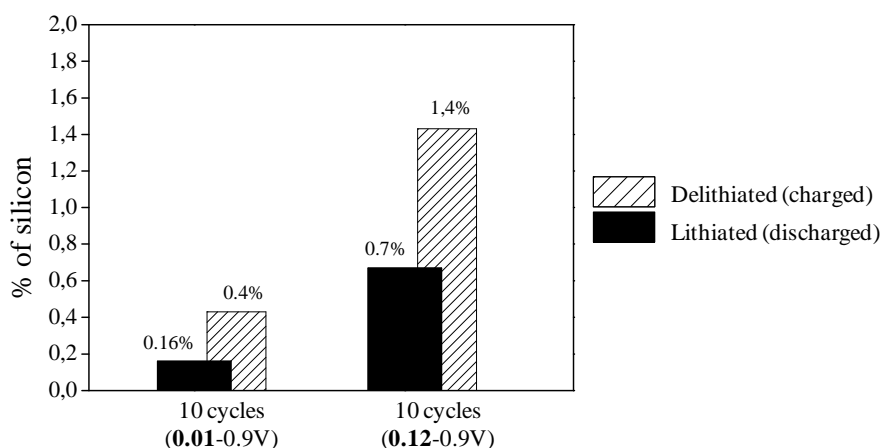
Figure III. 21 : The silicon content at the surface of charged and discharged electrodes cycled 10 times in the range 0.01-0.9V or 0.12-0.9V. The data are based on in-house PES (hν = 1486.6 eV).

The amount of silicon (Si at. %) detected at the surface of the electrodes after 10 cycles (charged and discharged state), with a cut-off voltage of 0.01 or 0.12 V is shown in Figure III. 21. These values can be related to the covering of the particles by the SEI. It is clear from this histogram that a thicker SEI is obtained when the capacity is not limited (full discharge at 0.01 V). A deep voltage discharge

enhances electrolyte degradation leading to thicker SEI at the end of the discharge. We have seen in Chapter 1 that continuous SEI formation can be observed as a result of the huge volume expansion of the Si particles. By limiting the capacity, the volume expansion is reduced and we can expect a more stable SEI not pulverized because of volume stress.

Upon charge, some SEI re-dissolution is observed (higher Si at.% in charge than in discharged state) but the SEI remains thinner when a limited voltage potential is applied.

The resulting Si 2p spectra of the Si-based electrode after 10 cycles in the voltage range 0.01-0.9V and 0.12-0.9V are shown in Figure III. 22. As previously seen, after 10 cycles between 0.12V and 0.9V, a weak component assigned to a fluorinated phase is observed at high binding energy (in green). The three other components attributed to SiO_2, Li_4SiO_4 and Li_xSi are also visible. With a lower cut-off voltage at 0.01V $vs.$ Li^+/Li, the intensity ratio between SiO_xF_y and SiO_2 components is significantly different suggesting that the formation of the fluorinated phase is enhanced after a full discharge. The differences between the two Si 2p spectra are also related to the SEI thickness. For a cut-off voltage of 0.01V, we have shown that a thicker SEI is obtained, therefore, just the outermost part of the Si particles is probed (SiO_2 and SiO_xF_y). For a cut-off voltage of 0.12V, thinner SEI allows to access deeper inside the Si particles and a clear increase of the intensity of the Li_xSi alloy component is observed.
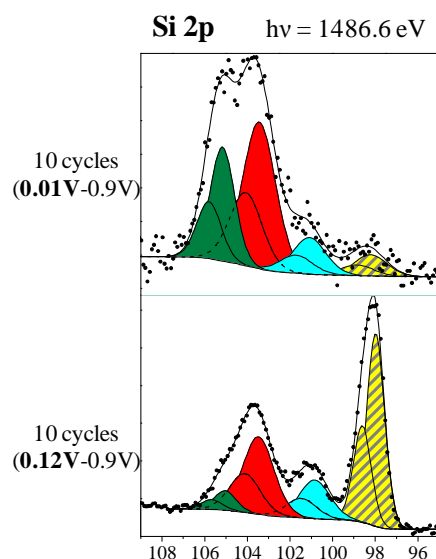
Figure III. 22 : Si 2p spectra (in-house PES, 1486.6 eV) of the Si/C/CMC electrode after 10 cycles between 0.01V and 0.9V (on the top) and after 10 cycles between 0.12V and 0.9V (on the bottom) at 700 mA.g^{-1} of Si.

Finally, limitation of the capacity gives thinner SEI and reduces the amount of SiO_xF_y formed compared to a full discharge at 0.01V. This difference can explain the better coulombic efficiency and the cyclability performance observed. The SEI formed is mechanically more stable and is not stressed by mechanical constraints, so electrolyte degradation is reduced upon cycling. In addition, the formation of SiO_xF_y is limited, minimizing the perturbations of the interaction between the Si particles and the other elements of the electrode (binder, conductive additives, current collectors).

1.2.4. Summary

The main conclusions related to this long-term cycling study of Si/C/CMC electrode in a LiPF$_6$ based electrolyte are listed below:

- Stable chemical composition and stable covering properties of the SEI upon a long-term cycling have been detected.
- Homogeneous chemical composition within the SEI layer regarding the inorganic species (LiF, LiPF$_6$, phosphates) and small fluctuations at the outermost surface regarding the organic part (oxygenated and carbonaceous species) are seen.
- Formation of fluorinated species SiO$_x$F$_y$ at the interface electrolyte/Si particles interface due to the reaction of the SiO$_2$ layer with HF (degradation product of LiPF$_6$) is evidenced.
- Li$_2$O is reversibly formed during the first cycle but slowly consumed upon cycling due to the reaction with HF.
- Limitation of the capacity (low cut-off potential of 0.12V *vs.* Li$^+$/Li) reduces the amount of cracks, gives thinner SEI and reduces the formation of the SiO$_x$F$_y$ phase compared to a full discharge at 0.01V *vs.* Li$^+$/Li.

1.3. Improved performances using the salt LiFSI

The formation of hydrofluoric acid as a result of the degradation of $LiPF_6$ induces many problems upon long-term cycling. We have shown that the etching of the SiO_2 layer at the surface of the Si particles by HF can change the interactions between the binder and the active material surface and an irreversible fluorinated phase SiO_xF_y is formed. These points may explain the capacity fading upon long-term cycling. HF acid also presents a safety risk and in case of ignition of the battery, a release of gaseous HF can occur. Therefore other lithium salts have to be considered as replacement of $LiPF_6$.

A new and promising imide salt has been investigated in this thesis work: lithium bis(fluorosulfonyl)imide $Li[N(SO_2F)_2]$(LiFSI).

In this section, and for the first time to our knowledge, the electrochemical performance of nano-silicon-based electrodes using LiFSI as conductive salt has been investigated and the evolution of the Li-Si alloy, the surface oxide and the passivation layer (SEI) after one cycle and upon long-term cycling has been studied by PES and SEM.

1.3.1. Electrochemical results

Figure III. 23 shows the electrochemical performances of Li//Si half-cells using either LiFSI (in blue) or $LiPF_6$ (in red). It is important to note that all Si/C/CMC composite electrodes arise from the same batch, and were cycled in similar conditions (electrolyte EC:DEC (2:1) + LiFSI or $LiPF_6$ 1M).

Figure III. 23 (a) and (b) show the discharge capacity *vs.* cycle number upon galvanostatic cycling between 0.12 and 0.9 V (current rates of 150 and 700 mA.g^{-1} of Si). At the lowest rate, the discharge capacity of the first cycle (after the four pre-cycles) is around 2000 mAh.g^{-1} with both salts and after 15 cycles, the capacity increases up to 2640 mAh.g^{-1} and 2330 mAh.g^{-1} for LiFSI and $LiPF_6$, respectively. Then, capacity decreases gradually for both salts, 66 % of the initial discharge capacity is retained using LiFSI salt whereas only 16 % with $LiPF_6$ after 120 cycles (300 mAh.g^{-1} with $LiPF_6$ and 1300 mAh.g^{-1} with LiFSI after 120 cycles).

The improved performances with LiFSI salt are confirmed at higher rate, the discharge capacity of the first cycle is lower and similar for both salts (about 1400-1500 mAh.g^{-1}) and the capacity fading upon cycling is more pronounced. However in the case of LiFSI, 66 % of the initial capacity is maintained after 100 cycles and 37 % after 400 cycles whereas the capacity retention with $LiPF_6$ is only 35% after 100 cycles and 13% after 400 cycles. LiFSI clearly outperforms $LiPF_6$ and sustains more stable capacities upon long-term cycling for both current rates.
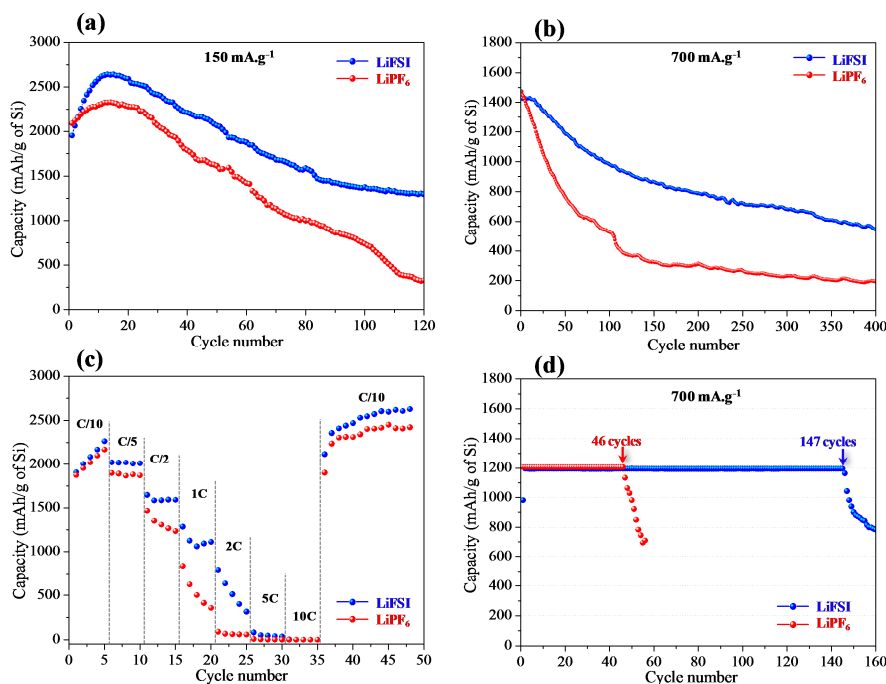
Figure III. 23 : Electrochemical tests of Li//Si cells using either LiFSI (in blue) or LiPF$_6$ (in red) salts: (a) and (b) Discharge capacity vs. cycle number upon galvanostatic cycling between 0.12 and 0.9 V at current rates of 150 and 700 mA.g^{-1} of Si (pre-cycling is not shown). (c) Discharge capacities vs. cycle number at different current rates from C/10 to 10 C (rate capability test). (Pre-cycling is not shown). (d) Fixed capacity test. The discharge capacity was limited to 1200 mAh.g^{-1} of Si (see chapter II).

Figure III. 23 (c) shows a rate capability test performed from C/10 to 10C (discharge capacities *vs.* cycle number of Li//Si cells at different current rates). The discharge capacities of the first cycle are similar for both salts (~1900 mAh.g^{-1}). When a higher cycling rate is applied, we can observe a significant decrease of the capacities as a function of the applied current and, for the highest rates, a rapid capacity fading as a function of the cycle number. However, the rate capability is clearly better with LiFSI than with LiPF$_6$. The final step consists in application of a low current rate (C/10). The initial capacities of 1900 mAh.g-1 (with LiPF$_6$) and 2100 mAh.g^{-1} (with LiFSI) are recovered and this result suggests that the electrode material is not significantly damaged during fast cycling with both salts. We can see from the electrochemical test that the capacity retention at high current rate is better when LiFSI salt is used.

The last electrochemical test presented in Figure III. 23 (d) compares the cycling performances of the half-cells when a limited discharge capacity is applied (1200 mAh.g^{-1}, see Chapter II). When this capacity value cannot be reached anymore upon cycling, the discharge is limited by a 0.005 V cut-off voltage and the capacity fades rapidly. We can see in Figure III. 23 (d) that a 1200 mAh.g^{-1} capacity can be retained for 46 cycles with LiPF$_6$, whereas 147 cycles can be achieved using LiFSI.

These four electrochemical tests showed that LiFSI outperforms LiPF$_6$ when used as salt in non-aqueous liquid electrolyte upon long-term cycling of a Si-based electrode *vs.* metallic lithium.

In the next part, we will try to understand why LiFSI allows such improved performances and we will focus our attention to the mechanisms occurring at the surface of the silicon electrodes.

1.3.2. Reactivity of the Si electrode towards the electrolyte

Electrolyte containing LiPF$_6$ has shown to be reactive with silicon electrodes by direct chemical contact, therefore, the first step of this study was to perform a similar experiment to investigate the reactivity of the Si/C/CMC electrode towards an electrolyte containing LiFSI.
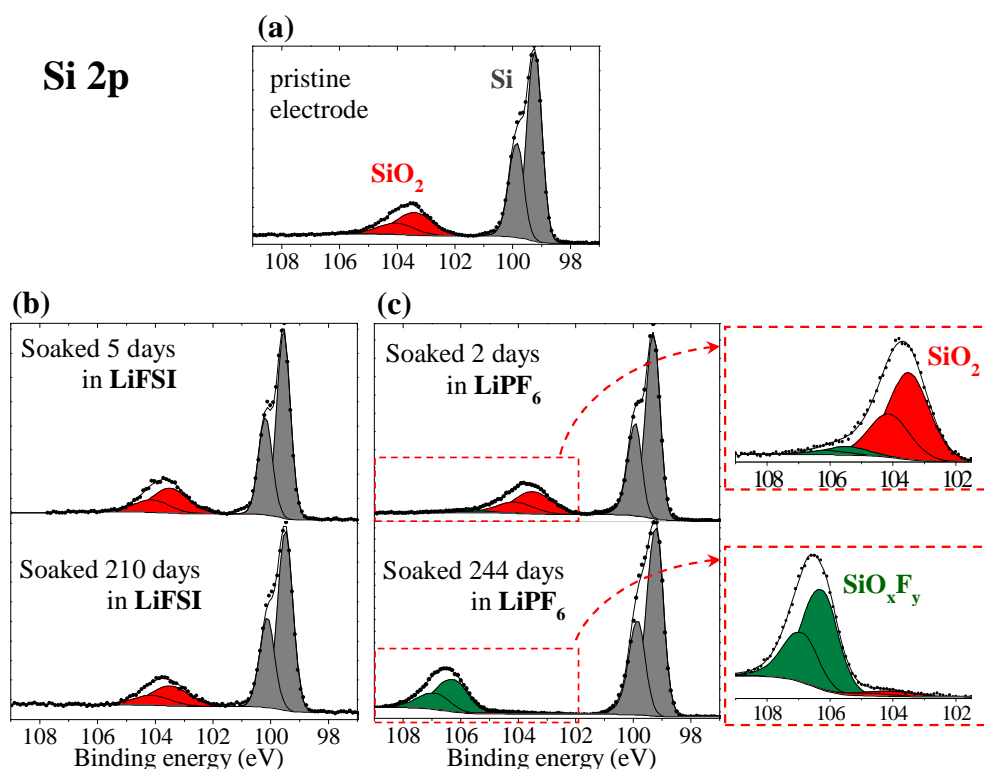
Figure III. 24 : Si 2p spectra (in-house PES, hν = 1486.6 eV) of (a) the pristine Si electrode, and after contact with an electrolyte containing either (b) LiFSI or (c) LiPF$_6$. A zoom of the 102-109 eV B.E. region is shown on the right for LiPF$_6$.

Figure III. *24* shows the Si 2p core peak of: (a) the pristine Si/C/CMC electrode, (b) after contact with an electrolyte containing LiFSI and after contact with an electrolyte containing LiPF$_6$.

After 5 and 210 days of contact of the silicon electrode with the electrolyte containing LiFSI, the overall shape of the spectra remains stable and no additional peak attributed to SiO$_x$F$_y$ species in the case of LiPF$_6$, appears. This shows that the surface of the silicon particles did not react with the electrolyte, a result consistent with the better stability of LiFSI towards hydrolysis compared to LiPF$_6$.

1.3.3. Interfacial mechanisms occurring during the 1st cycle – LiFSI salt

Interfacial mechanisms occurring upon the first discharge/charge cycle of Si/C/CMC composite electrodes cycled *vs.* metallic lithium will be described in this part and compared with the mechanisms observed with LiPF$_6$.

1.3.3.1. Morphology
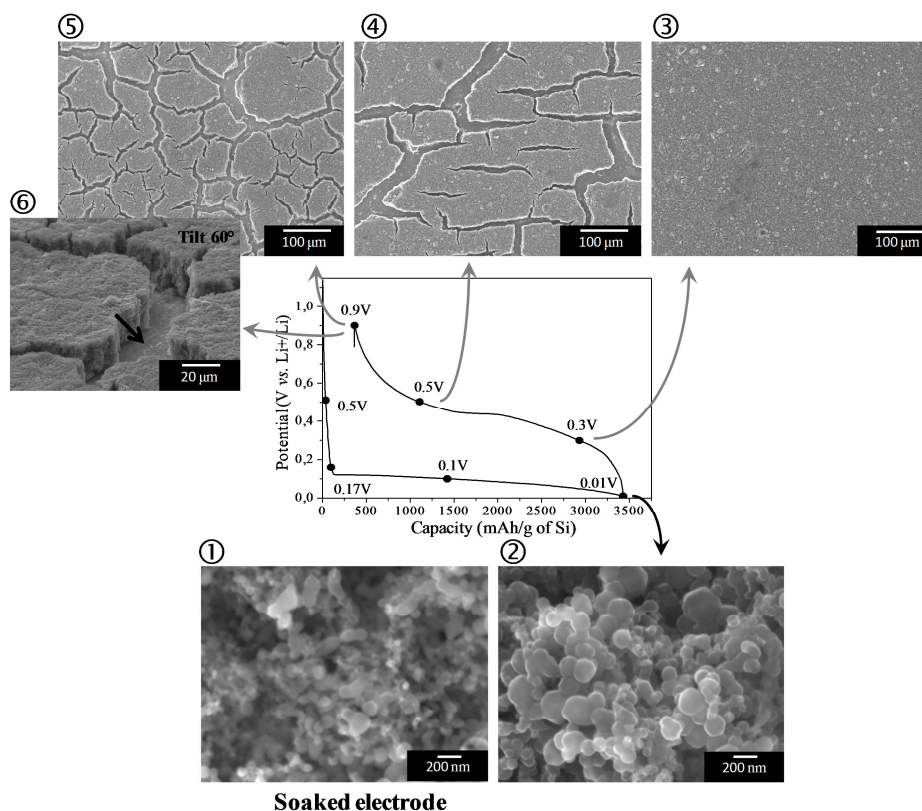
Figure III. 25 : **First discharge/charge cycle of the Si/C/CMC composite electrode vs. Li⁰ cell, between 0.01 and 0.9 V at 150 mA.g⁻¹ (1M LiFSI in EC:DEC (2:1)). The samples analyzed by PES are highlighted by black points. SEM images of the Si/C/CMC composite electrode of the soaked electrode (①, 200 nm scale horizontal) and cycled between 0.01 V and 0.9 V (a) after 1st discharge (②, 200 nm scale horizontal) and (b) after the charge at 0.3V, 0.5V and 0.9V (③,④,⑤ respectively, 100 μm scale horizontal). SEM image ⑥ presents the electrodes cycled after the 1ˢᵗ charge (0.9V) and was recorded with a tilt of 60°.**

The first electrochemical cycle performed between 0.01V and 0.9V at 150 mA.g⁻¹ and the evolution of the morphology (SEM images) of the silicon electrode during the first lithiation/delithiation cycle are presented in Figure III. 25.

Two important features can be observed in these SEM figures. First, upon discharge (from ① to②), we clearly see the increase in diameter of the particles composing the electrode. The insertion of Li into Si leads to volume change and particles with a diameter of ~ 100 nm in the soaked electrode increase to ~200 nm diameter at the end of the first discharge. The second point concerns the charge from 0.01 V to 0.9 V. As seen with LiPF₆, the removal of lithium forms cracks at the surface of the composite electrode (images ③ to ⑤ in Figure III. 25). At 0.3 V *vs.* Li⁺/Li, no cracks are observed and the morphology of the surface electrode is uniform. First cracks are observed at 0.5 V *vs.* Li⁺/Li and even more at 0.9 V *vs.* Li⁺/Li. SEM images ⑥ show that not only the surface of the electrodes is cracked but all the composite is affected, the copper foil can thus be observed (indicated by an arrow).

1.3.3.2. PES study
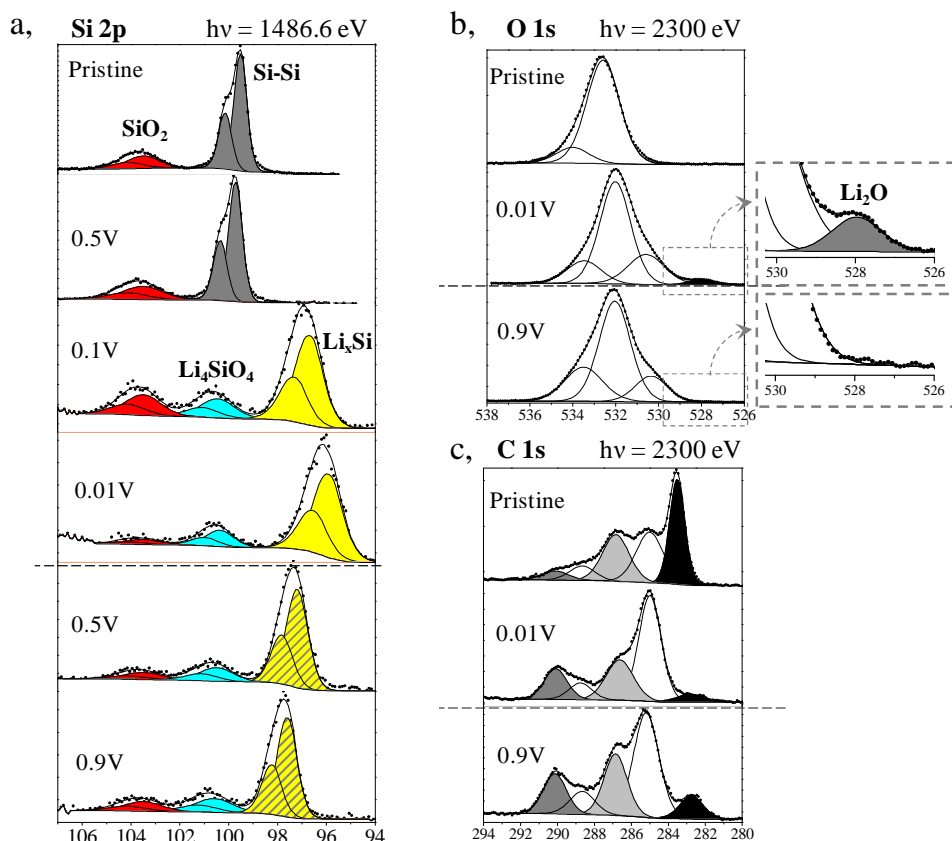
Figure III. 26 : (a) Si 2p (hν = 1486.6 eV) (b) O 1s (hν=2300 eV) and (c) C 1s (hν = 2300 eV) spectra of the Si/C/CMC composite electrodes upon the first discharge/charge cycle (1M LiFSI in EC:DEC (2:1)).

Figure III. 26 (a) shows the Si 2p spectra of the Si/C/ CMC composite electrode upon the first discharge/charge cycle with LiFSI salt (in-house PES, hν = 1486.6 eV). The evolution of the Si 2p spectra is very similar to the one observed when $LiPF_6$ is used (see Figure 2). As previously commented, the first changes occur at the beginning of the plateau (~0.17 V *vs.* Li^+/Li), with the appearance of two additional peaks corresponding to the alloy Li_xSi at low binding energy (in yellow) and to lithium silicate: Li_4SiO_4 at ~100-101 eV (in blue). The formation of Li_4SiO_4 is irreversible upon the first electrochemical cycle.

Figure III. 26 (b) shows the evolution of O 1s spectrum of the pristine Si-based electrode, after the first discharge at 0.01V *vs.* Li^+/Li and after the first charge at 0.9V *vs.* Li^+/Li (Bessy II, hν = 2300 eV). Spectra are rather similar to the ones presented in Figure III. 4 when $LiPF_6$ is used as electrolyte salt. After the first discharge and first charge, the two components at higher binding energies are attributed to oxygenated species present in the SEI (carbonates, alkyl carbonates and other oxygen species of the SEI) and the peak located at ~530 eV is assigned to the lithium silicate. We can notice the stability of the overall shape of the O 1s core peak that suggests a stable SEI in composition upon the first discharge/charge cycle. Finally, as previously seen with $LiPF_6$, a component at low binding energy (~530 eV) attributed to Li_2O appears upon discharge. The disappearance of this component upon charge shows the reversibility of the Li_2O formation process during the first electrochemical cycle.

Figure III. 26 (c) shows C 1s spectra of the pristine Si-based electrode, after the first discharge at 0.01V *vs.* Li^+/Li and charge at 0.9V *vs.* Li^+/Li (Bessy II, hν = 2300 eV). They look very similar to C 1s spectra previously commented for $LiPF_6$ (Figure III. 6) suggesting the presence of the same carbonaceous species in the SEI (carbonates, alkylcarbonates, oxalates and PEO). However, a lower amount of carbonates was systematically determined with LiFSI compared to $LiPF_6$ (respectively ~15% and ~26% for example at the end of discharge).

In addition, the evolution of F1s spectra provides information about inorganic species/LiF forming the SEI. Compared to $LiPF_6$ similar amounts of LiF were evaluated at the end of discharge (5.6% with LiFSI and 4.2% with $LiPF_6$).

Finally, the evolution of the thickness/covering by the SEI can be estimated by following the total amount of silicon at the surface of the electrodes (atomic % of Si 2p) (Figure III. 27). A dramatic drop of the Si 2p signal is observed upon discharge from 35.7% (soaked electrode) to 1% (at 0.01V *vs.* Li^+/Li). During charging, the percentage of silicon remains around 1% showing the irreversible formation of the SEI during the first electrochemical cycle.
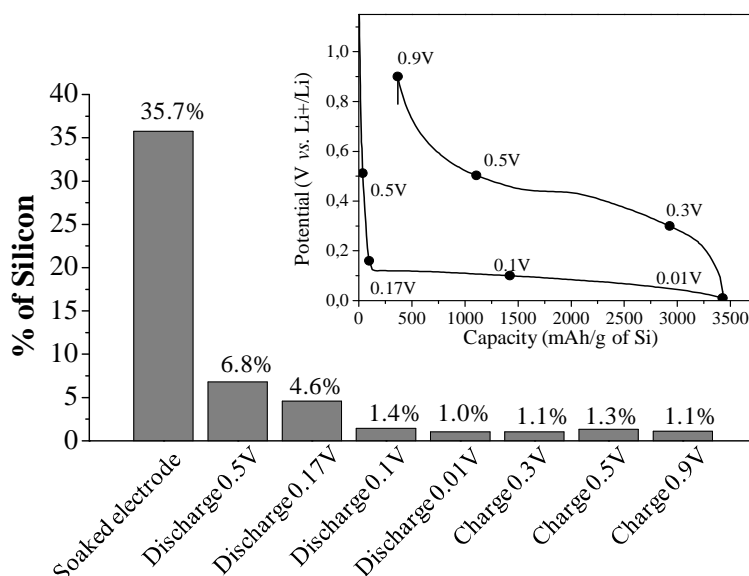
Figure III. 27 : **Evolution of silicon content at the surface of the electrodes determined from XPS spectra of the Si/C/CMC composite electrodes upon the first discharge/charge cycle using LiFSI as electrolyte salt (in-house XPS, 1487 eV).**

Some differences are observed compared to $LiPF_6$ (Figure III. 5). For example, at the end of the first discharge (0.01V *vs.* Li^+/Li), the covering by the SEI appears slightly more important with $LiPF_6$ (0.4% Si detected at the surface) than with LiFSI (1.0% Si at the surface).

A more detailed analysis of the SEI when LiFSI is used will be carried out in the next section.

The similarity of the results obtained with $LiPF_6$ and LiFSI during the first electrochemical cycle are not very surprising considering the electrochemical data, as the difference in cycling performance between the two salts emerges during long-term cycling. We will focus on this point in the following part.

1.3.4. Interfacial mechanisms occurring upon long-term cycling – LiFSI salt

In this part, Si//Li half cells were cycled between 0.12V and 0.9V at 700 mA.g^{-1} of Si. As previously described for the long-term cycling study using $LiPF_6$ salt, four pre-cycles where performed prior to standard galvanostatic cycling.

1.3.4.1. Morphology

Precycling + cycling between 0.12V and 0.9V
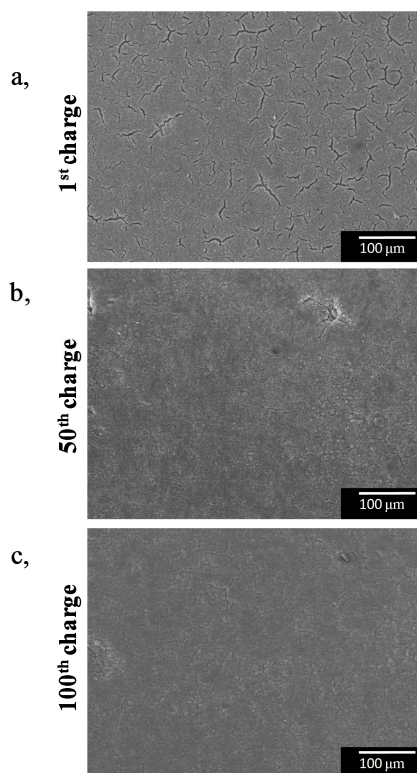
Figure III. 28 : SEM images of the Si/C/CMC composite electrode (100 μm scale horizontal bars): Cycling between 0.12 V and 0.9 V after the four steps precycling (a) after the 1st charge (b) after the 50th charge and (c) after the 100th charge

SEM images in Figure III. 28 show the changes in the silicon electrode morphology after one, 50 and 100 cycles (charged state). After one charge, only few and small cracks are observed (Figure III. 28 (a)). After 5 and 100 cycles (Figure III. 28 (c) and (d)), no cracks are observed on the delithiated samples. From the point of view of electrode morphology, these SEM pictures confirm the advantage of a limited voltage window (0.12V – 0.9V) as previously observed using $LiPF_6$ salt.

1.3.4.2. Effect of electrochemical cycling on the electrode surface

1.3.4.2.1. Evolution of Si compounds

HAXPES analysis of the long-term cycled Si-based electrodes has been carried out at Bessy and compared with the in-house data. Table III. 3 summarizes the variation of the K.E. as a function of the Si core level and photon energy.

Table III. 3 : Photon energies (hν) and binding energies (B.E.) of the Si core levels used in this work, with corresponding kinetic energies (K.E.). The analysis depths were estimated according to the model of Tanuma et al. [53]

Si core level Photon energy hν	Si 1s 2300 eV	Si 2p 1486.6 eV	Si 2p 2300 eV	Si 1s 6900 eV
B.E. (eV)	1840	100	100	1840
K.E. (eV)	460	1386	2200	5060
Analysis depth (nm)	4	9	14	27

110
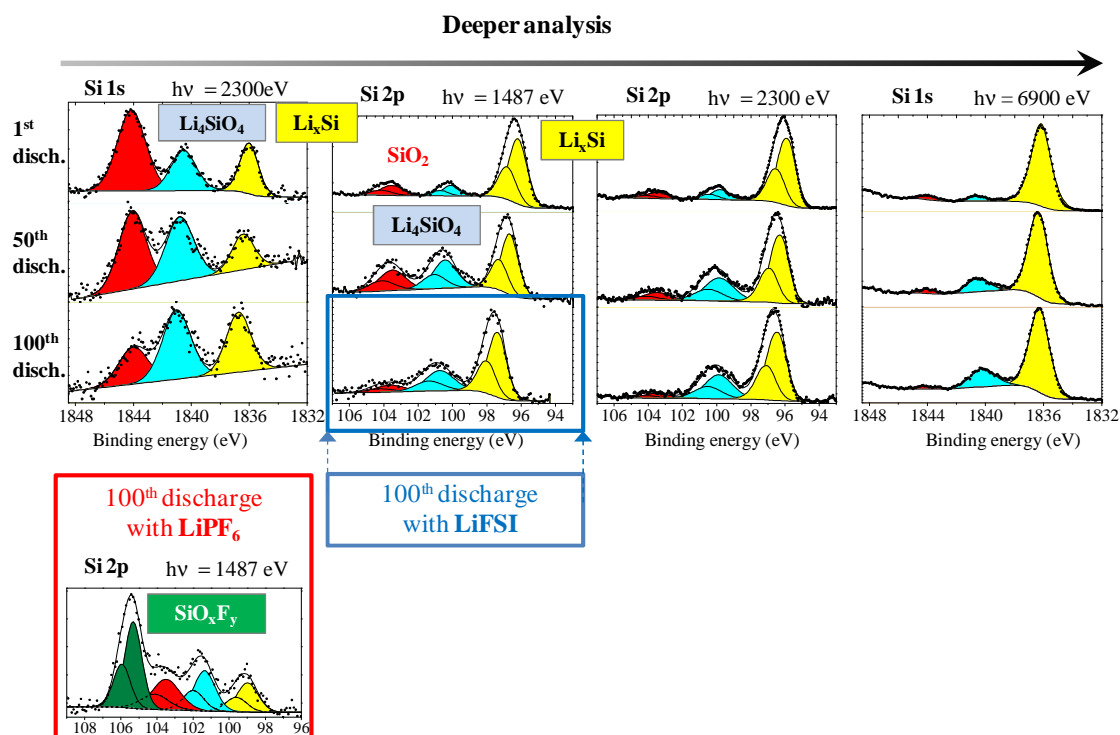
Figure III. 29: Evolution of Si 2p/Si 1s spectra of the Si electrode after the 1st, 50th and 100th discharge of a Li//Si cell with an electrolyte containing LiFSI. Evolution as a function of the analysis depth. Comparison with the 100th discharge using LiPF$_6$ in the bottom left corner.

The evolution of Si 2p/Si 1s core peaks of the Si/C/CMC composite electrode after 1st, 50th and 100th discharges at 0.12V with an electrolyte containing LiFSI is shown in Figure III. 29 as a function of the analysis depth. The Si 2p spectrum of the Si-based electrode when LiPF$_6$ is used as salt is presented after the 100th discharge in this figure as well.

Two important trends can be noted. First, we can see a gradual decrease of the SiO$_2$/Li$_4$SiO$_4$ area ratio upon long-term cycling, showing that the reaction of the surface oxide SiO$_2$ with lithium and thus the formation of lithium silicates is continuous upon cycling. Secondly, an important result is the absence of additional component at high binding energy. With LiPF$_6$ salt, the result was different (Figure III. 29) and the formation of a fluorinated compound SiO$_x$F$_y$ located at the surface of the particles was observed. With LiFSI, the absence of the SiO$_x$F$_y$ phase confirms that no reaction with HF occurs upon long cycling and this difference concerning the chemistry of the silicon particles surface is certainly linked to the improved performances of Li//Si electrochemical cells using LiFSI salt.

Finally, the observed capacity fading observed upon cycling (Figure III. 23) can be related to a gradual decrease of the lithium content in the Li$_x$Si alloy as suggested by the slight increase of the binding energy of the Li$_x$Si alloy component upon cycling.

1.3.4.2.2. Evolution of oxygenated species

Figure III. 30 presents the O 1s spectra of the uncycled Si electrode, and after the 1st, 50th and 100th discharges and charges, recorded with a photon energy of 6900 eV. The spectrum of the uncycled electrode has already been commented earlier (main component assigned to SiO$_2$ and CMC binder).

After cycling, the overall shape of O 1s spectra changes following the formation of the SEI, and thus the deposition of oxygenated species at the surface of the electrode. These species are similar to the ones previously commented. We can note the stability of the overall shape of O 1s spectra over 100 cycles both in charge and discharge, suggesting that the composition of oxygenated species in the SEI does not change significantly. As previously seen, the component observed at a B.E. of 530.3 eV

is in good agreement with lithium silicate Li_4SiO_4 and is easily observed in these spectra due to the high photon energy $hv = 6900$ eV (highest analysis depth (~33 nm)).

Compared to the study carried out with $LiPF_6$, the main difference concerns the O 1s signature ~528 eV assigned to Li_2O. We can see that lithium oxide can be detected in the lithiated state after the 1st, 50th and 100th discharges but not in the delithiated state showing the reversibility of its formation. The situation was different with $LiPF_6$ after long-term cycling. Indeed, in the lithiated state Li_2O was not detected after the 50th and 100th discharge and it was explained by the role of the HF acid reacting with the basic Li_2O.

The presence of Li_2O after 100 discharges with LiFSI is consistent with the lower sensitivity of this salt towards hydrolysis and the lower content of HF in the electrolyte.
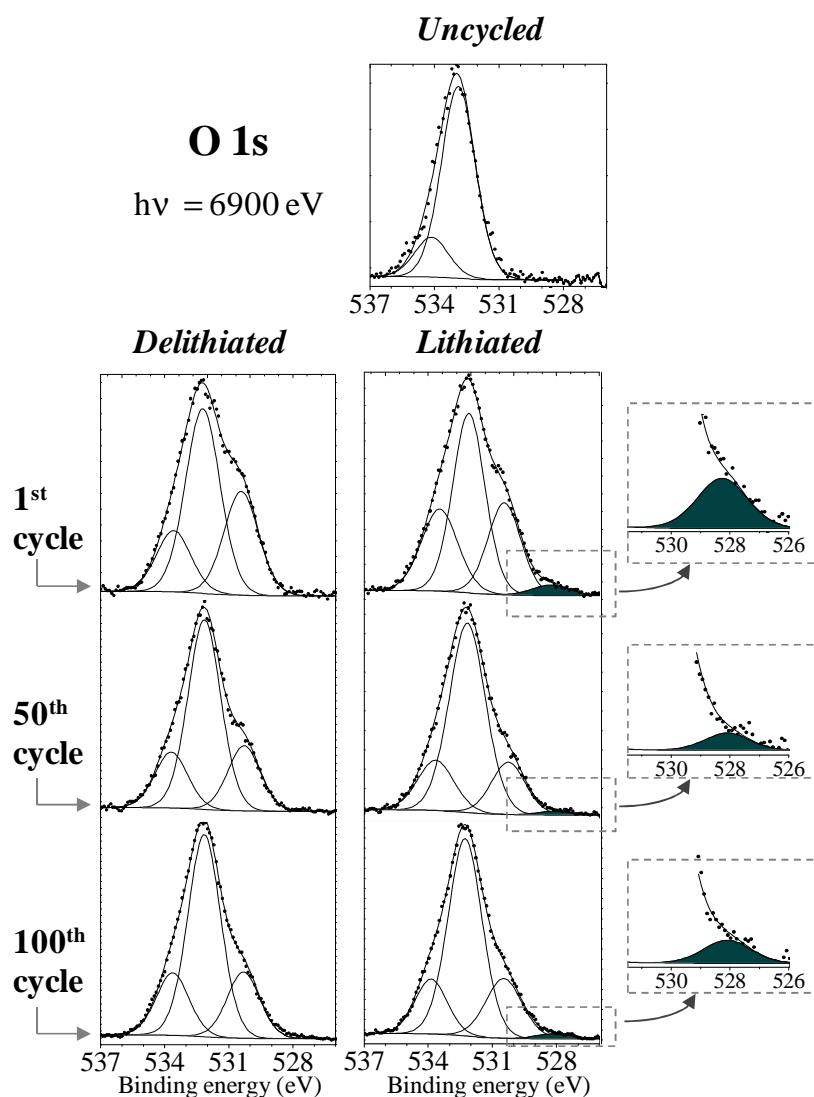
Figure III. 30 : O 1s spectra of the Si electrode soaked 5 days in the electrolyte (uncycled), and after the 1st, 50th and 100th discharges (lithiated) and charges (delithiated) with an electrolyte containing LiFSI. A zoom of the low B.E. region is shown on the right to highlight the signature of Li_2O. ($hv = 6900$ eV)
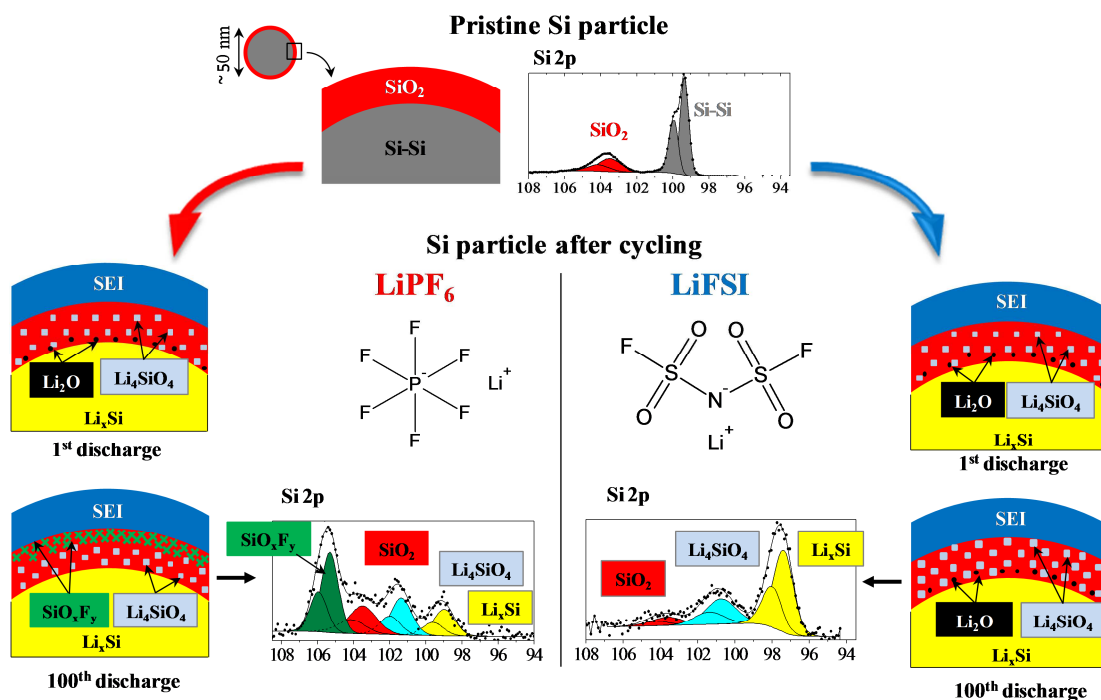
Figure III. 31 : Schematic comparison of the mechanisms occurring at the surface of silicon nanoparticles upon cycling of a Li//Si cell using either LiPF$_6$ or LiFSI salts.

These results obtained when LiPF$_6$ or LiFSI salts are used are summarized in Figure III. 31. The main conclusions are listed below:

Upon the first discharge, mechanisms are similar for both salts:

- Formation of the SEI layer during this first discharge,
- Formation of Li$_2$O and Li$_4$SiO$_4$ (reaction of Li with the SiO$_2$ layer) at the surface of Si nanoparticles,
- Formation of the Li$_x$Si alloy deeper inside the particles.

Upon long-term cycling, differences are observed with LiFSI salt compared to LiPF$_6$:

- Absence of the formation of fluorinated species SiO$_x$F$_y$ at the surface of the Si nanoparticles even after 100 cycles,
- Reversible formation of Li$_2$O upon discharge still observed after 100 cycles.

These differences lead to different surface chemistries on the particles and different interactions between the active material particles and the other electrode components (binder, carbon black, current collector). It is why we assume that they are at the origin of the better electrochemical behaviour observed when LiFSI is used instead of LiPF$_6$.

We will now focus our discussion on the characteristics of the SEI.

- ***Covering process***
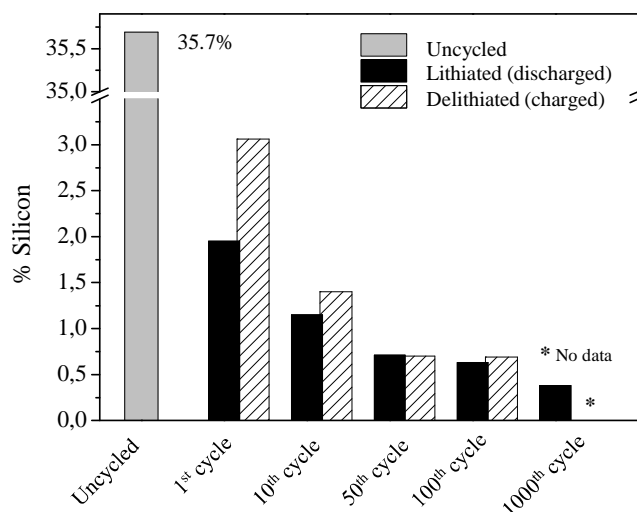
Figure III. 32 : Evolution of atomic percentage of silicon measured at the surface of the electrodes (in-house XPS, hv = 1486.6 eV) using LiFSI as salt as a function of cycle number (after pre-cycling). Charged (hatched) and discharged (black) states are differentiated.

Figure III. 32 shows the evolution of the amount of silicon measured at the surface of the electrodes by in-house XPS (hv = 1486.6 eV) after the 1st, 10th, 50th, 100th and 1000th cycles using LiFSI as salt (discharge down to 0.12V and charge up to 0.9 V, after the pre-cycling step) with respect to the uncycled electrode (soaked 5 days in the electrolyte).

After further cycles, a thickening of the SEI is noted with stabilization after 50 cycles. The same trend was observed with LiPF$_6$ but stabilization occurs as soon as the 10th discharge in this case (Figure III. 12). We can also note that the SEI is slightly thinner after charge than after discharge at each cycle corresponding to a slight re-dissolution of species of the SEI upon charge. This breathing effect fades upon long-term cycling.

- *Carbonaceous species of the SEI*

Deeper analysis
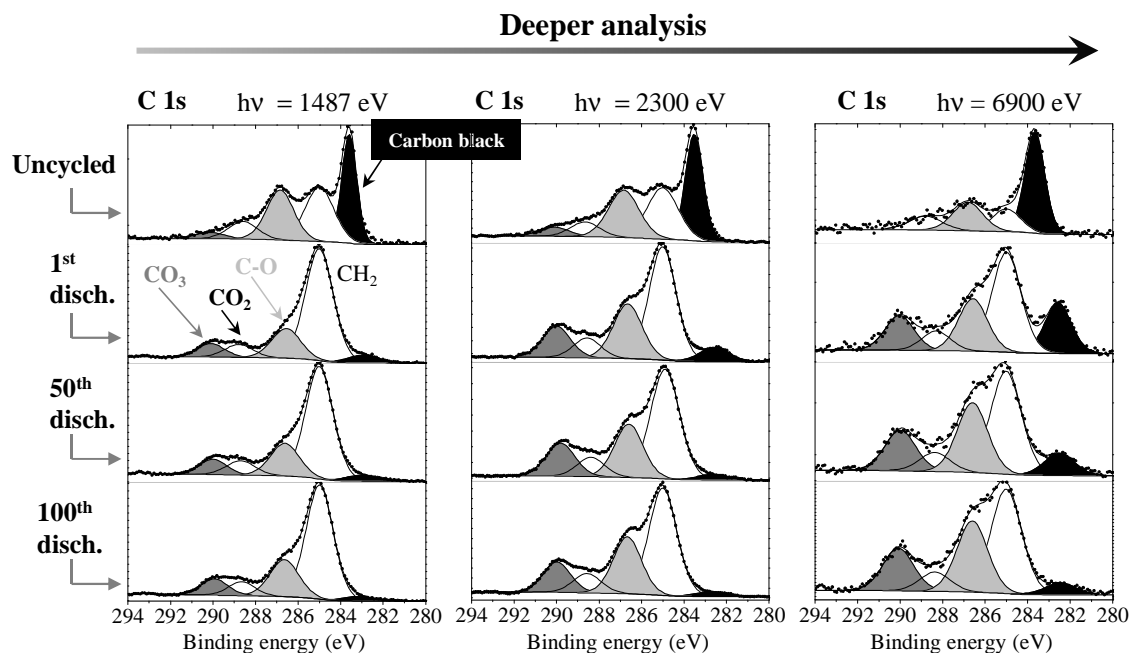
Figure III. 33 : C 1s spectra of the Si electrode soaked 5 days in the electrolyte (uncycled), and after the 1st, 50th and 100th discharges with an electrolyte containing LiFSI. Evolution as a function of the analysis depth.

Figure III. 33 shows C 1s spectra of the uncycled Si electrode (*i.e.* soaked 5 days in the electrolyte) and after the 1st, 50th and 100th discharges as a function of the photon energy, and thus of the analysis depth, from $h\nu$ = 1487 to 6900 eV.

We can observe similar features and evolutions as previously discussed for $LiPF_6$. Upon long-term cycling a gradual intensity decrease of the carbon black component is noted, illustrating a small increase of the thickness/covering by the SEI.

Considering carbonaceous compounds, we may observe that at given photon energy, the ratio between CH_2, CO, CO_2 and CO_3 peaks is maintained from the 1st to the 100th discharge, showing the stability of the composition in carbonaceous compounds within the SEI layer upon cycling. For a given cycle number, the intensity of the CH_2 peak (285 eV) decreases when the photon energy increases, showing this peak is partly assigned to hydrocarbon contamination located at the outermost surface of the SEI. The ratio between CO, CO_2 and CO_3 peaks is independent of either the cycle number or the analysis depth. This result shows the stability of the chemical composition of the SEI upon cycling and its homogeneity from its outermost surface to its deeper layers.

The similarity of the results obtained with $LiPF_6$ and LiFSI upon a long term cycling confirms the similarities reported after a single electrochemical cycle.

However, the inorganic part of the SEI is expected to be different and salt dependent regarding the chemical difference between $LiPF_6$ and LiFSI.

- *Inorganic species of the SEI*

The characterisation of the pure salt LiFSI was first carried out. The characteristic B.E. (eV) from F 1s, O 1s, N 1s, S 2p and Li 1s spectra of LiFSI are reported in Table III. 4. It was possible to fit F 1s, O 1s, N 1s and Li 1s spectra with only one single component and the S 2p spectrum with a sole doublet, all assigned to only one chemical environment, which confirms the high purity of the salt used. It should be noted that Li 1s, N 1s and O 1s binding energies are rather close to the values obtained for LiTFSI salt whereas binding energy values for F 1s and S 2p are quite different (shifts of - 0.7 eV for F 1s and +0.9 eV for S 2p) in relation with the existence of S-F bonds in LiFSI.

LiFSI peak	B.E. (eV)
F 1s	687.9
O 1s	533.2
N 1s	400.0
S 2p$_{3/2}$	170.3
Li 1s	56.8
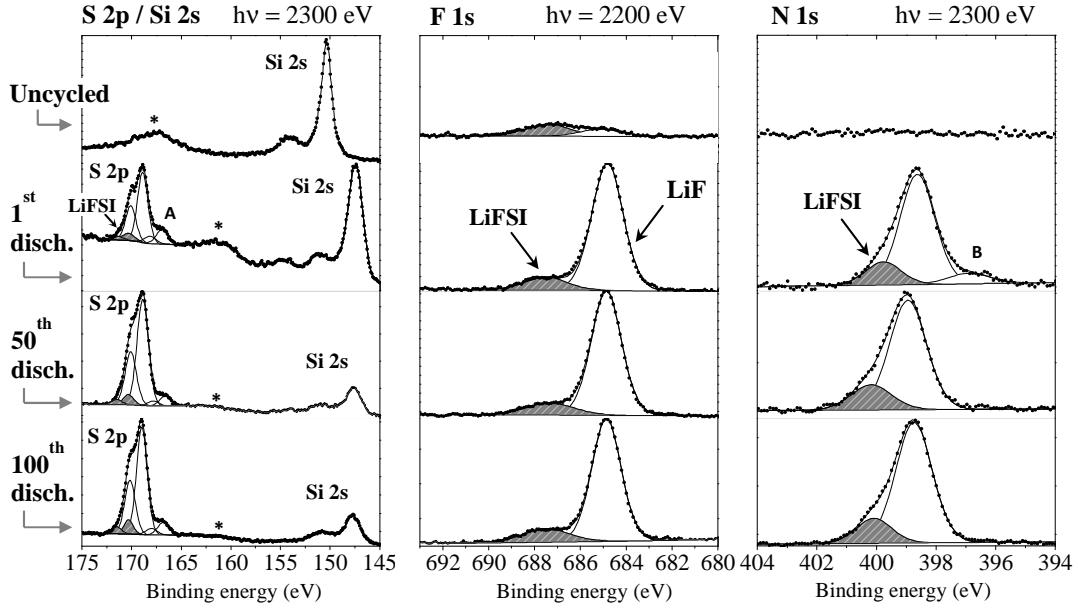
Figure III. 34: S 2p, Si 2s, F 1s and N 1s spectra of the Si electrode soaked 5 days in the electrolyte (uncycled), and after the 1st, 50th and 100th discharges with an electrolyte containing LiFSI (* = Si 2s plasmon sidebands).

Figure III. 34 shows the evolution of S 2p, Si 2s, F 1s and N 1s spectra of the Si electrode from the uncycled electrode (soaked 5 days in the electrolyte) after the 1st, 50th and 100th discharges. Si 2s and S 2p core levels signatures can be found in the spectra and we note the decrease of Si 2s/S 2p intensity ratio upon cycling, illustrating the gradual covering of the electrode surface by sulfur-containing species.

After the 1st, 50th and 100th discharges the S 2p spectrum of the electrode consists of three components. The main one (S 2p$_{3/2}$ at 169 eV) is attributed to a degradation product of LiFSI. The salt signature is detectable but very weak (S 2p$_{3/2}$ at 170.2 eV, grey in Figure III. 34). A third and weak component at low B.E. (peak A at ~167 eV) is also due to a degradation product of the salt but mainly results from the PES analysis itself (its intensity increases upon X-ray beam time exposure). Therefore it will not be considered in this discussion.

The F 1s spectrum of the uncycled electrode shows two weak components. The F 1s signature of LiFSI salt can be recognized at 687.8 eV, and another component attributed to LiF is observed at 685 eV, showing that a slight degradation mechanism of the salt occurs as soon as there is a direct contact of the electrode surface with the electrolyte.

After the 1st, 50th and 100th discharges the intensity of the F 1s peak assigned to LiFSI is very low and the main component is LiF, thereby the degradation mechanism is induced by electrochemical reaction at the surface of the electrode. After 50 and 100 cycles the surface (*i.e.* the 5-10 nm thick layer analyzed by in-house XPS) consists of ~10-11 % of LiF.

The N 1s peak of the uncycled electrode could not be distinguished from the noise due to its low photoionization cross section at $h\nu = 2300$ eV compared to the one of F 1s (2.5-3 times lower). After the 1st, 50th and 100th discharges the N 1s spectrum of the electrode consists of three components. The main one at ~398.7 eV corresponds to an undefined degradation product of the salt. The component assigned to LiFSI is rather weak (N 1s at 400 eV, grey in Figure III. 34), confirming the degradation mechanism discussed above. The third weak component, at low B.E. (peak B at ~397 eV) is a degradation product induced by X-ray beam exposure.

It is important to note that for all spectra of N 1s, F1s and S2p from the 1st to the 100th discharge, the ratio between LiFSI and its degradation compounds does not change upon cycling and thus the salt degradation mechanism occurs in the early first cycles (pre-cycling procedure).

To conclude this section, we have observed that the intensity ratios between the characteristic peaks of organic and inorganic species making up the SEI are independent of the cycle number, which shows the stability of its chemical composition upon cycling. Concerning the inorganic part, we have shown that it mainly consists of degradation compounds of the salt formed in the first cycles.

We will focus our analysis on the degradation mechanisms of the salt at the surface of the electrode.

1.3.4.3. Reactivity of LiFSI towards the electrode surface

1.3.4.3.1. PES study of the first discharge
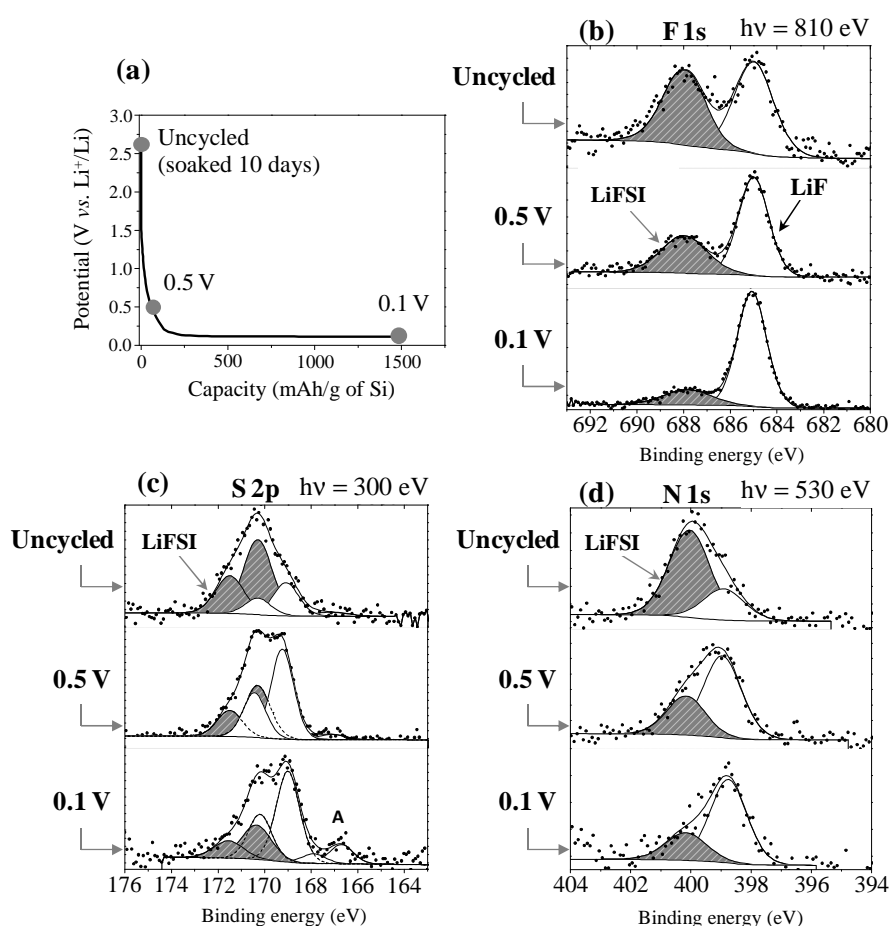
Figure III. 35 : (a) First discharge of a Li//Si cell using LiFSI salt (current rate 150 mA.g^{-1} of Si, no pre-cycling). The samples analyzed by PES are highlighted by grey points. (b) F 1s, (c) S 2p and (d) N 1s spectra of the Si electrode upon the 1st discharge.

The degradation mechanism of the salt seems to occur in the early steps of the electrochemical reaction. We have focused our study on the first discharge of the Si-based Li//Si cell (without any pre-cycling) to follow the formation of inorganic species composing the SEI and the degradation of LiFSI salt at the surface of the Si electrode.

Due to the very low thickness of the SEI at the first steps of the electrochemical reaction, and to avoid overlapping of the Si 2s plasmon sideband with S 2p spectrum, soft X-rays have been used (MAX IV, hν = 300-810 eV), with a fixed photoelectron kinetic energy of 130 eV which allows a very low analysis depth (~1-2 nm).

Figure III. 35 shows the evolution of F 1s, S 2p and N 1s spectra of the uncycled Si electrode (soaked 10 days in the electrolyte) and during the first electrochemical discharge at 0.5 V and 0.1 V $vs.$ Li$^+$/Li. The analyzed samples are highlighted by grey points in the electrochemical curve. Due to the very low analysis depth the F 1s, S 2p and N 1s PES spectra of the uncycled electrode are clearly and easily exploitable. They all show the presence of the salt LiFSI (grey) accompanied by a degradation product: F 1s spectrum shows the presence of LiF at 685 eV, whereas S 2p and N 1s spectra show the signatures of unidentified species (S 2p$_{3/2}$ at 169 eV and N 1s at 399 eV).

At 0.5V and 0.1V $vs.$ Li$^+$/Li, the same components are observed, but the intensities of LiFSI peaks decrease gradually with respect to the peaks assigned to its degradation compounds. This displays a reduction mechanism of LiFSI at the surface of the electrode taking place at the beginning of the first discharge. Note that spectra obtained after discharge at 0.1 V are similar to those obtained after 50 or 100 cycles. The additional component detected in S 2p spectra (peak A at ~167 eV) results from degradation of LiFSI under the X-ray beam.

As shown previously, the lower sensitivity of LiFSI towards hydrolysis has a beneficial impact on the electrochemical performances of Li//Si batteries. Concerning its sensitivity towards reduction, LiFSI appears to be more easily reducible than LiPF$_6$ at the surface of the electrode, but this does not perturb the good electrochemical behaviour. This behaviour is probably due to the formation of a protective layer at the surface of the electrode that prevents continuous reduction of the salt upon repeated discharges.

1.3.4.3.2. DFT calculations

DFT calculations have been performed to better understand the reactivity of LiFSI salt and its reduction products occurring upon discharge. The discussion related to these calculations is widely developed in paper IV and allows us to assume that reduction of the FSI$^-$ ion results in the break of S-F bonds. This is in good agreement with experimental PES observations showing that the amount of LiF increases upon the first discharge (*i.e.* reduction). Moreover, the S 2p spectra recorded after discharge (see Figure III. 35) have revealed the presence of a degradation compound with an S 2p$_{3/2}$ peak at 169 eV, which corresponds to a negative shift of -1.3 eV towards lower binding energy with respect to LiFSI. This is consistent with the loss of a very electronegative atom (fluorine) in the environment of sulfur. As a result, the reduction of FSI$^-$ at the electrode surface leads to the break of S-F bonds and to the formation of LiF.

1.3.5. Summary

We have clearly shown the beneficial role of the LiFSI salt to improve the electrochemical performances of Li//Si cells. This beneficial role is mainly attributed to the interfacial reactivity of the silicon electrode *vs.* the LiFSI-based electrolyte upon cycling. Especially, the much lower sensitivity of LiFSI towards hydrolysis with respect to $LiPF_6$ and its weaker tendency to form HF in the presence of traces of water is determinant.

Unlike $LiPF_6$, long-term cycling with LiFSI does result neither in the fluorination of the electrode surface to form SiO_xF_y species from the surface oxide SiO_2, nor in the dissolution of the surface lithium oxide Li_2O. Instead, a continuous reaction process of SiO_2 with lithium upon cycling leads to the increase of lithium silicate Li_4SiO_4 at the surface of the electrode. Therefore, the favourable interactions between the binder and the active material surface are preserved.

The passivation layer (SEI) contains an organic and an inorganic part as it is commonly observed for carbonate-based liquid electrolytes. The same carbonaceous species are observed as when $LiPF_6$ is used as salt but a lower amount of carbonate species is observed. A degradation mechanism of the LiFSI salt at the surface of the electrode could be evidenced, and this mechanism does not hamper the good operation of the battery. As it occurs right from the first discharge and because the amount of LiFSI degradation products increases only weakly after this first step, we believe these reduction products deposited at the surface of the electrode act as a passivation layer which prevents further salt reduction and preserves the electrochemical performances of the battery.

2. MnSn$_2$ electrodes

Tin is another element that can alloy with lithium but it suffers of a huge volume expansion upon lithium insertion (around 260% for Li$_{22}$Sn$_5$). One of the main strategies to reduce this expansion is the use of Sn-based intermetallics MSn$_x$, where M is a transition metal inactive used to buffer the volume expansion (see chapter I). Different tin intermetallics compounds such as FeSn$_2$, Ni$_3$Sn$_4$, CoSn$_2$, Cu$_6$Sn$_5$ and CuSn$_2$ have been proposed. Fewer studies about manganese compounds have been reported. Recently, studies were initiated on MnSn$_2$ electrodes. Electrochemical performances and detailed characterisations (*in-situ* XRD, *operando* Mössbauer spectroscopy, XPS and HAXPES) have been reported in papers IV and V. We focus here on the interfacial reactions occurring upon lithiation/delithiation of MnSn$_2$ electrodes with a step by step PES analysis during the first electrochemical cycle.

2.1. Characterization of the active material: MnSn$_2$

Firstly, XRD, Auger spectroscopy, in-house XPS and HAXPES have been used to characterize the pristine powder.

2.1.1. XRD
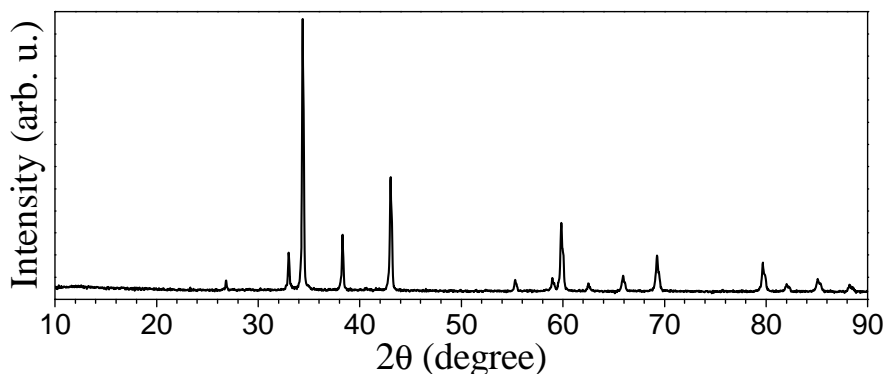
Figure III. 36 : X-ray diffraction patterns of MnSn$_2$

Figure III. 36 shows the XRD pattern of the pristine MnSn$_2$ materials used in this study. Bragg peaks of the XRD pattern can all be indexed to a primitive tetragonal type-structure (I 4/m c m space group) with a=6.63 Å and c=5.42 Å. Mn and Sn atoms are located at the 4*a* and 8*h* crystallographic sites, respectively. The Mn atoms are bonded to two Mn atoms at 2.71 Å and to eight Sn atoms at 2.84 Å forming quadratic antiprisms with basal planes in the bc plane. Each Sn atom has four Mn first-nearest neighbours at distances of 2.84 Å forming a square based pyramid and eleven Sn atoms at different distances between 3.03 Å and 3.52 Å. Rather narrow and symmetric Bragg lines are observed that indicate a good crystallinity of the MnSn$_2$ powder. There are no visible peaks due to βSn, or to oxides, which is a good indication of the purity of the material.

2.1.2. SEM and Auger spectroscopy
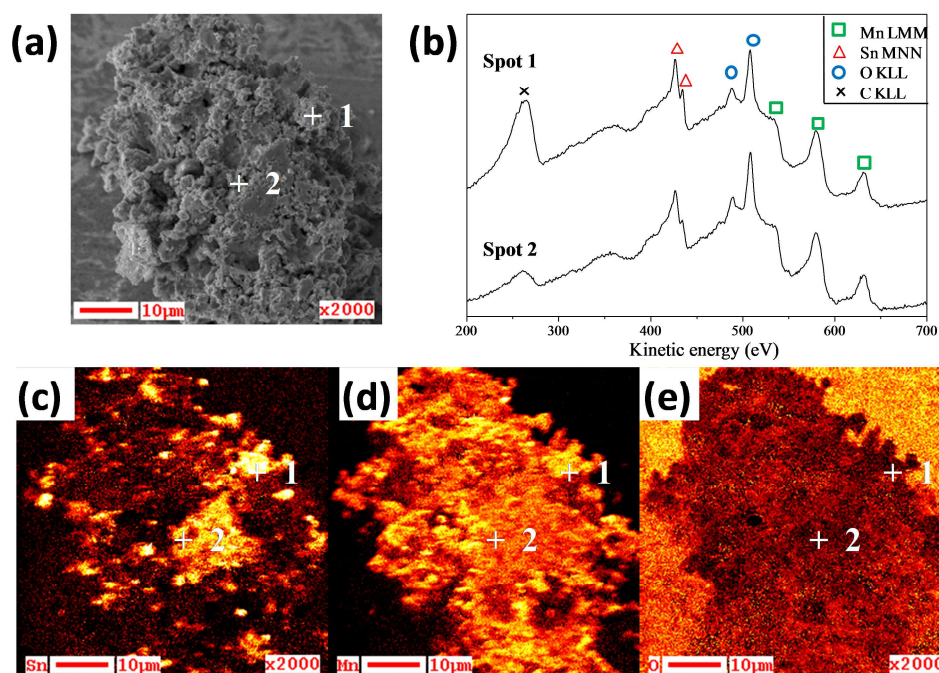
Figure III. 37 : (a) SEM image of a 40 μm diameter MnSn₂ aggregate; (b) Auger Electron Spectra (AES) of two selected ~20 nm diameter areas; (c), (d) and (e) Scanning Auger Microscopy (SAM) images of Sn, Mn and O elements, respectively, obtained by selection of their characteristic Auger kinetic energy signals.

The purity and homogeneity of the synthesized $MnSn_2$ powder at the surface was examined by Auger spectroscopy (AES) and elemental mapping on pristine $MnSn_2$ particles. Figure III. 37 shows: (a) SEM imaging of a 40 μm diameter aggregate; (b) the Auger electron spectra of two selected ~20 nm diameter areas; (c), (d) and (e) Scanning Auger Microscopy (SAM) images of Sn, Mn and O elements, respectively, obtained by selection of their characteristic Auger kinetic energies. In the AES spectra the three elements are easily recognizable by their Sn MNN (426 and 435 eV), Mn LMM (533, 580 and 631 eV) and O KLL (487 and 506 eV) main Auger peaks. Adsorbed carbonaceous species at the surface are also detectable by their C KLL peak. Mn and Sn SAM images (c) and (d) allow evidencing a non-uniform distribution of these two elements at the surface. Besides, the SAM image of oxygen shows no significant difference in the O KLL signal intensity, and therefore the intensity differences observed for Mn and Sn are not due to topographical effects of the surface, but actually to differences in the chemical composition at the surface. It is to be noted that these chemical heterogeneity only concerns the outermost surface of the particles, since bulk characterization of the material did not evidence unreacted metals nor separated oxide particles. However, this chemical state of the surface may have consequences concerning the reactivity of the electrode towards the electrolyte in a battery.

To complete the surface characterisation, PES analysis was carried out with two photon energies (hν = 1486.6 eV (in-house)) and 2300 eV (synchroton)).

2.1.3. PES
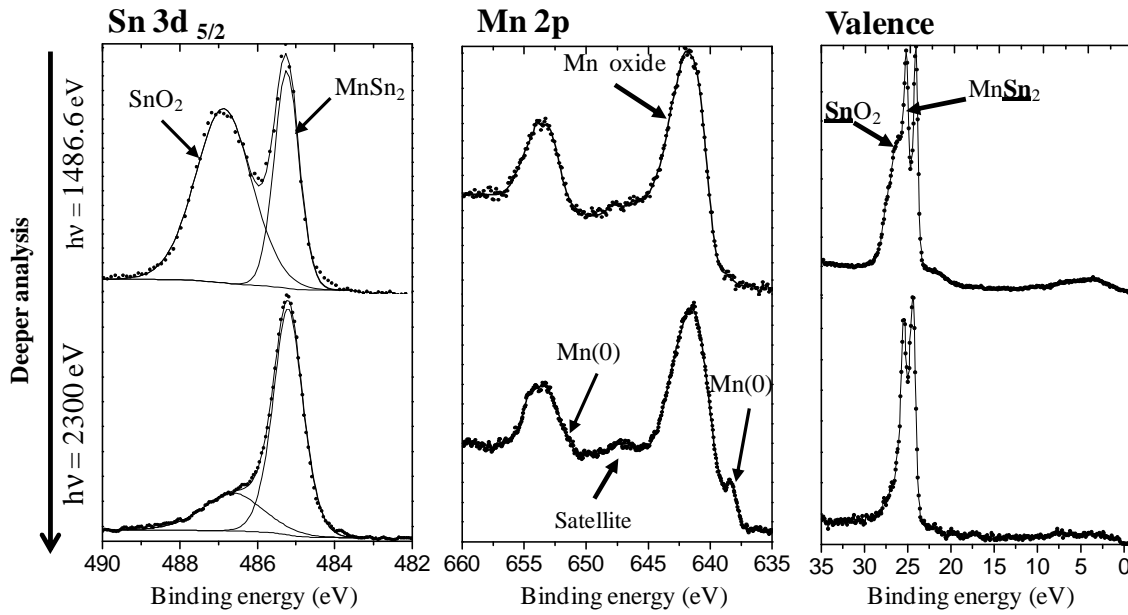
Figure III. 38 : Sn 3d$_{5/2}$ and Mn 2p core peaks and valence spectra of MnSn$_2$ shown as function of the analysis depth.

Table III. 5 : Binding energies (eV) and atomic percentages (%) of elements Mn, Sn, O and C from in-house XPS spectra of MnSn$_2$.

		MnSn$_2$
	B.E. (eV)	%
Sn 3d$_{5/2}$	485.2	4.2
	486.9	7.6
Mn 2p$_{3/2}$	641.2 + sat.	12.7
O 1s	530.4	17.7
	532.0	17.1
C 1s	285.0	20.9
	286.2	15.0
	289.6	4.8

The Sn 3d$_{5/2}$, Mn 2p core peaks and valence spectra of the pristine MnSn$_2$ powder are shown in Figure III. 38. The relevant binding energies and atomic percentages measured with in-house XPS (1486.6 eV) are reported inTable III. 5.

The Sn 3d$_{5/2}$ core peaks consists of two components. The first one, at 485.2 eV is assigned to metallic tin (Sn^0) of MnSn$_2$. The second, at 486.9 eV, is attributed to tin oxide SnO$_2$ (Sn^{4+}). When the photon energy increases (increase of the analysis depth), the relative proportion of SnO$_2$ decreases from 64% to 25% and this evolution illustrates the presence of tin oxide at the extreme surface of the sample.

The Mn 2p core peak displays a main peak at ~ 641.2 eV for Mn 2p$_{3/2}$ (653.2 eV for Mn 2p$_{1/2}$) assigned to a manganese oxide.

At the greatest analysis depth (hv= 2300 eV), a small component appears at low binding energy (638.2 eV) assigned to the metallic manganese located under the oxide layer. In agreement with the previous observations (elemental mappings), PES spectra confirm that manganese at the surface is mainly in its oxide phase.

In addition, the Mn/Sn ratio determined by XPS is higher than expected for MnSn$_2$. This is certainly due to the higher oxygen affinity of Mn explaining its segregation at the surface.

122

Finally, the valence spectrum shown in Figure 4 displays an intense signal at 23-28 eV with two peaks at 24.4 and 25.4 eV corresponding to the Sn $4d_{5/2-3/2}$ peak of $MnSn_2$. The broad peak observed at 26.4 eV not visible with the highest analysis depth (2300 eV) is assigned to the tin oxide.

To conclude, $MnSn_2$ samples obtained from ball milling + sintering process do not contain noticeable amounts of β-Sn, but Sn and Mn oxides can be detected at the surface of the particles. Secondary particles of several tens of microns are formed by aggregation of small well crystallized particles.

2.2. Reactivity of the pristine powder with the electrolyte
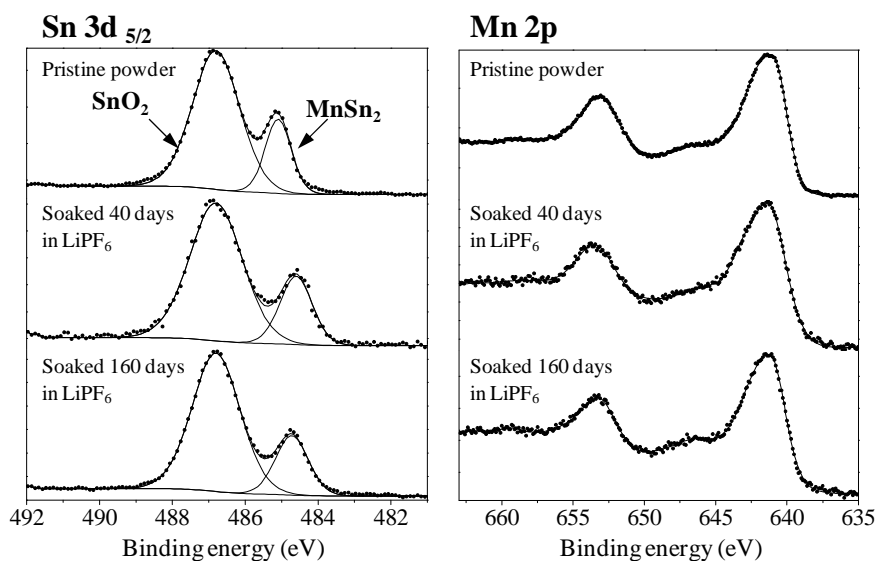
Figure III. 39 : Sn 3d$_{5/2}$ and Mn 2p spectra (in-house PES, hν = 1486.6 eV) of a pristine MnSn$_2$ powder and after contact with an electrolyte containing LiPF$_6$ (40 and 160 days)

Electrolyte containing $LiPF_6$ has shown to be reactive with pristine silicon electrodes by direct chemical contact. The identification of a fluorinated phase at the surface allows us to conclude to the reaction of the SiO_2 layer with HF (degradation product of $LiPF_6$).

A similar experiment was carried out to investigate the reactivity of the pristine $MnSn_2$ powder with both tin and manganese oxides at the surface. Figure III. 39 shows the Sn $3d_{5/2}$ and Mn 2p core peaks of pristine $MnSn_2$ powder after contact with an electrolyte containing $LiPF_6$.

After 40 and 160 days of contact of the $MnSn_2$ powder with the electrolyte, the overall shape of the Sn $3d_{5/2}$ spectra remains stable and no additional peak appears at ~ 488 eV (binding energy expected for tin fluorinated species). Moreover, no modification occurs to Mn 2p signal shape indicating even after 160 days no significant change in chemical environments. As the formation of a fluorinated phase has been clearly evidenced for silicon electrodes, these results suggest a difference in surface reactivity with HF for $MnSn_2$ powder.

Further work is necessary to complete these first results and understand these experimental observations.

2.3. Study of the 1ˢᵗ electrochemical cycle

2.3.1. Galvanostatic cycle
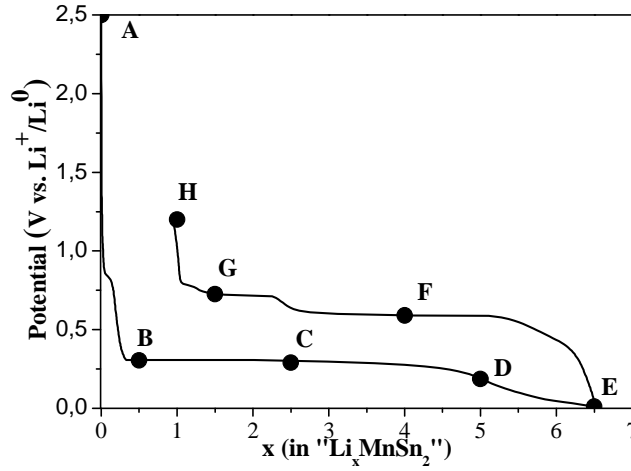
Figure III. 40 : First discharge/charge cycle of the MnSn₂/C composite electrode vs. Li⁰ cell.

Figure III. 40 shows the first galvanostatic discharge/charge cycle of a Li/ $MnSn_2$ electrochemical cell cycled at room temperature between 0.01 and 1.2V at C/10 rate. Points A-E of discharge (x = 0, 0.5, 2.5, 5 and 6.5 Li) and points F-H of charge (x = 4, 1.5 and 1 Li) correspond to the samples analyzed by XPS. Note that point A corresponds to an unsoaked composite electrode (90% $MnSn_2$ + 10% carbon black).

    The first discharge displays two parts. A first one from A to B (x=0.5 Li) where the potential quickly drops to 0.3V. This part is generally attributed to the reduction of the surface oxides by lithium in intermetallic alloys and the formation of the solid electrolyte interphase (SEI) is also expected to take place at this stage. The second part of the discharge is formed by a potential plateau at ~0.25V from B to E (x=6.5 Li).

    During charging, the potential curve shows two well-defined plateaus at ~ 0.6 V and ~0.7 V. This differs from other tin intermetallics like Cu_6Sn_5, Ni_3Sn_4, $CoSn_2$ and $FeSn_2$ that exhibit only one plateau. This also indicates that the mechanism upon charge does not correspond to a simple de-alloying process of the alloy formed upon discharge.

2.3.2. First discharge

2.3.2.1. XRD and Mössbauer results (Paper IV)

Variations of operando XRD patterns upon this first discharge have shown that the lithiation of $MnSn_2$ based anode does not affect the active species up to about 1 Li and then transforms $MnSn_2$ into Li_xSn nanoalloys.

    In order to obtain more information on electrochemically formed Li_xSn, [119]Sn Mössbauer spectroscopy has been used in operando mode. The existence of $MnSn_2$ at the end of discharge due to incomplete lithiation of the electrode has been observed. Mössbauer results have clearly shown that the reaction occurring upon discharge is:

$$MnSn_2 + 7\,Li \rightarrow Mn + Li_7Sn_2 \quad (1)$$
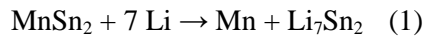
2.3.2.2. XPS
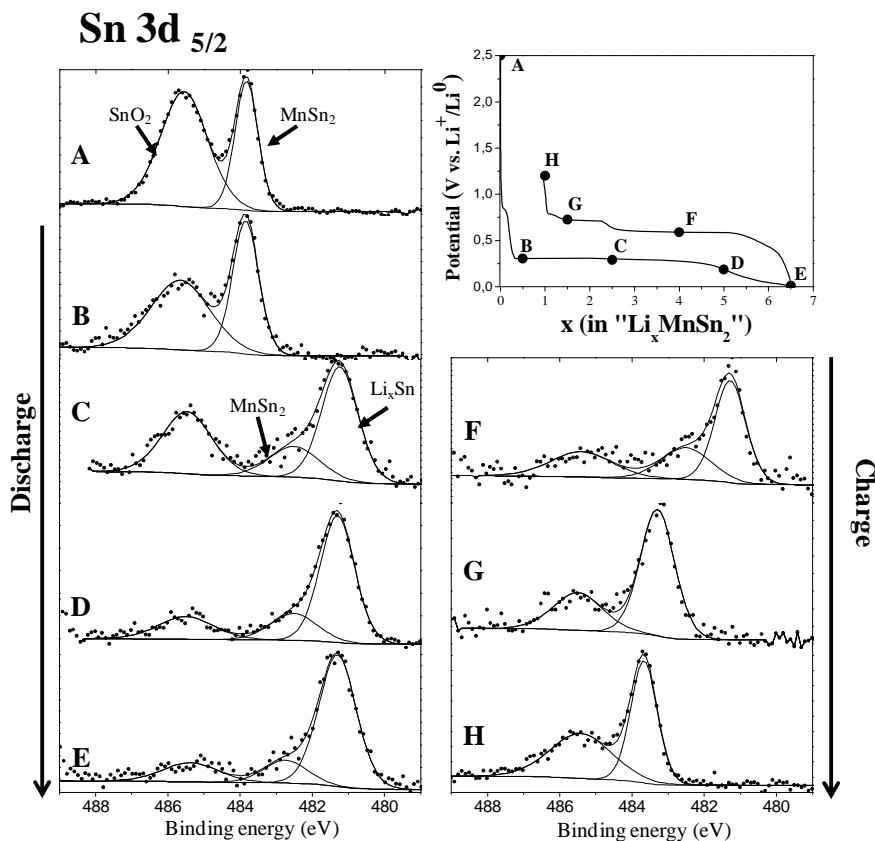
Sn 3d $_{5/2}$

Figure III. 41 : Sn 3d$_{5/2}$ spectra (in-house PES) of the MnSn$_2$/C composite electrode upon the first discharge/charge cycle.

Sn 3d$_{5/2}$ core peaks of the MnSn$_2$ electrode at the different electrochemical steps of the 1st cycle are reported in Figure III. 41. The Sn 3d$_{5/2}$ spectrum of sample A (MnSn$_2$ + carbon black) is similar to the one of the pristine powder (Figure III. 38) and consists of two peaks attributed to tin oxide (SnO$_2$) and to metallic tin: MnSn$_2$. From A to B (x=0.5 Li), the same components are observed but a clear decrease of the tin oxide component is noted in relation with the reduction of the surface oxide into metallic tin upon Li insertion.

These results suggest that the strong decrease of the potential at the beginning of the discharge is partially due to the reduction of the surface oxide, and that the Li-Sn alloying process has not started at this stage. This point will be developed below.

In the second part of the discharge, when the plateau is reached, from C to E (end of the discharge x = 6.5 Li), three components are observed and attributed to SnO$_2$ (~ 485.5 eV), to the formation of Li$_x$Sn alloy (~481 eV) and to the unreacted MnSn2 phase (483 eV). Indeed, shifts of the starting phase component towards lower binding energies due to differential charging effect are commonly observed. No gradual energy shift is observed for the Li-Sn component between 0.5 Li and 6.5 Li suggesting that no other Li$_x$Sn compound is formed during the alloying process. Such behaviour is different from the one observed for lithium reactions with Si-based electrode.

It is to be noted from sample C to the end of discharge (sample E) that MnSn$_2$/Li-Sn ratio only weakly changes.

At the end of the discharge (sample E), we can note that the component attributed to MnSn$_2$ is still detected confirming that the alloying reaction is not complete.

Moreover the MnSn$_2$/Li-Sn ratio is 17/83 which is rather close to the expected value for a 6 Li voltage plateau with respect to reaction (1)

2.3.3. First charge

2.3.3.1. XPS

Upon charge (Figure III. 41), on the 1st plateau (points F) we observe that the peak intensity of Sn^0 increases again due to lithium extraction from Li$_7$Sn$_2$. When the second plateau is reached, extraction of lithium is complete and we cannot detect any lithiated tin. SnO$_2$ and metallic Sn^0 are the only species present at the surface of the electrode.

Finally, from G to H, no change is observed in the Sn 3d$_{5/2}$ spectra suggesting that the delithiation is complete.

Figure III. 42 shows Li 1s/ Mn 3p spectra of the MnSn$_2$ electrode powder (A), after a discharge to x=0.5 Li (sample B), at the end of discharge (sample E) and at the end of charge (sample H).

Li 1s detected in Figure 42 originates from the SEI (mainly Li$_2$CO$_3$ at 55.5 eV and LiF at 56 eV) whereas Mn 3p is from the active material. The covering of the material by the SEI is associated with the disappearance/appearance of the manganese signature.

The evolution of Mn 3p peak shows the covering process of the SEI from B to E and its partial dissolution at the end of the charge (sample H).
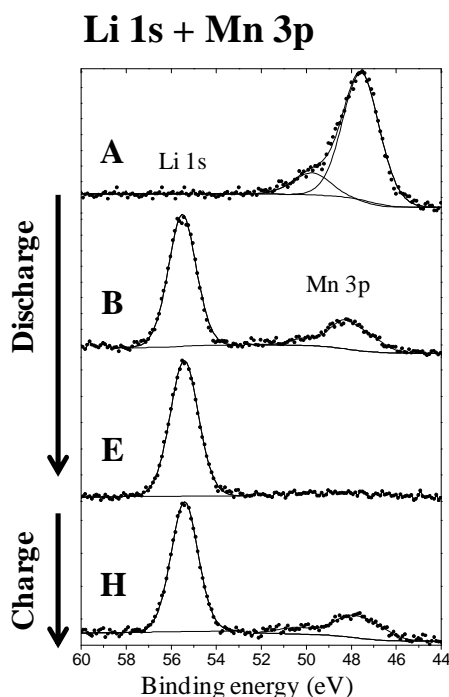
Li 1s + Mn 3p

Figure III. 42 : Li 1s/ Mn 3p spectra (in-house PES) of the MnSn$_2$/C composite electrode upon the first discharge/charge cycle.

2.3.3.2. Mössbauer results (Paper IV)

The results show that the first plateau is due to the delithiation of Li$_7$Sn$_2$ without the progressive formation of the Li$_x$Sn compounds or the direct transformation into MnSn$_2$ but probably with the formation of more complex metastable Li-poor Li-Sn and/or Li-Mn-Sn phases.

For the second plateau, the results indicate a direct transformation of the Li-poor tin based phases. At the end of charge, the Mössbauer spectrum is similar to that of bulk MnSn$_2$. At this step, the electrode is mainly formed of "magnetic MnSn$_2$" but also contains paramagnetic unreacted MnSn$_2$ and poorly lithiated Li-Mn-Sn phases.

2.3.4. Electrode/electrolyte interfacial reactions

2.3.4.1. SEI formation

2.3.4.1.1. Covering of the SEI
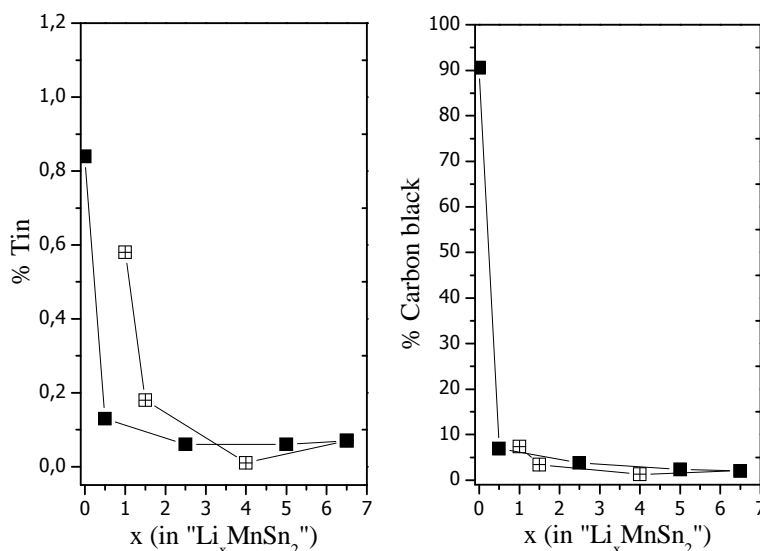
Figure III. 43 : Evolution of the atomic % of tin and carbon black determined from XPS spectra of the MnSn₂ composite electrodes during the first discharge/charge cycle (in-house XPS, 1484 eV) (dark squares: sample in discharge, open squares : sample in charge)

Figure III. 43 shows the evolution of the total amount of tin and carbon black measured at the surface of the MnSn$_2$ electrode from Sn 3d$_{5/2}$ and C 1s spectra upon the first electrochemical cycle (hν = 1486.6 eV). Values are given as traditional atomic %.

Both tin and carbon black are species found in the composite electrode but not as SEI components, consequently, the atomic % of these species are good indicators for the increase (or decrease) of surface thickness/covering of the electrode particles by the SEI.

At the beginning of the first discharge (between 0 and 0.5 Li), the amount of tin and carbon black dramatically fades and then slowly decreases until the end of the discharge to 0.07% and 2% respectively. This decrease results from the formation of the SEI covering the particles of the negative electrode and this formation mainly occurs at the beginning of the discharge (A to B in Figure III. 40).

2.3.4.1.2. Composition
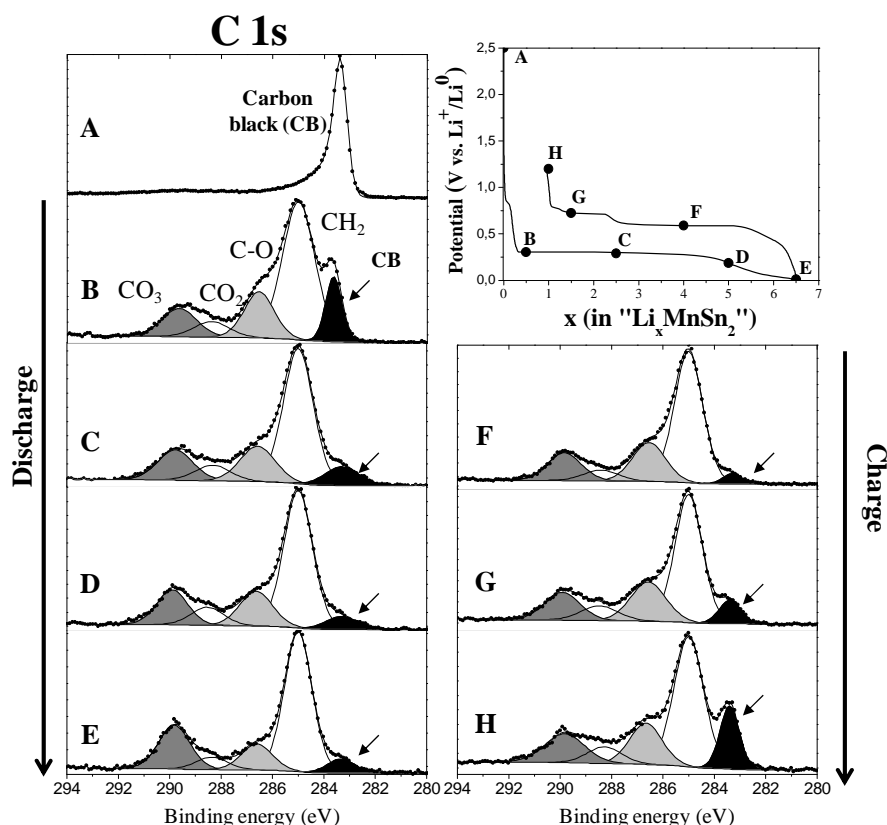
Figure III. 44 : C 1s spectra (in-house PES) of the MnSn₂/C composite electrode upon the first discharge/charge cycle.

Figure III. 44 shows the evolution of the C 1s core peak of the $MnSn_2$ electrode upon the first discharge/charge cycle (hν = 1486.6 eV).

The spectra of the pristine electrode (sample A) consists of an intense narrow peak at ~ 283.5 eV assigned to carbon black. No peak relating to any kind of surface layer can be detected at this stage.

At the beginning of discharge (x=0.5 Li, sample B in Figure III. 44), the formation of the SEI is already partly achieved. The peak attributed to carbon black (in black in Figure III. 44) is not the only one observed, and new carbonaceous species have been deposited at the surface. The overall shape of the C1s is very similar to the spectra observed on Si-based electrode and discussed at the beginning of this chapter. Note that the carbonaceous species found in the SEI are due to the electrochemical degradation of the solvents present in the electrolyte, therefore, the same chemical species are commonly found for the SEI formed at the surface of other negative electrodes as graphite, Si-based materials or Sb-based intermetallic electrodes. These species corresponds to carbonates (Li_2CO_3 and/or lithium alkyl carbonates $ROCO_2Li$) but oxalates and polyethylene oxide (PEO: $(-CH_2-CH_2-O-)_n$) may also be found in the SEI.

During this first cycle, the overall shape of C 1s peaks remains almost unchanged from x=0.5 Li to the end of the cycle. This indicates that the composition of the SEI is rather stable over the first discharge/charge cycle. Especially the amount of carbonates is rather stable and fluctuates between 37 and 44% of the chemical composition of the SEI.

Figure III. 45 : O 1s, F 1s and P 2p spectra (in-house PES) of the MnSn₂/C composite electrode upon the first discharge/charge cycle. A: pristine powder, B: x=0.5Li, E: end of discharge, H: end of charge.

The O 1s, F 1s and P 2p spectra of the MnSn$_2$ electrode powder (A), upon the discharge (x=0.5 Li (B)), at the end of the discharge (E) and at the end of the charge (H), are reported in Figure III. 45.

The O 1s spectrum of sample A consists of one main peak at 530.4 eV assigned to the surface tin and manganese oxide species and an additional peak at 532.0 eV attributed to oxygenated species adsorbed at the surface of the pristine electrode. No signal is observed for F 1s and P 2p core peaks because sample A has never been in contact with the electrolyte.

After reaction with 0.5 Li, SEI is already formed as we have shown with the analysis of the C 1s core peak: various oxygenated species are present on the particle surfaces and in the SEI layer. The O 1s spectrum consists of a main component at 531.7 eV and a component of low intensity at higher binding energy (~533.5 eV). These two signatures correspond to carbonates, alkyl carbonates and other organic species commonly found in SEI with carbonates solvents. Similar species have been observed on surfaces Si-based electrodes surfaces. It is important to note that the peak relating to tin and manganese oxide disappears totally. According to the thickness of the SEI and its rich nature in oxygenated species, the signature of the oxides of the pristine material might not be detected. The reduction process of surface tin oxide has also to be considered.

At the end of the discharge (E) and of the charge (H), the same two main peaks are observed. At the end of the discharge (E) the signature of Li$_2$O (~528.2 eV) resulting from the reduction of tin oxide can be detected. The reduction process can be written according to the following equation:

$$SnO_2 + 4Li^+ + 4e^- \rightarrow Sn^0 + 2Li_2O$$
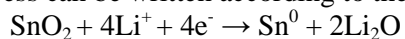
Li$_2$O is formed upon discharge and disappears during charge as for Si.

The F 1s spectra consist of two peaks at 684.7 eV (in white) corresponding to lithium fluoride (LiF), a product of the degradation of LiPF$_6$ and at 686.8 eV (in grey) attributed to PF$_6^-$ anions taking part in the SEI composition. The overall shape of the F 1s spectra is stable over the whole electrochemical cycle and the measured amount of LiF remains rather low (between 1 and 3%).

The P 2p spectra also consist of two peaks: a first one at 137 eV (in grey) attributed to the PF$_6^-$ anions, and a second at 133.7 eV assigned to phosphates which are commonly found in SEI layers using similar electrolytes and resulting from the degradation LiPF$_6$. As previously, the overall shape of the spectra is stable during the 1st electrochemical cycle of the cell.

Valence spectra of the MnSn$_2$ electrode measured at the different electrochemical steps are reported in Figure III. 46.

The spectrum of sample A is rather similar to that of the pristine MnSn$_2$ powder with the presence of the core peak Sn 4d. The two narrow peaks are assigned to MnSn$_2$ and to the SnO$_2$ component. The shape of the experimental curve from 20 eV to 0 eV is typical of a carbon black signature.

At the beginning of discharge ($x = 0.5$ Li), the Sn 4d core peak starts to be hidden by additional peaks due to the formation of fluorinated and oxygenated SEI compounds. For sample C, the Sn 4d signal of the electrode active material has totally disappeared.

During the charge phase, the Sn 4d signal reappears for sample G suggesting a partial dissolution of the SEI.

If we exclude the Sn 4d core peaks, the other characteristic features are rather stable upon cycling, which confirms that the composition of the SEI does not significantly change once it is formed. Typical peaks from LiF and Li$_2$CO$_3$ can be recognized in these spectra thanks to previous studies.[355] The peak observed at about 29 eV is characteristic of LiF. The main peak at around 24 eV and the three other peaks at 13, 11, and 6 eV are assigned to Li$_2$CO$_3$.
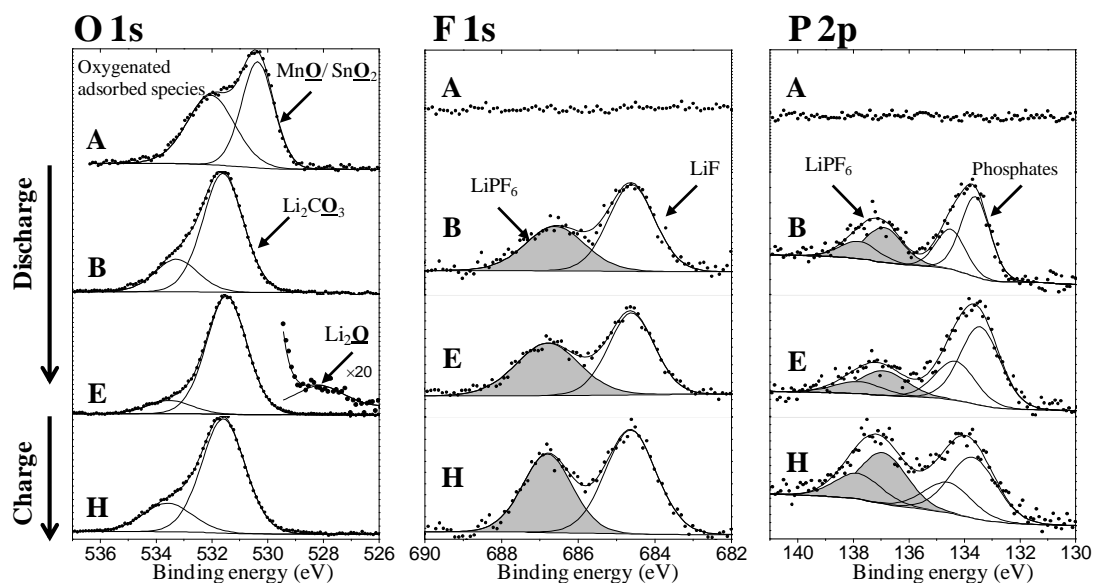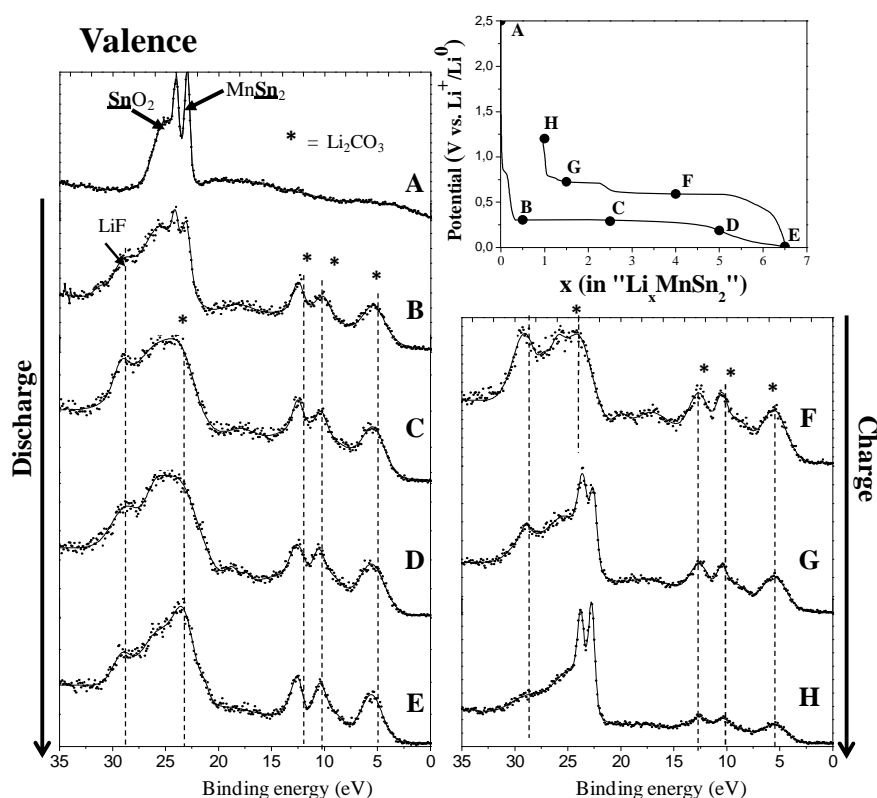

**Figure III. 46 : Valence spectra (in-house PES) of the MnSn$_2$/C composite electrode upon the first discharge/charge cycle.**

2.4. Summary

The careful study of the pristine $MnSn_2$ powder and the step by step analysis of the first electrochemical cycle of a $MnSn_2$ negative electrode cycled *vs.* Li^0 have led to the main conclusions listed below:

- Tin and manganese oxides are present at the extreme surface of the particles and do not react with the electrolyte by simple contact.
- Formation of the SEI occurs at the beginning of the first discharge. Mainly formed after the insertion of 0.5 Li, the SEI slightly increases in thickness until the end of the discharge.
- Gentle dissolution of the SEI appears at the end of the charge. This phenomenon is more important and pronounced on the surface of the active material than on the carbon black additive. After the first electrochemical cycle, the SEI layer composition is very stable with the same chemical species as previously observed for a graphite or Si-based electrode in similar conditions.

Concerning the Li insertion/des-insertion into $MnSn_2$:

- Between 0 and 0.5 Li, the reduction at the surface of tin oxide SnO_2 is observed resulting in the formation of Li_2O until the end of the discharge and its disappearance upon charge.
- In addition, Mössbauer spectra have revealed that the voltage plateaux could be attributed to complex electronic and structural mechanisms. Lithium insertion into $MnSn_2$ during the discharge plateau leads to the formation of a nano composite consisting of the Li-Sn alloy Li_7Sn_2 and of Mn nanoparticles. These Mn nanoparticles are immediately oxidized at their surface, by reaction with oxygen from the solvent molecules or from the pristine $MnSn_2$ surface oxide layer.

  Lithium extraction from this nano composite during the first charge plateau leads to the delithiation of Li_7Sn_2 and the formation of Li-poor Li-Sn and/or Li-Mn-Sn phases, without recovery of $MnSn_2$. During the second charge plateau, further de-lithiation leads to the formation of magnetic $MnSn_2$ particles and to our knowledge it is the first time such a mechanism is observed in tin based intermetallic electrode materials due to electrochemical reactions with Li.

Concluding remarks and perspectives

This thesis has been an effort to improve fundamental knowledge of interfacial mechanisms occurring during cycling of silicon and tin-based electrodes for Li-ion batteries.

A unique approach coupling in-house X-ray photoelectron spectroscopy and synchrotron PES using both soft and hard X-ray has been successfully used to provide detailed information about the repartition of chemical species at the surface of electrodes. The results highlight the interest of compositional profiles developed as a function of depth from the interface.

For silicon-based electrodes, interfacial mechanisms (reaction of the surface oxide, Li-Si alloying process, SEI formation) occurring upon and beyond the first lithiation/delithiation cycle have been investigated with the classical salt $LiPF_6$.

When the SEI has been formed (mainly during the first discharge), its chemical composition and its covering properties are stable during the subsequent cycling of the electrode. The chemical composition seems to be quite homogeneous within the SEI layer especially considering the inorganic compounds (LiF, $LiPF_6$, phosphates) and small fluctuations at the outermost surface are observed regarding the organic part (oxygenated and carbonaceous species).

Reaction of lithium with the surface SiO_2 layer leads to the formation (reversible during the first cycles) of Li_2O and to the irreversible formation of Li_4SiO_4 whereas, deeper inside, Li reacts with Si to form the Li_xSi alloy, with partial reversibility.

We have also illustrated the crucial importance of how the cycling procedure influences the overall surface morphology of the electrode.

Upon long-term cycling, the results have clearly evidenced the formation of fluorinated species (SiO_xF_y, $y \leq 3$) appearing at the interface between the Si particles and the SEI. This phase also appears by simple contact of the electrolyte with a pristine electrode upon time. Combining these observations, it is possible to explain the formation of such a phase pointing out the role of HF resulting from $LiPF_6$ degradation.

It is worth noting that the fluorinated silicon phase modifies the favorable interactions between the polymer binder (CMC in our case) and the active material surface and thus contributes to the capacity fading of the battery.

An alternative salt LiFSI more stable and less sensitive towards hydrolysis than $LiPF_6$ has been successfully used to improve the electrochemical performances of the Si/C/CMC//Li half-cells.

Upon the first discharge, the same reactivity of Li with the SiO_2 layer and Si, as previously described, is observed.

However, upon a long-term cycling, the results have revealed that LiFSI allows avoiding the fluorination process of the silicon particles as the dissolution of Li_2O resulting in a different surface chemistry compared to $LiPF_6$. Such differences are strong arguments to explain the better electrochemical behaviour upon cycling of Si//Li cells using LiFSI with respect to $LiPF_6$.

We have also investigated the SEI chemical features with this new salt. As for $LiPF_6$, its composition appears dominated by solvent degradation products, but with a lower amount of carbonate species. At the very beginning of the first discharge, a LiFSI reduction process occurs that leads by breaking of S-F bonds, to the formation of LiF. As no further amount of LiFSI degradation

products is observed after this first step, we assume that these degradation products act as a passivation layer.

These original results should stimulate other detailed SEI studies using this new salt to address the dependence on different factors usually affecting properties of the SEI.

In this thesis, a new tin-based intermetallic compound ($MnSn_2$) has also been studied. The simultaneous presence of two tin and manganese oxide environments has been evidenced at the extreme surface of the particles.

The results obtained during the first electrochemical cycle of $MnSn_2$//Li half-cells using $LiPF_6$ as salt have revealed similarities but also differences with Si based electrodes.

Indeed, the SEI chemical features are similar, Li reacts with SnO_2 layer to form Li_2O and the process is reversible upon charge.

However, after long soaking, no fluorinated species due to the reaction of the surface oxides with HF has been evidenced contrary to Si based electrodes, pointing out surface reactivity differences. Further work is necessary to understand and rationalize these experimental observations.

By the experimental method used (i.e., nondestructive depth-resolved XPS analysis by variation of the X-ray energy) and the results obtained in this thesis, we have illustrated the need for detailed in depth characterizations to properly understand interfacial mechanisms.

Based on these results, the following approaches are suggested:

-   Other investigations are necessary to further improve and understand interfacial properties of silicon particles. The selection of binders has significant impact on the cycle life and further research is needed on the use of new binders not requiring water as PAA or alginate.The dependence on the electrolyte salt has been highlighted and exploration of other electrolyte salts with lower fluorine contents and their possible decomposition products could further improve both performance and safety issues.

-   Several aspects of the complex surface chemistry of tin compounds remain to be explored. Various Sn based intermetallic compounds have drawn much attention in recent years but further improvement in material design and fundamental knowledge of Li-Sn alloying reactions are needed. In depth PES analysis could be used to extract more information and contribute to the overall understanding of lithiation/delithiation mechanisms.

-   In parallel with an increasing access to synchrotron radiation facilities, the use of complementary depth profiling methods as those very recently developed (using C_{60}^+ or Ar_n^+ ion sources) will surely enhanced the role of photoemission for surface/interface studies in the field of electrochemical energy storage.

Sammanfattning på Svenska

Att förstå gränsytor, kan det göra batterier bättre?

I dagens så kallade litiumjon batterier för mobiltelefoner, laptops och annan bärbar utrustning används grafit som den negativa elektroden och en litiuminnehållande metall-oxid som den positiva. Detta är ett väl fungerande uppladdningsbart batteri som innehåller mest energi av alla uppladdningsbara som just nu finns i användning. Trots detta behöver vi kunna lagra ännu mer energi i samma batterivolym för att vara riktigt nöjda. Batterierna är också för dyra och innehåller metaller som visserligen återvinns men som det inte finns så gott om. Därför försöker forskare ständigt föreslå och studera nya material för positiva och negativa elektroder.

Om grafit byts ut mot metaller som kan legera med litium kan det innebära en ökning av batteriets kapacitet med ca 20%. Det finns flera metaller och halvledare som kan legera med litium och de finns i beskrivna i figur 1. De två viktigaste ur batterisynpunkt är kisel (Si) och tenn (Sn). Båda dessa metaller kan legera med maximalt 4 litiumatomer. Allra effektivast är kisel då det också är en lättatom och det finns gått om kisel i jordskorpan.
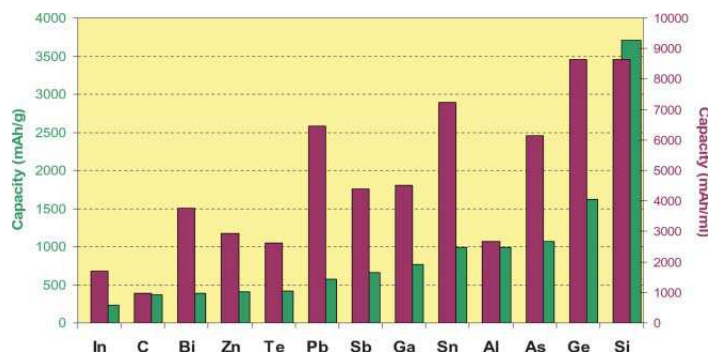
Figur 1. Kapaciteten hos olika metaller som kan legera med litium. Den röda stapeln visar den volymetriska kapaciteten och den gröna den gravimetriska.

Denna avhandling handlar om kisel och tenn som negativa elektrodmaterial i litium-jonbatterier. Det finns framförallt en svårighet att hantera när man vill använda partiklar av kisel eller tenn i batterier. När litium legerar sker en stor volyms-förändring. Partiklarna ökar ca 358% (tenn-litium) och 323% (kisel-litium) i storlek. Det finns flera sätt att komma förbi detta. Man kan använda nano-partiklar men det leder till andra problem som t ex agglomerering av partiklarna. Man kan använda glaser eller "buffra" den legerande metallen med metaller som inte legerar med litium (kopper, nickel eller järn är några exempel som har prövats) eller man kan välja mellan vilka potentialgränser som man cyklar batteriet. Ett fjärde sätt är att arbeta med ett bindemedel som klarar volymsexpansionen.

Den här avhandlingen tar fasta på ytterligare en frågeställning. Hur reagerar de vanligaste elektrolyterna med ytan på kisel och tennpartiklar? . En elektrolyt måste man ha i ett batteri. Elektrolyten ska leda positiva och negativa joner men inte elektronerna som behövs för att driva våra verktyg och leksaker. En typisk elektrolyt för ett litiumbatteri är ett organiskt lösningsmedel som innehåller ett litiumsalt.

Avhandlingens frågeställningar är:
- Hur ser kemin ut i gränsytan mellan elektrod (kisel eller ten) och elektrolyten?
- Vilken påverkan har elektrolyten på batteriets cyklingsprestanda?

- Sker det några förändringar när man cyklar batteriet under lång tid?
- Hur påverkas denna gränsyta om man byter salt?
- Går det att djupprofilera genom gränsytan ner i kisel- respektive tennpartiklarna?
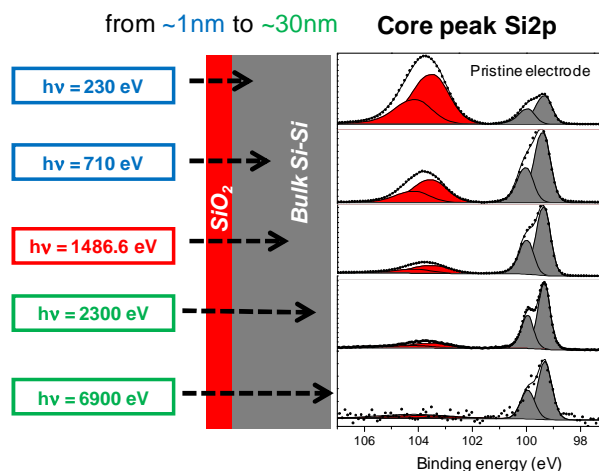
Figur 2. Ytan på en kiselpartikel som undersökts med fotoner med olika energi. Den röda toppen är kiseldioxid och den grå är kisel.

För att svara på dessa frågor har ett antal litiumbatterier gjorts med framförallt kisel uppblandad med nano-kol (kimrök) och det just nu kända bästa bindemedlet baserad på cellulosa. Batterierna har gjorts med två olika elektrolyter som bara skiljer sig åt vad gäller litiumsaltet. I det ena fallet är det LiPF$_6$ som är standard i kommersiella batterier. I det andra fallet är det saltet LiFSI (den kemiska formeln är LiN(SO$_2$F)$_2$). När det gäller tenn har vi använt oss av strategin att blanda ut tenn med en metall som inte legerar med litium. Vi har gjort en så kallad intermetall. Här har vi också gjort elektroder och satt samman batterier som har cyklats och testats.
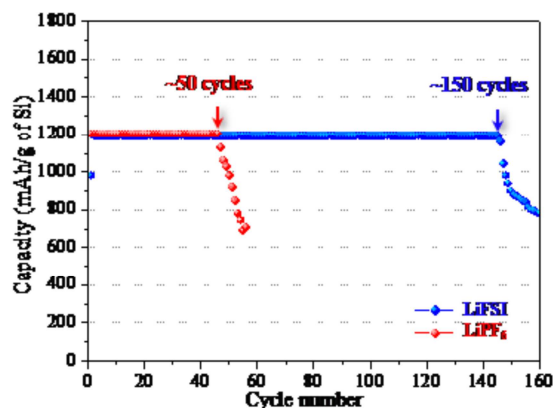
Figur 3. Kiselelektroder som har cyklats med elektrolyt som innehåller antingen LiPF$_6$ eller LiFSI.

De analyser som har genomförts på gränsytorna mellan kisel och elektrolyt respektive en mangan-tenn legering och elektrolyt är baserade på en metod som kallas fotoelektronspektroskopi. Genom att belysa provytan med fotoner slås elektroner ut från provet. Hastigheten hos dessa elektroner och hur många de är kan mätas upp och ger information om den kemiska omgivningen för varje atomslag som finns i provet. Det går t ex att skilja mellan energin för rent kisel och kisel som har reagerat med syre och bildat kiseldioxid. Det går också att bestråla ytan med fotoner som har olika energi. På så sätt kan den djupprofil uppmätas. Ett exempel på det finns i figur 2. I figuren visas att om man har låga fotonenergier kan man framförallt se kiseldioxiden på ytan. Om man ökar fotonenergi ser man längre in i provet och ser också kisel. Om man har riktigt höga energier vilket är en ovanlig mätmetod med några få utrustningar runt världen vid sk synkrotroner så kan man se kiseldioxiden som ett tunnt skikt på ytan av kisel. Dessa mätningar har när det gäller låga energier utförts vid MAX II synkrotronen i Lund och när det gäller höga energier utförts vid BESSY i Berlin.

De viktigaste resultaten från mätningarna är samman-fattade i figurna 3, 4 och 5. Figur 3 visar hur mycket bättre ett batteri cyklar om man har LiFSI i elektrolyten istället för LiPF$_6$. Figur 4 visar att när kiselelektroder cyklas i batterier med LiPF$_6$ så reagerar kiseldioxidytan med fluoratomer från saltet. Mer och mer av fluorföreningar bildas under cyklingen. Figuren visar också att när rena kiselpartiklar lagras i elektrolyten bildas också fluorföreningar. Om man bara cyklar en kort tid och bildar ett ytskikt som innehåller kolföreningar (symboliseras av det blå skiktet i figuren) så skyddar detta ytan från bildandet av fluorföreningar. Detta pekar på att om man tillsätter ett filmbildande additiv i elektrolyten så skulle man kunna cykla LiPF$_6$-baserade elektrolyter bättre än det renodlade systemet. Resultaten med LiFSI som jämförs i Figur 5 med de från LiPF$_6$ visar att det inte bildas några fluorföreningar. Istället får vi ett kolinnehållande skikt som växer till med antalet cykler. Mangan-tenn legeringen visar på liknande sammansättning för det kolbaserade lagret på ytan av elektroden som man finner också på kisel. Här är ytan inte alls lika känslig för LiPF$_6$ saltet utan de små mängder av tennoxid som finns på ytan är stabil.
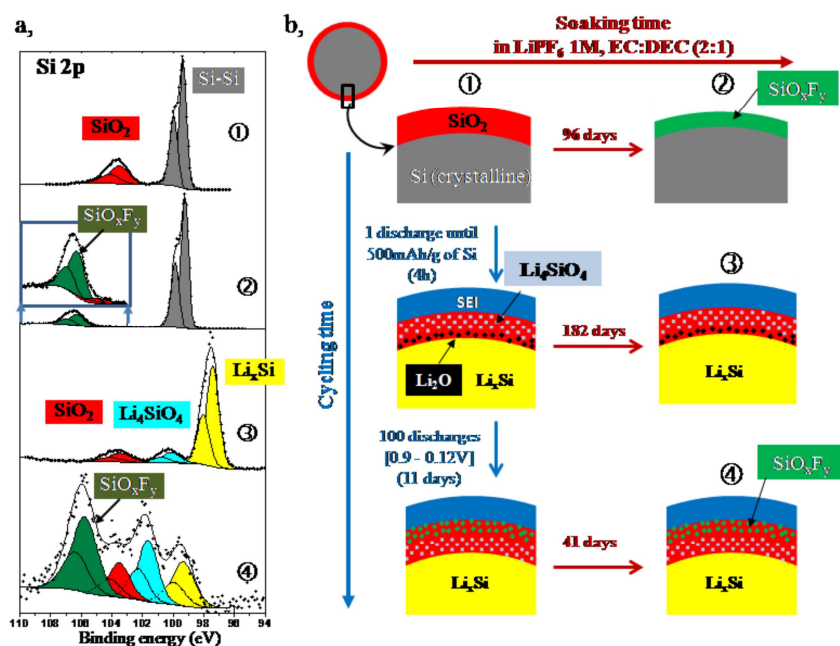
Figur 4. Kiselelektrod som har lagrats eller cyklats i elektrolyt som innehåller LiPF$_6$. I figur 4a visas spektra från de olika situationerna beskrivna i figur 4 b.

Dessa resultat visar på två viktiga saker: 1) elektrolytens sammansättning påverkar livslängden och cyklingsbarheten hos ett litiumbatteri och 2) den ansats som detta arbete har valt för att studera komplexa elektroders gränsytor fungerar för att ge tillförlitlig information om vad som händer på nano-meternivå i batteriet.
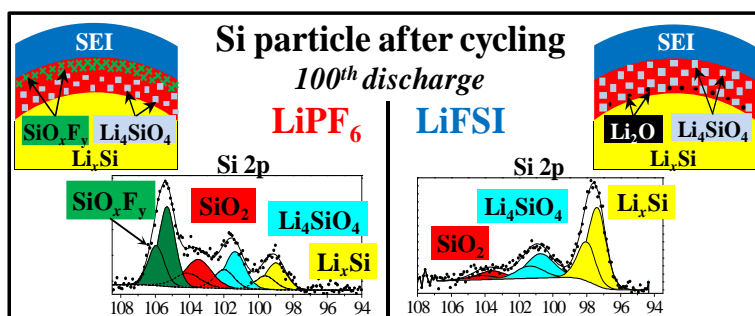
Figur 5. En jämförelse av ytan på kiselelektroder som har cyklat i LiPF$_6$ eller LiFSI.

Résumé en Français

Mieux comprendre les phénomènes d'interfaces pour concevoir des batteries plus performantes?

Les efforts de recherche importants engagés dans le secteur des accumulateurs Li-ion ont rendu possible le formidable essor de l'électronique portable (téléphones, ordinateurs, appareils photo numériques, etc.). Les enjeux actuels visent à accéder à des performances compatibles avec les nouvelles perspectives du marché (voitures électriques, hybrides, énergies renouvelables intermittentes, etc.). D'importants défis doivent être relevés en termes de performances accrues du point de vue énergétique, de durée de vie et de sécurité tout en répondant aux contraintes de coût et environnementales. Dans ce contexte, l'accumulateur le plus efficace et le plus prometteur est l'accumulateur Li-ion. Son principe repose sur la restitution sous forme électrique de l'énergie stockée sous forme chimique grâce à des réactions rédox ayant lieu aux électrodes avec transfert d'ions Li^+ (via l'électrolyte) et d'électrons (via le circuit extérieur). Un accumulateur Li-ion est constitué d'une électrode positive et d'une électrode négative, généralement des matériaux hôtes pour les ions lithium, et séparées par un électrolyte conducteur ionique mais isolant électronique et typiquement constitué d'un sel de lithium dissout dans un mélange de solvants carbonatés.

Un système type actuel est à base de graphite à l'électrode négative et d'un oxyde métallique lithié du côté de l'électrode positive ; cependant de nombreuses études sont menées sur de nouveaux matériaux dans le but d'adapter les performances des accumulateurs aux futures applications.

Une famille de composés constituée de métaux et semi-métaux formant avec le lithium un alliage est actuellement une alternative intéressante aux électrodes négatives à base de graphite. Comme illustré en Figure 1, les alliages Li-M présentent une capacité bien supérieure à celle du graphite (372 mAh/g). Le silicium (Si) et l'étain (Sn) notamment, semblent être les éléments les plus attractifs et peuvent accommoder jusqu'à 4 atomes de lithium par atome ($Li_{3.75}Si$ et $Li_{4.4}Sn$), augmentant considérablement la capacité théorique (3578 mAh/g et 994 mAh/g, respectivement). De plus, le silicium présente l'avantage d'être un constituant très léger, abondant et bien moins coûteux que ces éventuels concurrents.
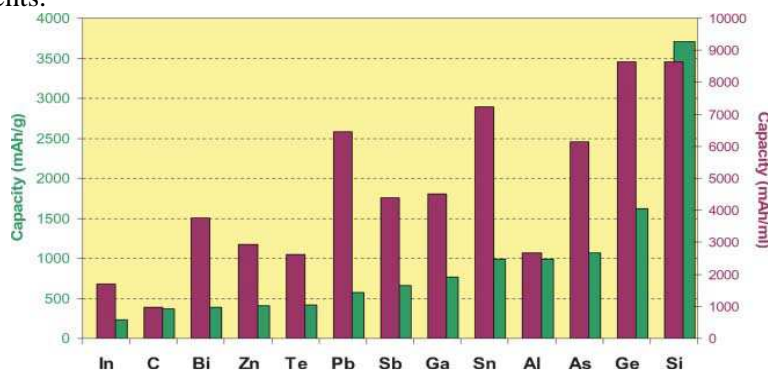
Figure 1 : Capacité gravimétrique et volumétrique (colonnes rouges et vertes, respectivement) de divers métaux formant un alliage avec le lithium.

Le principal problème de ces matériaux est la forte expansion volumique s'opérant lors de l'insertion du lithium (358% pour Li-Sn et 323% pour Li-Si). Un agent conducteur électrique est souvent incorporé dans la composition des électrodes, l'expansion volumique induit ainsi la perte de contact entre la partie active (le métal M) et le noir de carbone causant une chute de la capacité. Diverses stratégies ont permis de limiter cette expansion et d'améliorer la stabilité des électrodes à base de

silicium parmi lesquelles ont peut citer : l'utilisation de nanoparticules, la limitation des bornes de potentiel en cyclage (limitation de la capacité), l'incorporation d'une phase tampon ne réagissant pas avec le lithium ou encore l'incorporation d'un liant

La compréhension des phénomènes chimiques et électrochimiques ayant lieu aux interfaces électrode/électrolyte est aujourd'hui un point clé d'étude pour répondre aux défis actuels. Ces phénomènes sont encore peu connus pour les électrodes à base de Si ou Sn contrairement à celles à base de graphite.

Ce travail de thèse a été entrepris dans le but d'amener des éléments de réponse à différentes questions :

- Quelles sont les phénomènes interfaciaux ayant lieu entre l'électrode (à base de silicium ou d'étain) et l'électrolyte au cours du cyclage électrochimique de la batterie?
- Quelle est la réactivité chimique de l'électrolyte avec la surface des particules de Si et Sn ?
- Comment ces phénomènes évoluent au cours d'un long cyclage ?
- Quelle influence aura la modification du sel de l'électrolyte sur les performances de la batterie et les interfaces?
- Est- il possible par PES de réaliser un profil de composition en profondeur de ces zones interfaciales de façon fiable et exploitable ?

Des électrodes à base de silicium mélangé à un élément conducteur (noir de carbone) et un liant à base de cellulose, ont été cyclées en demi-piles (cyclage face à du lithium métallique). Deux sels d'électrolyte ont été utilisés, le sel classique $LiPF_6$ et un nouveau sel prometteur LiFSI ($LiN(SO_2F)_2$). Les électrodes ont été préparées, puis les batteries assemblées et testées à Uppsala (laboratoire Ångström). Concernant l'étain, du manganèse, un métal électrochimiquement inactif vis-à-vis du lithium a été utilisé donnant le composé intermétallique $MnSn_2$.
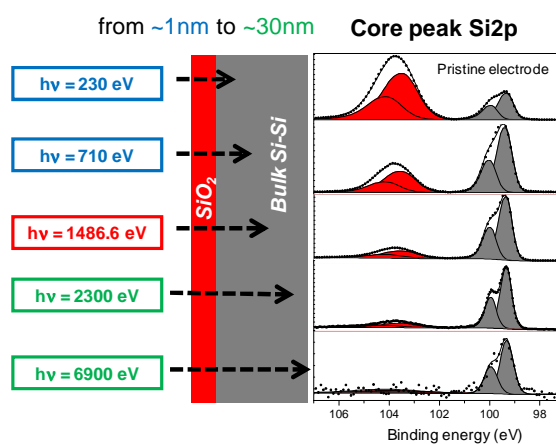
Figure 2 : Surface d'une particule de silicium étudiée avec des énergies de photons différentes. (SiO_2 en rouge, Si en gris)

Les analyses sur ces interfaces ont été réalisées par spectroscopie photoélectronique à rayonnement X. La surface des échantillons est irradiée par des photons (Rayons X) conduisant à une émission d'électrons. La mesure de l'énergie cinétique des électrons éjectés permet d'accéder aux énergies de liaison et fournissent des informations sur les états d'oxydation, l'environnement chimique local de chaque élément présent dans les dernières couches de surface. Il est par exemple possible de distinguer le silicium de cœur (Si) de l'oxyde de surface (SiO_2).

Il est également possible de modifier l'énergie des photons incidents afin de sonder la surface de l'échantillon à différentes profondeurs. Un exemple est donné Figure 2 où l'on peut voir qu'aux faible énergies d'excitation (hν), le pic Si 2p de l'oxyde de surface est nettement plus intense que le pic du silicium de cœur (Si), plus l'énergie augmente, et plus le pic du Si de cœur devient intense. Une telle variation de l'énergie du rayonnement incident est possible par utilisation du rayonnement synchrotron. Les analyses de cette thèse ont été effectuées au laboratoire MAXIV à Lund (Suède) pour

les faibles énergies et au synchrotron Bessy à Berlin (Allemagne) pour les plus hautes énergies. Ces analyses ont été combinées à celles réalisées avec un spectromètre haute résolution de laboratoire à Pau (IPREM-ECP).

Quelques résultats marquants sont illustrés dans les figures 3, 4 et 5. La figure 3 montre que les performances électrochimiques en cyclage d'une électrode à base de silicium avec un électrolyte contenant le sel LiFSI sont nettement meilleures que celles obtenues avec le sel classique LiPF$_6$.
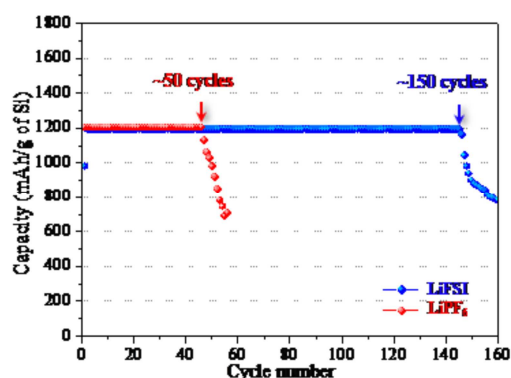
Figure 3 : Comparaison des performances électrochimiques en cyclage des électrodes à base de silicium (Si/C/CMC//Li) avec un électrolyte contenant LiPF$_6$ (en rouge) ou LiFSI (en bleu)

Les analyses réalisées pour les deux sels à différentes profondeur au cours du premier cycle électrochimique ont mis en évidence un ensemble complexes multi-interfaciales (figure 4) faisant intervenir à côté de la SEI et de l'alliage Li$_x$Si les phases Li$_2$O et Li$_4$SiO$_4$ résultant de la réaction (respectivement réversible et irréversible) du lithium avec la couche superficielle de SiO$_2$. Au cours d'un long cyclage avec le sel LiPF$_6$, l'évolution du pic Si 2p à énergie de photon fixe (Figure 5a) et variable (Figure 5b) a permis d'identifier à l'extrême surface des particules la formation d'une phase SiO$_x$F$_y$ résultant de la réaction de la couche superficielle de SiO$_2$ avec des produits de dégradation de LiPF$_6$.

L'absence d'une telle phase lors de l'utilisation du sel LiFSI a permis d'interpréter les meilleures performances électrochimiques
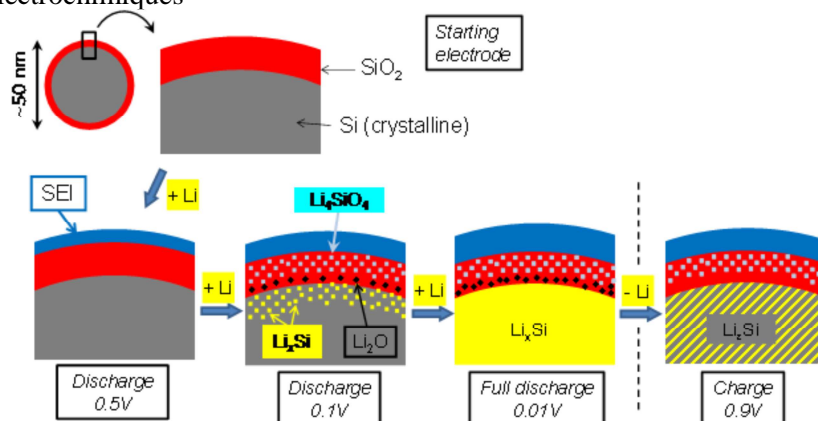
Figure 4 : Illustration des mécanismes se produisant à la surface des particules de silicium au cours du premier cycle électrochimique.
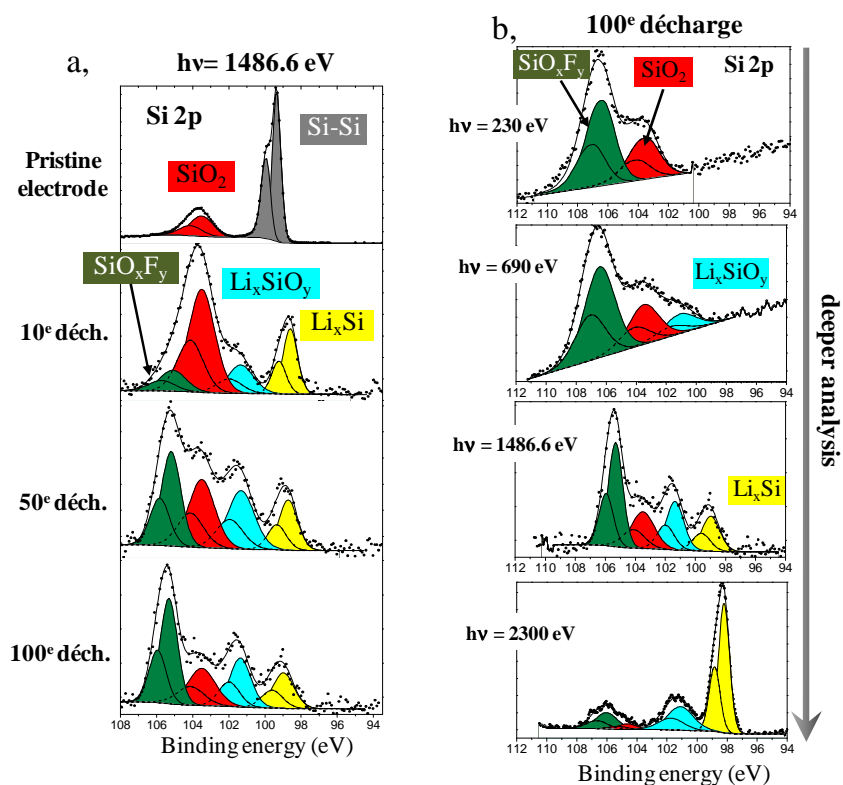
Figure 5 : Evolution du pic de cœur Si 2p (a) au cours d'un long cyclage avec LiPF$_6$ à énergie de photon fixe (hv = 1486.6 eV) (b) à énergie de photon variable (100e décharge)

L'étude au cours du premier cycle électrochimique d'électrodes à base de MnSn$_2$ a fait apparaître des points similaires (SEI de même nature avec le sel LiPF$_6$ et formation de Li$_2$O par réaction du lithium avec l'oxyde SnO$_2$ de surface), mais également des différences puisqu'aucune réactivité de l'oxyde de surface SnO$_2$ avec les produits de dégradation de LiPF$_6$ n'a été observée.

Ces résultats ont mis en relief plusieurs points importants :

1) Des informations fiables sur des mécanismes électrochimiques complexes se déroulant au niveau des interfaces à l'échelle nanométrique ont pu être obtenues via l'approche et la méthodologie innovantes de ces travaux de thèse.

2) La composition de l'électrolyte et notamment la nature du sel peuvent être déterminantes vis à vis de la longévité et la cyclabilité d'une batterie au lithium.

3) Les spécificités des surfaces des matériaux d'électrode (telle dans cette thèse la présence d'oxydes natifs) doivent être prises en compte pour appréhender dans leur globalité les réactions parasites susceptibles de dégrader les performances électrochimiques.

List of Papers

This thesis is based on the following papers, which are referred to in the text by their Roman numerals.

I **Philippe, B.**, Dedryvère, R., Allouche, J., Lindgren, F., Gorgoi, M., Rensmo, H., Gonbeau, D., Edström, K. (2012) Nanosilicon Electrodes for Lithium-Ion Batteries: Interfacial Mechanisms Studied by Hard and Soft X-ray Photoelectron Spectroscopy. *Chemistry of Materials*, 24, 1107-1115.

II **Philippe, B.**, Dedryvère, R., Gorgoi, M., Rensmo, H., Gonbeau, D., Edström, K. (2013) Role of the LiPF6 Salt for the Long-Term Stability of Silicon Electrodes in Li-Ion Batteries – A Photoelectron Spectroscopy Study. *Chemistry of Materials*, 25, 394-404.

III **Philippe, B.**, Dedryvère, R., Gorgoi, M., Rensmo, H., Gonbeau, D., Edström, K. (2013) Improved performances of nano-silicon electrodes using the salt LiFSI – A photoelectron spectroscopy study. *Submitted*

IV **Philippe, B.,** Mahmoud, A., Ledeuil, J.-B., Chamas, M., Edström, K., Dedryvère, R., Gonbeau, D., Lippens, P. – E. (2013) $MnSn_2$ negative electrodes for Li-ion batteries: mechanisms at the nano scale and electrode/electrolyte interface. (In manuscript)

V Mahmoud, A., Chamas, M., Jumas, J. –C., **Philippe, B.**, Dedryvère, R., Gonbeau, D., Saadoune, I., Lippens, P. – E. (2013) Electrochemical performances and mechanisms of $MnSn_2$ as anode material for Li-ion batteries. *Journal of Power Sources* (In press)

Reprints were made with permission from the respective publishers.

Comments on my own contribution to the appended papers in this thesis:

Paper I : Performed all the experimental work (battery preparation, electrochemical tests, in-house PES, synchrotron PES, sol-gel synthesis, SEM) and the analysis of the results. Contributed to discussion and part of the writing.

Paper II: Performed all the experimental work (battery preparation, electrochemical tests, in-house PES, synchrotron PES, SEM), analysis of the results. Contributed to discussion and major part of the writing.

Paper III: Performed major part of the experimental work (battery preparation, electrochemical tests, in-house PES, synchrotron PES) Auger analysis of the results. Contributed to discussion and major part of the writing.

Paper IV: Performed part of the experimental work (in-house PES, synchrotron PES, Auger spectroscopy and SEM) and the analysis of the results. Contributed to discussion and major part of the writing related to my work.

Paper V: Performed the in-house PES and the analysis of the results.

Did not perform the $MnSn_2$ synthesis, Mössbauer spectroscopy and the X-ray diffraction presented in the papers.

References

(1) Whittingham, M. S. *Science* **1976**, *192*, 1126-1127.

(2) Whittingham, M. S. *Progress in Solid State Chemistry* **1978**, *12*, 41-99

(3) Brandt, K. *Solid State Ionics* **1994**, *69*, 173-183

(4) Dampier, F. W. *Journal of The Electrochemical Society* **1974**, *121*, 656-660

(5) Walk, C. R.; Margalit, N. *Journal of Power Sources* **1997**, *68*, 723-725

(6) Murphy, D. W.; Christian, P. A.; DiSalvo, F. J.; Carides, J. N. *Journal of The Electrochemical Society* **1979**, *126*, 497-499

(7) Lazzari, M.; Scrosati, B. *Journal of The Electrochemical Society* **1980**, *127*, 773-774

(8) Mizushima, K.; Jones, P. C.; Wiseman, P. J.; Goodenough, J. B. *Materials Research Bulletin* **1980**, *15*, 783-789.

(9) Thackeray, M. M.; David, W. I. F.; Bruce, P. G.; Goodenough, J. B. *Materials Research Bulletin* **1983**, *18*, 461-472.

(10) Yazami, R.; Touzain, P. *Journal of Power Sources* **1983**, *9*, 365-371

(11) Nagaura, T.; Tozawa, K. Prog. *Batteries Sol. Cells* **1990**, 9, 209–217

(12) Tarascon, J. M.; Armand, M. *Nature* **2001**, *414*, 359-367.

(13) Palacín, R. *Chemical Society Reviews* **2009**, *38*, 2565-2575

(14) Dunn, B.; Kamath, H.; Tarascon, J.-M. *Science* **2011**, *334*, 928-935

(15) Bruce, P. G.; Freunberger, S. A.; Hardwick, L. J.; Tarascon, J.-M. *Nat Mater* **2011**, *11*, 19-29

(16) Palomares, V.; Serras, P.; Villaluenga, I.; Hueso, K. B.; Carretero-Gonzalez, J.; Rojo, T. *Energy & Environmental Science* **2012**, *5*, 5884-5901

(17) Su, F.-Y.; You, C.; He, Y.-B.; Lv, W.; Cui, W.; Jin, F.; Li, B.; Yang, Q.-H.; Kang, F. *Journal of Materials Chemistry* **2010**, *20*, 9644-9650

(18) Peled, E. *Journal of The Electrochemical Society* **1979**, *126*, 2047-2051

(19) Manthiram, A.; Muraliganth, T. *Handbook of Battery Materials* 2nd ed, (Wiley-VCH, 2011), 343-375

(20) Whittingham, M. S. *Chem. Rev.* **2004,** 104, 4271-4301

(21) Winter, M.; Besenhard, J. O.; Spahr, M. E.; Novák, P. *Advanced Materials* **1998**, *10*, 725-763

(22) Song, H.-K.; Lee, K. T.; Kim, M. G.; Nazar, L. F.; Cho, J. *Advanced Functional Materials*, **2010**, *20*, 3818-3834.

(23) Ellis, B. L.; Lee, K. T.; Nazar, L. F. *Chemistry of Materials* **2010**, *22*, 691-714

(24) Fergus, J. W. *J. Power Sources*, **2010** *195*, 939-954

(25) Goodenough, J. B.; Kim, Y. *Chem. Mater.*,**2010** *22*, 587-603

(26) Amatucci, G. G.; Tarascon, J. M.; Klein, L. C. *Journal of The Electrochemical Society* **1996**, *143*, 1114-1123

(27) Doh, C.-H.; Kim, D.-H.; Kim, H.-S.; Shin, H.-M.; Jeong, Y.-D.; Moon, S.-I.; Jin, B.-S.; Eom, S. W.; Kim, H.-S.; Kim, K.-W.; Oh, D.-H.; Veluchamy, A. *Journal of Power Sources* **2008**, *175*, 881-885

(28) Zhou, J.; Notten, P. H. L. *Journal of Power Sources* **2008**, *177*, 553-560

(29) Dahn, J. R.; von Sacken, U.; Juzkow, M. W.; Al-Janaby, H. *Journal of The Electrochemical Society* **1991**, *138*, 2207-2211

(30) Ebner, W.; Fouchard, D.; Xie, L. *Solid State Ionics* **1994**, *69*, 238-256

(31) Ohzuku, T.; Ueda, A.; Nagayama, M. *Journal of The Electrochemical Society* **1993**, *140*, 1862-1870

(32) Lu, W.; Lee, C. W.; Venkatachalapathy, R.; Prakash, J. *Journal of Applied Electrochemistry* **2000**, *30*, 1119-1124

(33) Chen, C. H.; Liu, J.; Stoll, M. E.; Henriksen, G.; Vissers, D. R.; Amine, K. *Journal of Power Sources* **2004**, *128*, 278-285

(34) Ohzuku, T.; Makimura, Y. *Chemistry Letters* **2001**, *30*, 642-643

(35) Thackeray, M. M.; de Kock, A.; David, W. I. F. *Materials Research Bulletin* **1993**, *28*, 1041-1049

(36) Thackeray, M. M.; Johnson, C. S.; Kahaian, A. J.; Kepler, K. D.; Vaughey, J. T.; Shao-Horn, Y.; Hackney, S. A. *Journal of Power Sources* **1999**, *81-82*, 60-66

(37) Liu, Y.; Li, X.; Guo, H.; Wang, Z.; Hu, Q.; Peng, W.; Yang, Y. *Journal of Power Sources* **2009**, *189*, 721-725

(38) Shigemura, H.; Sakaebe, H.; Kageyama, H.; Kobayashi, H.; West, A. R.; Kanno, R.; Morimoto, S.; Nasu, S.; Tabuchi, M. *Journal of The Electrochemical Society* **2001**, *148*, A730-A736

(39) Mateyshina, Y. G.; Lafont, U.; Uvarov, N. F.; Kelder, E. M. *Russian Journal of Electrochemistry* **2009**, *45*, 602-605

(40) Amine, K.; Tukamoto, H.; Yasuda, H.; Fujita, Y. *Journal of Power Sources* **1997**, *68*, 604-608

(41) Ooms, F. G. B.; Kelder, E. M.; Schoonman, J.; Wagemaker, M.; Mulder, F. M. *Solid State Ionics* **2002**, *152-153*, 143-153

(42) Imazaki, M.; Ariyoshi, K.; Ohzuku, T. *Journal of The Electrochemical Society* **2009**, *156*, A780-A786

(43) Eftekhari, A. *Solid States Ionics* **2004**, *167*, 237-242

(44) Manthiram, A.; Goodenough, J. B. *Journal of Solid State Chemistry* **1987**, *71*, 349-360

(45) Padhi, A. K.; Nanjundaswawy, K. S.; Goodenough, J. B. *Journal of electrochemical society* **1997**, *144*, 1188-1194

(46) Andersson, A. S.; Thomas, J. O.; Kalska, B.; HÃ¤ggstrÃ¶m, L. *Electrochemical and Solid-State Letters* **2000**, *3*, 66-68

(47) Chung, S.-Y.; Bloking, J. T.; Chiang, Y.-M. *Nat Mater* **2002**, *1*, 123-128

(48) Ravet, N.; Chouinard, Y.; Magnan, J. F.; Besner, S.; Gauthier, M.; Armand, M. *Journal of Power Sources* **2001**, *97â€"98*, 503-507

(49) Prosini, P. P.; Carewska, M.; Scaccia, S.; Wisniewski, P.; Passerini, S.; Pasquali, M. *Journal of The Electrochemical Society* **2002**, *149*, A886-A890

(50) Zhang, W.-J. *Journal of Power Sources* **2011**, *196*, 2962-2970

(51) Masquelier, C.; Padhi, A. K.; Nanjundaswamy, K. S.; Goodenough, J. B. *Journal of Solid State Chemistry* **1998**, *135*, 228-234

(52) Nytén, A.; Abouimrane, A.; Armand, M.; Gustafsson, T.; Thomas, J. O. *Electrochemistry Communications* **2005**, *7*, 156-160

(53) Kam, K. C.; Gustafsson, T. r.; Thomas, J. O. *Solid State Ionics* **2011**, *192*, 356-359

(54) Dominko, R.; Bele, M.; GaberÅ¡ ek, M.; Meden, A.; RemÅ¡kar, M.; Jamnik, J. *Electrochemistry Communications* **2006**, *8*, 217-222

(55) Islam, M. S.; Dominko, R.; Masquelier, C.; Sirisopanaporn, C.; Armstrong, A. R.; Bruce, P. G. *Journal of Materials Chemistry* **2011**, *21*, 9811-9818

(56) Barker, J.; Saidi, M. Y.; Swoyer, J. L. *Journal of The Electrochemical Society* **2003**, *150*, A1394-A1398

(57) Recham, N.; Chotard, J. N.; Jumas, J. C.; Laffont, L.; Armand, M.; Tarascon, J. M. *Chemistry of Materials* **2010**, *22*, 1142-1148

(58) Song, H.-K.; Lee, K. T.; Kim, M. G.; Nazar, L. F.; Cho, J. *Advanced Functional Materials* **2010** , *20*, 3818-3834

(59) Recham, N.; Chotard, J. N.; Dupont, L.; Delacourt, C.; Walker, W.; Armand, M.; Tarascon, J. M. *Nat Mater* **2010**, *9*, 68-74

(60) Rao, B. M. I.; Francis, R. W.; Christopher, H. A. *J. Electrochem. Soc.* **1977**, *124*, 1490-1492

(61) Visco, S.J.; Nimon; Y.S., Katz; B D.; De Jonghe, L.C. *United states Patent* US 7,282,295; **2004**

(62) Visco, S.J.; Nimon; Y.S., Katz; B D.; De Jonghe, L.C. *United states Patent* U.S. 7,491,458, **2004**

(63) Hérold, A. *Bulletin de la Société Chimique de France*, **1955**, *187,* 999

(64) Kinoshita, K.; Zaghib, K. Journal of Power Sources **2002**, 110, 416–423

(65) Verma, P.; Maire, P.; Novák, P. *Electrochimica Acta* **2010**, *55*, 6332-634

(66) Aurbach, D.; Ein-Eli, Y.; Chusid, O.; Carmeli, Y.; Babai, M.; Yamin, H. *Journal of The Electrochemical Society* **1994**, *141*, 603-611

(67) Endo, M.; Kim, C.; Nishimura, K.; Fujino, T.; Miyashita, K. *Carbon* **2000**, *38*, 183-197

(68) Li, H. ; Wang, Z. ; Chen, L. ; Huang, X. *Advanced materials* **2009**, *21*, 4593-4607

(69) Frackowiak, E.; Béguin, F. *Carbon* **2002**, *40*, 1775-1787

(70) Morris, R. S.; Dixon, B. G.; Gennett, T.; Raffaelle, R.; Heben, M. J. *Journal of Power Sources* **2004**, *138*, 277-280

(71) Ohzuku, T.; Ueda, A.; Yamamoto, N.; Iwakoshi, Y. *Journal of Power Sources* **1995**, *54*, 99-102

(72) Zhu, G.-N.; Wang, Y.-G.; Xia, Y.-Y. *Energy & Environmental Science* **2012**, *5*, 6652-6667

(73) Sorensen, E. M.; Barry, S. J.; Jung, H.-K.; Rondinelli, J. M.; Vaughey, J. T.; Poeppelmeier, K. R. *Chemistry of Materials* **2005**, *18*, 482-489

(74) Yang, Z.; Choi, D.; Kerisit, S.; Rosso, K. M.; Wang, D.; Zhang, J.; Graff, G.; Liu, J. *Journal of Power Sources* **2009**, *192*, 588-598

(75) Belharouak, I.; Amine, K. *Electrochemistry Communications* **2005**, *7*, 648-651

(76) Godbole, V. A.; Villevieille, C.; Sommer, H.-H.; Colin, J.-F. o.; Novák, P. *Electrochimica Acta* **2012**, *77*, 244-249

(77) Essehli, R.; El Bali, B.; Faik, A.; Benmokhtar, S.; Manoun, B.; Zhang, Y.; Zhang, X. J.; Zhou, Z.; Fuess, H. *Journal of Alloys and Compounds* **2012**, *530*, 178-185

(78) Guyomard, D.; Sigala, C.; de Gal La Salle, A.; Piffard, Y. *Journal of Power Sources* **1997**, *68*, 692-697

(79) Piffard, Y.; Leroux, F.; Guyomard, D.; Mansot, J. L.; Tournoux, M. *Journal of Power Sources* **1997**, *68*, 698-703

(80) Armstrong, A. R.; Lyness, C.; Panchmatia, P. M.; Islam, M. S.; Bruce, P. G. *Nat Mater* **2011**, *10*, 223-229

(81) Dey, A. N. *Journal of The Electrochemical Society* **1971**, *118*, 1547-1549

(82) Larcher, D.; Beattie, S.; Morcrette, M.; Edstrom, K.; Jumas, J.-C.; Tarascon, J.-M. *Journal of Materials Chemistry* **2007**, *17*, 3759-3772

(83) Zhang, W.-J. *Journal of Power Sources* **2011**, *196*, 13-24

(84) Chen, Z.; Christensen, L.; Dahn, J. R. *Electrochemistry Communications* **2003**, *5*, 919-923

(85) Wu, H.; Cui, Y. *Nano Today* **2012**, *7*, 414-429

(86) Kasavajjula, U.; Wang, C.; Appleby, A. J. *Journal of Power Sources* **2007**, *163*, 1003-1039

(87) Yang, J.; Winter, M.; Besenhard J. O. *Solid State Ionics* **1996**, *90*, 281-287

(88) Li, H.; Huang, X.; Chen, L.; Wu, Z.; Liang, Y. *Electrochemical and Solid-State Letters* **1999**, *2*, 547-549

(89) Besenhard, J. O.; Hess, M.; Komenda, P. *Solid State Ionics* **1990**, *40-41, Part 2*, 525-529

(90) Park, C.-M.; Kim, J.-H.; Kim, H.; Sohn, H.-J. Chemical Society Reviews **2010**, *39*, 3115–3141

(91) Thackeray, M. M.; Vaughey, J. T.; Johnson, C. S.; Kropf, A. J.; Benedek, R.; Fransson, L. M. L.; Edstrom, K. *Journal of Power Sources* **2003**, *113*, 124-130

(92) Fransson, L.M.L.; Vaughey, J.T.; Benedek, R.; Edstrom, K.; Thomas, J.O.; Thackeray, M.M.; *Electrochemistry Communications* **2001**, *3*, 317-323

(93) Vaughey, J. T.; Johnson, C. S.; Kropf, A. J.; Benedeck, R.; Thacheray, M. M.; Tostmann, H.; Sarakonsri, T.; Hackney, S.; Fransson, L.; Edstöm, K.; Thomas, J. O. *Journal of Power Sources* **2001**, *97-98*, 194-197

(94) Stjerndahl, M.; Bryngelsson, H.; Gustafsson, T.; Vaughey, J. T.; Thackeray, M.M.; Edström, K. *Electrochimica Acta* **2007**, *52*, 4947–4955

(95) Ionica, C. M.; Lippens, P. E.; Fourcade, J. O.; Jumas, J.-C. *Journal of Power Sources* **2005**, *146*, 478-481

(96) Fransson, L. ; Vaughey, J. T. ; Edström, K.; Thackeray, M. M. *Journal of Electrochemical Society*, **2003**, *15*, A86-A91

(97) Naille, S.; Mouyane, M.; Amraoui, M.; Lippens, P. E.; Jumas, J. C.; Olivier-Fourcade, J. *Hyperfine Interact.* **2008**, *187*, 19-26.

(98) Hu, R.; Zeng, M.; Li, C. Y. V.; Zhu, M. *J. Power Sources* **2009**, *188*, 268-273.

(99) O. Mao, R.A. Dunlap, J.R. Dahna, *J. Electrochem. Soc.* 146 (1999) 405.

(100) Amadei, I.; Panero, S.; Scrosati, B.; Cocco, G.; Schiffini, L. *J. Power Sources* **2005**, *143*, 227-230.

(101) Ehinon, K. K. D.; Naille, S.; Dedryvère, R.; Lippens, P.-E.; Jumas, J.-C.; Gonbeau, D. *Chemistry of Materials* **2008**, *20*, 5388–5398

(102) Xue, M.-Z.; Fu, Z.-W. *Solid State Ionics* **2006**, *177*, 1501-1507

(103) Naille, S.; Ionica-Bousquet, C. M.; Robert, F.; Morato, F.; Lippens, P. E.; Olivier-Fourcade, J. *J. Power Sources* **2007**, *174*, 1091-1094

(104) Kepler, K.; Vaughey, J.; Thackeray, M. M. *Electrochem. Solid-State Letts.* **1999**, *2*, 307-309.

(105) Sharma, S.; Fransson, L.; Sjöstedt, E.; Nordström, L.; Johansson, B.; Edström, K. *J. Electrochem. Soc.* **2003**, *150*, A330-A334.

(106) Beaulieu, L.; Larcher, D.; Dunlap, R. A.; Dahn, J. R. *J. Alloys Compd.* **2000**, *297*, 122-128

(107) Ferguson, P. P.; Martine, M. L.; George, A. E.; Dahn, J. R. *J. Power Sources* **2009**, *194*, 794-800

(108) Rom, I.; Wachtler, M.; Papst, I.; Schmied, M.; Besenhard, J.O.; Hofer, F.; Winter, M. *Solid State Ionics,* **2001**, *143*, 329

(109) Wachtler, M.; Besenhard, J. r. O.; Winter, M. *Journal of Power Sources* **2001**, *94*, 189-193

(110) Sougrati, M. T.; Fullenwarth, J.; Debenedetti, A.; Fraisse, B.; Jumas, J. C.; Monconduit, L. *Journal of Material Chemistry*, **2011**, *21*, 10069–10076

(111) Marino, C.; Sougrati, M. T.; Gerke, B.; Pöttgen, R.; Huo, H.; Ménétrier, M.; Grey, C. P.; Monconduit, L. *Chemistry of Materials* **2012**, *24*, 4735–4743

(112) Bryngelsson, H.; Eskhult, J.; Edström, K.; Nyholm, L. *Electrochimica Acta* **2007**, *53*, 1062–1073

(113) Idota, Y.; Kubota, T.; Matsufuji, A.; Maekawa, Y.; Miyasaka, T. *Science* **1997**, *276*, 1395-1397

(114) Courtney, I. A.; Dahn, J. R. *Journal of The Electrochemical Society* **1997**, *144*, 2045-2052

(115) Cabana, J.; Monconduit, L.; Larcher, D.; Palacín, M. R. *Advanced Materials* **2010**, *22*, E170-E192

(116) Balaya, P.; Li, H.; Kienle, L.; Maier, J. *Advanced Functional Materials* **2003**, *13*, 621-625

(117) Poizot, P.; Laruelle, S.; Grugeon, S.; Dupont, L.; Tarascon, J. M. *Nature* **2000**, *407*, 496-499

(118) Xu, K. *Chemical Reviews* **2004**, *104*, 4303-4418

(119) Feuillade, G.; Perche, P. *Journal of Applied Electrochemistry* **1975**, *5*, 63-69

(120) Armand, M. *Solid Ionic States* **1983**, *9-10*, 745-754

(121) Goodenough, J. B. *Solid State Ionics* **1997**, 94, 17-25

(122) Armand, M.; Endres, F.; MacFarlane, D. R.; Ohno, H.; Scrosati, B. *Nat Mater* **2009**, *8*, 621-629

(123) Stassen, I.; Hambitzer, G. *Journal of Power Sources* **2002**, *105*, 145-150

(124) Ue, M. *Journal of The Electrochemical Society* **1994**, *141*, 3336-3342

(125) Heider, U.; Oesten, R.; Jungnitz, M. *J. Power Sources* **1999**, *81-82*, 119-122.

(126) Campion, C. L., Li, W., & Lucht, B. L., *J. Electrochem. Soc* **2005**, *152*, A2327-A2334.

(127) Aurbach, D.; Markovsky, B.; Shechter, A.; Ein-Eli, Y. & Cohen, H. *J. Electrochem. Soc.* **1996,** *143*, 3809-3820.

(128) Plakhotnyk, A. V.; Ernst, L.; Schmutzler, R. *J. Fluorine Chem.* **2005**, *126*, 27-31.

(129) Xu, K.; Zhang, S.; Jow, T. R.; Xu, W.; Angell, C. A. *Electrochemical and Solid-State Letters* **2002**, *5*, A26-A29

(130) Zhang, S. S. *Electrochemistry Communications* **2006**, *8*, 1423–1428

(131) Schmidt, M.; Heider, U.; Kuehner, A.; Oesten, R.; Jungnitz, M.; Ignat'ev, N.; Sartori, P. *Journal of Power Sources* **2001**, *97-98*, 557-560

(132) Niedzicki, L.; Kasprzyk, M.; Kuziak, K.; Å»ukowska, G. Z.; Marcinek, M.; Wieczorek, W.; Armand, M. *Journal of Power Sources* **2011**, *196*, 1386-1391

(133) Dominey, L. A.; Koch, V. R.; Blakley, T. J. *Electrochimica Acta* **1992**, *37*, 1551-1554

(134) Krause, L. J.; Lamanna, W.; Summerfield, J.; Engle, M.; Korba, G.; Loch, R.; Atanasoski, R. *Journal of Power Sources* **1997**, *68*, 320-325

(135) Kanamura, K.; Umegaki, T.; Shiraishi, S.; Ohashi, M.; Takehara, Z.-i. *J. Electrochem. Soc.* **2002**, *149*, A185-A194.

(136) Han, H.; Guo, J.; Zhang, D.; Feng, S.; Feng, W.; Nie, J.; Zhou, Z. *Electrochemistry Communications* **2011**, *13*, 265-268.

(137) C. Michot, M. Armand, J.Y. Sanchez, Y. Choquette, M. Gauthier, *United States Patent US 5916475,* **1999**.

(138) Ishikawa, M.; Sugimoto, T.; Kikuta, M.; Ishiko, E.; Kono, M. *J. Power Sources* **2006**, *162*, 658-662.

(139) Paillard, E.; Zhou, Q.; Henderson, W. A.; Appetecchi, G. B.; Montanino, M.; Passerini, S. *J. Electrochem. Soc.* **2009**, *156*, A891-A895.

(140) Guerfi, A.; Duchesne, S.; Kobayashi, Y.; Vijh, A.; Zaghib, K. *J. Power Sources* **2008**, *175*, 866-873.

(141) Zaghib, K.; P. Charest, P.; Guerfi, A.; Shimb, J.; Perrier, M.; Striebel, K. *J. Power Sources* **2005**, *146*, 380–385

(142) Li, L.; Zhou, S.; Han, H.; Li, H.; Nie, J.; Armand, M.; Zhou, Z.; Huang, X. *J. Electrochem. Soc.* **2011**, *158*, A74-A82.

(143) Han, H.-B.; Zhou, S.-S.; Zhang, D.-J.; Feng, S.-W.; Li, L.-F.; Liu, K.; Feng, W.-F.; Nie, J.; Li, H.; Huang, X.-J.; Armand, M.; Zhou, Z.-B. *J. Power Sources* **2011**, *196*, 3623-3632.

(144) Zhang, S. S. *Journal of Power Sources* **2006**, *162*, 1379-1394

(145) Herstedt, M.; Rensmo, H.; Siegbahn, H.; Edström, K. *Electrochimica Acta* **2004**, *49*, 2351-2359

(146) El Ouatani, L.; Dedryvère, R.; Siret, C. ; Biensan, P. ; Reynaud, S. ; Iratçabal, P.; Gonbeau, D. *Journal of The Electrochemical Society,* **2009***, 156*, A103-A113

(147) El Ouatani, L.; Dedryvère, R.; Siret, C. ; Biensan, P. ; Gonbeau, D. *Journal of The Electrochemical Society* **2009,** *156*, A468-A477

(148) Leroy, S. ; Blanchard, F. ; Dedryvère, R. ; Martinez, H. ; Carré, B. ; Lemordant, D. ; Gonbeau D. *Surface and Interface Analysis* **2005**, *37*, 773–781

(149) Edström, K.; Herstedt, M.; Abraham, D. P. *Journal of Power Sources* **2006**, *153*, 380-384

(150) Besenhard, J. O.; Winter, M.; Yang, J.; Biberacher, W. *Journal of Power Sources* **1995**, *54*, 228-231

(151) Vetter, J.; Novák, P.; Wagner, M.R.; Veit, C.; Möller, K.-C.; Besenhard J. O.; Winter, M.; Wohlfahrt-Mehrens, M.; Vogler, C.; Hammouche, A. *Journal of Power Sources* **2005**, *147*, 269–281

(152) Peled, E.; Golodnitsky, D.; Ardel, G. *Journal of The Electrochemical Society* **1997**, *144*, L208-L210

(153) Aurbach, D. *Journal of Power Sources* **2000**, *89*, 206-218

(154) Zaban, A.; Aurbach, D. *Journal of Power Sources* **1995**, *54*, 289-295

(155) Andersson, A. M.; Henningson, A.; Siegbahn, H.; Jansson, U.; Edström, K. *Journal of Power Sources* **2003**, *119-121*, 522-527

(156) Dedryvère, R.; Gireaud, L.; Grugeon, S.; Laruelle, S.; Tarascon, J.-M.; Gonbeau, D. *J. Phys. Chem. B* **2005**, *109,* 15868-15875

(157) Aurbach, D.; Markovsky, B.; Weissman, I.; Levi, E.; Ein-Eli, Y. *Electrochimica Acta* **1999**, *45*, 67-86

(158) Geniès, S.; Yazami, R.; Garden, J.; Frison, J. C. *Synthetic Metals* **1998**, *93*, 77-82)

(159) Andersson, A. M.; Edstrom, K. *Journal of The Electrochemical Society* **2001**, *148*, A1100-A1109

(160) Aurbach, D.; Zaban, A.; Gofer, Y.; Ely, Y. E.; Weissman, I.; Chusid, O.; Abramson, O. *Journal of Power Sources* **1995**, *54*, 76-84

(161) Yoshida, H.; Fukunaga, T.; Hazama, T.; Terasaki, M.; Mizutani, M.; Yamachi, M. *Journal of Power Sources* **1997**, *68*, 311-315

(162) Dedryvère, R.; Leroy, S.; Martinez, H.; Blanchard, F.; Lemordant, D.; Gonbeau, D. *J. Phys. Chem. B* **2006**, *110,* 12986-12992

(163) Dedryvère, R.; Laruelle, S.; Grugeon, S.; Gireaud, L.; Tarascon, J.-M.; Gonbeau, D. *Journal of The Electrochemical Society,* **2005**, *152*, A689-A696

(164) Augustsson, A.; Herstedt, M.; Guo, J. H.; Edström, K.; Zhuang, G. V.; Ross, J. P. N.; Rubensson, J. E.; Nordgren, J. *Physical Chemistry Chemical Physics* **2004**, *6*, 4185-4189

(165) Peled, E.; Bar Tow, D.; Merson, A.; Gladkich, A.; Burstein, L.; Golodnitsky, D. *Journal of Power Sources* **2001**, *97-98,* 52-57

(166) Sloop, S. E.; Pugh, J. K.; Wang, S.; Kerr, J. B.; Kinoshita, K. *Electrochemical and Solid-State Letters*, **2001**, 4, A42-A44

(167) Tasaki, K.; Kanda, K.; Nakamura, S.; Ue, M. *Journal of The Electrochemical Society* **2003**, *150*, A1628-A1636.

(168) Heider, U.; Oesten, R.; Jungnitz, M. *Journal of Power Sources* **1999**, 81-82, 119-122.

(169) Campion, C. L., Li, W., & Lucht, B. L., *J. Electrochem. Soc* **2005**, 152, A2327-A2334

(170) Andersson, A PhD Thesis, Uppsala University, 2001.

(171) Herstedt, M. PhD Thesis, Uppsala University, 2003.

(172) Laruelle, S.; Pilard, S.; Guenot, P.; Grugeon, S.; Tarascon, J.-M. *Journal of The Electrochemical Society* **2004**, *151*, A1202-A1209

(173) Leroy, S. PhD thesis, Université de Pau et des Pays de l'Adour, 2006

(174) Zhang, W.-J. *Journal of Power Sources* **2011**, *196*, 877-885

(175) Yin, Y.; Wan, L.; Guo, Y. *Chinese Science Bulletin* **2012**, 1-7

(176) Sharma, R. A.; Seefurth, R. N. *Journal of The Electrochemical Society* **1976**, *123*, 1763-1768

(177) Wen, C. J.; Huggins, R. A. *Journal of Solid State Chemistry* **1981**, *37*, 271-278

(178) Boukamp, B. A.; Lesh, G. C.; Huggins, R. A. *Journal of The Electrochemical Society* **1981**, *128*, 725-729

(179) Limthongkul, P.; Jang, Y.-I.; Dudney, N. J.; Chiang, Y.-M. *Journal of Power Sources* **2003**, *119-121*, 604-609

(180) Obrovac, M. N.; Christensen, L. *Electrochemical and Solid-State Letters* **2004**, 7, A93-A96

(181) Hatchard, T. D.; Dahn, J. R. *Journal of The Electrochemical Society* **2004**, *151*, A838-A842

(182) Li, H.; Huang, X.; Chen, L.; Wu, Z.; Liang, Y. *Electrochemical and Solid-State Letters* **1999**, *2*, 547-549

(183) Li, J.; Dahn, J. R. *Journal of The Electrochemical Society* **2007**, *154*, A156-A161

(184) Himpsel, F. J., McFeely, F. R., Taleb-Ibrahimi A. & Yarmoff, J. A., *Phys. Rev. B*, **1988**, *38*, 6084-6096

(185) Grunthaner, P. J., Hecht, M. H., Grunthaner, F. J., & Johnson, N. M., *J. Appl. Phys.*, **1987**, *61*, 629-637

(186) Miyachi, M.; Yamamoto, H.; Kawai, H.; Ohta, T.; Shirakata, M. *Journal of The Electrochemical Society* **2005**, *152*, A2089-A2091

(187) Morita, T.; Takami, N. *Journal of The Electrochemical Society* **2006**, *153*, A425-A430

(188) Kim, T.; Park, S.; Oh, S. M. *Journal of The Electrochemical Society* **2007**, *154*, A1112-A1117

(189) Kim, J.-H.; Park, C.-M.; Kim, H.; Kim, Y.-J.; Sohn, H.-J. *Journal of Electroanalytical Chemistry* **2011**, *661*, 245-249

(190) Liu, X.; Zheng, M.-C.; Xie, K. *Journal of Power Sources* **2011**, *196*, 10667-10672

(191) Choi, I.; Lee, M. J.; Oh, S. M.; Kim, J. J. *Electrochimica Acta* **2012,** *85*, 369-376

(192) Hwa, Y.; Park, C.-M.; Sohn, H.-J. *Journal of Power Sources* **2013**, *222*, 129-134.

(193) Yang, X.; Wen, Z.; Xu, X.; Lin, B.; Huang, S. *Journal of Power Sources* **2007**, *164*, 880-884

(194) Chang, W.-S.; Park, C.-M.; Kim, J.-H.; Kim, Y.-U.; Jeong, G.; Sohn, H.-J. *Energy & Environmental Science* **2012**, *5*, 6895-6899

(195) Guo, B.; Shu, J.; Wang, Z.; Yang, H.; Shi, L.; Liu, Y.; Chen, L. *Electrochemistry Communications* **2008**, *10*, 1876-1878

(196) Sun, Q.; Zhang, B.; Fu, Z.-W. *Applied Surface Science* **2008**, *254*, 3774-3779

(197) Jung, H.; Park, M.; Yoon, Y.-G.; Kim, G.-B.; Joo, S.-K. *Journal of Power Sources* **2003**, *115*, 346-351

(198) Obrovac, M. N.; Krause, L. J. *Journal of The Electrochemical Society* **2007**, *154*, A103-A108

(199) Li, J.; Lewis, R. B.; Dahn, J. R. *Electrochemical and Solid-State Letters* **2007**, *10*, A17-A20

(200) Liu, X. H.; Zhong, L.; Huang, S.; Mao, S. X.; Zhu, T.; Huang, J. Y. *ACS Nano*, **2012**, 6, 1522–1531

(201) Graetz, J.; Ahn, C. C.; Yazami, R.; Fultz, B. *Electrochemical and Solid-State Letters* **2003**, *6*, A194-A197

(202) Beaulieu, L. Y.; Eberman, K. W.; Turner, R. L.; Krause, L. J.; Dahn, J. R. *Electrochemical and Solid-State Letters* **2001**, *4*, A137-A140

(203) Lee, S.-J.; Lee, J.-K.; Chung, S.-H.; Lee, H.-Y.; Lee, S.-M.; Baik, H.-K. *Journal of Power Sources* **2001**, *97-98*, 191-193

(204) Ohara, S.; Suzuki, J.; Sekine, K.; Takamura, T. *Journal of Power Sources* **2004**, *136*, 303-306

(205) Lee, K.-L.; Jung, J.-Y.; Lee, S.-W.; Moon, H.-S.; Park, J.-W. *Journal of Power Sources* **2004**, *129*, 270-274

(206) Yoshio, M.; Tsumura, T.; Dimov, N. *Journal of Power Sources* **2005**, *146*, 10-14

(207) Li, H.; Cheng, F.; Zhu, Z.; Bai, H.; Tao, Z.; Chen, J. *Journal of Alloys and Compounds* **2011**, *509*, 2919-2923

(208) Jiang, T.; Zhang, S.; Qiu, X.; Zhu, W.; Chen, L. *Electrochemistry Communications* **2007**, *9*, 930-934

(209) Kim, H.; Han, B.; Choo, J.; Cho, J. *Angewandte Chemie* **2008**, *120*, 10305-10308

(210) Bang, B. M.; Lee, J.-I.; Kim, H.; Cho, J.; Park, S. *Advanced Energy Materials* **2012**, *2*, 878-883

(211) Shin, H.-C.; Corno, J. A.; Gole, J. L.; Liu, M. *Journal of Power Sources* **2005**, *139*, 314-320

(212) Yao, Y.; McDowell, M. T.; Ryu, I.; Wu, H.; Liu, N.; Hu, L.; Nix, W. D.; Cui, Y. *Nano Letters* **2011**, *11*, 2949-2954

(213) Chen, D.; Mei, X.; Ji, G.; Lu, M.; Xie, J.; Lu, J.; Lee, J. Y. *Angewandte Chemie International Edition* **2012**, *51*, 2409-2413

(214) Xiao, X.; Liu, P.; Verbrugge, M. W.; Haftbaradaran, H.; Gao, H. *Journal of Power Sources* **2011**, *196*, 1409-1416

(215) Green, M.; Fielder, E.; Scrosati, B.; Wachtler, M.; Moreno, J. S. *Electrochemical and Solid-State Letters* **2003**, *6*, A75-A79

(216) He, Y.; Yu, X.; Wang, Y.; Li, H.; Huang, X. *Advanced Materials* **2011**, *23*, 4938-4941

(217) Lee, S. W.; McDowell, M. T.; Choi, J. W.; Cui, Y. *Nano Letters* **2011**, *11*, 3034-3039

(218) Goldman, J. L.; Long, B. R.; Gewirth, A. A.; Nuzzo, R. G. *Advanced Functional Materials* **2011**, *21*, 2412-2422

(219) Cui, L.-F.; Ruffo, R.; Chan, C. K.; Peng, H.; Cui, Y. *Nano Letters* **2008**, *9*, 491-495

(220) Chan, C. K.; Peng, H.; Liu, G.; McIlwrath, K.; Zhang, X. F.; Huggins, R. A.; Cui, Y. *Nat Nano* **2008**, *3*, 31-35

(221) Cho, J.-H.; Li, X.; Picraux, S. T. *Journal of Power Sources* **2012**, *205*, 467-473

(222) Chakrapani, V.; Rusli, F.; Filler, M. A.; Kohl, P. A. *Journal of Power Sources* **2012**, *205*, 433-438

(223) Chen, H.; Dong, Z.; Fu, Y.; Yang, Y. *Journal of Solid State Electrochemistry* **2010,** *14,* 1829-1834

(224) Chan, C. K.; Ruffo, R.; Hong, S. S.; Huggins, R. A.; Cui, Y. *Journal of Power Sources* **2009**, *189*, 34-39

(225) Park, M.-H.; Kim, M. G.; Joo, J.; Kim, K.; Kim, J.; Ahn, S.; Cui, Y.; Cho, J. *Nano Letters* **2009**, *9*, 3844-3847

(226) Liu, X. H.; Zheng, H.; Zhong, L.; Huang, S.; Karki, K.; Zhang, L. Q.; Liu, Y.; Kushima, A.; Liang, W. T.; Wang, J. W.; Cho, J.-H.; Epstein, E.; Dayeh, S. A.; Picraux, S. T.; Zhu, T.; Li, J.; Sullivan, J. P.; Cumings, J.; Wang, C.; Mao, S. X.; Ye, Z. Z.; Zhang, S.; Huang, J. Y. *Nano Letters* **2011**, *11*, 3312-3318

(227) Ryu, I.; Choi, J. W.; Cui, Y.; Nix, W. D. *Journal of the Mechanics and Physics of Solids* **2011**, *59*, 1717-1730

(228) Liu, X. H.; Wang, J. W.; Huang, S.; Fan, F.; Huang, X.; Liu, Y.; Krylyuk, S.; Yoo, J.; Dayeh, S. A.; Davydov, A. V.; Mao, S. X.; Picraux, S. T.; Zhang, S.; Li, J.; Zhu, T.; Huang, J. Y. *Nat Nano* **2012**, *7*, 749-756

(229) Liu, G.; Xun, S.; Vukmirovic, N.; Song, X.; Olalde-Velasco, P.; Zheng, H.; Battaglia, V. S.; Wang, L.; Yang, W. *Advanced Materials* **2011**, *23*, 4679-4683

(230) Li, H.; Huang, X.; Chen, L.; Zhou, G.; Zhang, Z.; Yu, D.; Jun Mo, Y.; Pei, N. *Solid State Ionics* **2000**, *135*, 181-191

(231) Liu, W.-R.; Guo, Z.-Z.; Young, W.-S.; Shieh, D.-T.; Wu, H.-C.; Yang, M.-H.; Wu, N.-L. *Journal of Power Sources* **2005**, *140*, 139-144

(232) Saint, J.; Morcrette, M.; Larcher, D.; Laffont, L.; Beattie, S.; Pérès, J. P.; Talaga, D.; Couzi, M.; Tarascon, J. M. *Advanced Functional Materials* **2007**, *17*, 1765-1774

(233) Wilson, A. M.; Dahn, J. R. *Journal of The Electrochemical Society* **1995**, *142*, 326-332

(234) Holzapfel, M.; Buqa, H.; Krumeich, F.; Novak, P.; Petrat, F. M.; Veit, C. *Electrochemical and Solid-State Letters* **2005**, *8*, A516-A520

(235) Holzapfel, M.; Buqa, H.; Scheifele, W.; Novak, P.; Petrat, F.-M. *Chemical Communications* **2005**, *0*, 1566-1568

(236) Chen, L.; Xie, X.; Wang, B.; Wang, K.; Xie, J. *Materials Science and Engineering: B* **2006**, *131*, 186-190

(237) Dimov, N.; Kugino, S.; Yoshio, M. *Journal of Power Sources* **2004**, *136*, 108-114

(238) Kim, I.-s.; Blomgren, G. E.; Kumta, P. N. *Journal of Power Sources* **2004**, *130*, 275-280

(239) Luo, Z.; Fan, D.; Liu, X.; Mao, H.; Yao, C.; Deng, Z. *Journal of Power Sources* **2009**, *189*, 16-21

(240) Ng, S.-H.; Wang, J.; Wexler, D.; Konstantinov, K.; Guo, Z.-P.; Liu, H.-K. *Angewandte Chemie International Edition* **2006**, *45*, 6896-6899

(241) Liu, N.; Wu, H.; McDowell, M. T.; Yao, Y.; Wang, C.; Cui, Y. *Nano Letters* **2012**, *12*, 3315-3321

(242) Iwamura, S.; Nishihara, H.; Kyotani, T. *The Journal of Physical Chemistry C* **2012**, *116*, 6004-6011

(243) Hertzberg, B.; Alexeev, A.; Yushin, G. *Journal of the American Chemical Society* **2010**, *132*, 8548-8549

(244) Wu, H.; Zheng, G.; Liu, N.; Carney, T. J.; Yang, Y.; Cui, Y. *Nano Letters* **2012**, *12*, 904-909

(245) Arie, A.; Chang, W.; Lee, J. *Journal of Solid State Electrochemistry* **2010**, *14*, 51-56

(246) Zhou, X.; Yin, Y.-X.; Wan, L.-J.; Guo, Y.-G. *Advanced Energy Materials* **2012**, *2*, 1086-1090

(247) Zhou, X.; Cao, A.-M.; Wan, L.-J.; Guo, Y.-G. *Nano Research* **2012**, *5*, 845-853

(248) Shu, J.; Li, H.; Yang, R.; Shi, Y.; Huang, X. *Electrochemistry Communications* **2006**, *8*, 51-54

(249) Wang, W.; Kumta, P. N. *Journal of Power Sources* **2007**, *172*, 650-658

(250) Zhou, Z.; Xu, Y.; Liu, W.; Niu, L. *Journal of Alloys and Compounds* **2010**, *493*, 636-639

(251) Li, Y.; Guo, B.; Ji, L.; Lin, Z.; Xu, G.; Liang, Y.; Zhang, S.; Toprakci, O.; Hu, Y.; Alcoutlabi, M.; Zhang, X. *Carbon* **2013**, *51*, 185-194

(252) Ji, L.; Zhang, X. *Electrochemistry Communications* **2009**, *11*, 1146-1149

(253) Ji, L.; Zhang, X. *Energy & Environmental Science* **2010**, *3*, 124-129

(254) Li, Y.; Lin, Z.; Xu, G.; Yao, Y.; Zhang, S.; Toprakci, O.; Alcoutlabi, M.; Zhang, X. *ECS Electrochemistry Letters* **2012**, *1*, A31-A33

(255) Gu, M.; Li, Y.; Li, X.; Hu, S.; Zhang, X.; Xu, W.; Thevuthasan, S.; Baer, D. R.; Zhang, J.-G.; Liu, J.; Wang, C. *ACS Nano* **2012**, *6*, 8439-8447

(256) Epur, R.; Datta, M. K.; Kumta, P. N. *Electrochimica Acta* **2012**, *85*, 680-684

(257) Evanoff, K.; Khan, J.; Balandin, A. A.; Magasinski, A.; Ready, W. J.; Fuller, T. F.; Yushin, G. *Advanced Materials* **2012**, *24*, 533-537

(258) Guo, J.; Chen, X.; Wang, C. *Journal of Materials Chemistry* **2010**, *20*, 5035-5040

(259) Hu, L.; Liu, N.; Eskilsson, M.; Zheng, G.; McDonough, J.; Wågberg, L.; Cui, Y. *Nano Energy* **2013**, *2*, 138-145

(260) Li, Y.; Xu, G.; Xue, L.; Zhang, S.; Yao, Y.; Lu, Y.; Toprakci, O.; Zhang, X. *Journal of The Electrochemical Society* **2013**, *160*, A528-A534

(261) Lee, H.-Y.; Lee, S.-M. *Journal of Power Sources* **2002**, *112*, 649-654

(262) Kim, J.-B.; Lee, H.-Y.; Lee, K.-S.; Lim, S.-H.; Lee, S.-M. *Electrochemistry Communications* **2003**, *5*, 544-548

(263) Park, M.-S.; Rajendran, S.; Kang, Y.-M.; Han, K.-S.; Han, Y.-S.; Lee, J.-Y. *Journal of Power Sources* **2006**, *158*, 650-653

(264) Wang, Z.; Tian, W. H.; Liu, X. H.; Li, Y.; Li, X. G. *Materials Chemistry and Physics* **2006**, *100*, 92-97

(265) Sethuraman, V. A.; Kowolik, K.; Srinivasan, V. *Journal of Power Sources* **2011**, *196*, 393-398

(266) Au, M.; He, Y.; Zhao, Y.; Ghassemi, H.; Yassar, R. S.; Garcia-Diaz, B.; Adams, T. *Journal of Power Sources* **2011,** *196,* 9640-9647

(267) Weydanz, W. J.; Wohlfahrt-Mehrens, M.; Huggins, R. A. *Journal of Power Sources* **1999**, *81-82*, 237-242

(268) Lee, Y.-S.; Lee, J.-H.; Kim, Y.-W.; Sun, Y.-K.; Lee, S.-M. *Electrochimica Acta* **2006**, *52*, 1523-1526

(269) Zhou, S.; Liu, X.; Wang, D. *Nano Letters* **2010**, *10*, 860-863

(270) Cao, F.-F.; Deng, J.-W.; Xin, S.; Ji, H.-X.; Schmidt, O. G.; Wan, L.-J.; Guo, Y.-G. *Advanced Materials* **2011**, *23*, 4415-4420

(271) Kang, Y.-M.; Lee, S.-M.; Kim, S.-J.; Jeong, G.-J.; Sung, M.-S.; Choi, W.-U.; Kim, S.-S. *Electrochemistry Communications* **2007**, *9*, 959-964

(272) Zeng, Z. Y.; Tu, J. P.; Yang, Y. Z.; Xiang, J. Y.; Huang, X. H.; Mao, F.; Ma, M. *Electrochimica Acta* **2008**, *53*, 2724-2728

(273) Kim, H.; Choi, J.; Sohn, H. J.; Kang, T. *Journal of The Electrochemical Society* **1999**, *146*, 4401-4405

(274) Yu, Y.; Gu, L.; Zhu, C.; Tsukimoto, S.; van Aken, P. A.; Maier, J. *Advanced Materials* **2010**, *22*, 2247-2250

(275) Suzuki, M.; Suzuki, J.; Sekine, K.; Takamura, T. *Journal of Power Sources* **2005**, *146*, 452-456

(276) Ahn, H.-J.; Kim, Y.-S.; Park, K.-W.; Seong, T.-Y. *Chemical Communications* **2005**, *0*, 43-45

(277) Rock, N. L.; Kumta, P. N. *Journal of Power Sources* **2007**, *164*, 829-838

(278) Chen, L. B.; Xie, J. Y.; Yu, H. C.; Wang, T. H. *Electrochimica Acta* **2008**, *53*, 8149-8153

(279) Memarzadeh, E. L.; Kalisvaart, W. P.; Kohandehghan, A.; Zahiri, B.; Holt, C. M. B.; Mitlin, D. *Journal of Materials Chemistry* **2012**, *22*, 6655-6668

(280) Liu, W.-R.; Yang, M.-H.; Wu, H.-C.; Chiao, S. M.; Wu, N.-L. *Electrochemical and Solid-State Letters* **2005**, *8*, A100-A103

(281) Buqa, H.; Holzapfel, M.; Krumeich, F.; Veit, C.; Novák, P. *Journal of Power Sources* **2006**, *161*, 617-622

(282) Lestriez, B.; Bahri, S.; Sandu, I.; Roué, L.; Guyomard, D. *Electrochemistry Communications* **2007**, *9*, 2801-2806

(283) Ding, N.; Xu, J.; Yao, Y.; Wegner, G.; Lieberwirth, I.; Chen, C. *Journal of Power Sources* **2009**, *192*, 644-651

(284) Hochgatterer, N. S.; Schweiger, M. R.; Koller, S.; Raimann, P. R.; Wohrle, T.; Wurm, C.; Winter, M. *Electrochemical and Solid-State Letters* **2008**, *11*, A76-A80

(285) Mazouzi, D.; Lestriez, B.; Roue, L.; Guyomard, D. *Electrochemical and Solid-State Letters* **2009**, *12*, A215-A218

(286) Bridel, J. S.; Azaiⱡˆs, T.; Morcrette, M.; Tarascon, J. M.; Larcher, D. *Chemistry of Materials* **2010,** *22*, 1229-1241

(287) Maver, U.; Znidarsic, A.; Gaberscek, M. *Journal of Materials Chemistry* **2011**, *21*, 4071-4075

(288) Key, B.; Morcrette, M.; Tarascon, J.-M.; Grey, C. P. *Journal of the American Chemical Society* **2011**, *133*, 503-512

(289) Bridel, J. S.; Azais, T.; Morcrette, M.; Tarascon, J. M.; Larcher, D. *Journal of The Electrochemical Society* **2011**, *158*, A750-A759

(290) Guo, J.; Wang, C. *Chem. Commun.,* **2010**, *46*, 1428–1430

(291) Magasinski, A.; Zdyrko, B.; Kovalenko, I.; Hertzberg, B.; Burtovyy, R.; Huebner, C. F.; Fuller, T. F.; Luzinov, I.; Yushin, G. *ACS Applied Materials & Interfaces* **2010**, *2*, 3004-3010

(292) Komaba, S.; Yabuuchi, N.; Ozeki, T.; Han, Z.-J.; Shimomura, K.; Yui, H.; Katayama, Y.; Miura, T.*Electrochemistry* **2010**, *79*, 6-9

(293) Komaba, S.; Yabuuchi, N.; Ozeki, T.; Han, Z.-J.; Shimomura, K.; Yui, H.; Katayama, Y.; Miura, T. *The Journal of Physical Chemistry C* **2012**, *116*, 1380-1389

(294) Han, Z.-J.; Yabuuchi, N.; Shimomura, K.; Murase, M.; Yui, H.; Komaba, S. *Energy & Environmental Science* **2012**, *5*, 9014-9020

(295) Han, Z.-J.; Yabuuchi, N.; Hashimoto, S.; Sasaki, T.; Komaba, S. *ECS Electrochemistry Letters* **2013**, *2*, A17-A20

(296) Kovalenko, I.; Zdyrko, B.; Magasinski, A.; Hertzberg, B.; Milicev, Z.; Burtovyy, R.; Luzinov, I.; Yushin, G. *Science* **2011**, *334*, 75-79

(297) Murase, .; Yabuuchi, N.; Han, Z.-J.; Son, J.-Y.; Cui, Y.-T.; Oji, H.; Komaba, S. *ChemSusChem,* **2012**, *5*, 2307-2311

(298)Chew, S. Y.; Guo, Z. P.; Wang, J. Z.; Chen, J.; Munroe, P.; Ng, S. H.; Zhao, L.; Liu, H. K. *Electrochemistry Communications* **2007**, *9*, 941-946

(299)Guo, Z. P.; Wang, J. Z.; Liu, H. K.; Dou, S. X. *Journal of Power Sources* **2005**, *146*, 448-451

(300)Liu, Y.; Matsumura, T.; Imanishi, N.; Hirano, A.; Ichikawa, T.; Takeda, Y. *Electrochemical and Solid-State Letters* **2005**, *8*, A599-A602

(301)Liu, G.; Xun, S.; Vukmirovic, N.; Song, X.; Olalde-Velasco, P.; Zheng, H.; Battaglia, V. S.; Wang, L.; Yang, W. *Advanced Materials* **2011**, *23*, 4679-4683

(302) Xu, K.; von Cresce, A. *Journal of Materials Chemistry* **2011**, *21*, 9849-9864

(303) Lee, Y. M.; Lee, J. Y.; Shim, H.-T.; Lee, J. K.; Park, J.-K. *Journal of The Electrochemical Society* **2007**, *154*, A515-A519

(304) Chan, C. K.; Ruffo, R.; Hong, S. S.; Cui, Y. *Journal of Power Sources* **2009**, *189*, 1132-1140

(305) Nakai, H.; Kubota, T.; Kita, A.; Kawashima, A. *Journal of The Electrochemical Society* **2011**, *158*, A798-A801

(306) Arreaga-Salas, D. E.; Sra, A. K.; Roodenko, K.; Chabal, Y. J.; Hinkle, C. L. *The Journal of Physical Chemistry C* **2012**, *116*, 9072-9077

(307) Martin, L.; Martinez, H.; Ulldemolins, M.; Pecquenard, B.; Le Cras, F. *Solid State Ionics* **2012**, *215*, 36-44

(308) Pereira-Nabais, C.; Åšwiatowska, J.; Chagnes, A.; Ozanam, F. o.; Gohier, A. l.; Tran-Van, P.; Cojocaru, C.-S.; Cassir, M.; Marcus, P. *Applied Surface Science* **2012**, *266*, 5-16

(309) Choi, N.-S.; Yew, K. H.; Lee, K. Y.; Sung, M.; Kim, H.; Kim, S.-S. *Journal of Power Sources* **2006**, *161*, 1254-1259

(310) Chen, L.; Wang, K.; Xie, X.; Xie, J. *Journal of Power Sources,* **2007**, *174*, 538-543

(311) Schroder, K. W.; Celio, H.; Webb, L. J.; Stevenson, K. J. *The Journal of Physical Chemistry C* **2012,** *116,* 19737-19747

(312) Etacheri, V.; Haik, O.; Goffer, Y.; Roberts, G. A.; Stefan, I. C.; Fasching, R.; Aurbach, D. *Langmuir* **2012**, *28*, 965-976

(313) Dalavi, S.; Pradeep, G.; Brett, L. L. *Journal of The Electrochemical Society* **2012**, *159*, A642-A646

(314) Song, S.-W.; Baek, S.-W. *Electrochemical and Solid-State Letters* **2009**, *12*, A23-A27

(315) Nguyen, C. C.; Song, S.-W. *Electrochimica Acta* **2010**, *55*, 3026-3033

(316) Profatilova, I. A.; Stock, C.; Schmitz, A.; Passerini, S.; Winter, M. *Journal of Power Sources* **2013**, *222*, 140-149

(317) Trill, J. H.; Tao, C.; Winter, M.; Passerini, S.; Eckert, H. *Journal of Solid State Electrochemistry* **2010**, 1-8

(318) Key, B.; Morcrette, M.; Tarascon, J.-M.; Grey, C. P. *Journal of the American Chemical Society* **2009**, *131*, 9239–9249

(319) Wu, J. J.; Bennett, W. R. In *Energytech, 2012 IEEE*, p 1-5

(320) Oumellal, Y.; Delpuech, N.; Mazouzi, D.; Dupré, N.; Gaubicher, J.; Moreau, P.; Soudan, P.; Lestriez, B.; Guyomard, D. *Journal of Materials Chemistry* **2011**, *21*, 6201-6208

(321) Li, M.-Q.; Qu, M.-Z.; He, X.-Y.; Yu, Z.-L. *Electrochimica Acta* **2009**, *54*, 4506-4513

(322) Ryu, Y.-G.; Lee, S.; Mah, S.; Lee, D. J.; Kwon, K.; Hwang, S.; Doo, S. *Journal of The Electrochemical Society* **2008**, *155*, A583-A589

(323) Choi, N.-S.; Yew, K. H.; Kim, H.; Kim, S.-S.; Choi, W.-U. *Journal of Power Sources* **2007**, *172*, 404-409.

(324) Livage, J. Vers une chimie écologique. Quand l'air et l'eau remplacent le pétrole. *Le monde* **1977**.

(325) Brinker, C. J.; Scherer, G. W. *Sol-gel Science: The Physics and Chemistry of Sol-gel Processing*; Gulf Professional Publishing, **1990.**

(326) Livage, J. *Curr. Opin. Solid State Mater. Sci.* **1997**, *2*, 132–138.

(327) Sanchez, C.; Julian, B.; Belleville, P.; Popall, M. *J Mater Chem* **2005**, *15*, 3559–3592.

(328) Sanchez, C.; Rozes, L.; Ribot, F.; Laberty-Robert, C.; Grosso, D.; Sassoye, C.; Boissiere, C.; Nicole, L. *Comptes Rendus Chim.* **2010**, *13*, 3–39.

(329) "*Pratical Surface Analysis by Auger and X-ray Photoelectron Spectroscopy*", Briggs, D.; Seah, M. P. (eds), Wiley, **1983**

(330) "*Electron Spectroscopy: Theory, Techniques and Applications*", C. R. Brundle, A. D. Baker (eds), Academic Press, New York, **1978**

(331) Fadley, C. S. *Journal of Electron Spectroscopy and Related Phenomena* **2010**, *178-179*, 2-32

(332) Siegbahn, K. et al., *Nova Acta Regiae Soc. Sci.*, **1967**, Ser. IV, 20

(333) Hertz, H. *Ann. Physik,* **1887** 31, 983

(334) Einstein, A. *Ann. Physik*, **1905** 17, 132

(335) Lewis, R. T.; Kelly, M. A. *J. Electron Spectrosc. Relat. Phenom.* **1980***, 20*, 105-115

(336) Barr, T. L. *"Practical Surface Analysis"*, Chap. 8, D. Briggs, M. P. Seah (eds), Wiley, New York **1983**

(337) Barr, T. L. *Appl. Surf. Sci.* **1983***, 15*, 1-35

(338) Shirley, D. A. "*Advances in Chemical Physics*", Vol. 23, Wiley, New York **1973**

(339) Gandubert, A. D.; Krebs, E.; Legens, C.; Costa, D.; Guillaume, D.; Raybaud, P. *Catalysis Today* **2008**, *130*, 149-159

(340) Costa, D.; Marcus, P. *Surface Science* **2010**, *604*, 932-938

(341) Scofield, J. H. *Journal of Spectroscopy and Related Phenomena* **1976**, *8*, 129-137

(342) Yeh, J. J.; Lindau, I. *Atomic data and nuclear data tables* **1985**, *32*, 1-155

(343) Seah, M. P.; Dench, W. A. *Surface and Interface Analysis* **1979**, *1*, 2-11

(344) Tanuma, S.; Powell, C. J.; Penn D. R. *Surface and Interface Analysis* **1991**, *17*, 911-926

(345) Dedryvère, R.; Leroy, S.; Martinez, H.; Blanchard, F.; Lemordant, D.; Gonbeau, D. *J. Phys. Chem. B* **2006**, *110,* 12986-12992

(346) Dedryvère, R.; Gireaud, L.; Grugeon, S.; Laruelle, S.; Tarascon, J.-M.; Gonbeau, D. *J. Phys. Chem. B* **2005**, *109,* 15868-15875

(347) Gelius, U.; in *"Electron spectroscopy"*, D. A. Shirley (ed.), **1972** North-Holland, Amsterdam, 311

(348) Edström, K.; Herstedt, M.; Abraham, D. P. *Journal of Power Sources* **2006**, *153*, 380-384

(349) Dedryvère, R. ; Laruelle, S.; S. Grugeon , S. ; Poizot , P. ; Gonbeau , D. ; Tarascon J. M. *Chemistry of Materials* **2004**, *16* , 1056-1061

(350) Winick,H.; Brown, G.; Halbach, K.; Harris, J. *Physics Today*, **1981**, *34*, 50-63

(351) Aksela, S.; Kivimäki, A.; Nyholm, R.; Svensson, S. *Rev. Sci. Instrum.* **1992**, 63, 1252-1255

(352) Schaefers, F.; Merlin, M.; Gorgoi, M. *Rev. Sci. Instrum.* **2007**, *78*, 123102

(353) Gorgoi, M.; Svensson, S.; Schäfers, F.; Öhrwall, G.; Mertin, M.; Bressler, P.; Karis, O.; Siegbahn, H.; Sandell, A.; Rensmo, H.; Doherty, W.; Jung, C.; Braun, W.; Eberhardt, W. *Nucl. Instrum. Methods Phys. Res., Sect. A* **2009**, *601*, 48-53

(354) Mitra, A.; Rimstidt, J. D. *Geochim. Cosmochim. Acta* **2009**, 73, 7045–7059.

(355) Dedryvère, R.; Gireaud, L.; Grugeon, S.; Laruelle, S.; Tarascon, J. M.; Gonbeau, D. *J. Phys. Chem. B* **2005**, *109*, 15868-15875.